THE RELATIONSHIP BETWEEN MICROSCALES AND WIND-WAVE SPECTRAL DEVELOPMENT

Craig Emery Dorman

THE RELATIONSHIP BETWEEN MICROSCALES AND WIND-WAVE SPECTRAL DEVELOPMENT

by

CRAIG EMERY DORMAN

B.A., Dartmouth College
(1962)

M.S., The Naval Postgraduate School
(1968)

SUBMITTED IN PARTIAL FULFILLMENT OF THE
REQUIREMENTS FOR THE DEGREE OF
DOCTOR OF PHILOSOPHY

at the

MASSACHUSETTS INSTITUTE OF TECHNOLOGY
and the
WOODS HOLE OCEANOGRAPHIC INSTITUTION

October, 1971

TABLE OF CONTENTS

THE RELATIONSHIP BETWEEN MICROSCALES AND WIND-WAVE SPECTRAL DEVELOPMENT

Craig Emery Dorman

Submitted to the Joint Committee in the Earth Sciences, Massachusetts Institute of Technology and Woods Hole Oceanographic Institution, in October, 1971 in partial fulfillment of the requirements for the degree of Doctor of Philosophy

ABSTRACT

The objective of this study was to describe the mechanics of wind wave generation and spectral development. Intermittency, high frequency microstructure in wind and wave fields, and strong nonlinear coupling involving a wide range of scales are shown to be crucial elements in the transfer of momentum to, from, and within the wave field. None of these elements are included in available theories.

Measurements of wave height and of the turbulent atmospheric and subsurface boundary layers were made from a small surface following platform and from a stable 38.5m spar buoy. The structure of moving gust patterns (cat's paws) is described and related to the generation of surface waves. Results from this and other background studies are then applied to a discussion of spectral growth during a two day period of active wave generation.

Cat's paws contain 'bursts' of intense turbulent stress and buoyancy fluctuations separated by quiescent 'intervals'. There is a difference of over three orders of magnitude in fluctuation strength between these features. Rapid growth rate generation of high frequency surface waves and atmospheric turbulence occurs during the bursts. The resultant microscale components aid the growth of lower frequency instabilities by strong nonlinear coupling between scales of motion and by acting as drag or roughness elements. Evidence of strong coupling between frequency bands and of weakly resonant capillary-gravity wave interactions is presented. Thermal stratification has a strong influence on fluctuation magnitude and can delay the onset of surface wave generation.

Major spectral growth is highly unsteady. Much of the momentum flux from air to sea occurs during intermittent events that are similar in nature to cat's paws, and goes directly into high frequency waves. The bursts occur predominantly over large groups of surface waves and involve strong nonlinear interactions between media and frequency bands. The long-term equilibrium balance between wind and water is disrupted by variations in surface currents. There are 'critical' wind speeds characterized by anomalous relationships between parameters of the predominantly logarithmic velocity profile.

I. INTRODUCTION

Description of the Study

This paper describes an experimental study of the mechanics of wind-wave generation and the spectral development of sea surface waves. Emphasis is placed on the time history of generation and development, and on the nature and time scales of air-sea coupling. The basic objective was to describe and illustrate the physics involved in the transfer of momentum to, from, and within the wave field. The underlying hypothesis is that this process is highly nonlinear and depends strongly on the microstructure of the wave and wind fields. The experiments were consequently focused upon investigation of intermittent interactions between variables and scales of motion.

Two separate experiments are described. The first is a detailed investigation of the structure of moving gusts. The second is an analysis of spectral growth during a two day period of increasing wind. Both separately and together their results indicate that wind-wave generation and spectral development involve strong nonlinear interactions with the wind and current fields; representation of these processes in terms of linear or weakly nonlinear coupling is inadequate.

Background

The available linear and weakly nonlinear wave generation models fail to yield satisfactory estimates of wave growth. In addition there exist unexplained anomalies such as spectral overshoot and the degenerative effect of surface slicks on long waves. This combination of qual-

itative and quantitative unpredictability indicates that the physics of wave generation and spectral development is still inadequately understood. Until the correct physics is described, there can be little significant progress in either theoretical modeling or forecasting.

Since 1957, most wind-wave generation experiments have been designed around the linear Miles-Phillips models (Miles [1957], Phillips [1957, 1966]). Early studies compared observed spectral growth with theoretical values; they soon showed that spectral shape and initial growth rates were reasonably well predicted, but that growth rates of the major portion of the spectrum were severely underestimated. Consequently, more recent work in the low frequency range has concentrated on the direct relationship between wind and wave fields in attempts to determine the adequacy of the theory's representation of momentum transfer mechanisms. The high frequency range ($f > 1hz$) has been treated as a separate entity, primarily relevant to initial generation.

Work based on the simplified linear model has essentially dealt with the general or time-averaged characteristics of wind-wave coupling and spectral development. It has neglected the relationship between portions of the wave spectrum, and in particular has deemphasized the role of high frequency wavelets and the coupling between waves and turbulence. There has thus been very little work encompassing the full range of spectral growth and relating it to interactions within and among the wind, wave, and surface current fields. Hasselmann's Hamiltonian type model (1967) was so general (and unfamiliar to field workers) that it also failed to inspire experimental investigation along these lines (with the exception of some ongoing parts of JONSWAP).

A second experimental approach to the problem of spectral growth

has been through parameterization of wind and wave fields and the development of spectral transfer functions for use in forecasting. Such studies have described the generally logarithmic nature of the atmospheric boundary layer over water, specified the characteristics of wave spectra in some detail, indicated the significance of energy transfer between wave components, hinted at the importance of high frequency elements, and yielded partially valid prediction schemes. They provide little direct information about the physics of momentum transfer processes, but rely upon theory and experience for guidance in the choice of empirically applied parameters.

It is highly unlikely that either forseeable modifications to the available models or additional parametric type studies will correct the known theoretical deficiences. Further advances will require a more complete understanding of the physics of generation. Important elements in a reevaluation of the wave generation process must include the detailed structure of the turbulent boundary layers and nonlinear couplings, both weak and strong, within and among the three fields of motion. Theoretical and experimental studies have shown that such couplings do exist. Turbulence is known to be intermittent and strongly dependent on boundary conditions; a large number of scales are involved in the dynamics of flow at typical geophysical Reynolds numbers; and the generation of waves is inseparable from the generation of turbulence. These considerations imply that wave and turbulence generation may be a strongly nonlinear process involving a large variety of forces and scales, and that the evaluation of experimental results in terms of mean values and long averaging times can easily obscure the physics. Viewed in these terms the time history of events during wave generation becomes an important factor; the

microstructure of the air and water boundary layers and the wave field reassumes great significance; and the ability to distinguish the differences between generation, transfer, and detritus becomes a major experimental goal.

The pair of experiments described herein was designed to investigate the waves and near-naviface boundary layers and to determine the nature and time scales of the important processes in wave generation and spectral development. Events ranging in duration from less than one second to two days were examined to obtain answers to the following questions:

1. What are the important time scales in the transfer of momentum to, from and among surface waves?

2. What are the nature and magnitude of the fluctuations involved in these transfers?

3. What is the nature of the coupling between media, and between scales of motion both within and between media?

4. What is the 'imprint' of wave generation in the air and in the water; and can this imprint be used to distinguish events of importance in the generation process (i.e., both to predict and to permit conditional sampling)?

5. Is there a similarity between scales, and if so, for what variables and over what range of scales does the similarity exist?

The first experiment was designed to isolate and intensively analyze an event of known significance - the 'cat's paw'. The cat's paw is an

isolated parcel of atmospheric turbulence. It contains anomalously large velocity and temperature fluctuations, and can be visually delineated by the 'dark', moving patch of high frequency waves which it creates. The second experiment yielded data from a larger system. It was designed to extend the time scales and number of forces involved to values typical of open ocean spectral development. The experiments are first individually discussed in separate papers; then the above questions are answered and the development of a wave field is described in terms of the results. An outline of experimental details is contained in appendices; complete descriptions and all significant data are available in additional reports of the M.I.T. Buoy Project.

II. THE STRUCTURE OF MOVING GUST PATTERNS (CAT'S PAWS) AND THEIR ROLE IN WAVE GENERATION

Abstract

Measurements of wave height, turbulent velocity, and temperature fluctuations within 1 meter of the sea surface were taken from a small surface following platform. The resultant data show that moving gusts are highly structured, consisting of bursts of turbulent stress separated by relatively quiescent intervals. Magnitudes of stress and buoyancy fluctuations vary between bursts and intervals by over 3 orders of magnitude. The bursts are associated with the generation of very high frequency wavelets which in turn serve to couple the wave field to the mean air flow. A large range of scales of motion interact, leading to a lognormal distribution of turbulent velocity fluctuations and to energy transfer among wave components.

Introduction

Gust patterns moving over the sea surface (cat's paws) are well-known to sailors, both those seeking a strong wind and those trying not to capsize. Cat's paws can be located by their imprint on the water surface, namely the change in surface reflectivity caused by the high frequency wavelets generated. Associated with these gusts are large magnitude, high frequency, turbulent stress and buoyancy fluctuations. Cat's paws are patches of intense air-sea interaction with correspondingly large transfers of momentum, heat, and moisture. This study reports an attempt to measure, describe, and find relationships among the fluctuations within a cat's paw, with particular reference to the mechanisms involved in momentum transfer and wave growth.

Incorporated in a cat's paw are three elements of wave generation and spectral development that are neglected in the available modern models (Jeffreys [1925, 26], Phillips [1957, 1966], Miles [1957], Hasselmann

[1967]). These are intermittency of generation, the role of wavelets in spectral development, and direct, strong nonlinear coupling between scales of motion and between the sea surface and atmospheric turbulence. The cat's paw is itself an intermittent or burst type phenomenon; the activity within it is qualitatively and quantitatively different than that observed on the average. As an experimental objective, a gust serves as a realization one type of wave generation event, with constraints determined by the environment, at Reynolds numbers unattainable in the laboratory.

Although the above three elements have been largely neglected, substantial eveidence of their significance is available in the literature. Munk noted in 1955 that while high frequency waves account for an insignificant portion of total wave energy, they play a disporportionate role in both wind stress and the development of the spectrum. This had been exemplified by Van Dorn's (1953) experiment, where the presence of a surface slick significantly reduced setup in an artificial pond. This effect of slicks was recently reemphasized (Ruggles [1969], Barger, et al, [1970]) by a demonstration that removal of wavelets resulted in a reduction of wave energy accompanied by an increase in mean wind, decrease of roughness length, and significant reduction of coherence between wind and waves.

Stewart (1961, 1967) has long maintained that much if not most of the momentum transfer from air to water is effected by wave drag. Van Dorn (1953) and Wu (1969 a, 1969 b, 1970) attribute this wave or form drag to the high frequency wavelets superimposed on larger waves. Wu further relates the wavelets to roughness height and states that the momentum flux to wavelets accounts for a substantial fraction of the wind stress; the stress appears as a normal component to the wavelets, but

feels like a tangential stress to the underlying waves. Longuet-Higgins (1969a) has shown that such a fluctuating tangential stress, occurring selectively near the crests and leading faces of longer waves where the shorter ones are 'trapped' (Munk [1955], Cox [1958]), is dynamically equivalent to a normal pressure fluctuation in quadrature with them.

The role of turbulence and turbulent Reynolds stress in wave generation is commonly viewed as minor or negligible. Miles-Phillips theory holds that the waves do not affect turbulence; Hasselmann includes a weak interaction through a disturbance of mean flow by one wave component, interaction of the disturbance with a turbulence component, and a feedback of the resulting pressure perturbation into another wave element. Stewart (1967) has shown that wave energy is typically comparable with the energy of turbulence in the entire troposphere, and consequently has suggested that while turbulence can serve as a catalyst for transfer of momentum from the mean flow, it can by itself add very little to the wave energy.

Two of the more important properties of atmospheric turbulence with respect to wave generation are intermittency and the associated large growth rates of localized high frequency instabilities (Greenspan and Benney [1963]). Laboratory experiments (e.g., Klebanoff, et al; [1962], Kline, et al, [1967]) have shown that the progression of events leading to instability and transition of laminar boundary layers involves successively the formation of travelling Tollmien-Schlichting waves, development of spanwise disturbances leading to formation of local shear layers, and explosive development of the flow into short turbulent length scales in bursts of high frequency instability fluctuations. The turbulent boundary layer is itself intermittent, with periods of intense activity

separated by relatively quiescent intervals (e.g., Frenkiel & Klebanoff [1971], Rao and Narayanan [1971]). Reverse transition is similarly abrupt (Steiner [1971]) and is due to the restoring action of buoyancy forces. Furthermore, Klebanoff, et al, (1962) demonstrated that the spatial structure of turbulent breakdown is strongly dependent on boundary irregularities, and Gupta, et al, (1968) showed that unstable oscillations induced by the simultaneous introduction of Tollmien-Schlichting waves and free surface waves resulted in a large, unpredicted amplification rate of small wavelengths.

The combined effects of intermittency, high growth rates, and boundary influence were illustrated (Mollo-Christensen [1970]) by filtering, squaring, and plotting selected frequency components from wave gauge and anemometer signals recorded during a period of wave generation. The plots showed that ripples and high turbulent wind energy were associated with groups of large amplitude, low frequency waves. This suggests that generation of waves and turbulence are coupled, intermittent, and associated with the presence of wavelets on longer wave crests. The basic roles of the high frequency waves are the coupling of wind and wave fields and the enhancement of low frequency instabilities; the wavelets are generated by bursts of high frequency turbulence, and growth rates in these local instabilities are extremely rapid and due to strong nonlinear coupling. In turn the turbulence patterns are controlled by the major wave field. The combined result is a strongly coupled system with growth rates much larger than those predicted by linear or weak coupling theory.

Implicit in this outline of spectral development is the participation of a large range of scales, coupled by nonlinear interactions. The

high frequency waves are in the capillary-gravity and capillary wave ranges. As pointed out by Stewart and Manton (1971), the important time scale for generation by turbulent pressure fluctuations (Phillips' resonance mechanism) is that of the wave group generated, i.e., the wave frequency. Similarly, the large amplification rates in shear layer instability (Greenspan & Benney,[1963]) have a typical time scale of a half period of the primary wave. Water surface waves of the capillary-gravity type have second order resonant interactions (McGoldrick [1965], Simmons [1969]) with effective time scales of two to three waves periods. Turbulent bursts or spots are similarly of short duration. It can therefore be anticipated that the generation of wavelets is a short-lived but intensive phenomenon which is capable of rapidly depleting the locally available energy of the mean flow. At the same time, as pointed out by Mollo-Christensen (1971), "work done on the water to make waves must equal a stress times a strain, and the reactions of the stresses on the water act on the air to produce turbulence."

The intermittency and selectivity of the location of high frequency waves on the underlying long ones is only partially attributable to the coupling with atmospheric turbulence. Variations in surface tension near the crests of steep waves produce a local increase in normal stress which in turn generates capillary waves (Longuet-Higgins,[1963], Crapper [1970]). The short waves steepen on the forward faces of longer waves due to horizontal contraction; this leads to breaking and the transfer of mass and momentum from the short to the longer waves (Longuet-Higgins [1969b]). Hasselmann (1971) has shown that the work done on the long waves by the "interaction stresses" is balanced to first order by the loss of potential energy involved in mass transfer, and to second order results in

a slight attenuation of the longer waves. The basic physical idea suggested by Longuet-Higgins has not been negated by Hasselmann's rescaling of the terms; there does exist a considerable energy interchange between scales of motion within the water, and this interchange is strongly dependent on the presence and location of high frequency waves.

A similar interplay occurs in the atmosphere. Mollo-Christensen (1970, 1971) has shown that when the velocity field is described in terms of three components - mean flow, long wavelength and short wavelength fluctuations - the resultant energy equations involve interaction or production terms, in the form of stress times strain, among all three components. If the interactions occur with the proper phase relationship, a primary instability can be enhanced by the work done by Reynolds' stresses of the secondary instability, and both instabilities can for a while gain energy from the mean flow. This type of interaction can occur similataneously on many scales, in both the wind and the wave fields. The essential points are that Reynolds stresses are inseparable from the generation of fluctuations, and that by nonlinear couplings between scales, the growth of short waves can enhance the growth of longer ones.

On the basis of these considerations from the literature, it is suggested that the major reason for the inability of available theories to satisfactorily predict spectral growth is that they fail to include the correct physics of the momentum transfer process. The inclusion of strong nonlinear couplings tremendously increases the complexity of the problem (and makes it as yet mathematically intractable), but appears to be necessary for a proper understanding of wave generation.

The cat's paw is a readily accessible phenomenon that provides a realistic geophysical framework within which to initially investigate these

ideas. The wind tunnel is too small for studies at the Reynolds numbers and hence the range of scales involved in the proposed mechanisms, and the dynamic range of wave height on the open ocean makes detailed near-naviface measurements exceedingly difficult. This experiment was designed to investigate the time history of cat's paws and to determine the scales involved in them. The primary features sought were the relative magnitudes of the fluctuations in air and water and an indication of coupling between media. Thus the variables of major concern were turbulent Reynolds stress and buoyancy fluctuations, and high frequency wave activity. Interactions between scales of motion were examined in terms of the basic cat's paw structure, turbulent velocity fluctuations, and nonlinear wave interactions. Specifically, answers were sought to the following questions:

Is there a demonstrable relationship between the generation of turbulence and the generation of high frequency waves? Is the process intermittent or is it typically near the mean or average flux?

What is the evidence for coupling between scales of motion?

On what time scales does instability-associated high growth rate generation occur?

What is the imprint of a generation 'event' in the air and water?

The Experiment

The measurements were taken from a small (1 m long) surface following catamaran (cat; Figure 1). The cat was free in pitch, roll, and heave (design natural frequency 1.5 hz) and restrained in yaw and horizontal position. It could be oriented into the wind through the full range of acceptable fetch directions. The experiment was conducted in March 1971 from the dock of the M.I.T. Yacht Club on the Charles River, Cambridge, Massachusetts.

Instruments included 6, DISA type 55A81 hot film anemometers, a capacitance wave gauge with .076 cm diameter sensor, and VECO 42A70 (air) and Fenwall K496 (water) thermistors balanced against precision resistors in a differential bridge circuit. Subsidiary equipment included an accelerometer for sensing catamaran motion and cup and propeller anemometers for determining mean wind. Data were recorded on magnetic tape in analog mode, accompanied by a voice narration that was later used for subjective conditional digitization.

Two of the hot films were orthogonally mounted to permit determination of horizontal (U) and vertical (W) velocities and hence Reynolds stress ($-\overline{\rho u' w'}$). The sensors were attached to the forward vertical cat support to minimize tilt ($< 1°$ mean, $< 3°$ fluctuating). Table 1 lists the instrumental arrangement and mean conditions for the seven 2-hour runs that were analyzed. Data from runs 2, 4, and 6b, which represent the full range of conditions encountered, were selected for presentation herein.

The data were analyzed using a combination of digital and analog methods. Pre-analysis, demodulation, and filtering (100 hz low pass) were analog. The data were then digitized at 250 hz and recorded on 7

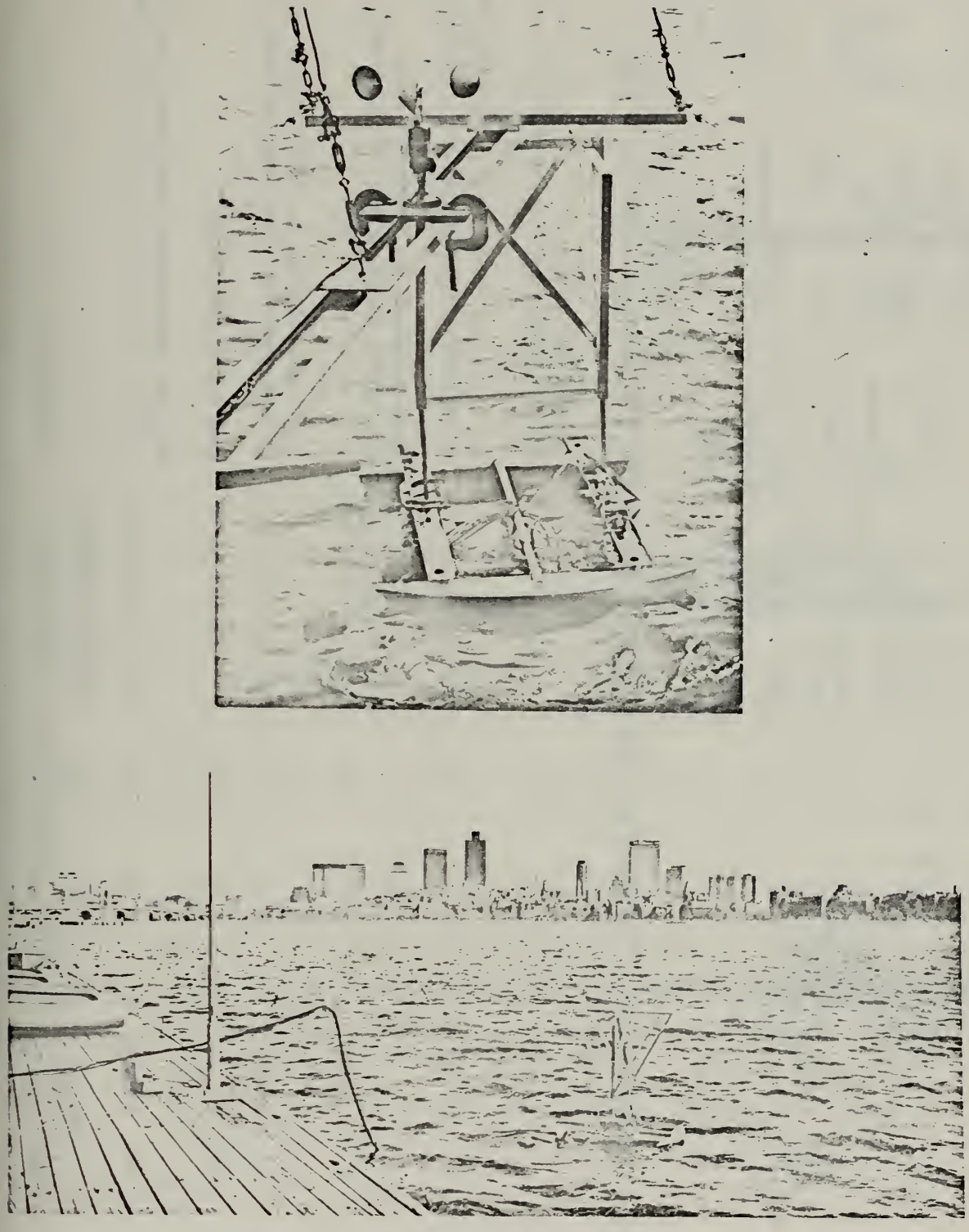

Figure 1. Catamaran and Support Structure

TABLE 1: Catamaran Runs (2 hour duration)

Run #	Insts.	U m/sec	T_{air} °C	T_{H2O} °C	$Ri_b = 2(\Theta_a - \Theta_w)/U_a^2$	Mean waves Period, Height	Comments
2	A+	W,6-8	5.0	4.12	.05	1.3-1.7 sec,4-6"	Gusting to 12 m/sec, many cat's paws and active generation; sea nearly fully devlpd
3A	A+	W, 2	6.7	4.20	1.25	calm	Low wind, few gusts
3B	A+	W,0-5	7.2	4.22	..75	calm-1 sec, .5"	Two periods of slow wind increase to 5m/sec, then return to calm.
4	A	E/W,3-5	11.9	5.0	.85	start 1.2sec,5-6" end 1 sec, 2"	Generally dying winds, gusty near start. Some segments in natural slick.
5	B	W,4-5	9.2	5.4	.31	1.35, 4-5"	Occasional gusts to 8m/sec; large T fluctuations from cloud passage;some slicks
6A	B	E/W,0-1	9.4	5.8	7.2	calm	Sunny, light and variable winds with occasional gusts.
6B	C	E/W,0-1	11.2	6.9	8.6	calm	Same as 6A

+: H.F. 10 inoperative. *: based on long averages; for 6B,e.g., R_b roughly ≤ .16 for a gust

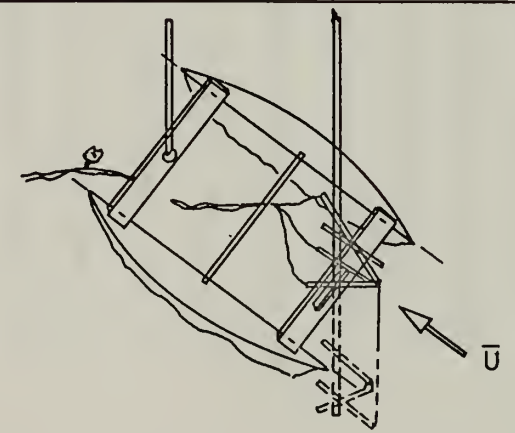

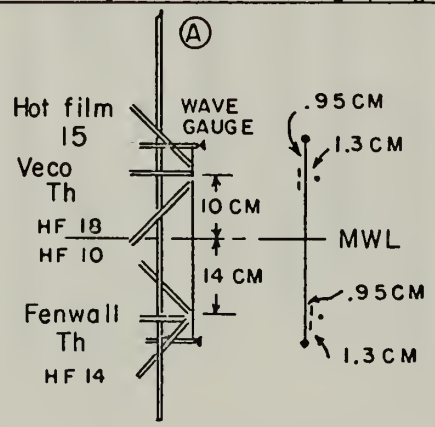

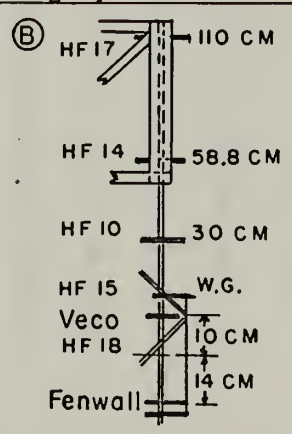

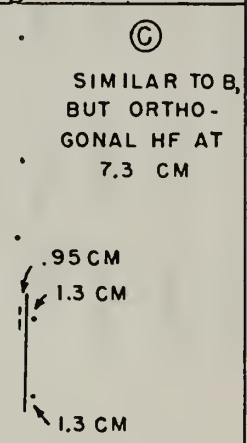

track digital magnetic tape. Final analysis was accomplished using locally generated software on the M.I.T. IBM 360. All available channels were analyzed simultaneously for each run segment of interest. Extensive use was made of graphical output from a Stromberg-Carlson 4020 plotter.

The major contraints on the analysis were the cat motion and the nature of the cat's paw itself. Cat motion could be successfully removed from the data, but the very fact that it did follow the low frequency waves prevented meaningful quantitative estimates of spectral growth. The cat's paw will be shown to consist of patches of strong fluctuations separated by relatively quiescent intervals. Thus time averaging and the selection of data segments for analysis had to be very carefully done to avoid distortion of fluctuation magnitudes and to prevent obscuring events of importance. The time history of events proved to be of crucial importance. Further, the momentum transfer processes involve both internal and external interactions; they are highly non-stationary, non-homogeneous, and anisotropic, so that the standard statistical theories of turbulence are inapplicable and time averaging could not be substituted for ensemble averaging. Therefore data from any one gust possesses little if any statistical significance, and conclusions could be drawn only on the basis of the change with time in the individual properties of a variable and in the relationship between variables, and then tested on the basis of similarity among a number of identically treated events. Each cat's paw, and each segment within a cat's paw, must be viewed as a single realization. No meaningful error bars or confidence limits can yet be placed on the data since a statistically insufficient number of events has been evaluated. The data were subjectively viewed

in terms of the relative changes with time, the sequence or pattern of events, and the relationship between variables in both time and frequency domains. Reported magnitudes can be considered only as order of magnitude estimates. This is particularly true of wave autospectra, where filtering and the necessarily very short averaging times preclude even rough estimates of the magnitude of spectral growth and decay.

Emphasis was placed on understanding the intermittent nature of turbulent fluctuations, their interaction with the free surface, and changes in the presence and structure of capillary-gravity and pure capillary waves. These features were then evaluated in terms of their significance to the generation of surface waves.

Results and Discussion

A. Cat's Paw Structure in Time and Frequency. Separating velocity and temperature fields into steady (U,T) and fluctuating (u',T') components, the equation for the total kinetic energy of turbulence can be written (Lumley and Panofsky [1964])

$$\frac{\rho}{2}\frac{\partial}{\partial t}\overline{(u_i'u_i')} = -\rho\overline{u_i'u_j'}\frac{\partial \bar{U}_i}{\partial x_j} + \frac{g}{T_o}\rho\overline{u_i'T'}\delta_{i3} - \frac{\partial u_i'}{\partial x_j}\mu\left(\frac{\partial u_i'}{\partial x_j} + \frac{\partial u_j'}{\partial x_i}\right) + \text{diffusion} + \text{divergence terms},$$

(A) (B) (C)

where Einstein's summation convention holds, μ is dynamic viscosity, and T_o the temperature of the undisturbed atmosphere. (A) is commonly called the production term; it represents the turbulent energy produced by fluctuations detracting energy from the mean motion by instability mechanisms as work=stress x strain. (B) represents work done against buoyancy in terms of heat flux, $H_i = \rho C_p \overline{T'u_i'}$; an upward heat flux acts as a source, a downward flux a sink of kinetic energy. (C) is the rate of working against viscous forces and represents dissipation of energy to heat (ϵ).

The term $-\rho\overline{u'w'}$ from A is the Reynolds stress (τ); it commonly represents momentum flux from the air to the sea surface (downward flux for $\tau > 0$). This transfer across the boundary acts as an additional sink term as seen from the viewpoint of atmospheric turbulence. Similarly, it is apparent that the reaction stresses caused by the generation of waves acts as a source term for the generation of turbulence. Thus generation of waves and generation of turbulence are inseparable.

Horizontal (U) and vertical (W) velocities, termperature (T), wave height (η), Reynolds stress ($\tau = -\rho u'w'$), and buoyancy ($\beta = w'T'$) were measured or computed and related in time and frequency domains to depict cat's paw structure. All data were taken at a single horizontal location, and w' and T were measured at only one height in air and water; it was therefore impossible to determine a meaningful quantitative energy balance, although the qualitative interplay of production and stability terms was apparent.

A.1. Individual Variables. Figures 2 through 7 (Figs. 2 - 7) depict the imprint of three gusts. Fig. 2, from run 2, shows the fluctuations in η , U, T, τ , and β for 40 seconds (4, 10-second time periods [T.P.]) starting just in advance of the leading edge of a gust and ending aft of the trailing adge. Fig. 3 shows samples of the computer generated (SC-4020) plots from which Fig. 2 was drawn (W is also shown). (The arrows and slant numerals on the τ plot of Fig. 2 indicate the 2-second and 1-second segments chosen for detailed analysis.) Fig. 4 and Fig. 5 are similar representations of a cat's paw from run 4. η ,U, W, τ , a switch or intermittency function of $\tau \geq 100$ dynes/cm^2, T, T_{water}, and τ_{water} are shown. The three non-consecutive T.P. are from before the gust, near the leading edge, and about 5 seconds later, still within the

gust. Fig. 6 and Fig. 7 are similar diagrams from run 6B. In run 6B there are three consecutive 10-second T.P. starting just at the leading edge, and one T.P. from 10 seconds after the gust. These gusts were selected to illustrate the full range of velocity and bulk stability values encountered (Table 1).

The basic features in all three runs are as follows. The leading edge of a gust is marked by rapid increases in both mean and turbulent wind velocities. Within a very short time (< 1 second), the air temperature drops as the boundary layer is mixed and destabilized by the turbulent stresses. T continues to drop as the winds increase; it starts to increase after U has reached its maximum value. There is commonly a secondary increase in U near the trailing edge that causes an additional drop of T. In run 6B, this second T drop is more rapid than the first, since the boundary layer has not yet recovered its initial static stability and the stress fluctuations are consequently more effective in mixing. After gust passage, T rapidly rises to its initial value as the boundary layer restabilizes. There is no clear-cut relationship between atmospheric variables and the low frequency wave field or water temperature.

Both τ and β traces are highly intermittent. There are bursts of high frequency, large magnitude fluctuations, separated by quieter intervals. Further, there are well-defined sub-bursts and intervals within the larger bursts. The τ fluctuations are a maximum during increasing wind, but are not restricted to these periods. They are strongest and contain most high frequency components not at the gust leading edge, but rather in the central bursts, after the boundary layer has been mixed and near the point of U_{max}. Bursts in τ are generally asso-

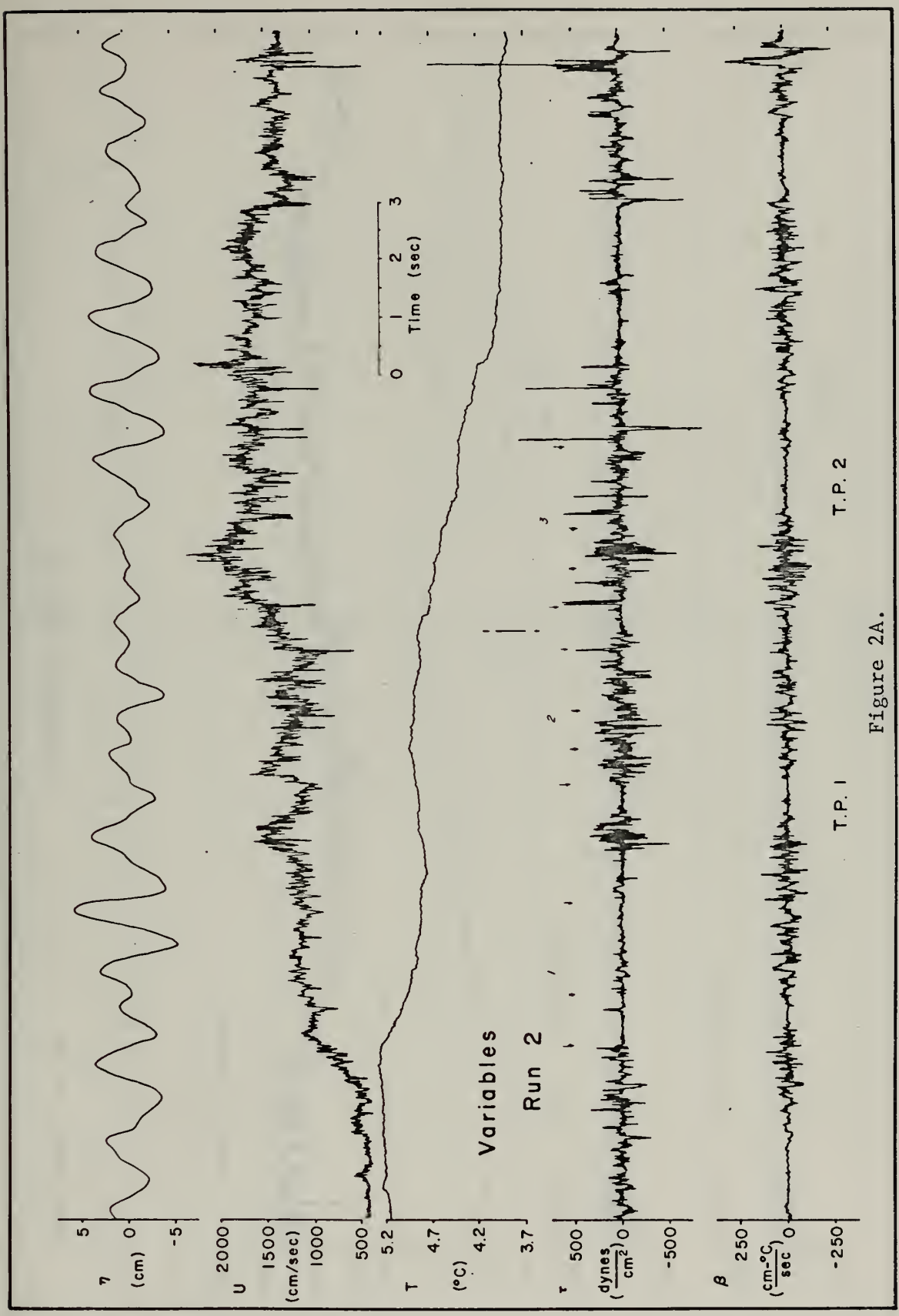
η
(cm)
5
0
-5
U
(cm/sec)
2000
1500
1000
500
T
(°C)
5.2
4.7
4.2
3.7
0
1
2
3
Time (sec)
Variables
Run 2
τ
(dynes/cm²)
500
0
-500
β
(cm.°C/sec)
250
0
-250
T.P. 1
T.P. 2

Figure 2A.

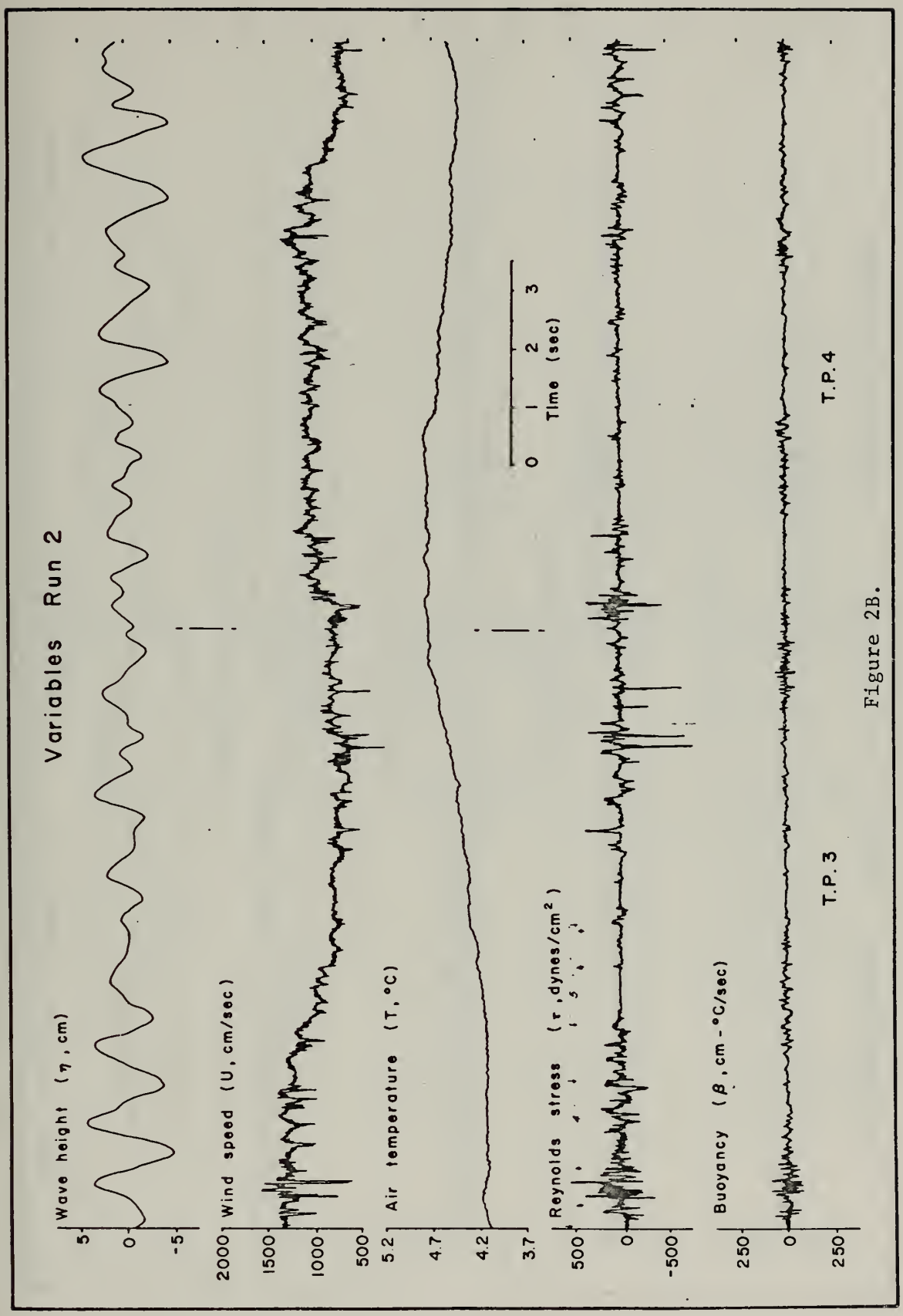
Variables Run 2
Wave height (η, cm)
5
0
-5
Wind speed (U, cm/sec)
2000
1500
1000
500
Air temperature (T, °C)
5.2
4.7
4.2
3.7
Reynolds stress (τ, dynes/cm²)
500
0
-500
Buoyancy (β, cm - °C/sec)
250
0
250
0 1 2 3
Time (sec)
T.P.3
T.P.4

Figure 2B.

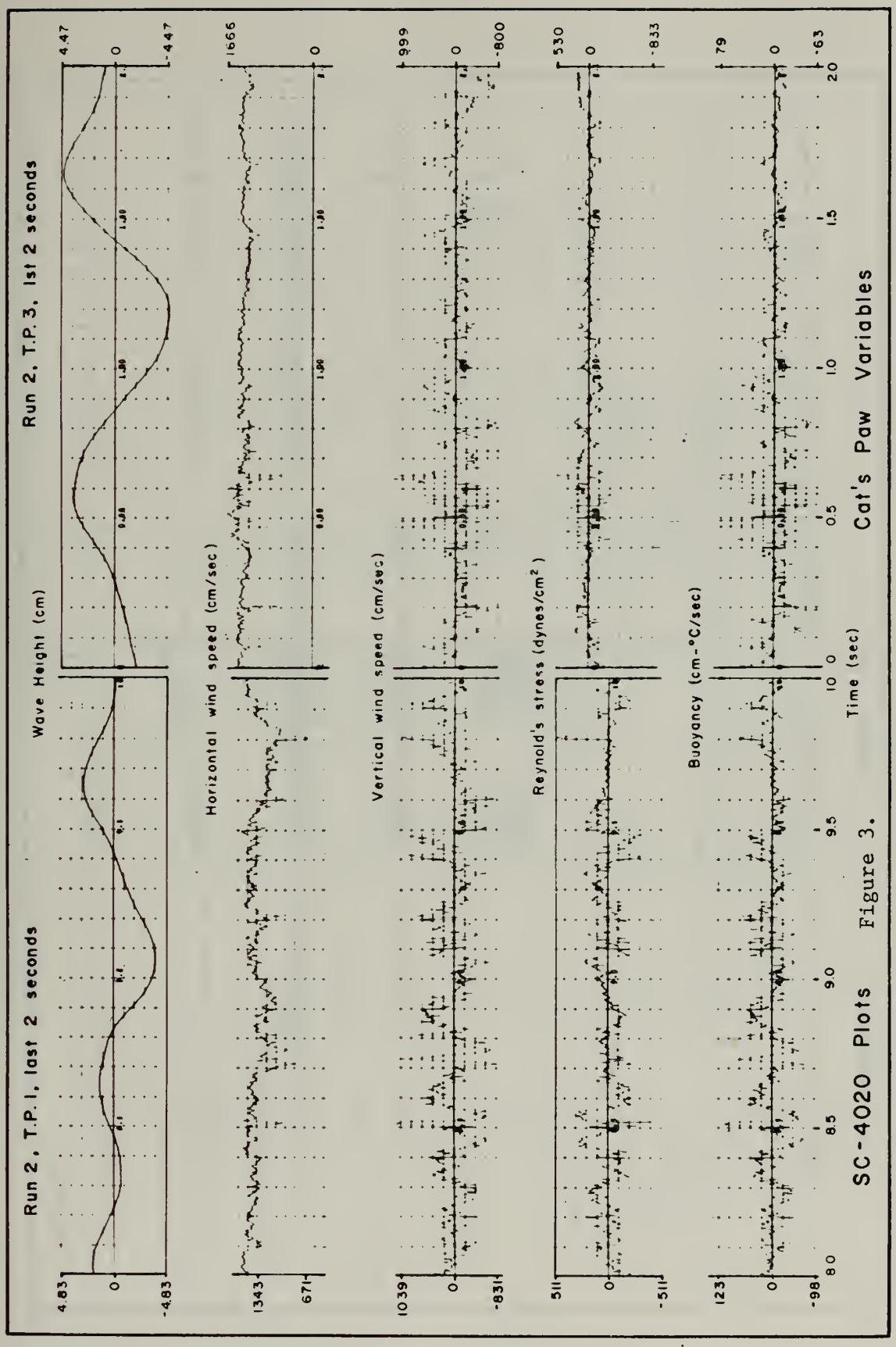

SC-4020 Plots Figure 3. Cat's Paw Variables

Figure 4. Variables Run 4

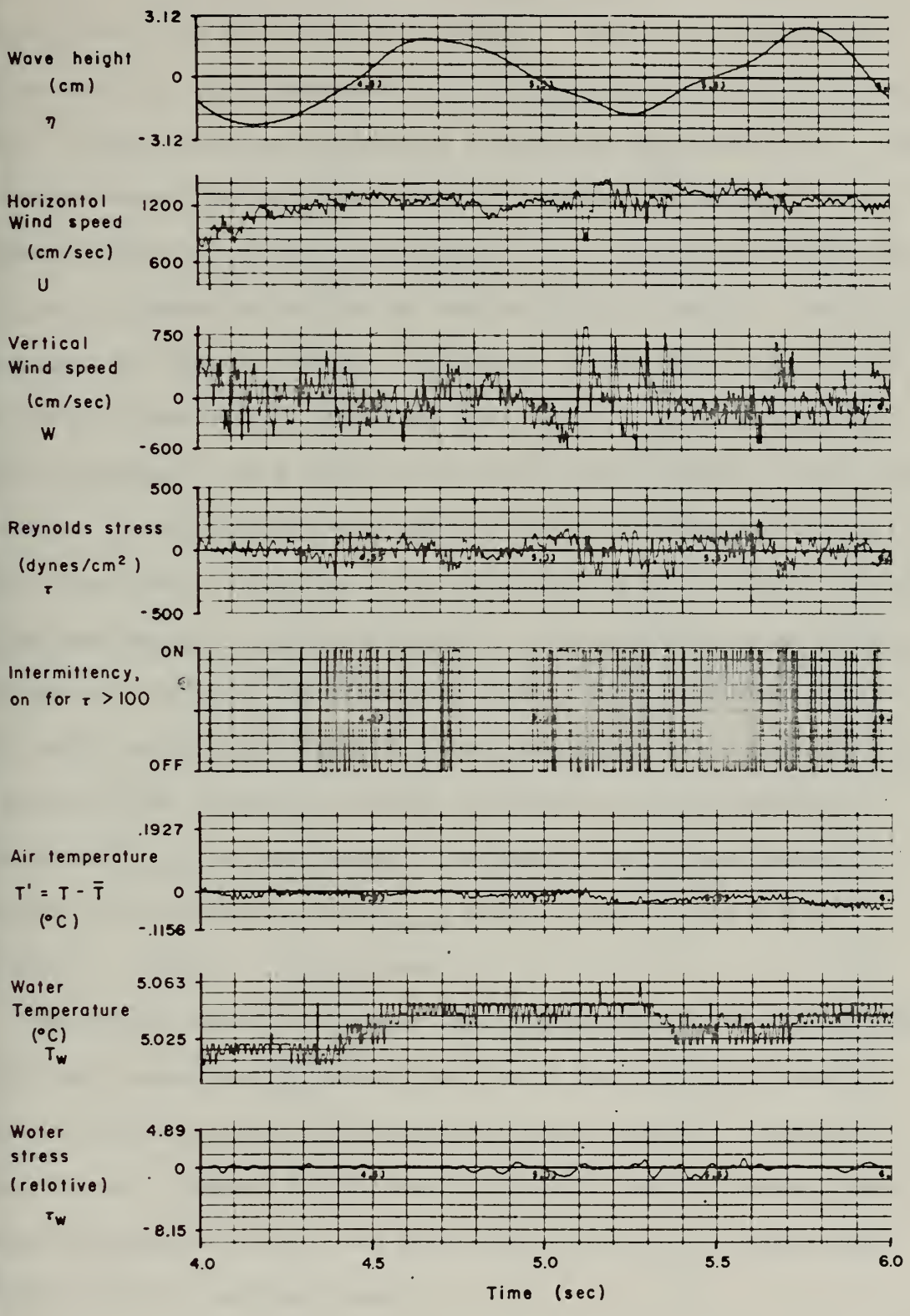

Computer Plot of Cat's Paw Variables (SC-4020)
Run 4, T.P.2, seconds 4-6

Figure 5.

ciated with similar but shorter and weaker events in β ; such coupled events are followed by T decreases. Bursts in β also occur independently or with relatively stronger magnitude than the τ fluctuations. These events are followed by a levelling off or rise in T. The stress dominated fluctuations destabilize and mix the boundary layer, and buoyancy forces act rapidly to restratify it. The buoyancy forces are relatively stronger during run 6B, with high bulk stability. Here the sub-bursts are clearly evident. Comparison of the three runs, and of the two T.P. from run 6B, indicates that there are both stronger and higher frequency τ and β fluctuations during higher winds. In the stable run 6B, β fluctuations die out before those in τ ; in nearly neutral run 2, even small τ anomalies cause variations in β . τ water fluctuations are also seen to be intermittent. They appear to occur during atmospheric bursts and under breaking waves. T_{water} fluctuations are very small, and strongly coupled to the wave field (i.e., they are due to motion of the thermistor through the vertical stratification); a small mean T_{water} decrease results from mixing during the passage of the gust. (The spikes on the T_{water} traces of Fig. 5 are due to least bit noise in the digitizer.)

The overall pattern indicates that fluctuations in the leading edge of the gust cause initial destabilization of the stratified boundary layer. This is followed by intermittent large magnitude instability fluctuations. Buoyancy forces start to restabilize the boundary layer during quiescent intervals, and fully restore stability within 10-15 seconds after the gust has passed.

The stress mean values, $\langle\tau\rangle_{10\,sec}$, are on the order of 10^{1} dynes/cm^2 for run 2, 5 x 10° for run 4, and 10° for run 6B. $\langle\beta\rangle_{10\,sec}$ is approximately

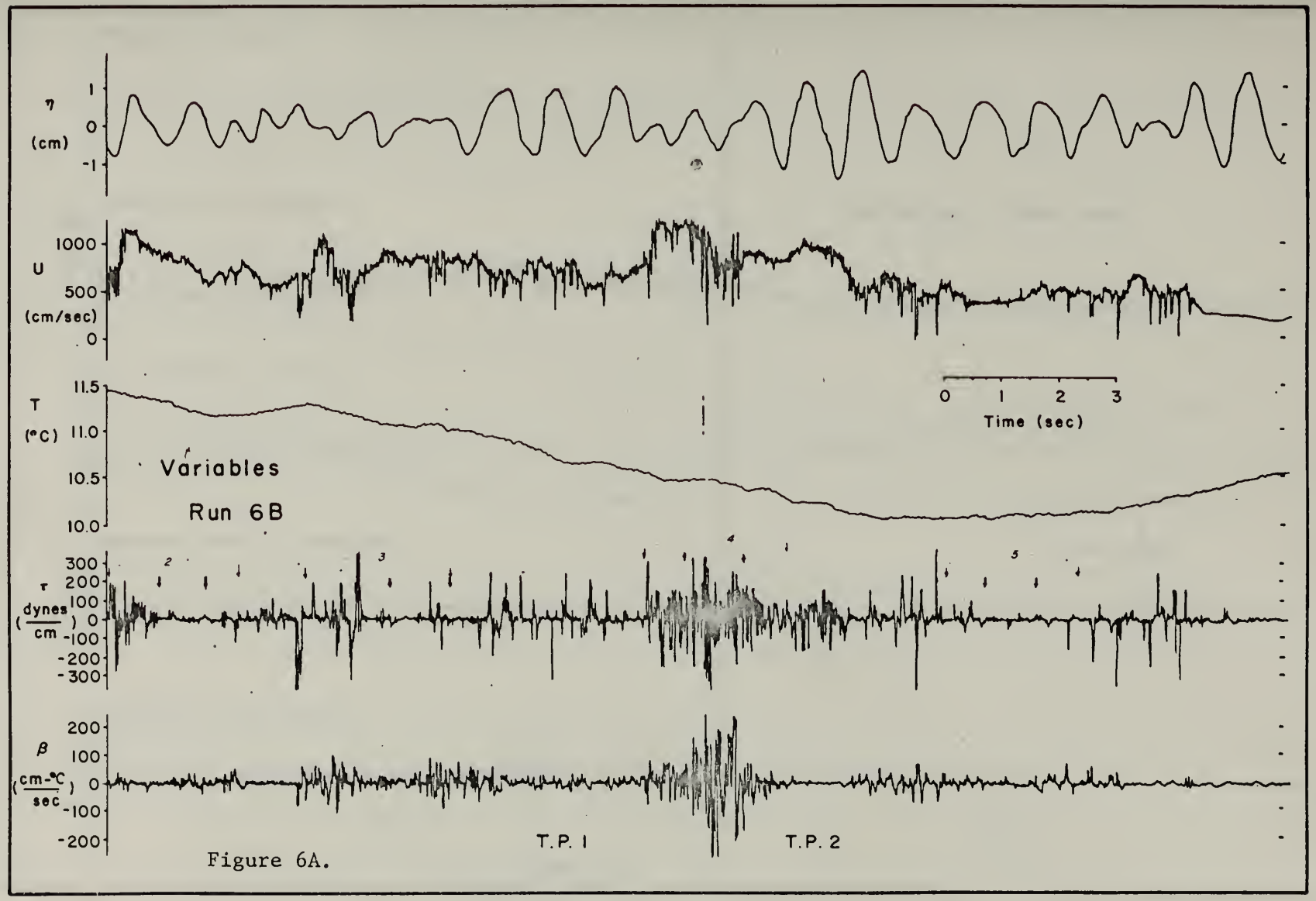
η
(cm)
1
0
-1
U
1000
500
(cm/sec)
0
T
(°C)
11.5
11.0
10.5
10.0
0 1 2 3
Time (sec)
Variables
Run 6B
τ
(dynes/cm)
300
200
100
0
-100
-200
-300
2
3
4
1
5
β
(cm-°C/sec)
200
100
0
-100
-200
T.P. 1
T.P. 2

Figure 6A.

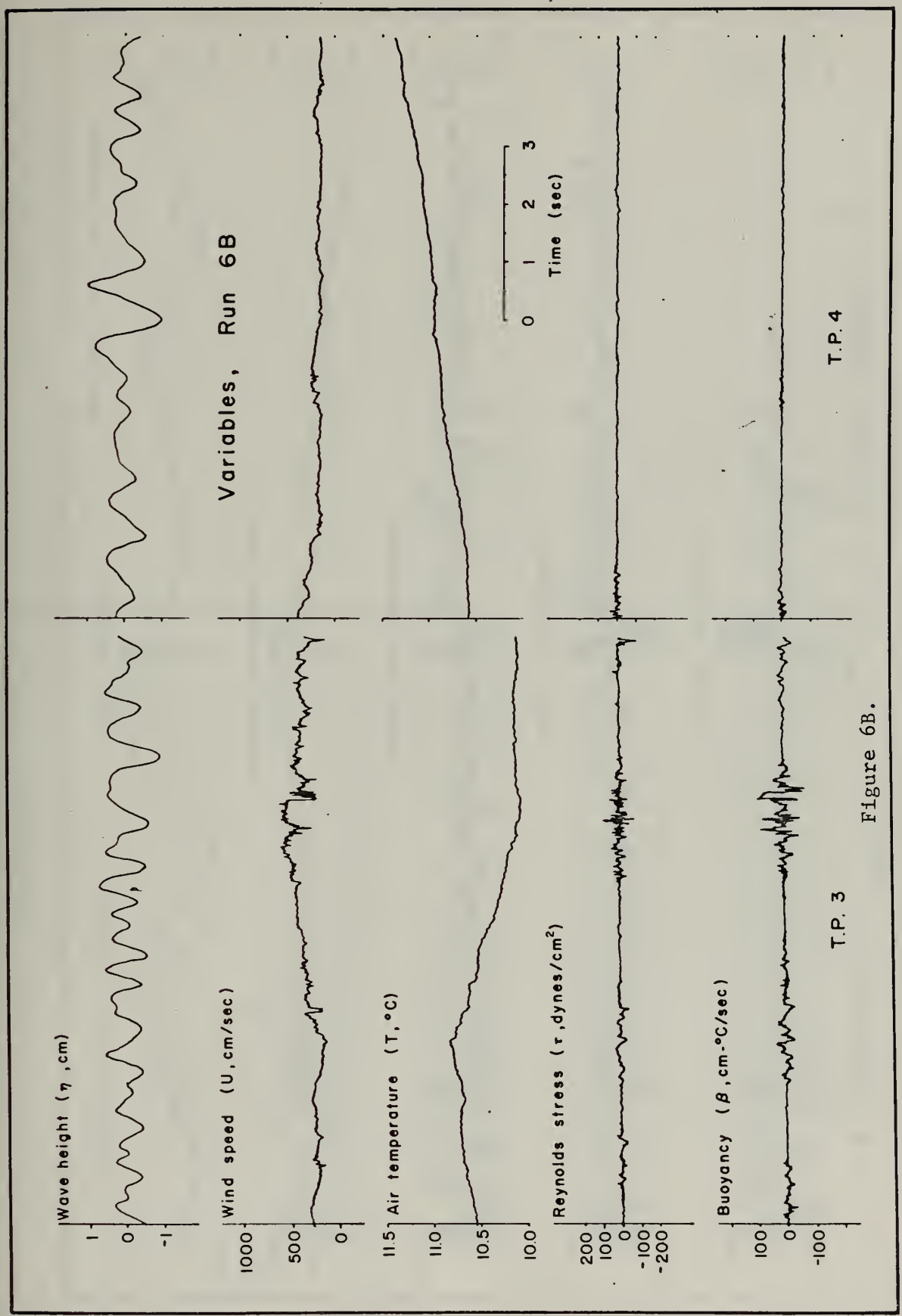
Variables, Run 6B
Wave height (η, cm)
1
0
-1
Wind speed (U, cm/sec)
1000
500
0
Air temperature (T, °C)
11.5
11.0
10.5
10.0
Reynolds stress (τ, dynes/cm²)
200
100
0
-100
-200
Buoyancy (β, cm-°C/sec)
100
0
-100
0 1 2 3
Time (sec)
T.P. 3
T.P. 4

Figure 6B.

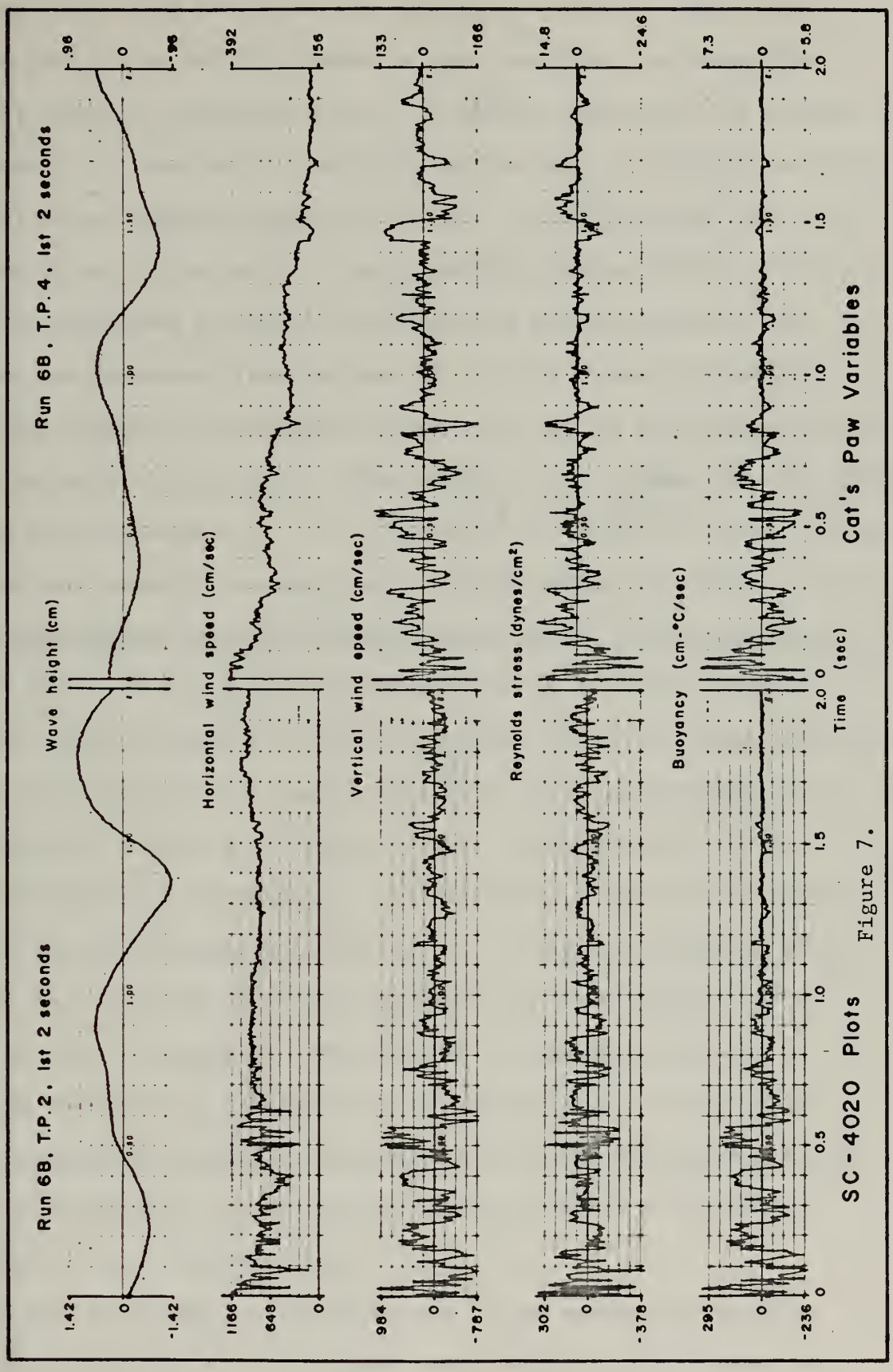
Run 68, T.P.2, 1st 2 seconds
Wave height (cm)
Run 68, T.P.4, 1st 2 seconds
Horizontal wind speed (cm/sec)
Vertical wind speed (cm/sec)
Reynolds stress (dynes/cm²)
Buoyancy (cm-°C/sec)
Time (sec)
SC-4020 Plots
Cat's Paw Variables

Figure 7.

-10^{-1} cm- °C/sec for run 2, and $+10^{-1}$ for runs 4 and 6B. These values are consistent with the differences in mean conditions and comparable with the commonly assumed values used in dynamic modeling of the exchange processes (τ = 1 dyne/cm^2, H = $3x10^{-3}$ gm-cal/cm-sec). The 'instantaneous' (250 hz) values commonly approach or exceed $\tau \sim 10^3$ dynes/cm^2 and $\beta \sim 3x10^2$ cm-°C/sec in the bursts. The strong high frequency fluctuations thus have amplitudes typically three orders of magnitude greater than the mean, or departures from the mean of 10 to 50 standard deviations.

Similar types of measurements taken 5.6 to 22.6 m over a wheat field during unstable stratification (20 hz sampling rate) (Haugen, et al, [1971]) yielded burst magnitudes of $\tau \sim 10^2$ dynes/cm^2, $\beta \sim 3x10^2$ cm °C/sec. Burst duration was roughly 10 seconds, and $< U >_{15MIN.} \sim 600$ cm/sec. This data also showed the presence of bursts within bursts. McBean (1970) also found similar values over land, with a strong effect of stability (momentum transfer efficiency decreased and heat transfer efficiency increased with decreasing stability). The major qualitative patterns of intermittent gusts are thus similar over land and water. Quantitatively, the time interval selected for averaging is deterministic in estimates of instantaneous fluctuation magnitude (Section C). A 15-minute averaging period for the cat's paw data would have increased the above estimates by at least an order of magnitude. The difference in magnitude between cat and land results is an indication of the significance of stability and the enhancement of frequency and magnitude of stress fluctuations caused by the participation of a fluctuating boundary capable of supporting well-defined high frequency waves.

Fig. 8 shows some typical histograms of the individual variables from the 10 second T.P. of all three runs. Fluctuation magnitudes and

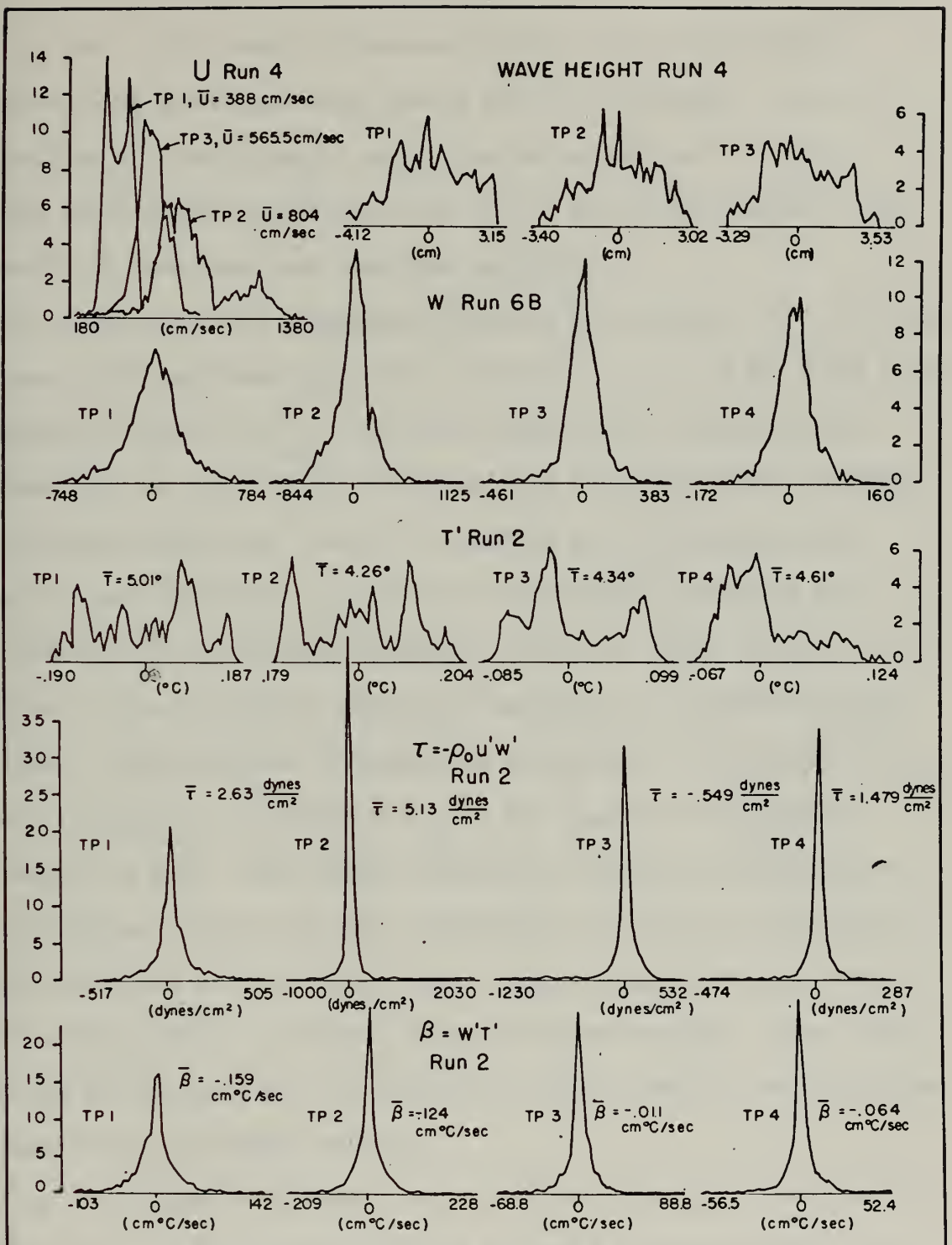

SAMPLE HISTOGRAMS FROM RUNS 2, 4, & 6B

10 SECOND SEGMENTS

Distributions in % of total samples (2520) per interval

Figure 8.

variance are much larger during than before or after the gusts; the peakedness of the τ, β, and w histograms is due to the high frequency fluctuations and consequent large number of axis crossings. U and T' distributions are more unimodal after than during the gust. There are few other basic differences between the T.P.'s for any one variable when the relatively long 10-second intervals are used.

Fig. 9 shows typical autospectra based on the 10 second T.P. (6 degrees of freedom; 90% confidence limits are $.63 \times 10^{n-1}$ to 1.74×10^{n} for a spectral density estimate of 10^{n}). With this comparatively long averaging time there are only generalized differences in frequency content between gusts and mean conditions. With the exception of the wave gauge data, the spectra are fairly white, with (note run 6B data) a slightly more rapid drop-off with increasing frequency in the T.P. after the gust. As also shown in the time plots, the high frequencies are augmented during the bursts. The differences in magnitude between gust and no gust conditions are apparent; the peaks of $\Phi_{\tau\tau}(f)$ and $\Phi_{\beta\beta}(f)$ are 3 decades lower after the gust. This basic similarity of pattern, but difference in high frequency content and major difference in intensity reflects the patterns displayed in Fig. 7 where the τ and β scales have been determined by the computer on the basis of the 10-second extrema. Wave propagation and the presence of long period wave groups prohibit any deductions from magnitudes of the wave spectra.

Fig. 10 displays the changes in the 0.5 second vertical profiles of U from run 6B. It also shows $< U >$ 0.5 sec and a measure of the turbulent kinetic energy production term. Profile perturbations, the development of unstable shear layers, and turbulent production occur predominantly during bursts. As with the τ and β fluctuations, production has

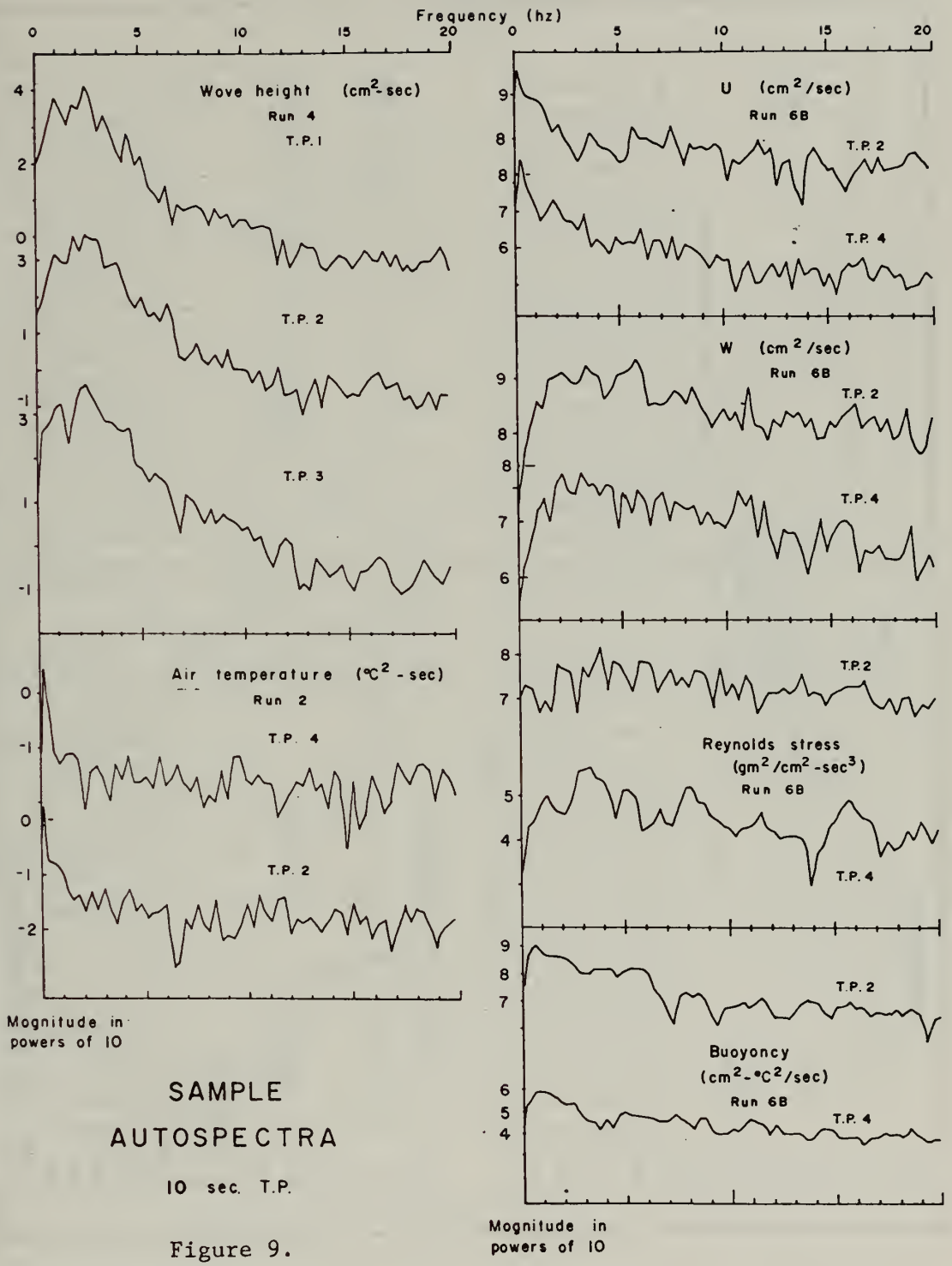

SAMPLE AUTOSPECTRA

10 sec. T.P.

Figure 9.

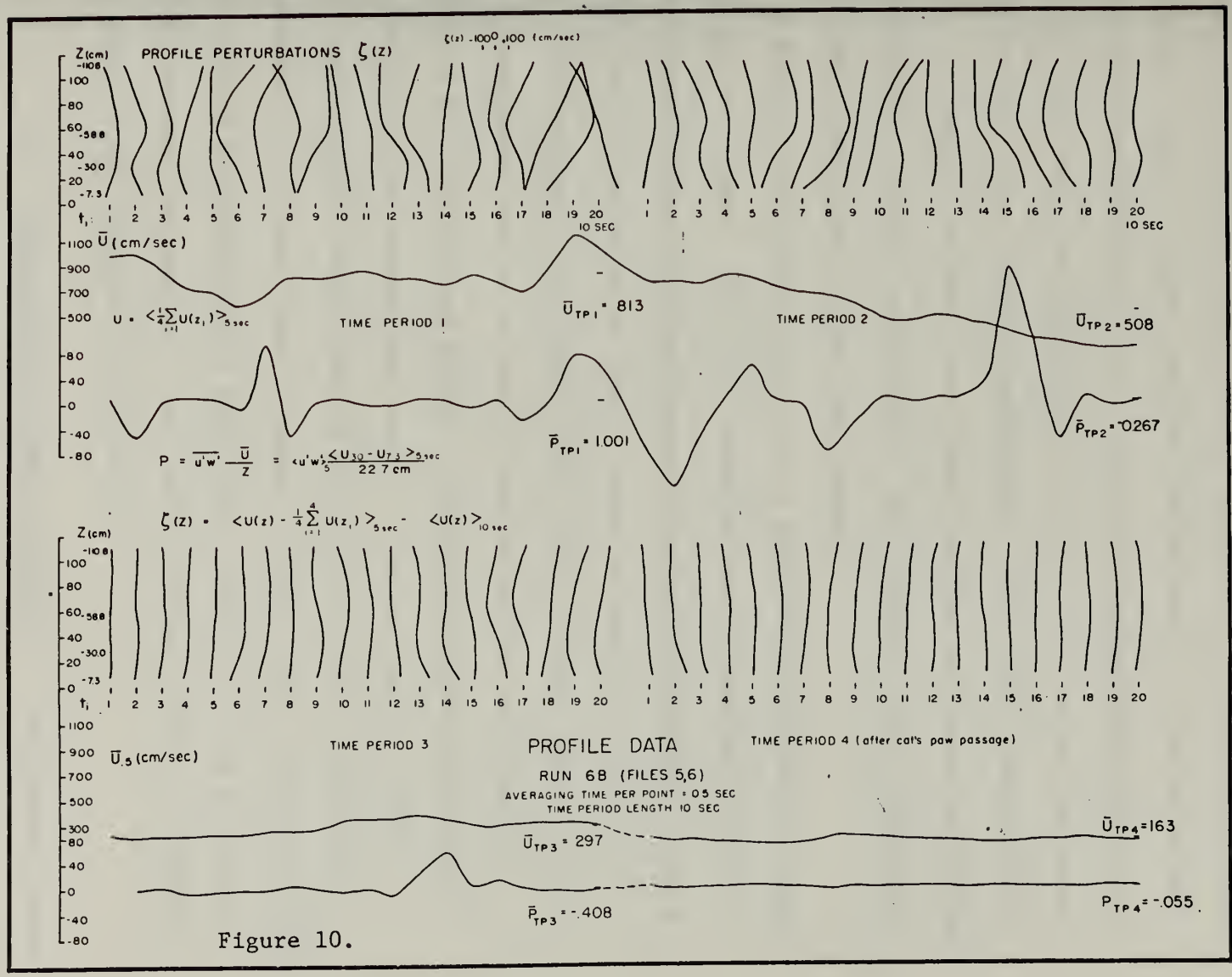
PROFILE PERTURBATIONS ζ(Z)
Z(cm)
ζ(z) -100 0 100 (cm/sec)
10 SEC
Ū (cm/sec)
U = ⟨¼ Σ U(z_i)⟩_5 sec
TIME PERIOD 1
Ū_TP1 = 813
TIME PERIOD 2
Ū_TP2 = 508
P = u'w' Ū/Z = ⟨u'w'⟩_5 ⟨U30 - U7.3⟩_5 sec / 22.7 cm
P̄_TP1 = 1.001
P̄_TP2 = -.0267
ζ(Z) = ⟨U(z) - ¼ Σ U(z_i)⟩_5 sec - ⟨U(z)⟩_10 sec
Ū_5 (cm/sec)
TIME PERIOD 3
PROFILE DATA
RUN 68 (FILES 5,6)
AVERAGING TIME PER POINT = 0.5 SEC
TIME PERIOD LENGTH 10 SEC
TIME PERIOD 4 (after cat's paw passage)
Ū_TP3 = 297
Ū_TP4 = 163
P̄_TP3 = -.408
P_TP4 = -.055

Figure 10.

a range of ± 3 to 4 orders of magnitude and is highly intermittent. The comparatively long averaging times (0.5 sec) are incapable of showing the extremely rapid fluctuations within the bursts; instead, the profile changes are similar to those that would be produced by a set of eddies propagating past the sensor array. Again, the maximum turbulence production occurs after the leading edge in T.P. 2, i.e., after the atmospheric boundary layer has been destabilized. The profile remains nearly steady, and production nearly zero, after the gust has passed and thermal stratification has been reestablished. Both stability and intermittency are of major importance in gust time history.

A sample time history of three cat's paws thus indicates that gusts are highly structured. Averaging techniques such as spectra and histograms tend to obscure the significance of the microstructure. τ and β fluctuations in bursts are at least 3 orders of magnitude above the mean. The localized instabilities also contain a larger range of frequency components than is the case in quieter periods and intervals. Production of turbulence and mixing in the boundary layer are strongly associated with the intermittent bursts; τ fluctuations are largest after the mixing and destabilization associated with the leading edge. Participation of a large range of scales of motion and of the fluctuating water surface enhances the burst magnitudes. The use of long averaging periods obscures the details of the transfer processes that are dependent upon these strong localized instabilities.

A.2. Relationships between Variables. Relationships were depicted by joint histograms (JH) and time plots in the time domain, and by coherence (Coh) plots in the frequency domain. This duality of representation helped to lend confidence to conclusions based on a limited

amount of data. Coherence may be defined as

$$Coh_{s\varphi}(f) = \int_{-\infty}^{\infty} e^{2\pi i f t} \frac{\langle \varphi(t)\, s(t-t)\rangle}{(\langle s^2\rangle \langle \varphi^2\rangle)^{1/2}}\, dt \quad .$$

It is represented in terms of its magnitude and phase,

$$Coh_{s\varphi}(f) = \gamma_{s\varphi}(f)\, e^{i\theta_{s\varphi}(f)} \quad .$$

It was computed using fast fourier transform techniques. In the conventions adopted, $\theta_{s\varphi} > 0$ means φ leads s . Averaging was over 25 adjacent frequency bands for 10 second T.P., 9 for the shorter intervals. As shown by McBean (1970), the 'spectral correlation coefficient' (or Coh) is an actual measure of transfer efficiency as a function of frequency (or scale).

a. 10 Second Intervals. Fig. 11 shows JH(U,T') (with 10 second mean and trend both removed from T) from run 6B. Associated with the decrease and increase of $\langle T \rangle$ 10 sec is the boundary layer destabilization and mixing by the leading edge, violent mixing during the major bursts, and subsequent restabilization of a nearly constant temperature after gust passage. The top of Fig. 12 shows a similar pattern in the frequency domain using $Coh_{T'\eta}$ from run 4. Before the gust the waves and temperature fluctuations (above 5 hz) are quite coherent and nearly out of phse. This is the pattern to be expected if the catamaran rides up and down through a thermally stratified layer that follows the pattern of the waves. (Ramzy and Young [1968]). Near the leading edge $\gamma_{T'\eta}$ is slightly lower and extends to lower frequencies; $\theta_{T'\eta}$ begins to shift, particularly in higher frequencies, as the atmosphere is mixed. Later in the gust the temperature field has been effectively inverted, and T and η are more nearly in phase. The lower half of Fig. 12 shows $Coh_{\tau\beta}$ from the same T.P. Here $\gamma_{\tau\beta}$ is much lower but $\theta_{\tau\beta}$ shows effectively

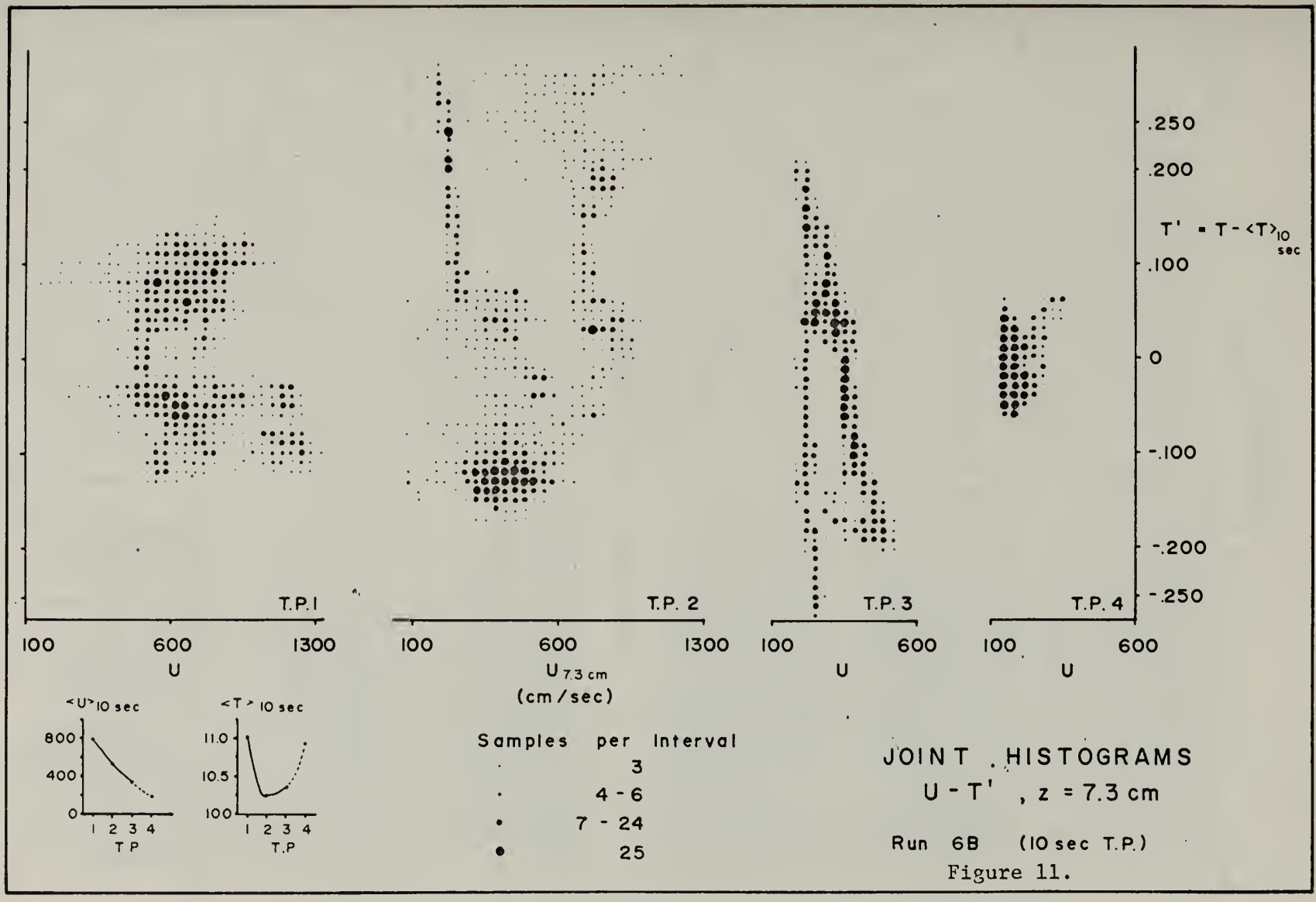
.250
.200
T' = T - <T>10 sec
.100
0
-.100
-.200
-.250
T.P.1
T.P. 2
T.P. 3
T.P. 4
100
600
1300
U
U 7.3 cm
(cm/sec)
<U>10 sec
800
400
0
1 2 3 4
TP
<T> 10 sec
11.0
10.5
100
T.P
Samples per Interval
3
4 - 6
7 - 24
25
JOINT HISTOGRAMS
U - T' , z = 7.3 cm
Run 6B (10 sec T.P.)

Figure 11.

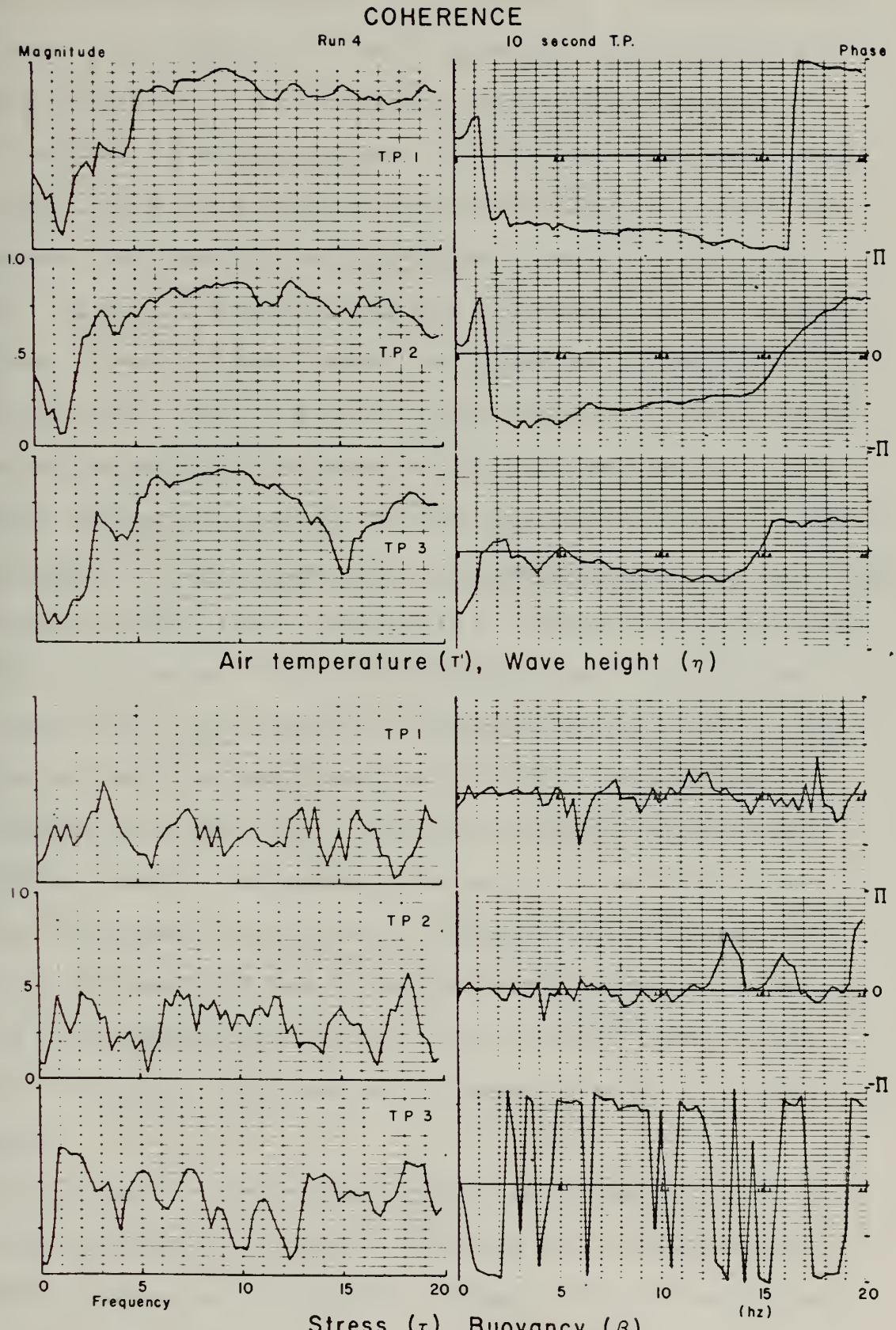

Air temperature (τ'), Wave height (η)

Stress (τ), Buoyancy (β)

Figure 12.

the same temperature inversion.

Fig. 13 and Fig. 14 show JH(τ, β) and $\text{Coh}_{\tau\beta}$ from run 6B; Fig. 15 shows JH(τ, β) from run 2. These diagrams show that the mixing and tumbling is effected by τ fluctuations destabilizing the boundary layer, and that the following restabilization is due to the predominance of buoyancy forces. The change of the patterns with time is most clear in the more stable run 6B (note the change in scales); in the nearly neutral run 2 the fluctuations show less correlation, are more randomly scattered. Here the stress fluctuations predominate and remain intermittently large even after the gust has passed, while in run 6B the buoyancy forces rapidly debilitate the momentum flux as the gust departs. The coherence diagrams also indicate the phase reversals of stress and buoyancy fluctuations as the boundary layer is turned and mixed. The rapid, nearly linear shift of $\Theta_{\tau\beta}$ with f in the 9.5-17 hz range of T.P. 4 implies that fluctuations of similar frequency are 'slipping' past each other, or effectively that in the presence of strong stratification, weak τ fluctuations are unable to overturn and mix the stable boundary layer.

Boundary layer stability is effective in retarding momentum flux by turbulent velocity fluctuations. This effect is particularly large near the leading edge of cat's paws. Wave generation during high frequency instabilities will thus be less efficient during stable than neutral stratification, and delayed or reduced by the conversion from kinetic to potential energy involved in disruption of the stability structure.

Fig. 16 and Fig. 17 show the JH and Coh represetations of the relationship between U at two heights during run 6B. As with the other variables, fluctuations are largest at and just after the leading edge,

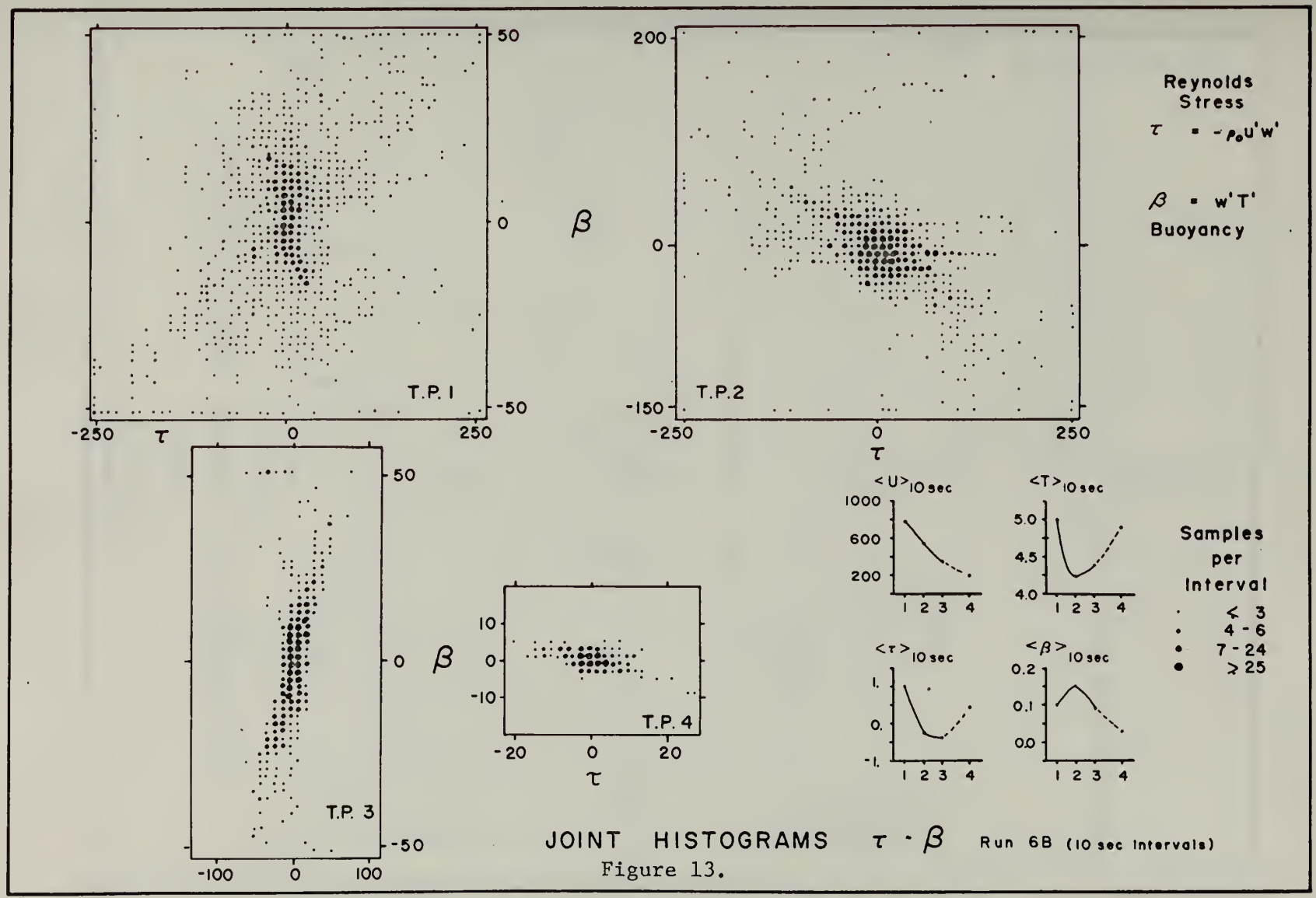

JOINT HISTOGRAMS $\tau \cdot \beta$ Run 6B (10 sec Intervals)

Figure 13.

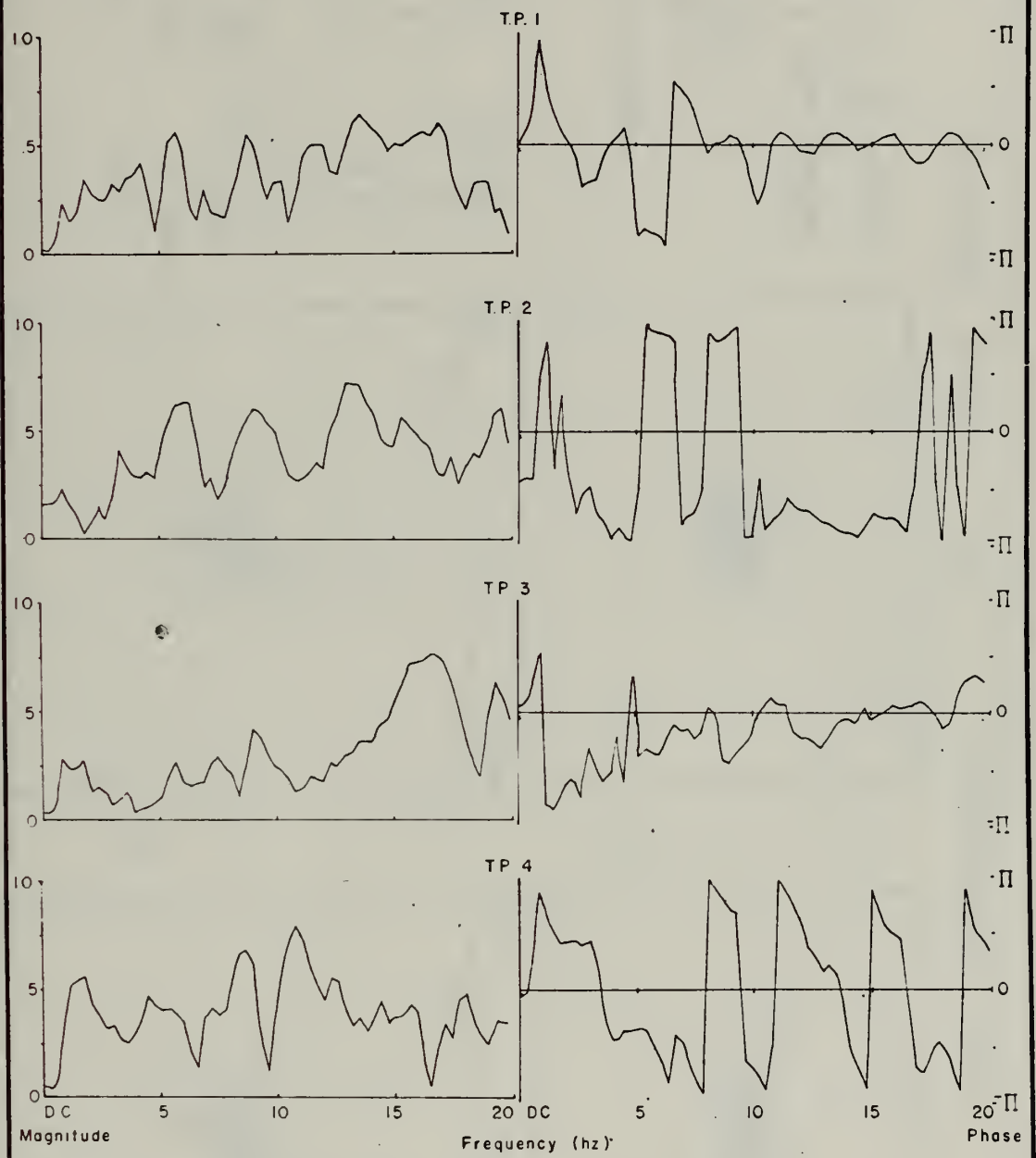

Coherence between Stress (τ) and Buoyancy (β)

Run 6B

10 second T.P

Figure 14.

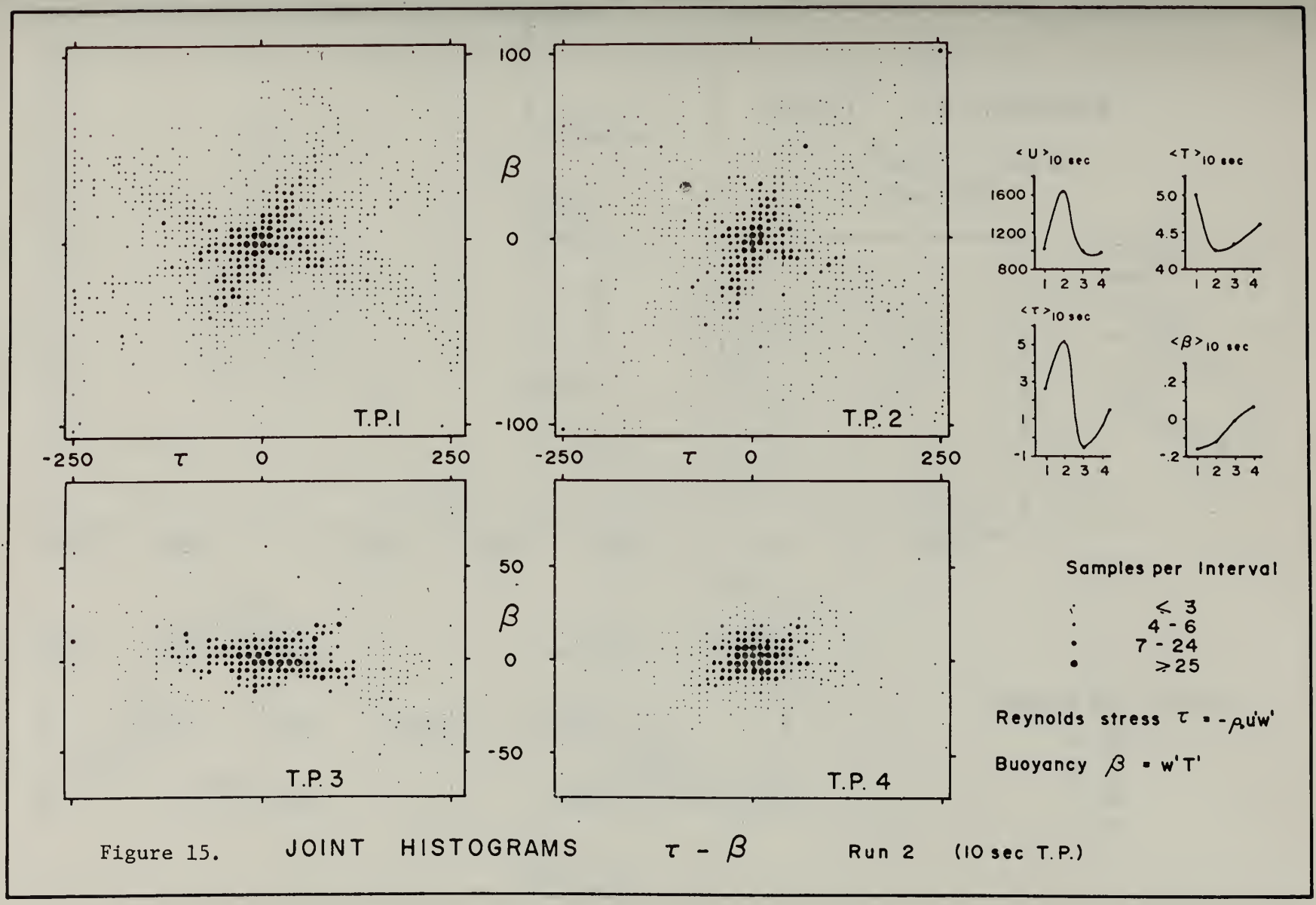

Figure 15. JOINT HISTOGRAMS $\tau - \beta$ Run 2 (10 sec T.P.)

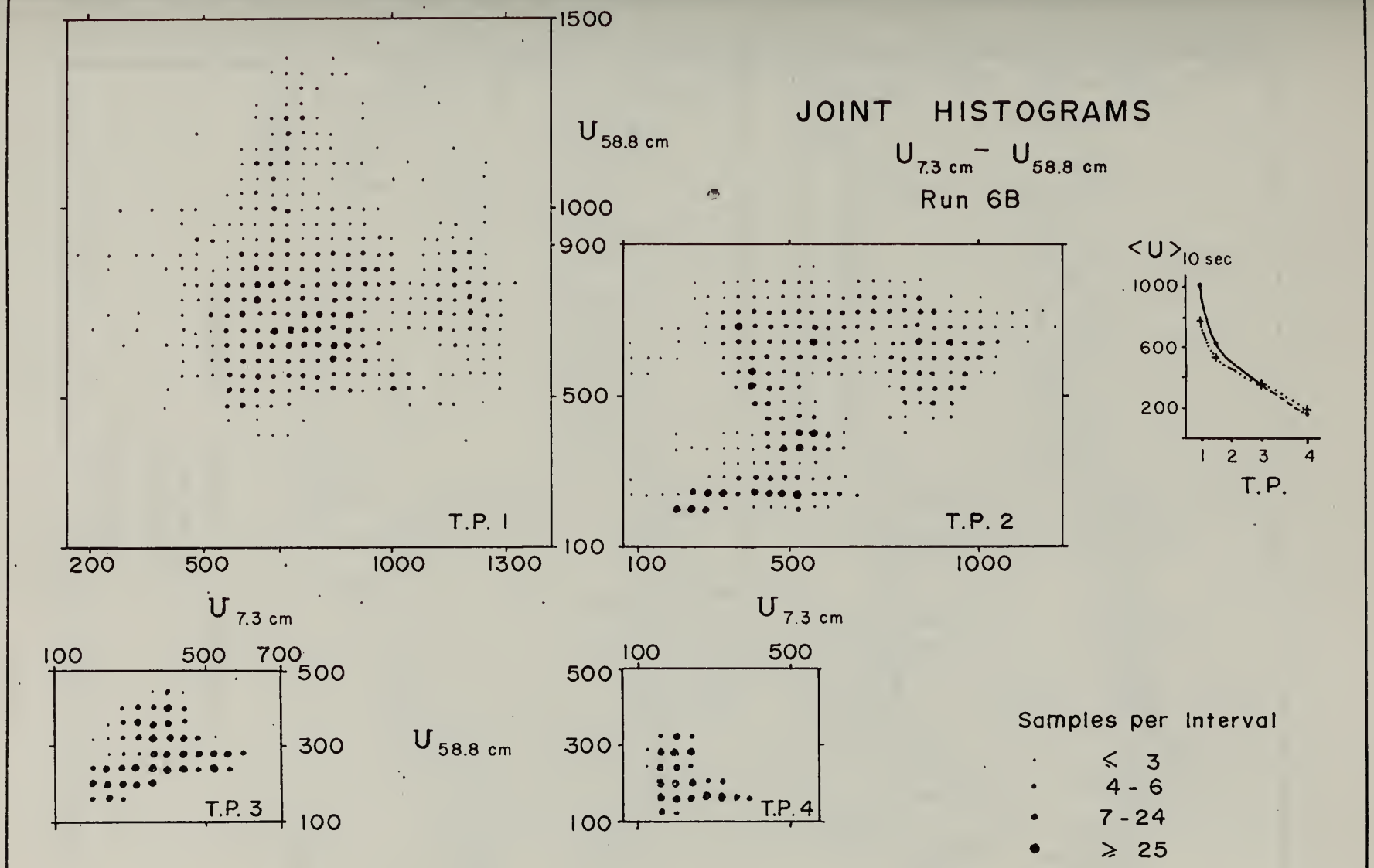
JOINT HISTOGRAMS
$U_{7.3\ cm}$ – $U_{58.8\ cm}$
Run 6B
$U_{58.8\ cm}$
$U_{7.3\ cm}$
T.P. 1
T.P. 2
T.P. 3
T.P. 4
<U>10 sec
T.P.
Samples per Interval
≤ 3
4 - 6
7 - 24
≥ 25

Figure 16.

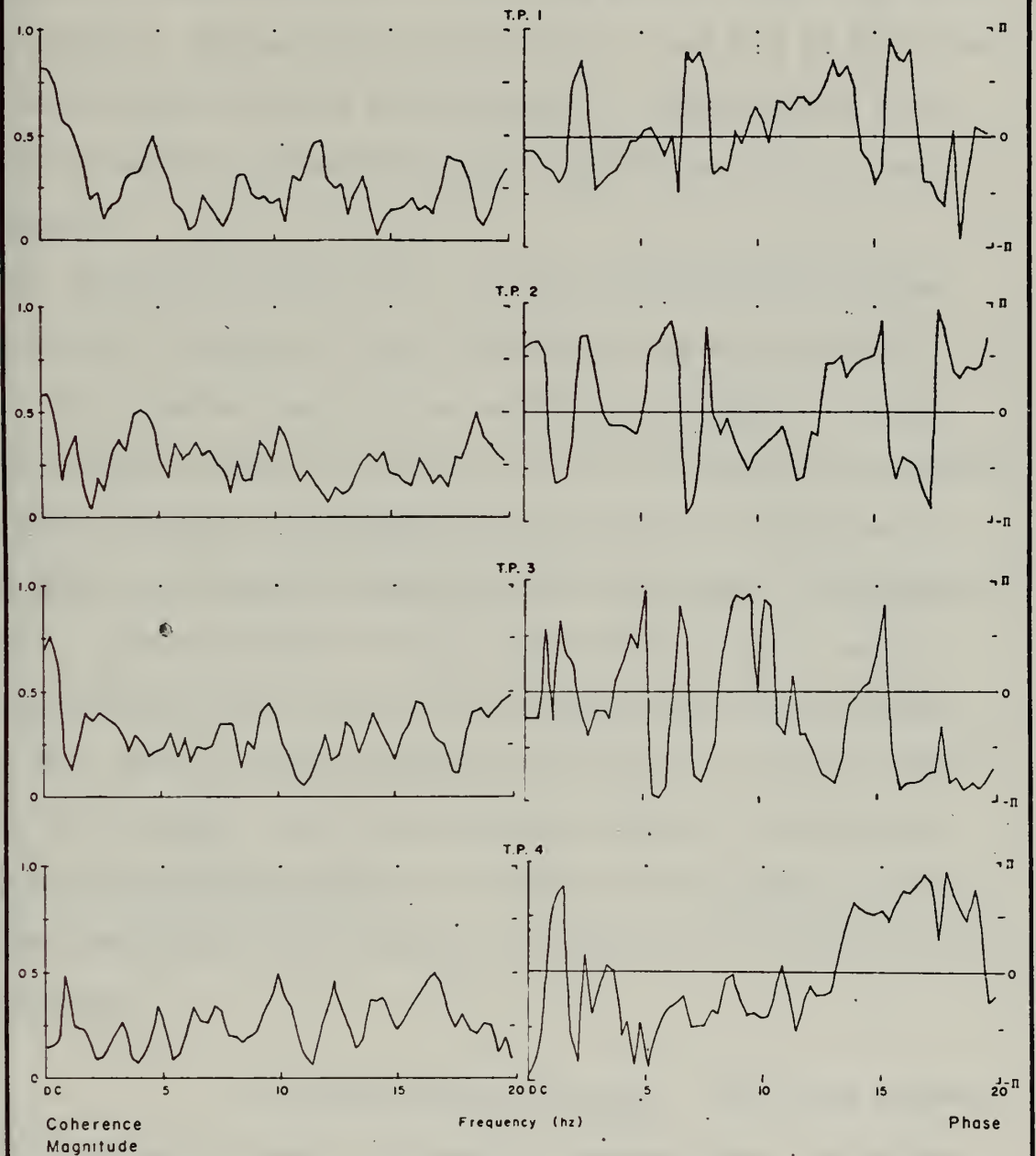

Coherence between $U_{73\,cm}$ and $U_{58.8\,cm}$

Run 68

4, 10 Second Segments

Figure 17.

with a collapse of the histogram after the gust has passed. γ_{uu} is significant only at the DC level (T.P. 1-3) and the reversals of θ_{uu}(D.C.) demonstrate the large variations in mean wind velocity shear that occur during the gust. The generally low level of γ_{uu} and lack of JH patterns over even this short distance are indicative of strong vertical structure and the anisotropic character of the high frequency intermittent fluctuations.

Fig. 18 and Fig. 19 are JH(τ , η) from run 6B and Coh $_{\tau\eta}$ from during and after the gusts of runs 2 and 6B and from all three T.P. of run 4. It is apparent that there is no effective evidence of strong wind-wave coupling during the gust when viewed from this averaging period. The effective generation mechanisms are obscured by the 'detritus' or by averaging over events of radically differnt character. If anything, τ and η are more coherent in the 7-12 hz range (of runs 2 and 6B) after than during the gust; and in this frequency band the continuous linear $\theta_{\tau\eta}$ drift is evidence that the fluctuations of similar frequency slip by one another rather than strongly coupling. The turbulent stress-wave relationship that will be demonstrated has again been obscured by considering averaging intervals much longer than the effective intermittent events.

b. 2 and 1 Second Intervals. Two second segments containing primarily 'burst' or primarily 'interval' type fluctuations were selected from runs 2 and 6B. The location of these 2-second T.P. is shown in Fig. 2 and Fig. 6 (with the exception of T.P. 1 from run 6B which was taken about 3 seconds prior to arrival of the leading edge.) A portion of the results is shown in Fig. 20, JH(τ , β) from run 2,

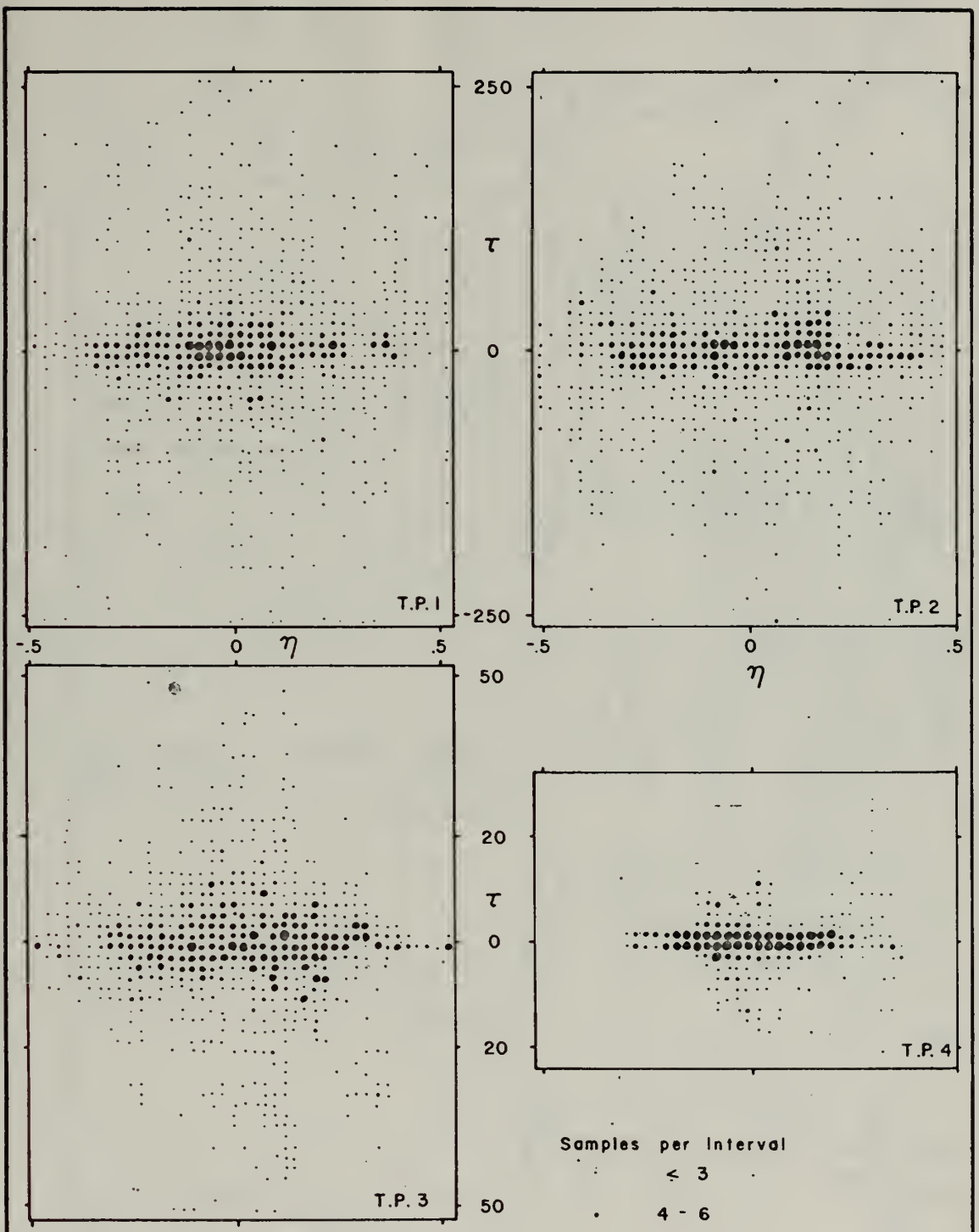
250
τ
0
-250
T.P. 1
-.5
0
η
.5
T.P. 2
-.5
0
η
.5
50
20
τ
0
20
50
T.P. 3
T.P. 4
Samples per Interval
≤ 3
4 - 6
7 - 24
≥ 25
JOINT HISTOGRAMS
Reynolds stress, τ
Wave height, η
Run 6B (10 second T.P.)

Figure 18.

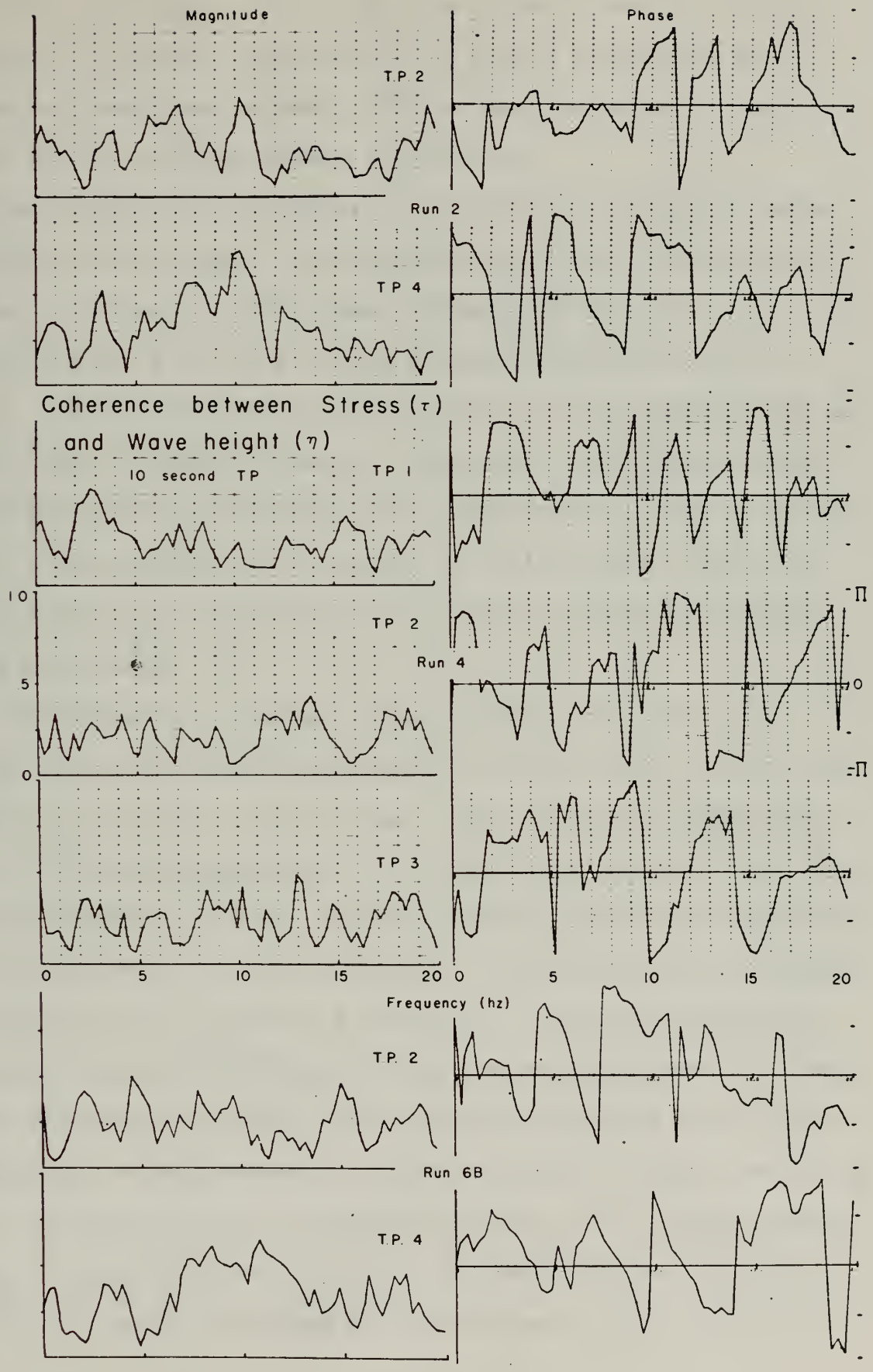
Magnitude
Phase
T.P. 2
Run 2
TP 4
Coherence between Stress (τ)
and Wave height (η)
10 second TP
TP 1
10
5
0
TP 2
Run 4
TP 3
Π
0
-Π
0
5
10
15
20
Frequency (hz)
T.P. 2
Run 6B
T.P. 4

Figure 19.

and in Fig. 21, Coh $_{\tau\eta}$ from run 6B. These figures show some overall similarity to those of the 10 second T.P.; some of the segments still contain both bursts and intervals, and this tends to partially blur the effects of the very high frequency fluctuations.

Fig. 20 shows that the mixing and destabilization process is indeed associated with the bursts. Relatively weak, positively correlated fluctuations occur near the leading edge; mixing occurs during the next strong burst and is followed directly by negative correlation of τ and ρ and consequent further destabilization of the boundary. With the boundary layer inverted the buoyancy forces work toward restabilization and rapidly degrade the strength of the momentum fluxes. Both the mixing and the restabilization occur rapidly; the intial boundary layer structure is wiped out by the leading edge but is never firmly reestablished during gust passage.

The wind-wave coupling begins to be apparent on this time scale. Fig. 21 shows that stress fluctuations are intially (before the gust) out of phase with the waves (7-15 hz range). They are almost totally incoherent during the leading edge, i.e., during destabilization. $\gamma_{\tau\eta}$ then increases slightly in T.P. 3. This T.P. contains several well-defined subbursts and intervals so that the picture is confused, but $\theta_{\tau\eta}$ is relatively constant at the $\gamma_{\tau\eta}$ peaks at 5.9 and 12 hz. During the major burst, the high frequency instabilities and high frequency waves serve to strongly and immediately couple the lower frequency fluctuations to the underlying waves. The high frequency coupling is still not evident, but $\gamma_{\tau\eta}$ is high at and below the main wave period, with $\theta_{\tau\eta} \doteq \pi/2$, or the maximum stress occurring aft of the crests. In the immediately following interval $\gamma_{\tau\eta}$ at the D.C. end drops off slightly and the phase shifts; in

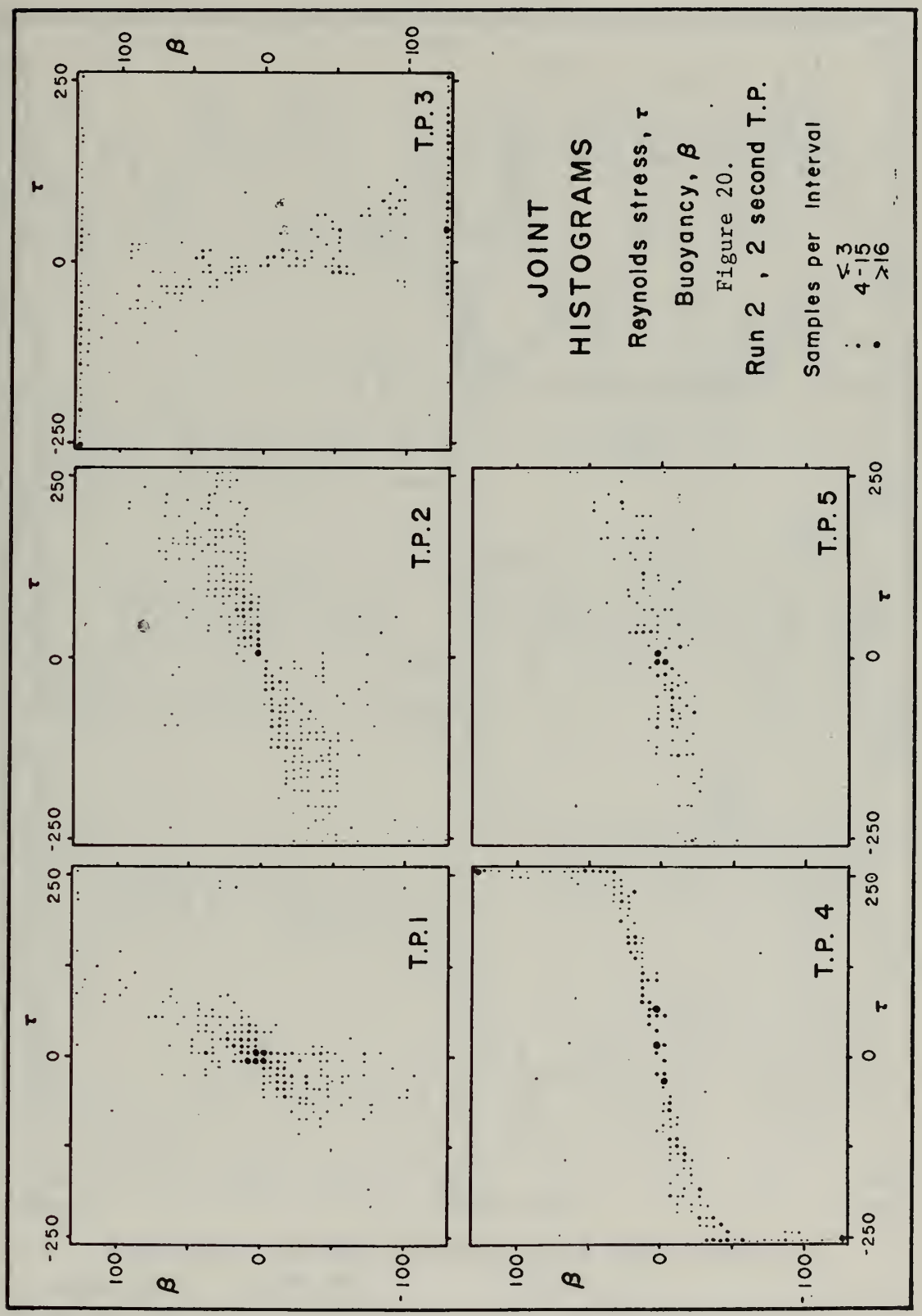
JOINT
HISTOGRAMS
Reynolds stress, τ
Buoyancy, β
Run 2 , 2 second T.P.
Samples per Interval
≤3
4-15
≥16
T.P.1
T.P.2
T.P.3
T.P. 4
T.P.5
β
τ
100
0
-100
250
-250

Figure 20.

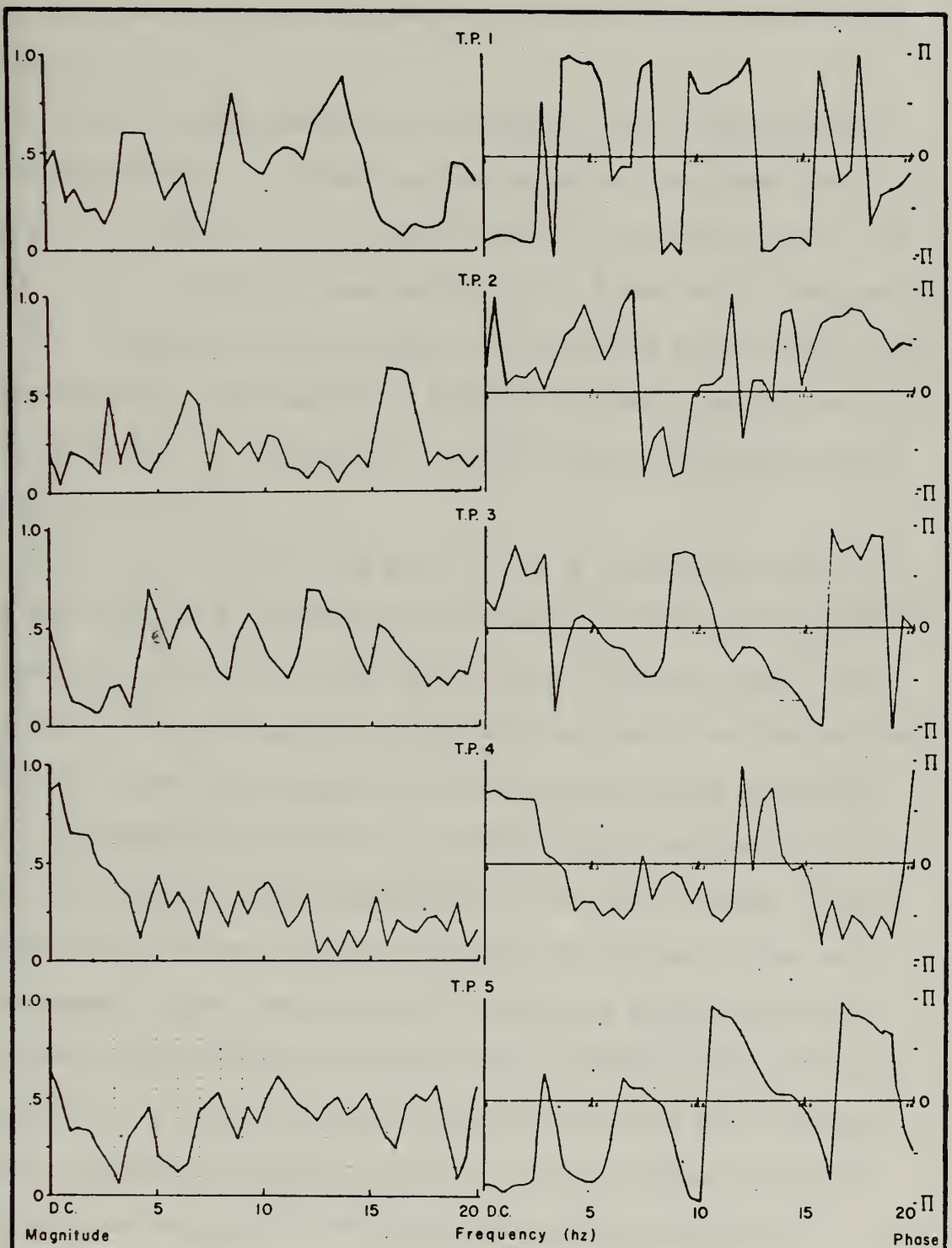

Coherence between Stress (τ) and Wave height (η)

Figure 21. Run 68 2 second T.P.

the higher frequencies $\gamma_{\tau\eta}$ is slightly higher but the propogating capillary waves now 'slip' with respect to stress fluctuations of the same frequency.

In order to further decrease the blurring of burst and interval, segments approximately 1 second long were selected from within the 2-second T.P. (see Fig. 6). The results from run 6B are shown in Fig. 22-Fig. 24. T.P. 1 is prior to gust arrival; T.P. 2 just behind the leading edge; T.P. 3 during a short but intense fluctuation 2 seconds later; T.P. 4 during the major burst and T.P. 5 from the quiescent interval 3-4 seconds after T.P. 4. The pattern of events during this sequence may be described as follows.

Prior to the arrival of the gust, τ and β are nearly totally coherent and in phase. τ fluctuations are small, loosely coupled to the main wave field, and out of phase with the high frequency waves. With the arrival of the leading edge of the cat's paw the stress fluctuations increase in frequency and magnitude and the boundary layer is tumbled; the τ & β fluctuations decrease in coherence and become nearly out of phase; little effect is noted immediately on the water surface, as the turbulent kinetic energy is utilized to stir the boundary; waves and τ are incoherent. After the intial burst the air is mixed and high frequency waves are generated, associated with the short, strong bursts of momentum flux. τ and β are again coherent, but out of phase, and the wind-wave coupling is apparently random. With the boundary layer destabilized, the magnitude of the stress fluctuations increases (T.P. 4) and the high frequency instabilities become strongly associated with the generation of surface waves. $\gamma_{\tau\beta}$ is quite low at frequencies above 15 hz with $\Theta_{\tau\beta}$ more variable than before but centered around 0 . $\gamma_{\tau\eta}$

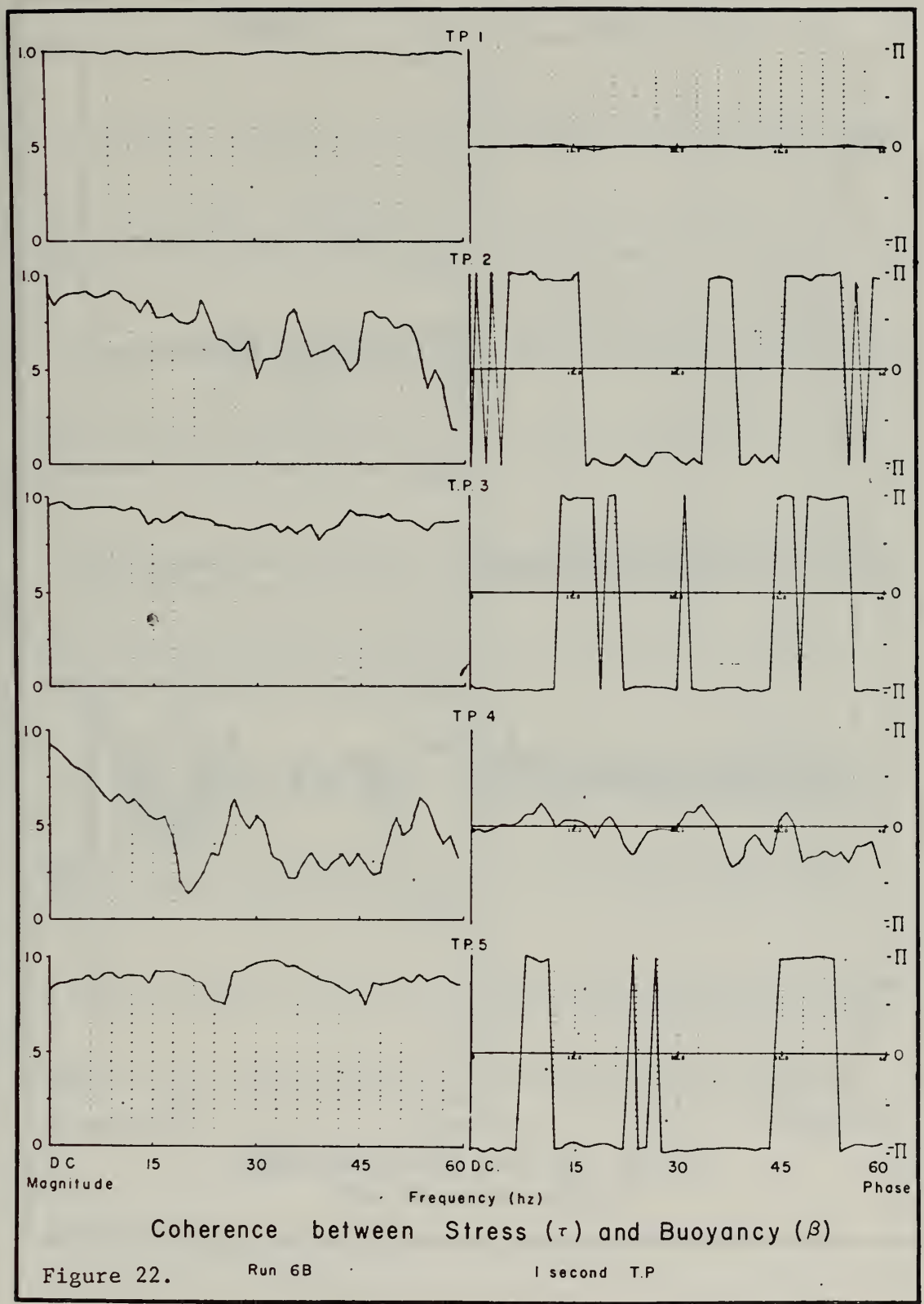

Coherence between Stress (τ) and Buoyancy (β)

Figure 22. Run 6B 1 second T.P

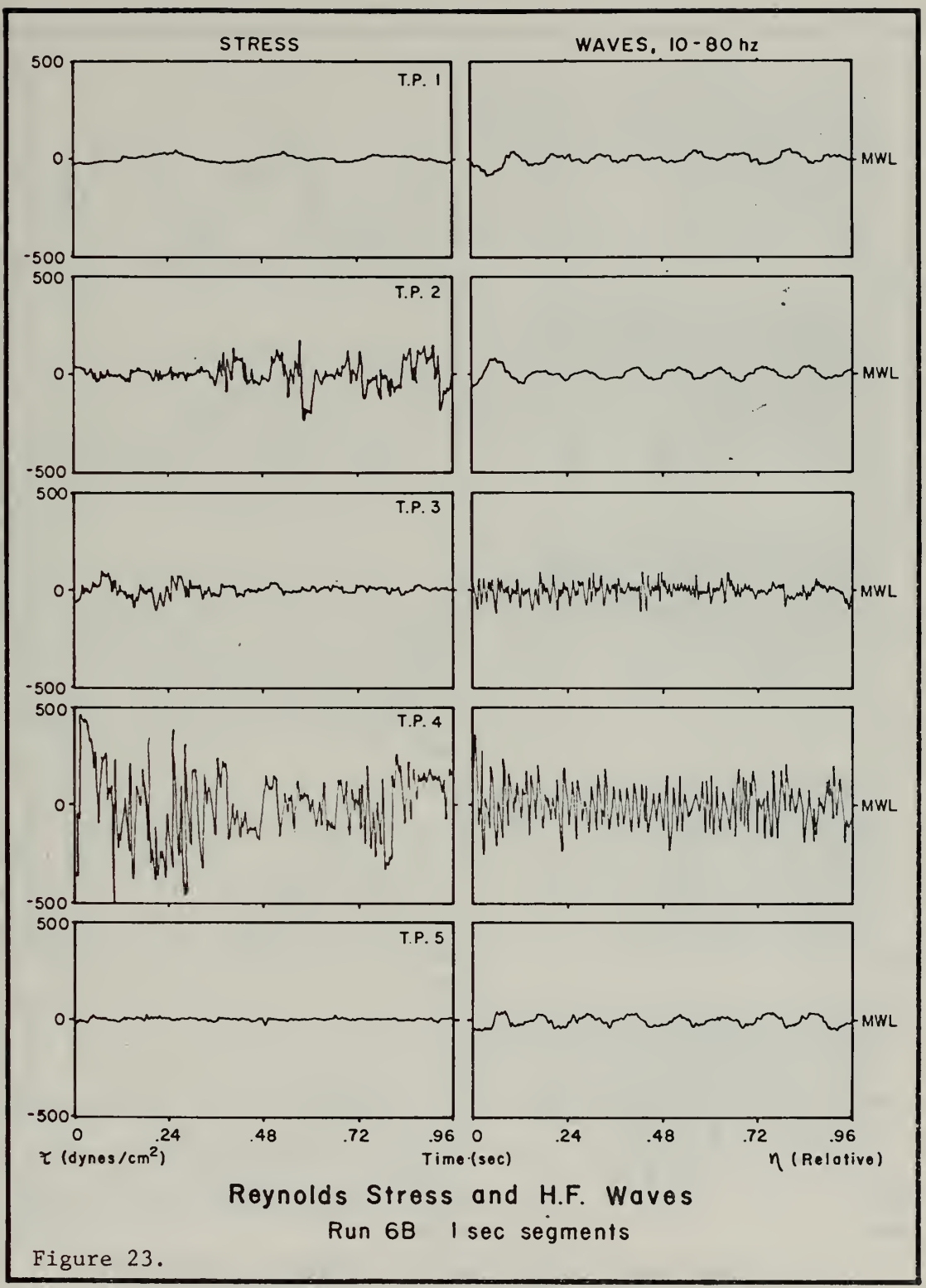

Reynolds Stress and H.F. Waves

Run 6B 1 sec segments

Figure 23.

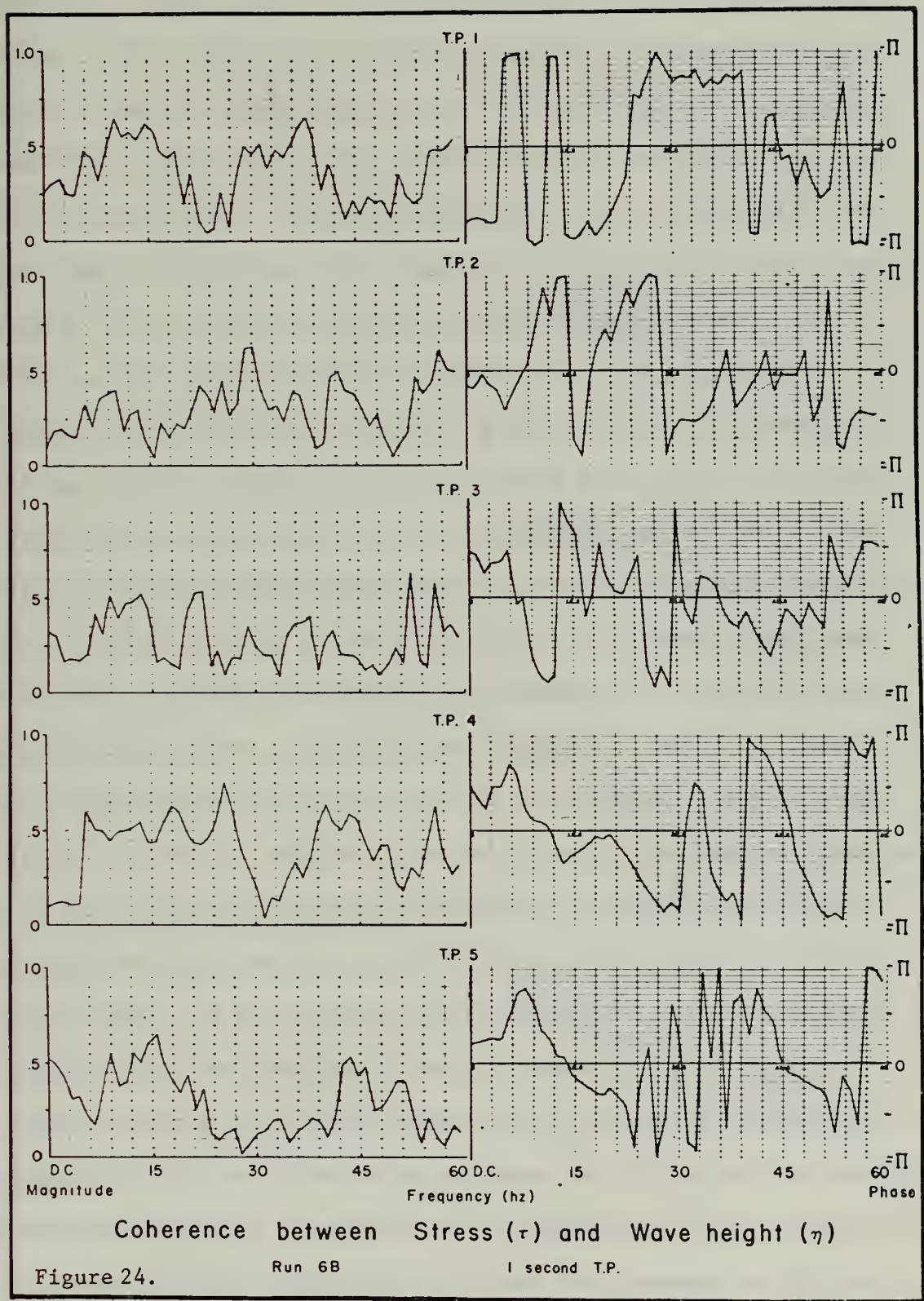

Coherence between Stress (τ) and Wave height (η)

Run 68 1 second T.P.

Figure 24.

increases considerably in the 6 - 28 hz range, but remains fairly low for lower frequencies. $\Theta_{\tau\eta}$ slips across part of the coherent ranges but shows a major reversal of trend in the center of the coherent band. During the quiescent period immediately after this event τ fluctuations are much smaller and less strongly coupled to the short wave field, with slightly increased $\gamma_{\tau\eta}$ in lower frequencies. τ & β fluctuations are again strongly coupled, and out of phase due to the mixing of the preceeding burst. This process is repeated during subsequent bursts, until the cat's paw has passed the site and stability is reestablished.

The change in character of the high frequency stress and wave patterns (Fig. 23) is strong evidence of the large growth rates associated with intermittent, large magnitude, high frequency instabilities. The generation of high frequency waves, as in T.P. 3 and especially in T.P. 4, is indeed strongly coupled to the generation of turbulence. The large value of $\gamma_{\tau\eta}$ for lower frequencies in 2-second T.P. 4 indicates that the high frequency waves can rapidly and effectively couple the lower frequency waves and instabilities, and aid their growth. It is obvious that little statistical confidence can be placed in low frequency measures based on such short time periods; nevertheless the change between time periods and averaging lengths, the similarity of this pattern in other bursts and gusts, and the enhanced high frequency $\gamma_{\tau\eta}$ in 1-second T.P. 4 lend strong subjective credence to the hypothesis.

Figs. 23 and 24 also clearly show how wave generation is delayed by the stability structure. Generation processes act only after the boundary layer has been initially destabilized. The continuous $\Theta_{\tau\eta}$ slipping in T.P. 5 (across the full width of the coherent band) appears to be characteristic of 'detritus', in this case, of the propagation and advection of

the waves and turbulence generated during the high frequency, localized instabilities. The slipping pattern is similar in T.P. 4 except for the 10 - 18 hz range, where $\theta_{\tau\eta}$ levels off and reverses direction near the zero level. Most of the generation and momentum transfer occurs in this frequency range (see Fig. 27).

Generation appears to be a very strong but selective and short-lived phenomenon. The time scales associated with the sub-bursts and instability associated transfers are very short, typically on the order of 1 to 1.5 seconds, which is also the typical period of the immediately underlying major wave field. The strongest coupling and high growth rates associated with the localized instabilities occur in a narrow high frequency band. Averaging times significantly longer than these scales can depict the general changes in atmospheric structure but fail to show the detailed nature of the coupling and transfer processes. The important scales are thus those of the waves, the bursts, and the internal fluctuations within the bursts. Momentum is transferred to the water at scales associated with these features.

B. Interaction Between Scales. The microscales in both wind and wave fields account for only an insignificant portion of the total energy, yet as shown above they are the active participants in the localized high growth rate instabilities. They are effective in aiding the growth rate of lower frequency components and in coupling wind and wave fields, as was heuristically explained by Mollo-Christensen (1970, 1971) and as demonstrated in the time plots and coherence diagrams of the preceeding section. Other evidence of nonlinear coupling between scales may be shown by an examination of the probability distribution of turbulent

velocity fluctuations and of the shape of the high frequency wave spectrum.

B.1. Scale Interaction in Velocity Fluctuations. A gust has been shown to consist of a wide range of sizes of bursts or eddies of strong, high frequency fluctuations, separated by relatively quiet intervals. The cat's paw itself is merely a burst on a larger time scale. The absolute magnitude of a single fluctuation is thus dependent not only on the instantaneous departure from adjacent values, but also on the departure of the fluctuation and its neighbors from similarly sized parcels, and on the departure of the mean magnitude of those patches from segments on yet larger scales; and so on up the range of scales to an averaging period covering the largest perturbations involved. Thus each scale of motion involves fluctuations whose magnitude depends both upon the strength of internal instabilities, and upon the forcing of and interactions between the scale itself and larger scales or larger anomalies. Following Cramér (1955), let the instantanious magnitude of a random variate be ξ_i ; and let the change of this variate caused by a forcing ζ_i be proportional both to the forcing and to the magnitude ξ_{i-1} which had in turn been produced by the previous ζ_{i-1} impulses.

Then $\xi_{i+1} - \xi_i = c\,\zeta_i\,\xi_i$, c = constant,

and $$\sum_{i=1}^{N} \zeta_i = \frac{1}{c} \sum_{i=1}^{N} \frac{\xi_{i+1} - \xi_i}{\xi_i}$$

which in turn, in the limit of small change, $\rightarrow \frac{1}{c} \int_{\xi_1}^{\xi} \frac{d\nu}{\nu} = \frac{1}{c} \ln\left(\frac{\xi}{\xi_1}\right)$

For large N, the central limit theorem states that ζ_i is normally

distributed. Hence ξ has the lognormal distribution,

$$P_\xi(x) = \frac{1}{\sigma(x-a)\sqrt{2\pi}} \exp\left(-\frac{(\ln(x-a) - E(x))^2}{2\sigma^2}\right), x > a; \; P_\xi(x) = 0, \; x \leq a,$$

where $P_\xi(x)$ is the probability $\xi = x$, σ^2 is the standard deviation of ξ, $E(x) = \langle \xi \rangle$, and a is an appropriate normalizing or cut-off value of ξ.

The lognormal distribution can thus be expected to occur when a large number of impulses, or a large range of scales, interact to contribute to the increase of a variable at a rate proportional to its instantaneous value. For example, Rao and Narayanan (1971) have shown that the intervals between bursts in a turbulent boundary layer were lognormally distributed. This indicates that the scales of the bursts and intervals are determined by coupling with the scales of the boundary and of the outer or main flow as suggested by Mollo-Christensen (1970).

Within a cat's paw or gust, one variable which should act in a lognormal fashion is the turbulent energy dissipation, ϵ. Dissipation is primarily dependent upon the magnitude of the velocity fluctuation rate, which in turn depends strongly on the amount of 'rubbing' or interaction between different scale eddies. The dissipation is due to the working of molecular viscous stress against this coupled rate of strain or deformation of the fluid particles. Provided that the range of scales involved in the deformations is sufficiently large, say including interaction between the localized high frequency instabilities, fluctuations on the scale of bursts and intervals, and similarly between groups of sub-bursts and bursts up to the scale of the full cat's paw, dissipation should be approximately lognormally distributed.

Another variable which should be lognormally distributed, and for

much the same reasons, is the magnitude of the squared time derivative of horizontal velocity. Time derivatives, like space derivatives, are enhanced by the interactions between a variety of scales of eddies or instabilities. The interaction between high frequency velocity fluctuations and bursts has already been demonstrated in the preceeding section. Define the normalized squared magnitude of the velocity derivative as

$$\xi_i \equiv \frac{(\partial u_i/\partial t)^2}{\langle (\partial u_i/\partial t)^2 \rangle} \quad .$$

Chen (1971) has analyzed the distribution of $\ln(\xi_i)$ with data taken from FLIP during BOMEX. He pointed out that squaring the derivative emphasizes the large fluctuations and minimizes the magnitude of small ones. (Gurvich and Yaglom [1967] showed that a lognormal distribution with large variance corresponds to a high probablity of values close to 0 or much larger than the rms, but small probablities of intermediate values.) The natural logarithm of such a variable will have $P_\xi(x) \to \infty$ as $\xi \to 0$ due to the $(\partial u/\partial t)^2 \doteq 0$ 'tail' imposed by the rapid axis crossing of $\partial u/\partial t$. Taking the average of a small number of values (i.e., $\ln\left(\frac{1}{M}\sum_{i=-M/2}^{M/2}\xi_i\right)$, M small) wipes out this tail. In physical terms this corresponds to averaging the fluctuations over a very small but finite volume, or numerically to limiting the analysis to scales slightly larger than the cut-off imposed by the sampling rate. This averaging will increase the tendency toward lognormality, provided that the number of scales interacting is sufficiently large and that the averaging time is short enough to include the important structure. Chen's data were from a roughly 4-minute period at mean heights of 3 and 31 meters above the sea surface. The resulting distribution was almost identically lognormal for averages over 8 data points.

Similar results from runs 2 and 6B of this study are shown in Figs. 25 and 26. The burst/no burst/both character of the T.P. is noted in the figures. Fig. 25, with the data in histogram form (run 2, 2-second T.P.), clearly shows how averaging (over 5 points) removes the 'tail' of the distribution. In Fig. 26, the cumulative probabilities of $\ln(\overline{\xi_i})$ from both runs, 2-and 1-second T.P., are plotted on a normal probability scale. Purely lognormal distributions with comparable means and variances are indicated by straight lines.

Since only a relatively small number of points was used, the central limit theorem can not be strictly applied and none of the plots are strictly lognormal, though most of them show relatively minor departures. As shown best by the 1-second periods from the low stability run 2, periods of intense activity show a deficit of intermediate values, an excess of large and small ones. The quiet periods show the opposite effect, particularly in T.P. 6, taken after the passage of the gust (past the end of Fig. 2). In this very quiet T.P. the fluctuations are more nearly normally than lognormally distributed. The 2-second T.P. show these effects less clearly due to averaging over both bursts and intervals, but the tendency toward normality is clear in the quiescent T.P. 5. The run 6B data (high bulk stability) shows similar results, with intermediate deficits during bursts, excesses during intervals. One major exception is T.P. 2, from the leading edge of the cat's paw. It was shown in the preceeding section that in this time period the major effect of the stress fluctuations was the local tumbling and destabilization of the boundary layer. The excess of intermediate departures in this distribution is further evidence of the initial effectiveness of the buoyancy forces in retarding momentum transfer and limiting fluctuation strength.

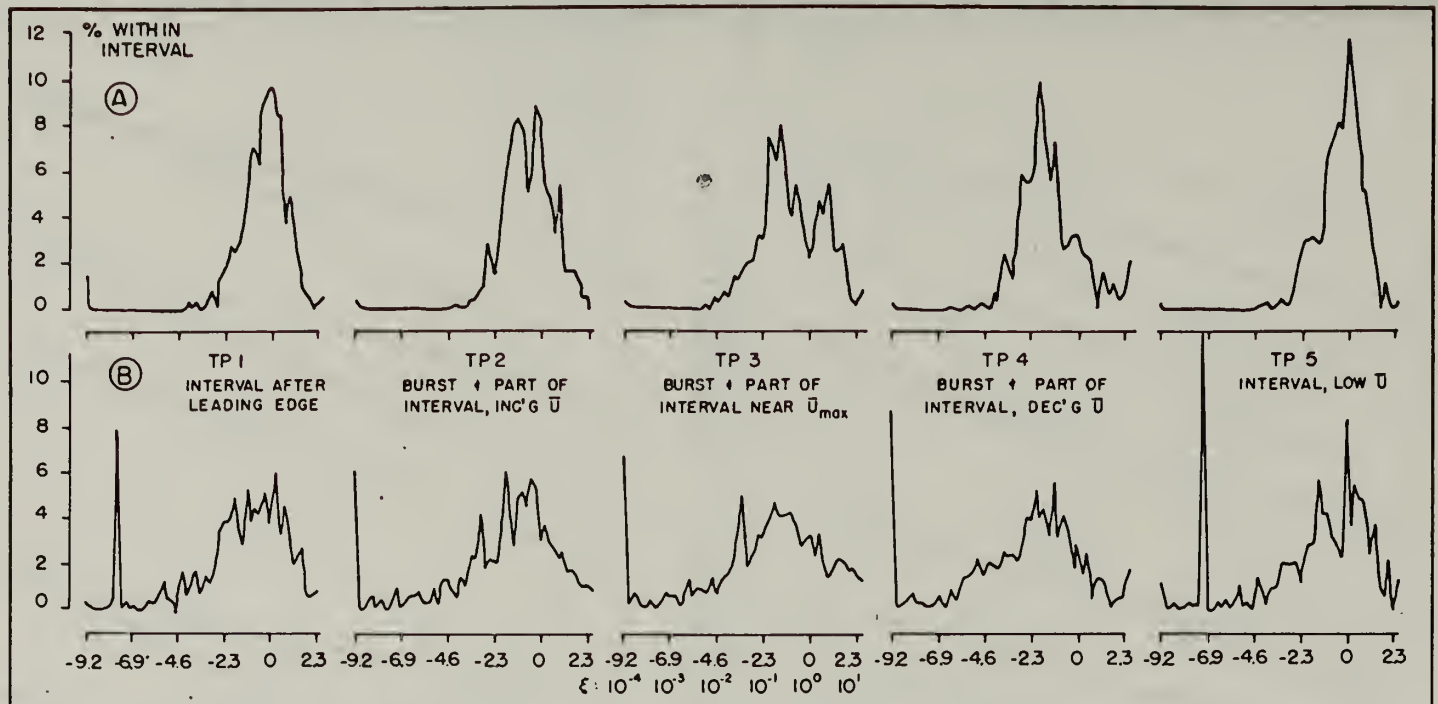

Histograms of dissipation measure:

$$\xi_i = \frac{(\partial u_i/\partial t)^2}{\langle (\partial u_i/\partial t)^2 \rangle_{2\,sec}}$$

(A) $\ln\left(\frac{1}{5}\sum_{i=1}^{5}\xi_i\right)_{\text{Running mean}}$

(B) $\ln(\xi_i)$

(540 points)

Figure 25.

STATISTICS		MEAN	VARIANCE	SKEWNESS	KURTOSIS
T.P.1	A	-0.59	3.01	-42.07	943
	B	-1.77	6.83	-18.93	173
T.P.2	A	-0.26	3.16	-40.35	916
	B	-2.29	13.04	-94.13	1250
T.P.3	A	-1.11	4.04	-38.24	866
	B	-2.42	8.84	-21.19	264
T.P.4	A	-1.56	3.95	-33.83	806
	B	-3.28	15.14	-88.73	1190
T.P.5	A	-0.54	2.99	-42.55	951
	B	-1.93	8.57	-26.88	265

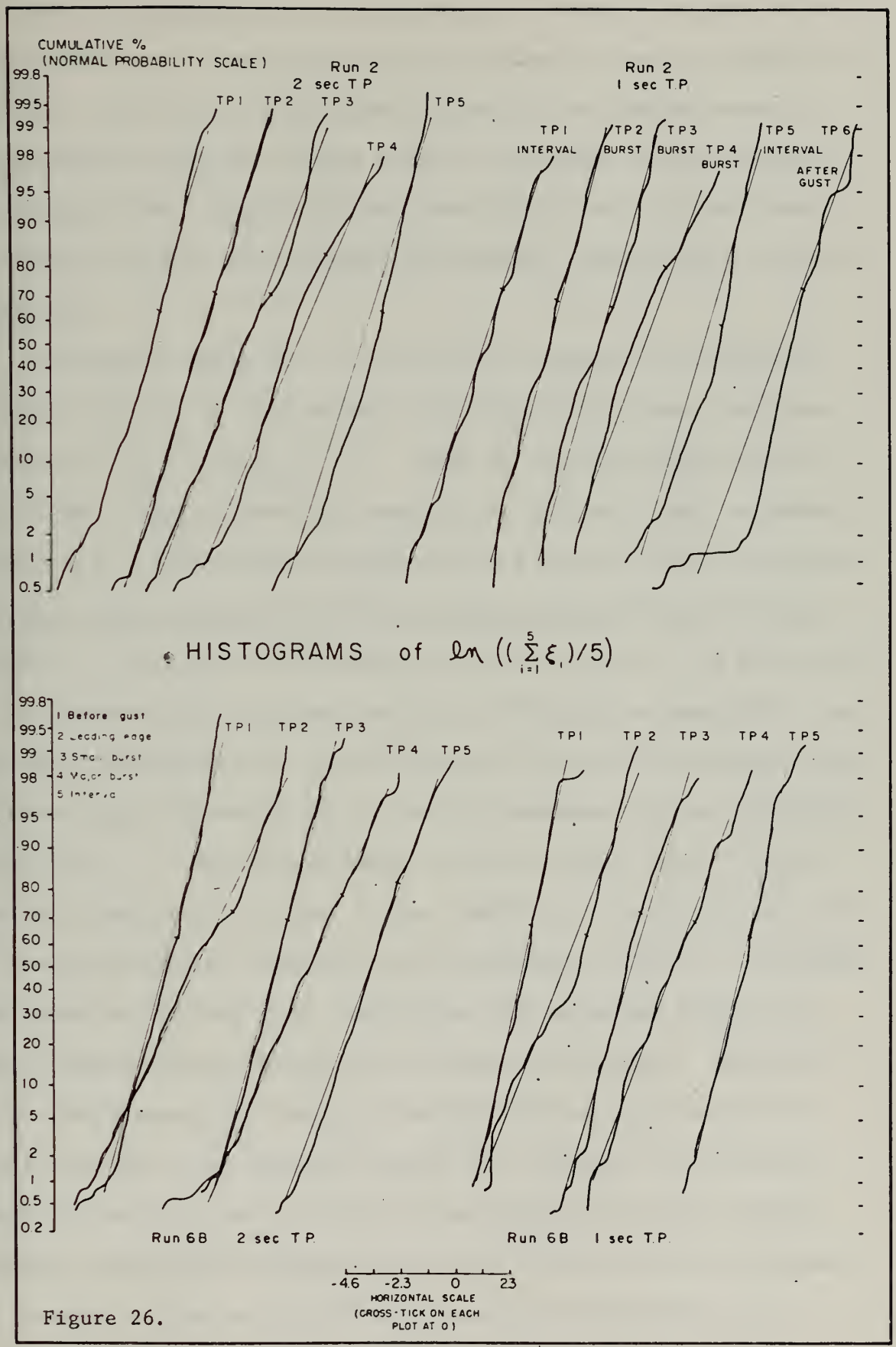
CUMULATIVE %
(NORMAL PROBABILITY SCALE)
99.8
99.5
99
98
95
90
80
70
60
50
40
30
20
10
5
2
1
0.5
Run 2
2 sec T P
TP1
TP2
TP3
TP4
TP5
Run 2
1 sec T.P
TP1
INTERVAL
TP2
BURST
TP3
BURST
TP4
BURST
TP5
INTERVAL
TP6
AFTER
GUST
HISTOGRAMS of $\ln((\sum_{i=1}^{5}\xi_i)/5)$
1 Before gust
2 Leading edge
3 Small burst
4 Major burst
5 Interval
99.8
99.5
99
98
95
90
80
70
60
50
40
30
20
10
5
2
1
0.5
0.2
TP1
TP2
TP3
TP4
TP5
TP1
TP2
TP3
TP4
TP5
Run 6B 2 sec T.P
Run 6B 1 sec T.P
-4.6
-2.3
0
23
HORIZONTAL SCALE
(CROSS-TICK ON EACH
PLOT AT 0)

Figure 26.

The distribution of the squared velocity derivative is thus an effective indicator of the range of scales involved in boundary layer turbulence. Interactions are strongest and involve the largest number of scales during the bursts. During quiescent intervals and particularly between gusts, fewer scales interact; coupling is weak or non-existant, and $\ln(\xi_i)$ tends to have a normal distribution, indicative of a lack of interaction.

It should be noted that for isotropic, homogeneous turbulence, ξ is related directly to dissipation by use of Taylor's frozen turbulence hypothesis, $\frac{\partial}{\partial t} = -U\frac{\partial}{\partial x}$. Chen in fact regarded his data in these terms. Ruggles (1969) has demonstrated that the frozen turbulence hypothesis is quantitatively inapplicable in a case even less restrictive than this study; and indeed the above results indicate that it is not necessary to so restrict the assumptions on the nature of the flow in order to account for the lognormal behavior of fluctuation magnitude. The well-known intermittency of the small scale structure of turbulence, the consequent large dispersion of ϵ , and the dependence of the probability structure of ϵ upon larger scales (Obukhov [1962], Landau [1959]) have been theoretically applied to the statistics of turbulence only for the locally isotropic, homogeneous case (Kolmogorov [1962]). The present development has avoided these restrictions and emphasized strong nonlinear coupling between scales as the causative phenomenon. Further, it has been demonstrated that local departures from lognormality are also indicative of the relative strength of coupling of the turbulent components, and that many features of the boundary layer and transfer processes, such as the spacing of bursts and intervals and the frequency and strength of local velocity fluctuations, are controlled by this

coupling.

B.2. An Example of Weak Resonant Wave Interactions.

Nonlinear wave-wave interactions have been theoretically studied in considerable detail during the last 10 years (Kinsman [1965] provides a good summary of the major concepts). Energy exchange among gravity waves of different wave numbers is only seen when the perturbation analysis extends to third order; it involves triads of primary waves interacting to feed energy into a fouth component. For waves in the capillary-gravity range, the analysis shows that interaction occurs at second order (as well as at third order); two waves interact to feed energy into a third (McGoldrick [1965], Simmons [1969]). This weak resonant interaction has been demonstrated in the laboratory (McGoldrick [1970]).

McGoldrick (1965) has discussed the implications of this energy transfer with respect to wind-wave generation. Of particular importance is the fact that the interaction times involved in the growth of the resonant wave are only 2-3 periods of the initial waves creating it. Because of this short interaction time, the amount of energy that the wave field can receive from the wind at a given frequency is determined not just by breaking but also by nonlinear transfer to other components.

Of particular interest is the 'self-resonant' wave, of wave number $k_* = \sqrt{g/2T}$. (T = surface tension/density). This is commonly known as Wilton's wave; he noted the presence of a singularity at this wave number in his (1915) perturbation analysis. The general requirements for resonance at 2nd order are $\vec{k}_1 \pm \vec{k}_2 \pm \vec{k}_3 = 0$, $\tilde{w}_1 \pm \tilde{w}_2 \pm \tilde{w}_3 = 0$, and $\tilde{w}_i = g k_i + T k_i^3$, $i = 1,2,3$

where $\tilde{w} = 2\pi f$ and $k = 2\pi/\lambda = |\vec{k}|$.

k_* fulfills this relationship for $k_1 = k_3 = -1/2\ k_2$, or $k_z = \sqrt{\frac{zg}{T}}$.

Simmons noted that waves shorter than k_2 are hydrodynamically unstable at 2nd order; further, k_2 is the longest wave which can interact with two longer waves. Waves at k_* are extremely unstable and can occur only as a transient state; they can not continuously exist as free surface waves and once generated will rapidly transfer their energy to the k_2 waves. For clean water, $T \doteq 75\ cm^3/sec^2$ and k_* and k_2 roughly correspond to frequencies of 10 and 20 hz, respectively.

Fig. 27 shows the wave autospectra from the 2-second segment analysis of run 6B (80% confidence limits are roughly 1 decade wide). All 5 T.P. display the peak of the major wave field at around 1 hz. T.P. 1, from before the gust, is rather smooth in the band above 3 hz. T.P. 2, near the leading edge, shows a slight deficit around 9.5 hz, followed by a levelling off to 14 hz, a rapid drop to 19 hz, and a slight increase around 20 hz. During the 'active' T.P. 3 and the major burst in T.P. 4, spectral slope is less steep and the spectrum shows a slight bulge near 10 hz (i.e., near the frequency where $\Theta_{\tau\eta}$ leveled off and reversed slope); in T.P. 4, there is also a local maximum just above 20 hz. In T.P. 5, immediately after the burst, there is a significant deficit near 10 hz, and again a local minimum near 19 and maximum just above 20 hz. This sequence of events, particularly the change between T.P. 4 and 5, is strongly suggestive of the picture given by McGoldrick. During generation the k_* waves are not only present but near saturation because of the energy input from the wind; as soon as the forcing disappears, so do the extremely unstable k_* waves. Their energy is 'drained' to higher frequencies. Fig. 28 shows a similar example from run 2,

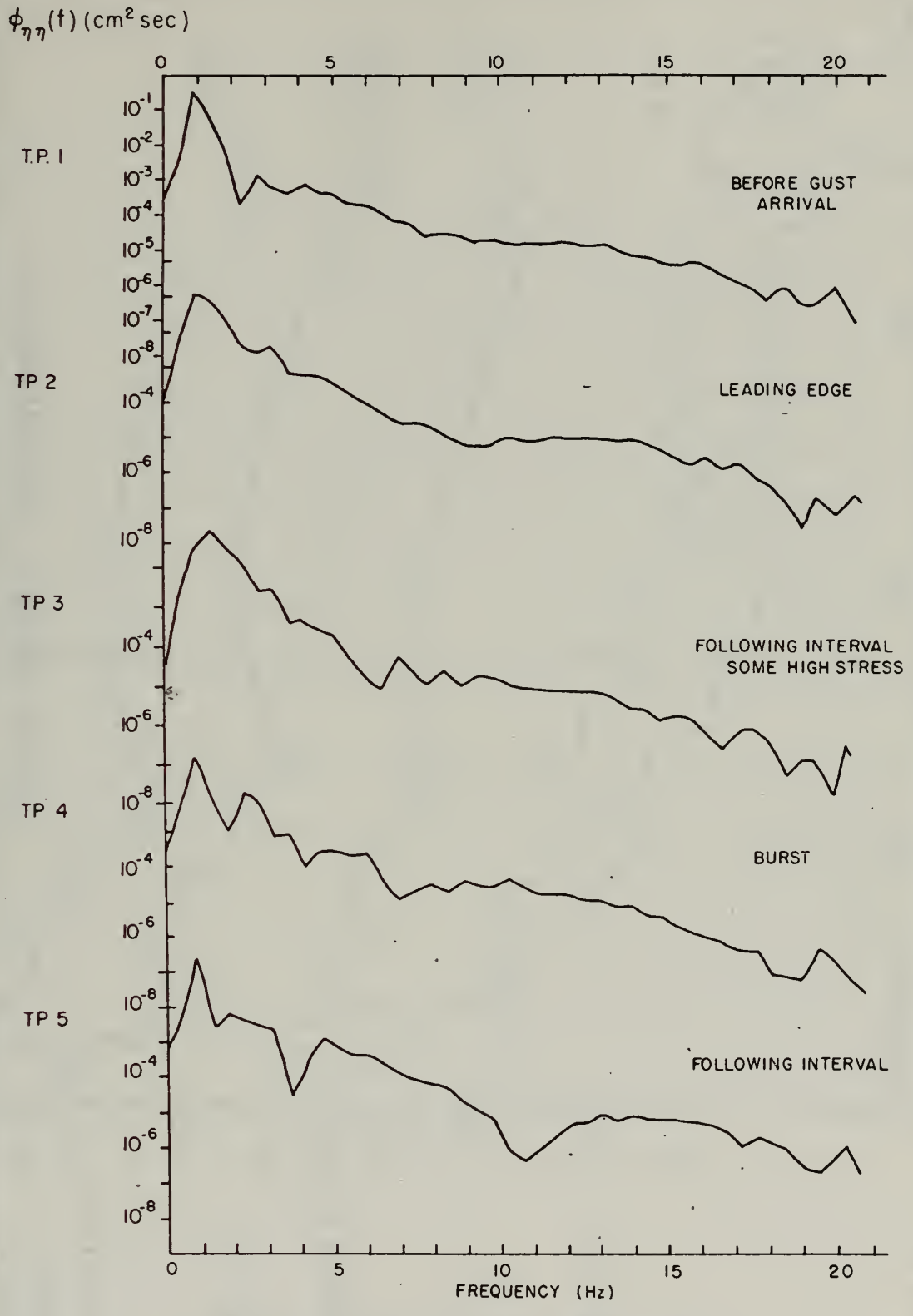

$\Phi_{\eta\eta}(f)$: AUTOSPECTRA OF WAVE HEIGHT

RUN 6B 2 SECOND AVERAGING PERIOD

Figure 27.

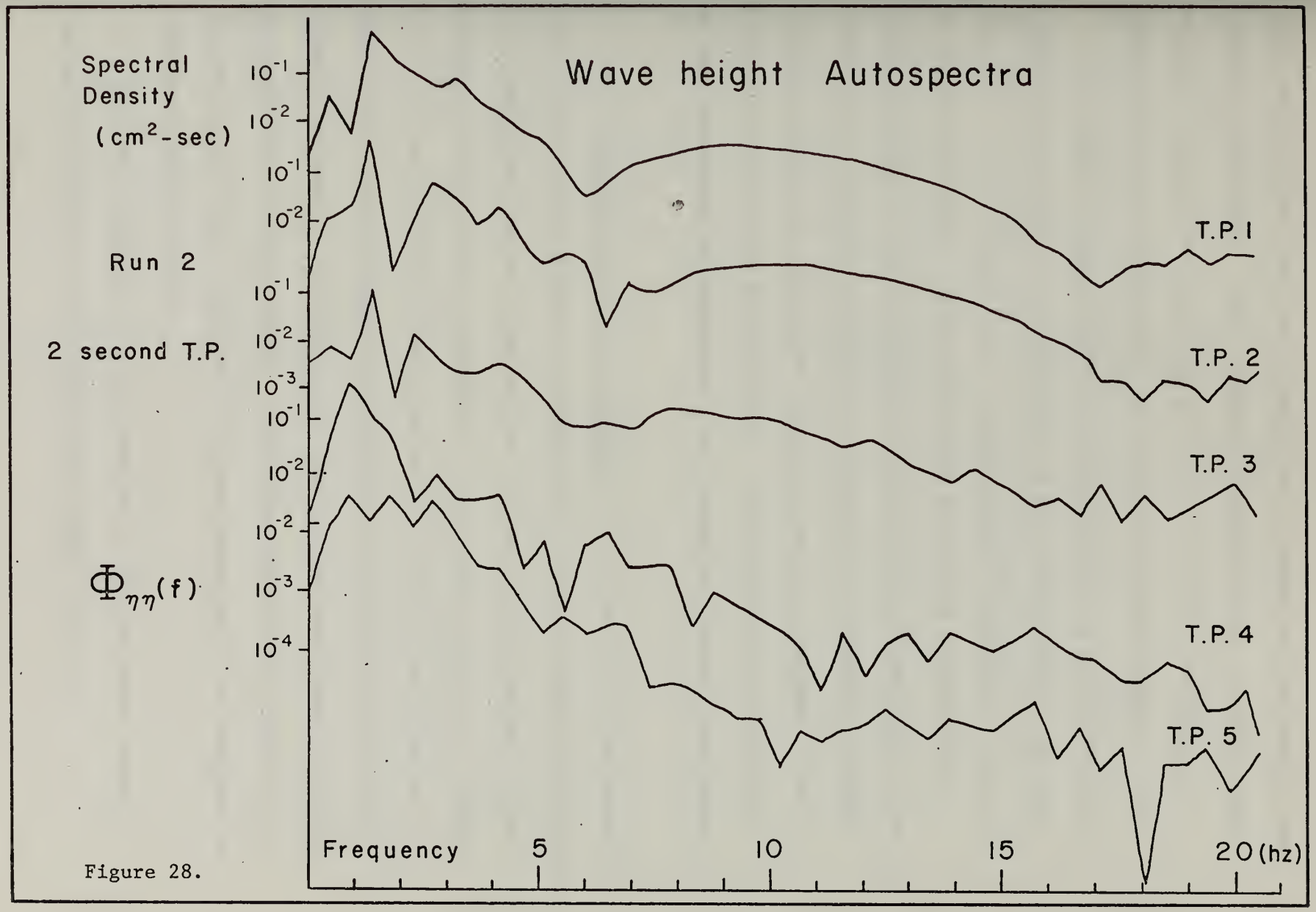
Wave height Autospectra
Spectral Density (cm²-sec)
Run 2
2 second T.P.
$\Phi_{\eta\eta}(f)$
10^{-1}
10^{-2}
10^{-1}
10^{-2}
10^{-1}
10^{-2}
10^{-3}
10^{-1}
10^{-2}
10^{-2}
10^{-3}
10^{-4}
T.P. 1
T.P. 2
T.P. 3
T.P. 4
T.P. 5
Frequency
5
10
15
20 (hz)

Figure 28.

where the mean wave field was significantly larger and the results consequently less clear. Here the major burst was in T.P. 3, with lesser activity in T.P. 4 and quiescent in T.P. 5. In T.P. 5 the spectral deficits occur at 10 and 18 hz, with the local maximum around 19.5 hz.

The slight frequency shifts of the postulated k_* and k_2 waves are readily attributable to contamination of the Charles River. The very fact that the predicted effects of weak resonant interactions stand out at all in other than a 'carefully tuned' laboratory experiment is strong evidence of their importance in wave spectral development. Evidence that perturbation analysis is suitable for predicting continuum nonlinear effects in major wave fields was recently provided by the bispectral analyses of Garrett (1970). Nonlinear transfer of energy is thus apparently of importance at all stages of spectral development.

C. A Further Note on Time Averaging. The results of the preceeding sections have emphasized the importance of high frequency fluctuations, the intermittent nature of generation, and the coupling between scales. Averages over time scales comparable to the entire gust or to a combination of burst and interval have been shown to obscure the selective high growth rates associated with the local instabilities, the effectiveness of wavelets in coupling the wind and the waves, and the nature of interactions between scales. One further example will serve to illustrate the critical importance of proper averaging in the analysis of wind-wave generation data.

Consider a typical cat's paw from run 2. Typical mean velocity values for different scales can be very roughly taken as

$\langle U \rangle_{2\,hours} = 7$ m/sec , $\langle U \rangle_{gust} = 15$ m/sec ,

$\langle U \rangle_{burst} = 20$ m/sec , $\langle U \rangle_{interval} = 10$ m/sec .

Similarly, temperature means may be estimated, with $\Delta T_{air\text{-}sea} = 1°C$, as

$\langle T \rangle_{2\,hours} = 5°$, $\langle T \rangle_{gust} = 4.3°$,

$\langle T \rangle_{burst} = 4.0°$, $\langle T \rangle_{interval} = 4.6°$.

Next, assuming rms turbulence levels of 10% (a very low estimate for a gust or burst), $3.75° < T'_{burst} < 4.25°$, 18 m/sec $< u'_{burst} <$ 22 m/sec.

As demonstrated in Section A, the important fluctuations in heat and momentum transfer and wave and turbulence generation are $\mathcal{B} = w'T'$ and $\tau = -\rho\, u'w'$ (assuming symmetry in v' and $\overline{V} = 0$). Then

$$U = \langle U \rangle + u', \quad W = \langle W \rangle + w', \quad T = \langle T \rangle + T'$$

and since $\langle W \rangle$ and $\langle w' \rangle$ are taken $= \emptyset$ over whatever averaging period is chosen,

$$u'w' = w'(U - \langle U \rangle) \quad \text{and} \quad w'T' = w'(T - \langle T \rangle).$$

Because of the impressed zero mean of W, the long term mean fluxes will be independent of the choice of $\langle U \rangle$ and $\langle T \rangle$; however, both the magnitude and the sense (sign) of the instantaneous fluxes (or of very short averages) are strongly affected by this choice. For the example above, choosing $U = \langle U \rangle_{gust}$, $T = \langle T \rangle_{gust}$, and plotting a joint histogram of the resultant values of τ and $\mathcal{B}$ for the burst, the result will appear as in Fig. 29B (Fig. 29 is from run 2, 2-second T.P. 2); while if the means are chosen as the burst means, results are as shown in Fig. 29A.

When viewed against the general gust background it appears as if the τ and β fluctuations are negatively correlated (of opposing effect in turbulence production) and very strong; when viewed against the 2-second background, mostly burst, the fluctutations are relatively much smaller and show a weak positive correlation. Similarly, when the results are applied to the turbulent kinetic energy balance, the effects on production,

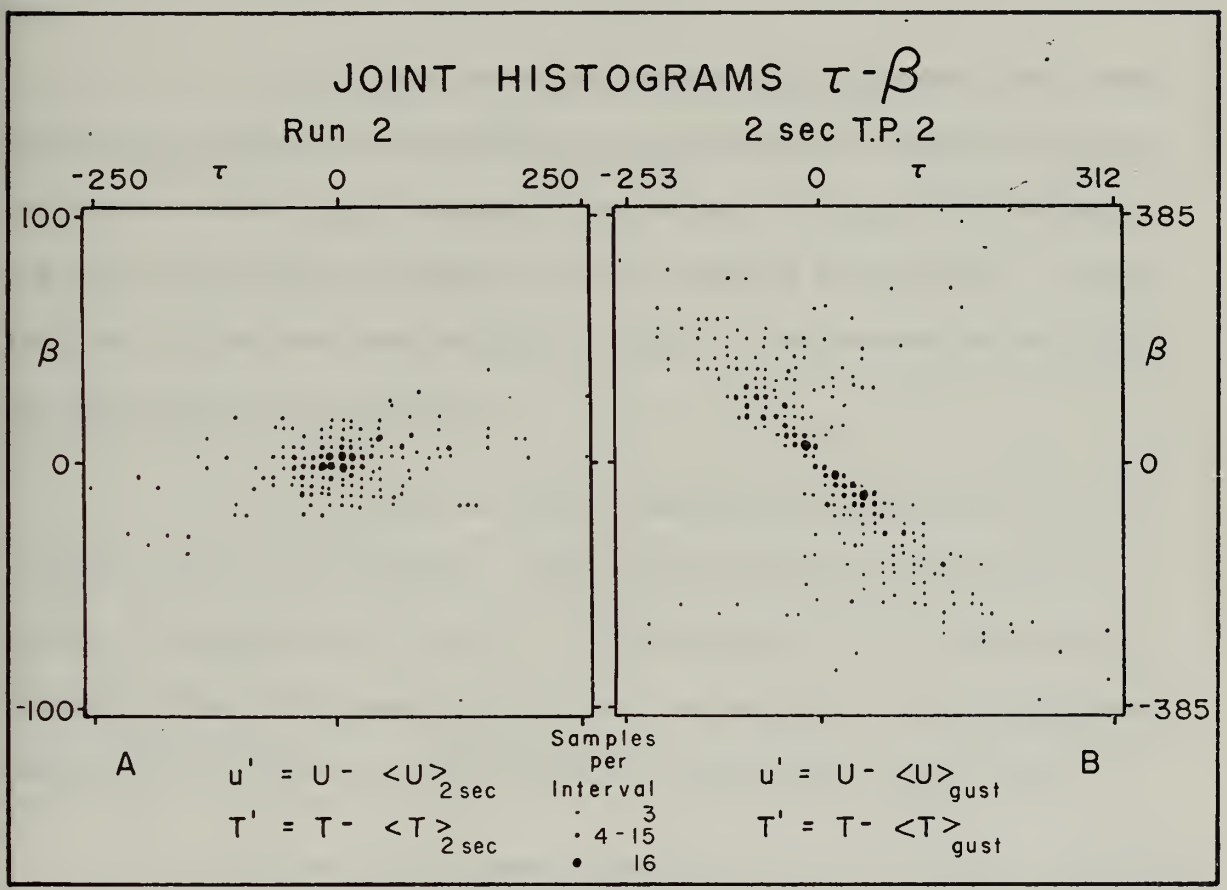

Figure 29

and hence on the stability structure of the boundary layer, are opposite.

This is an extrememly straightforward but seldom applied result. The proper choice of averaging period must be made on the basis of the important scales in the process under consideration. For wave generation and air-sea momentum transfer, these have been shown to be the scales of and within the bursts and the main wave field. Consideration of the wave generation process in terms of long term mean effects can totally obscure

the physical realities.

Summary of Results and Conclusions

The primary facts to emerge from this study may be summarized as follows,

1. Cat's paws are highly intermittent phenomena that themselves are composed of localized bursts separated by quiescent intervals. The bursts contain high frequency fluctuations of stress and buoyancy 3-4 orders of magnitude larger than that observed in the mean. The variability in time was shown in Fig. 2 - Fig. 7; representative magnitudes are shown there and in Fig. 8.

2. The bursts are associated with the generation of high frequency waves and turbulence. This is best demonstrated by the sequence of events shown in Fig. 23. Participation of the fluctuating boundary enhances the magnitude of the fluctuations, as shown by a comparison of the results of this study with measurements over land.

3. The high frequency instabilities not only have large growth rates on their internal scales, but also are associated with the growth of lower frequncy components. Both high and low frequency fluctuations are strongly enhanced in the bursts, as shown by the changes in magnitude and shape of autospectra (Fig. 9) and on the detailed SC-4020 plots. This is not only true for couplings within but also for couplings between media as demonstrated by the differences in coherence between stress and surface waves in the 2- and 1-second time periods (especially T.P. 4, Figs. 21 and

24). The bursts are also associated with the development of shear layers in the wind profile and with large values of turbulence production (see Fig. 10), a further indication of the importance of localized instabilities.

4. The boundary layer is mixed and tumbled by the instability fluctuations in the bursts. The effect of strong temperature stratification in the boundary layer is to delay the onset of wave generation by requiring intial utilization of available turbulent kinetic energy for destabilization. Buoyancy forces are very effective in degrading the magnitude and effectiveness of momentum flux, and quickly cause restabilization after passage of the gust.

The general mixing and boundary layer inversion patterns are shown in the joint histograms of U - T' (Fig. 11) and τ-β (Figs. 13, 15) and in the phase reversals in the coherence of T' - η and τ -β (Figs. 12, 14). The mixing associated with the bursts, and the partial restabilization during intervals, is shown by the changes in correlation between τ and β in Fig. 20. The delay of generation attributable to the utilization of kinetic energy for mixing is demonstrated in Figs. 22 - 24, where the burst at the leading edge (T.P. 2), uncoupled to the waves, has little effect upon the water surface but effectively inverts the boundary layer.

The effects of stability have also been demonstrated by the excess of intermediate sized velocity fluctuations in the leading edge (Fig. 26, runs T.P. 2), by the rapid rise of T after gust passage (Figs. 11, 15), and by the temperature increases and decreases associated with τ and β fluctuations of different relative strength (e.g., Fig. 6).

5. The coupling between scales is strongly nonlinear, as illustrated by the lognormality of the distribution of squared velocity

fluctuations during bursts (Figs. 25, 26), the strong association of high frequency instabilities with large magnitude velocity, stress, and buoyancy perturbations (Figs. 2 - 7 and 9), and the association of burst length with the period of the major underlying wave components (Figs. 2, 4, 6).

6. Weakly resonant nonlinear interactions are effective in transferring energy among capillary-gravity waves. This was demonstrated by the change in the k_* and k_2 components (Figs. 27, 28) between 'generation' (burst) and 'detritus' conditions.

7. The important momentum transfer processes are of short duration, highly nonlinear, frequency selective, and strongly associated with intermittent high frequency instabilities and coupling between scales. This was demonstrated by the variations in τ-η coherence patterns between different averaging times and burst/no burst conditions (Figs. 21, 24), by the simultaneous occurrance of strong Reynolds stress and capillary wave activity,(Fig. 23), and by the selectivity of coherence and spectral change (Figs. 24, 27, 28).

8. The differences between 'generation' and 'detritus' can be described by the changes in coherence between variables and in the probability distribution of velocity fluctuations. Detritus coherence is characterized by low magnitude (γ) and/or by continuous phase (Θ) slippage in any coherent bands; during strong coupling and generation, γ is high and Θ is nearly constant in the frequency bands that participate most strongly in the transfers (Figs. 19, 21, 24). Velocity fluctuations (measured as ξ) in detritus have excesses of intermediate values and approach normal distributions; those from generation periods are more nearly lognormally distributed with excesses of very large values and

values near zero. These differences are due to the enhanced range of scales and strength of the couplings involved in wave generation and turbulent interactions.

The intermittency switch function ($I = 1$, $\tau \geq 100$ dynes/cm^2, $I = 0$, $\tau < 100$ dynes/cm^2), shown only in Fig. 5 but computed in all runs and used for selection of the 2 and 1 second time periods, appears to be a suitable first approximation for a conditional sampling switch. When smoothed over a time period ≤ 0.5 seconds it provided a reliable indicator of the presence of a burst and instability-associated generation.

9. There is a rough, qualitative similarity between scales of motion (e.g., gust and burst), events of different magnitude (Fig. 7), and between turbulence patterns over land and water surfaces. The similarity lies in the presence of a large range of scales. The significant differences are caused by the strength of coupling between these scales; the larger the number of participating scales and media, the stronger the coupling and the more efficient the associated heat and momentum fluxes. These features were demonstrated by a comparison of flux measurements over land and water, and illustrated in the time plots of the variables. The simultaneous enhancement of frequency range and fluctuation magnitude in bursts is perhaps best displayed in Fig. 7, where the 'instantaneous' magnitudes are based on the 10 second means.

It was also demonstrated (Section C, Fig. 29) that the effect of τ and ρ fluctuations can be different when their magnitude and sense are evaluated over different scales; e.g., a burst may contribute to boundary layer instability as seen from the long term mean, while the local and immediate effect of the fluctuations is to temporarily reestablish a

portion of the initial temperature stratification. Averaging over time scales other than those of importance in the momentum transfer process can lead to misinterpretation.

10. Evaluation of generation in terms of the 'mean' can be misleading and obscures the physics of the transfers. Since much wave and turbulence generation does not occur on the mean but in localized, frequency selective, high growth rate instabilities (as depicted in Figs. 23, 24, and 27), and since the mean itself is a seldom if ever assumed state (as shown in the time series diagrams [Figs. 2-7] and the histograms [Fig. 8]), representation of the generation mechanisms only in these terms is unsatisfactory.

On the basis of these results it is concluded that microscales play a predominant role in wave generation. High frequency waves and turbulence are intermittently generated during high growth rate, local instabilities, and the wavelets subsequently act as drag elements to couple the longer waves to the wind. Further, the high frequency instabilities aid the growth of similar, lower frequency fluctuations. This combination of events leads to spectral growth rates much larger than those predicted on the basis of linear and weakly nonlinear theories.

III. THE ROLE OF MICROSTRUCTURES IN WIND-WAVE SPECTRAL DEVELOPMENT

Abstract

Measurements of the wind, wave and surface current fields were made from a 38.5 meter spar buoy at the mouth of a tidal channel. Statistical analysis of velocity profiles showed that both air and water boundary layers were predominantly logarithmic (neutral stability), and confirmed Ruggles' (1970) finding of anomalous behavior of atmospheric profile parameters at critical wind speeds. A lack of simple relationships among profile measures indicates that wind-wave coupling can be only very poorly characterized on the basis of means, that the time history of spectral evolution is crucial to an understanding of the physics governing the momentum transfer, and that more than one wave generation regime exists.

A two-day history of spectral development, which did not include the major profile anomalies, was analyzed to determine the nature and scales of momentum transfer processes. Wave generation was found to occur predominantly in short, intermittent, burst-type events, and to involve strong nonlinear coupling of wind and wave fields with associated rapid growth of the high frequency components. These important events involve coupling between wave groups in wind and surface wave fields and strong interactions between the media and between frequency bands in both fields. Tidal currents modulate the wave field and cause imbalance of wind-wave equilibrium conditions.

Introduction

Microscale studies in cat's paws have demonstrated the importance of intermittent, strong interactions between scales of motion and between atmospheric turbulence and the sea surface in the generation of high frequency waves. Similar types of interactions are also significant in the development of the major portion of the wind-wave spectrum.

In the open ocean, typical Reynolds numbers are on the order of 10^8; local wave generation occurs under the influence of surface drift, tidal currents, propagating swell, and stability, precipitation, wind speed and direction shifts associated with large weather systems. The large

number of participating scales and phenomena can all interact, with both strong and weak coupling, to have a significant effect on spectral development. It will be shown that there are separate regimes of wave generation, and that the time history of events is of crucial importance in development of the wave field.

Most previous open ocean studies of spectral development have dealt with mean or long time average wave energy growth and have examined the influence of only atmospheric conditions upon the wave field. Airborne measurements (e.g., Barnett and Wilkerson, 1967; Schule et al, 1971) and other laboratory and oceanic studies which extended over a range of fetch (e.g., Snyder and Cox, 1966; Sutherland, 1967; Mitsuyasu, 1969) have dealt extensively with the major features of spectral development with little or no experimental reference to the causative momentum transfer mechanisms. From these types of studies spectral growth rates, the frequency shift of the spectral peak, the existence of an equilibrium range for high frequencies, and the overshoot/undershoot phenomena have become well known features.

Studies from stationary buoys or platforms (e.g., Seesholtz, 1968; Ruggles, 1969) have evaluated growth rates in terms of wind velocity profile characteristics with minimal consideration of the effects of the underlying current and subsurface boundary layer conditions. Such studies have shown that the atmospheric boundary layer is essentially logarithmic (at least for near-neutral stability) and that spectral growth rates are substantially larger than those predicted by the inviscid laminar Miles theory (Miles, 1957).

Investigations of the direct interplay between wind and waves have concentrated on the transfer mechanisms suggested by this theory. One of

its critical elements is that turbulent and wave induced Reynolds stresses do not interact, and that momentum transfer occurs by means of an instability in the mean shear flow. The momentum is extracted from the mean flow in the critical layer and transmitted downwards by wave induced Reynolds stresses.

The recent work of Kendall (1970) demonstrated that a fixed wave pattern caused significant modulation of the turbulent structure, but that the induced fluctuations did not have a constant phase relation to the waves. Davis (1970) and Stewart (1970) theoretically and experimentally investigated the vertical structure of Reynolds stress and found poor quantitative agreement with the wave-turbulence Reynolds stress profile predicted by instability theories. Wave induced Reynolds stresses accounted for only about half of the momentum carried to the wave surface by the pressure component in phase with wave slope.

Ruggles (1969), Davidson (1970), and Shemdin and Lai (1970) have all demonstrated the existence of wave induced perturbations in the wind field and have shown that these wave induced Reynolds stresses do interact with turbulent stresses. There is thus substantial evidence that interaction between atmospheric turbulence and surface waves is one of the crucial mechanisms involved in the transfer of momentum to the waves. This problem is being studied by Saeger and Reynolds (1971); their initial results indicate that the inviscid model, by neglecting the important structure of the critical layer, gives very poor predictions of the Reynolds stress and hence of momentum flux to the waves.

The cat's paw studies have demonstrated the importance of detailed, near-surface measurements in determining the interactions among forces. Dobson (1969,1971) recently made the first successful detailed field

measurements of atmospheric pressure on wind generated waves. His important results showed that the observed phase shifts were an order of magnitude larger than predicted by Miles' theory, and that energy and momentum flux spectra were strongly peaked at or above the peak of the locally generated waves. Further, the inviscid laminar Miles model underpredicted increases in wave energy by factors of 5-8. These facts suggested a strong interaction between wave induced and turbulent Reynolds stresses. Dobson also noted that energy flux and wave supported momentum flux were negligible above relatively low frequencies, contrary to an assumption that much of the momentum transferred goes into short waves (Wu, 1969; and the cat's paw and present studies) but not contradicting the suggestion that short waves aid the growth of lower frequency instabilities by nonlinear coupling between scales of motion. Near surface pressure measurements over waves made by Elliott (1970) confirmed Dobson's pressure shift findings. Elliott noted that pressure lagged the wave by about 135° during generating, and by 180° during non-generating conditions. There was no vertical phase shift at heights above the crests. Elliott's work also suggested strong interactions between wave induced components and normal boundary layer turbulence.

The basic conclusion from detailed investigations of near-naviface structure and air-sea coupling is that turbulence and waves interact strongly and intermittently. Only a relatively small portion of the wave growth is due to processes which act on the 'mean', and these processes are themselves strongly dependent upon the presence and location of high frequency components and associated strong nonlinear coupling.

The structure of the underwater boundary layer is also of major importance in transfer processes. It has been repeatedly demonstrated

that the magnitudes as well as the mechanisms involved in transfer of momentum, heat, and moisture across an interface are radically different for flat plates or solid surfaces and fluctuating or moving surfaces (e.g., Chambers et al, 1970; Mangaralla et al, 1970). Over water, the processes are different for the cases of wind waves alone and wind waves with the added presence of swell and surface drift.

Few experimental studies have considered the effect of the water near-surface layer motions upon wind-wave coupling, although the weak interactions between waves and currents or very long swell are well known theoretically (e.g., Longuet-Higgins and Stewart, 1960, 1961). The available experimental evidence on the structure of and interactions in the water boundary layer is somewhat contradictory. Shonting (1967, 1968) noted that u-w phase relations were close to those predicted by classical theory, with no phase shift with depth and only minor interaction between wind waves and swell. Shonting, Stewart and Grant (1962) and Yefimov and Khristoforov (1969) have all found that wave stress is strongly concentrated very near the surface, and that essentially all dissipation occurs above the trough. The transfer between high and low frequencies caused by dissipation (breaking) and viscous decay of short waves (Longuet-Higgins, 1969b; Hasselman, 1971) is also a surface phenomenon, and involves non-linear coupling between scales. Shemdin and Lai (1970) found that the wind-induced drift in a wind/water tunnel had a logarithmic profile, and that the surface stresses computed from the air and water profile parameters were roughly equivalent. Introduction of mechanical waves disrupted the wind driven current. The couplings between the adjacent boundary layers and the interface are thus as yet imperfectly described.

This experiment was designed to investigate the nature and time scales of air-sea coupling during wave generation. It was conducted during a variety of wind, weather and current conditions. The analysis was divided into three segments. First, a study was made of the air and water boundary layers in terms of a logarithmic profile model. This section extends and complements the investigations of Ruggles (1970) and Groscup (1971), and describes the general environmental background of the more detailed analyses. Second, the time history of spectral growth during a two day period of increasing winds was investigated. In this section the general nature of coupling between wind, wave and current fields is described. Finally, segments of the two day record were studied in detail to emphasize the importance of strong, intermittent generation of high frequency waves and resultant wave-turbulence couplings that were demonstrated in the cat's paw study. Generation 'events' are described and their influence on the main wave field is displayed.

The major objectives of the study were to demonstrate the wide range of interactions involved in wave generation and spectral development, and to emphasize the importance of high frequency 'microscales' and intermittency in the momentum transfer process.

The Experiment

Measurements of wind and water speed profiles and wave height were taken from a stable, 38.5m spar buoy (Mollo-Christensen and Dorman, 1971) (Fig. 1). The buoy was slack moored in 31.1m of water (MLLW) and faced into the tidal current (NE flood, SW ebb, 1.5m/sec maximum current). The experiment ran from July through October, 1970. The site was at

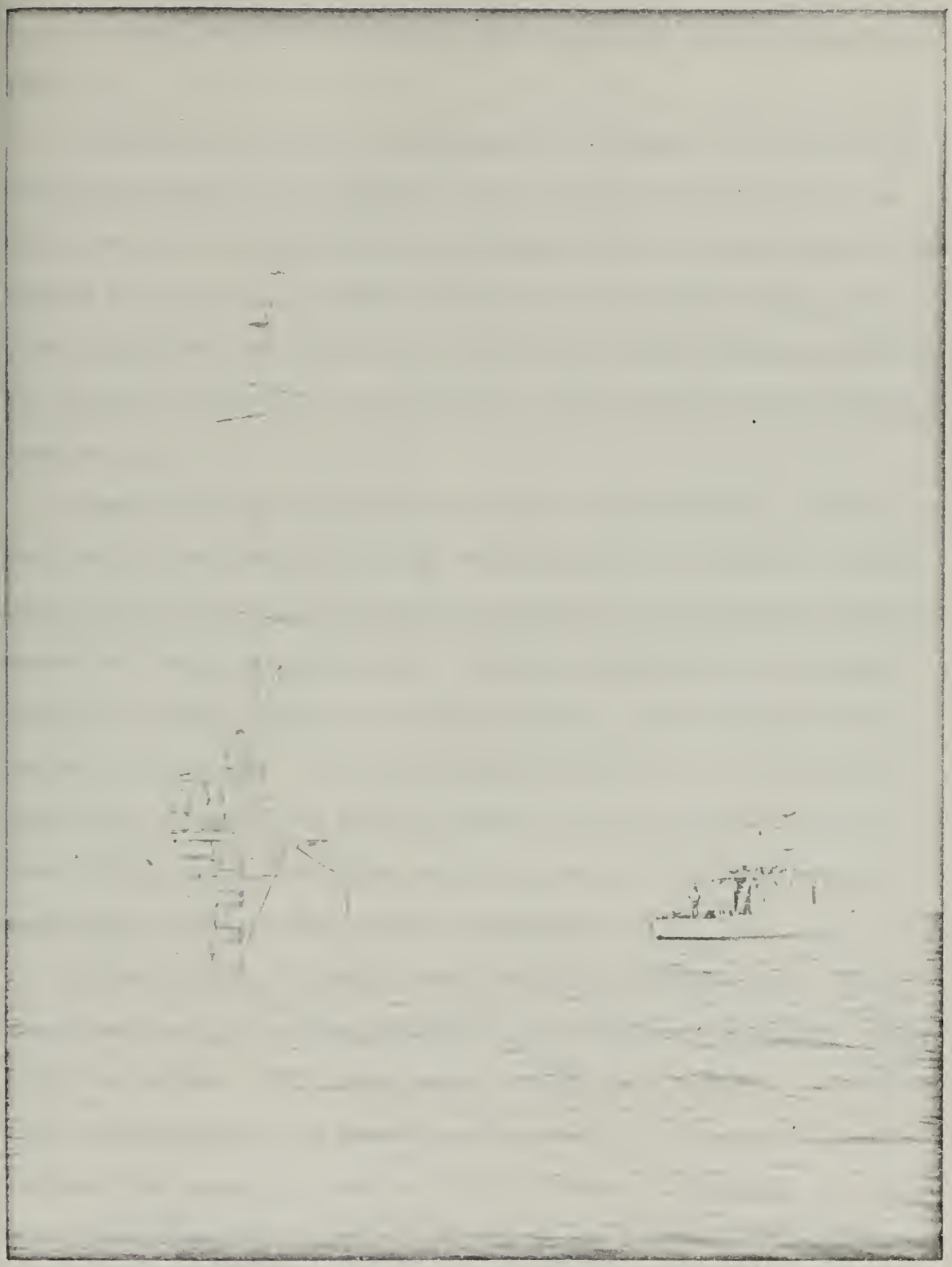

Figure 1. M.I.T. Air-Sea Interaction Buoy

the mouth of a tidal channel (Vineyard Sound, Massachusetts); minimum fetch to the S and SW (direction of prevailing winds and sea breeze) was 50km.

Instruments included 5 cup anemometers at heights of 2.4m to 11.4m, 3 ducted-propeller (5cm diameter) current meters at depths of -1.5 to -4.7m, and two capacitance type wave gauges with 4.6m sensor length. The primary wave gauge was mounted directly over the current meters, 2.5m cross-stream from the anemometers. Thermistors were attached to arms of the velocity transducers at +5 and -2.5m. Buoy tilt was sensed with a pendulum pot.

Signals from the transducers were mixed, telemetered to a shore support facility on Cuttyhunk Island, Massachusetts and recorded in analog mode. Time, voice log, and 25kc clock signals were transmitted and recorded for use in synchronization. Velocity information was in pulse format, wave gauge signals a variable frequency, and thermistor data a variable D.C. voltage. Data processing was done at M.I.T. and used a combination of analog and digital methods. Digitization rate for the time history analysis was 10hz; velocities were pre-filtered at 2.5hz, wave gauge signals at 5hz, to avoid aliasing.

A total of 146, 10 minute 'mean condition' runs were made. There were 5 series of runs, with data taken once each hour for periods ranging from 6 to 53 hours. 109 of the runs contained data suitable for analysis. Winds and waves were from the S-SW during almost all runs, with 10 minute mean wind speeds (at 10m) of 1.5 to 12.5m/sec. Because of the large fetch the atmospheric boundary layer was nearly neutrally stable during all runs (Δ T air-sea $\leq$ 3°C and $-.02 \leq Ri_{(bulk)} \leq .05$). Similarly, the water surface layers were generally well mixed down to a depth of at

least 8-10m.

The analysis was conducted in three parts. First, a distribution analysis was made of the parameters obtained from a comparison of velocity data with a neutral stability logarithmic profile model. Of the 109, 10 minute anemometer runs, 96 (88%) had correlations $\geq$ 0.94 with the model. Of the 51 minimeter profiles used (from the longest nearly continuous segment, runs 109-159, also used in the time history analysis), 48 or 94% were logarithmic to within the required contraint; 49 of the anemometer profiles from the same period were logarithmic. Much of the analysis was based on 30 second averaging times. For the anemometers there were 2467 samples (81% logarithmic; 1057 samples with 91% logarithmic for runs 109-159), for the minimeters 1060 samples (85% logarithmic). Ruggles (1969, 1970) has discussed the significance of the correlation coefficient; Groscup (1971) has described the increasing tendency to a logarithmic profile with increasing averaging time for the runs discussed herein. Only the runs satisfying the $\rho \geq 0.94$ criterion were used in the histogram analysis, since the parameters are computed from the assumed model. This procedure is really only satisfactory for parameterization and description of the general background conditions and generation regimes, since as shown in the cat's paw study strong intermittent events are associated with large profile deflections and the development of unstable shear layers. The approach to a logarithmic profile with increasing averaging time is merely another indication that long term averages can obscure the physics of the transfer processes.

The longest set of runs was then analyzed using standard time series techniques. The data is presented in terms of spectral growth and the related changes with time of atmospheric and water variables, and the

coherence-phase relationship between horizontal wind speed and waves. Spectral estimates have 6 to 20 degrees of freedom (dof); the 80% and 90% confidence limits of the χ^2 distribution (at $\Phi = 10^n$, n integer) are shown on the spectral growth and spectral density estimate diagrams. Garrett (1970) has recently demonstrated the independence and normal distribution of the real and imaginary parts of the Fourier coefficients implicit in the use of this measure for mean wave fields. The confidence limits are applicable only to each individual realization of the spectrum, and do not provide estimates of variance of the wavefield for times longer than the overall averaging period; e.g., the 30 second spectra are strongly affected by the presence or absence of swell and major wave groups. Coherence magnitude (γ) was tested on the assumption that the variates were random with a bivariate gaussian distribution (Amos and Koopmans, 1963). (As demonstrated in the cat's paw study and further displayed herein, this is a poor assumption for strongly coupled variables; unfortunately it is the only readily available method). The results may be generally stated (for 5 minute time segments) as, at the .05 level of significance, the probability that the hypothesis $\gamma = 0$ is incorrect for a measured $\gamma \geq 0.5$ is 97%. (For the 30 second segments, this probability has dropped to 70%).

Finally, several 10 minute segments from the start, middle, and end of the set of 51 runs were analyzed using 30 second averaging periods. The data is presented in a similar fashion, with the added utilization of analog strip chart displays of 'events'.

Results and Discussion

A. Boundary Layer Profiles. With the assumption that the averaged stress (τ) in the near surface region is constant with height, a characteristic velocity of the turbulent boundary layer may be defined,

$$U_* = \sqrt{\frac{\tau}{\rho}} = \sqrt{-\overline{u'w'}}.$$

This is termed the friction velocity. Using similarity arguments, for a neutrally stable atmosphere the only characteristic length is height. The resulting profile equation is

$$U(z) = \frac{U_*}{\kappa} \ln\left(\frac{z + z_o}{z_o}\right)$$ where κ is Von Kármán's constant = 0.40 and z_o, the roughness length, is generally not added to the height in the numerator (see, e.g., Lumley and Panofsky, 1964).

There is general agreement that this simple model gives a good description of the mean velocity profile in conditions of neutral stability over both land and water, but there is still considerable debate on the meaning of and relationships between the profile parameters (U_* and z_o) and other variables computed from the model. From the development of the model, U_* and z_o are independent similarity parameters characterizing the boundary layer; however, Sadeh, et al, (1971) have demonstrated that once the roughness elements are sufficiently high compared to boundary layer thickness, U_* and z_o become local variables.

Measurements of the profile parameters over waves have been reviewed and discussed in detail by Wu (1969a, 1969b, 1970) and Ruggles (1969, 1970). Wu states that the wind stress ($\tau = \rho U_*^2$) is supported by form drag provided by wavelets superimposed on the larger waves; air flow

separates from the wavelets whose phase speed is less than U_*. z_o becomes a measure of the height of these roughness elements (roughness height = 30 z_o) and is related to friction velocity by Charnock's relationship, $z_o / (U_*^2/g) = \text{constant}$. This is manifested by an increase in the drag coefficient ($Cd_z = \tau/\rho U_z^2 = (U_*/U_z)^2$) with U up to a 'saturation' value, U = 15 m/sec. Above 15 m/sec the wind speed is larger than the average wave phase speed and Cd and z_o become nearly constant. Effectively, the Charnock relation implies that a single parameter can be used to describe the flow and thus the momentum balance of waves and atmosphere. The development of the profile model on the other hand assumed that U_* and z_o are statistically independent.

Ruggles showed that over waves, the wind speed is more appropriately represented as the sum of a mean profile component (supporting atmospheric dynamics), and a term representing the correlation between U_* and z_o (from wind-wave interaction). The 'correlation' wind component represents that portion of atmospheric momentum required to support air-sea interaction dynamics. It is roughly 10% to 20% of U_{total} above 4 m/sec, and negative below 2 m/sec (indicating a minimum wind speed for generation). Ruggles also found marked changes in z_o and Cd, with excessively high peaks and excessively large variances, at around U_{10m} = 2, 4, and 8 m/sec. These anomalies correspond to the division points of the Beaufort scale, i.e., to marked changes in the physical appearance of the sea surface. Similar anomalies are shown by Wu, who attributes the changes to the differences of flow in aerodynamically smooth, transition, and rough regimes. Hicks and Dyer (1970) found a simpler relationship, with Cd = .0011 and aerodynamically smooth flow below 6 m/sec, and Cd = .0015 with rough flow for U_{10} = 10 m/sec. They did not report any anomalies.

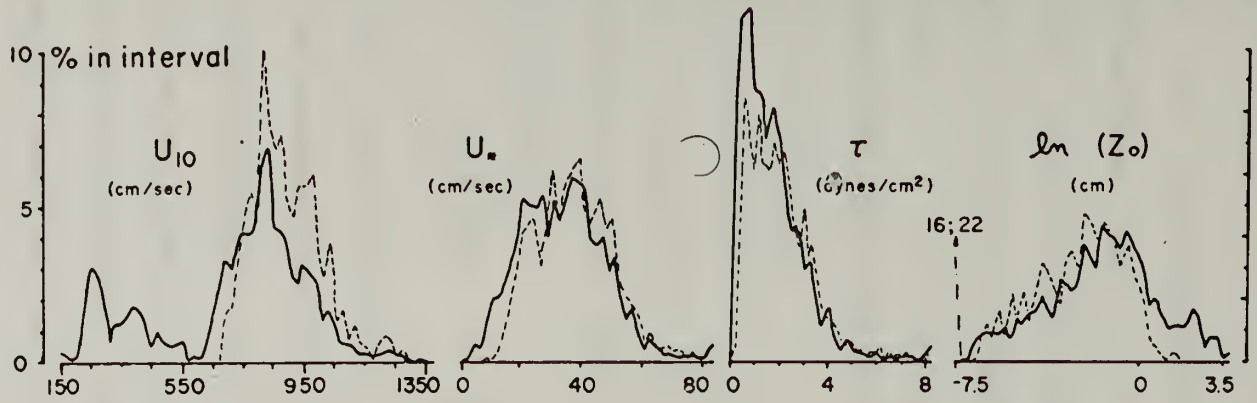

HISTOGRAMS

30 sec.avg. Wind Speed Profile Parameters

— All Runs (1994 Samples)

--- Runs 109-159 (957 Samples)

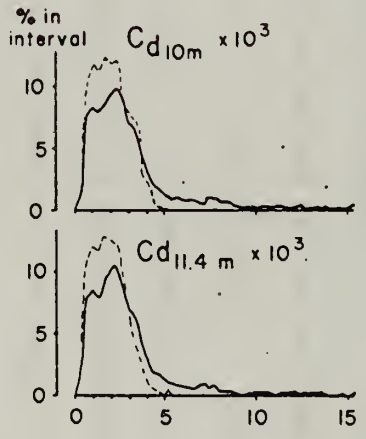

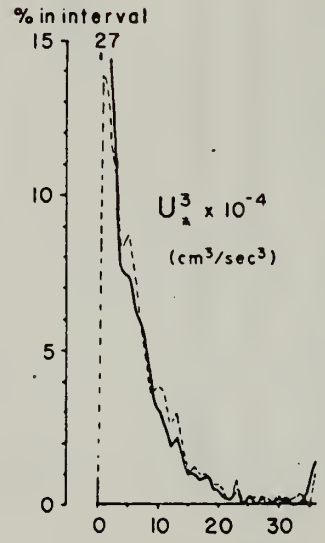

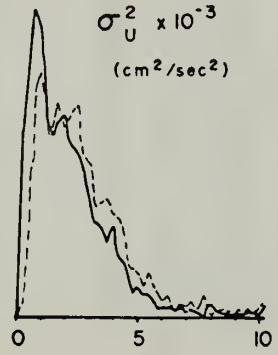

STATISTICS

Variable	Run Type	Mean	Variance
U_{10}	All, 30 sec avg	710	6.3×10^4
	109-159, 30 sec avg	888	1.4×10^4
	All, 10 min avg	690	7.9×10^4
U_*	All, 30 sec avg	32.75	200
	109-159, 30 sec avg	36.36	170
	All, 10 min avg	29.31	190
τ	All, 30 sec avg	1.59	1.81
	109-159, 30 sec avg	1.87	1.78
	All, 10 min avg	1.31	1.31
$Cd_{10} \times 10^3$	All, 30 sec avg	2.72	5.77
	109-159, 30 sec avg	1.77	0.88
	All, 10 min avg	2.32	4.07
$Cd_{11.4} \times 10^3$	All, 30 sec avg	2.62	5.20
	109-159, 30 sec avg	1.72	0.80
	All, 10 min avg	2.24	3.66
$U_*^3 \times 10^{-4}$	All, 30 sec avg	5.63	59.40
	109-159, 30 sec avg	6.78	58.82
	All, 10 min avg	4.26	33.26
$\sigma_U^2 \times 10^{-3}$	All, 30 sec avg	2.05	3.01
	109-159, 30 sec avg	2.58	3.46
	All, 10 min avg	1.75	2.59

Figure 2.

Additional evidence of anomalous wind speeds was given in the work of Groscup (1971) and Mollo-Christensen and Groscup (1971) (based on the data of this study). They further demonstrated a bi- and tri-modal distribution of z_o in the vicinity of the U_{10} = 8 m/sec discontinuity, and a bimodal distribution of U_* at or near the z_o and Cd discontinuities at 4 and 8 m/sec. The anomalies are indicative of enhanced air-sea interaction at specific wind speeds and of changes in the nature of wind-wave coupling. The large variances and bimodal distributions are evidence of enhanced nonlinear coupling at critical wind speed/surface condition values.

Fig. 2 shows the distribution (smoothed histograms) of 30 second average wind speed and of atmospheric logarithmic profile parameters from this study, both for all runs and for the subset 109-159 (those used in the time history analysis). Fig. 3 through Fig. 6 show selected joint histograms of the variables.

U_{10} was found from the profile model, using the computed values of U_* and z_o. The drag coefficient, Cd, was determined for both the computed 10 m and measured 11.4 m speeds. U_*^3 is a measure of turbulent kinetic energy production,

$$-\overline{u'w'}\frac{\partial \bar{U}}{\partial z} = u_*^2 \frac{u_*}{kz} = u_*^3/kz$$

and σ_u^2 is the variance of velocity in the profile, $\sigma_u^2 = \overline{(U(z)-\bar{U})^2}$.

The histograms show that a large percentage of the runs had very small roughness length ($\ln(z_o) < -7.5$ or $z_o < 1.8 \times 10^{-3}$ cm; values of $z_o < 10^{-3}$ cm were lumped into the $\ln [z_o] = -10$ category so that statistics were not computed). Stress values are in rough agreement with the long term averages found by other investigators; the mean is largest for the continuous strong winds of runs 109 - 159, and decreases with

increasing averaging time. The values of Cd are comparable for the measured and computed heights; Ruggles (1969) computed Cd_z for 5 anemometer heights and 10 m, and found similar results, with as expected a slight decrease with increasing z. The Cd values are concentrated in the normal range for runs 109 - 159, but when all runs are considered together, the 30-second and 10-minute means are excessively large and there are numerous exceptionally high drag values. These major, average changes in the drag effect of waves on the wind suggest the existence of more than one wave generation regime. σ_u^2 , Cd_{10} , and U_* (and thus U_*^3 and τ) all have decreasing mean values with increasing averaging times, indicating that profile distortion and resulting turbulence and wave generation occur infrequently; the short, strong, important anomalies are obscured by long term averaging.

Fig. 3 shows JH (U_{10}, U_*), JH(U_{10}, ln(z_o)), and JH(U_{10}, Cd_{10}) for the 30-second average profiles. In this figure, anomalies of U_* ln(z_o), and Cd_{10} all occur at roughly 2.5, 3.5, 6.4, 7.7, 10, 11, and 12.2 m/sec (they are particularly striking at 2.5, 3.5, and 7.7 m/sec, i.e., near those found by Ruggles). The anomalies are in the form of exceptionally large variances and wide departures of the interval means from any postulated simple fit of the data. The values are in general quite scattered and poorly represented by means. Also shown is JH(U_*^2/g, K) where K = 30 z_o is height of the roughness elements (wavelets) as postulated by Wu. It is obvious that a simple relation such as suggested by Charnok and found by Wu does not hold here. There are bimodal distributions and anomalies in both directions. A single parameter can not characterize the profile, because of the interplay between atmospheric dynamics and the wave field. None of the data can be fit with a linear relationship; in particular,

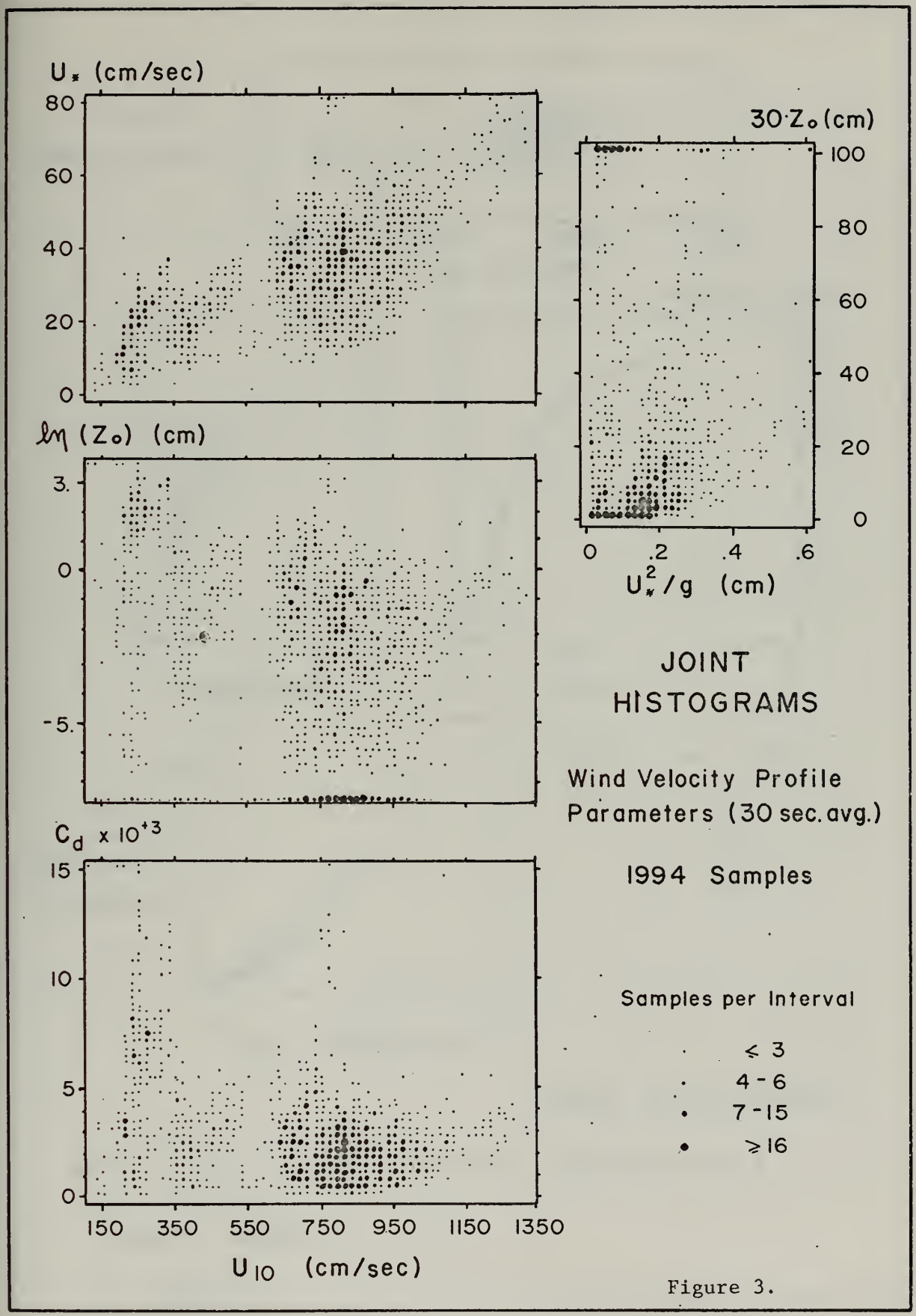
U* (cm/sec)
80
60
40
20
0
ln (Z₀) (cm)
3.
0
-5.
Cd x 10+3
15
10
5
0
150 350 550 750 950 1150 1350
U10 (cm/sec)
30·Z₀ (cm)
100
80
60
40
20
0
0 .2 .4 .6
U*²/g (cm)
JOINT
HISTOGRAMS
Wind Velocity Profile
Parameters (30 sec. avg.)
1994 Samples
Samples per Interval
≤ 3
4 - 6
7 - 15
≥ 16

Figure 3.

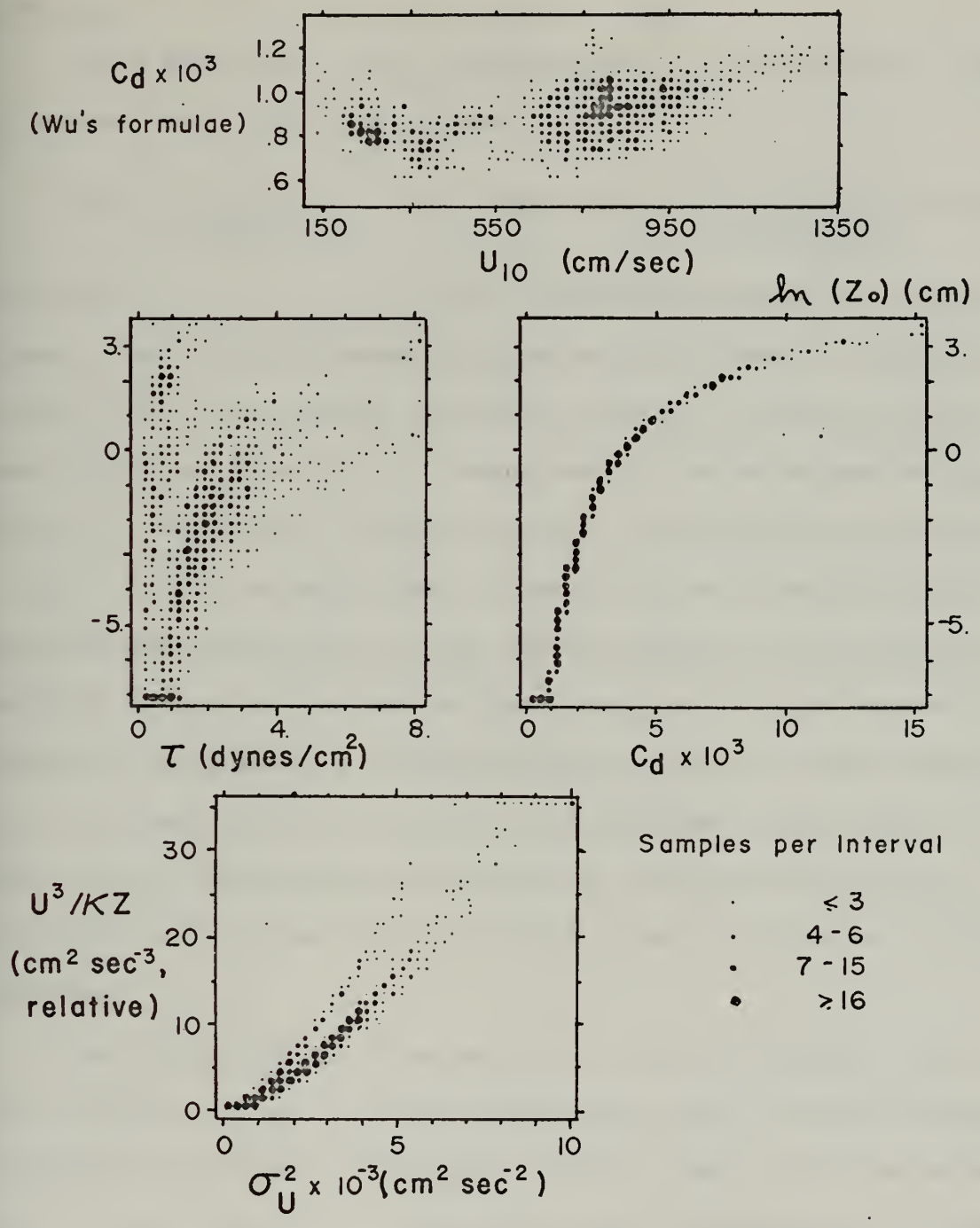

JOINT HISTOGRAMS

Wind Velocity Profile Parameters (30 sec. avgs.)

1984 Samples

Figure 4.

Ruggles's suggested $U_* = 0.04U_{10}$ intersects the minima of the mean of U_* on U_{10}.

Fig. 4 shows JH(U_{10}, Cd_{10}) computed using the formulae of Wu (1969b) for 'breeze' and 'light wind' regimes,

$$Cd_{10} = \left[\frac{\kappa}{\ln\left(\frac{9.1U_* \cdot 10m}{\nu}\right)} \right]^2 , U < 3 \text{ m/sec} \; ; \; Cd_{10} = \left[\frac{\kappa}{\ln\left(\frac{10m}{.015 U_*^2/g}\right)} \right]^2 3 \text{ m/sec} < U < 15 \text{ m/sec}.$$

The anomalies at 2.5 - 3.5, 7.5, and 12 m/sec again appear, but much less strongly than in direct computation from the profile model; in addition, the mean value of Cd computed using this technique is excessively small. Large scatter was found in joint histograms of other relationships suggested by Wu. The failures of these postulated simple models on the relatively short (30 sec) averaging times indicates that the dynamics of wind flow over open ocean wave fields at large Reynolds numbers can be only poorly described in terms of long time averages, even when the significance of wavelets is considered. Wu's contention that the small surface components support the majority of wind stress is not disproven by these data; the results merely indicate that the dynamics of the wind-wave coupling is considerably more complex than that caused by just form drag and air flow separation.

Fig. 4 also displays 30 second JH(τ , $\ln(z_o)$), JH(Cd_{10}, $\ln(z_o)$) and JH(σ_u^2 , $U_*^3/\kappa z$). The τ -$\ln(z_o)$ relationship shows a distinct bimodality, with generally increasing stress with roughness length and stress maxima for $z_o \geq 1$ cm ($\ln(z_o) = 0$). High stress occurs predominantly over large 'roughness elements', but only under certain conditions as yet undetermined. The $Cd_{10} = (U_*/U_{10})^2$ vs $\ln(z_o)$ plot is very closely fit by the profile relationship, $\ln(z_o) = 6.9 - \frac{1}{2.5(Cd)^{1/2}}$

(using $\kappa = 0,40$; Businger, et al, 1971, have recently noted that $\kappa = 0.35$

is a better value of Von Kármán's constant for neutral stability over a land surface); this is merely a check on the consistency of the logarithmic profile assumption and on the continuity of data from different time periods, and serves to emphasize the significance of the anomalies of the other plots (i.e., they appear not to be due to instrumental or analysis peculiarities, and the 0.94 correlation is a sufficient criterion for assuming a logarithmic distribution). The $\sigma_u^2 - u_*^3/\kappa z$ relationship shows that turbulent production increases with increasing fluctuations, but with a very strong bimodality, indicative of the presence of more that one production-generation regime.

Fig. 5 shows JH(U_{10}, ln(z_o)) and JH(U_{10}, Cd_{10}) for averaging periods of 2 and 10 minutes. The basic patterns of anomalies at specific values of U_{10} persist at the longer averaging times, but with less variance. (The 10-minute averages have been compared by Groscup [1971] to those of Ruggles [1970] [on the basis of log10 (z_o)]). The basic patterns remain, irrespective of averaging time, but the decreasing intensity of the anomalies shows that, as in the cat's paw studies, the strong and intermittent events are blurred or obscured by long time averaging. Even with these long averages and highly logarithmic profiles, it remains clear that the 'mean' is a very poor characterization of physical reality. The time history of events and the regimes and instantaneous characteristics of wind and wave fields, are highly significant in determining the nature of the boundary layer dynamics.

This point is further emphasized in Fig. 6, which shows JH of U_{10} with U_*, ln(z_o), and Cd_{10} for runs 109 - 159, and JH(U_{10}, U_*) for all runs for the two subclasses $|(\Delta\langle u\rangle_{30\,sec})_{30\,sec}| \geq 50$ cm/sec and ≤ 10 cm/sec. The JH of runs 109 - 159, characterized by strong and increasing wind and a large wave

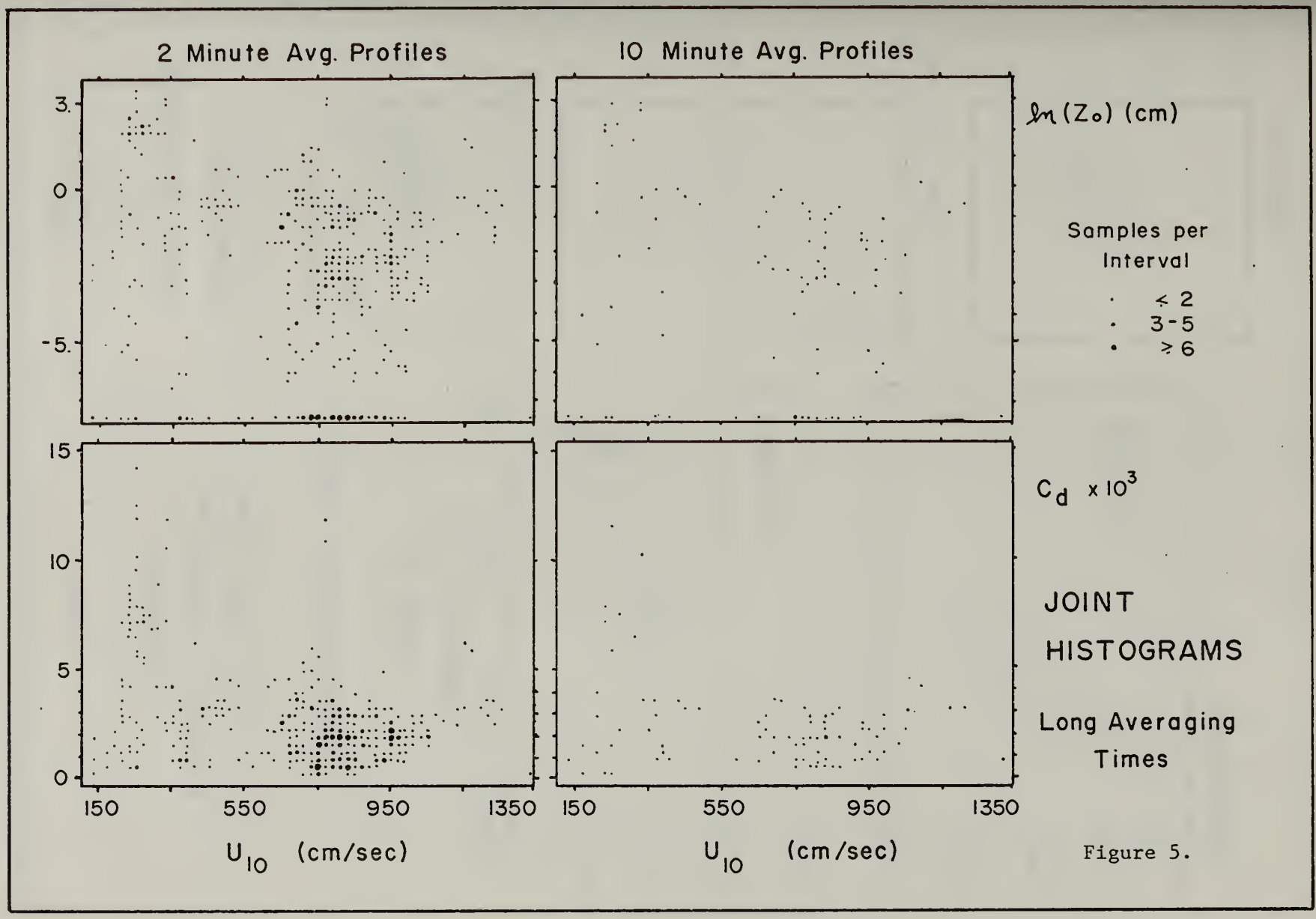
2 Minute Avg. Profiles
10 Minute Avg. Profiles
3.
0
-5.
15
10
5
0
150
550
950
1350
U_{10} (cm/sec)
$\ln(Z_o)$ (cm)
Samples per Interval
· ≤ 2
· 3-5
• ≥ 6
$C_d \times 10^3$
JOINT HISTOGRAMS
Long Averaging Times

Figure 5.

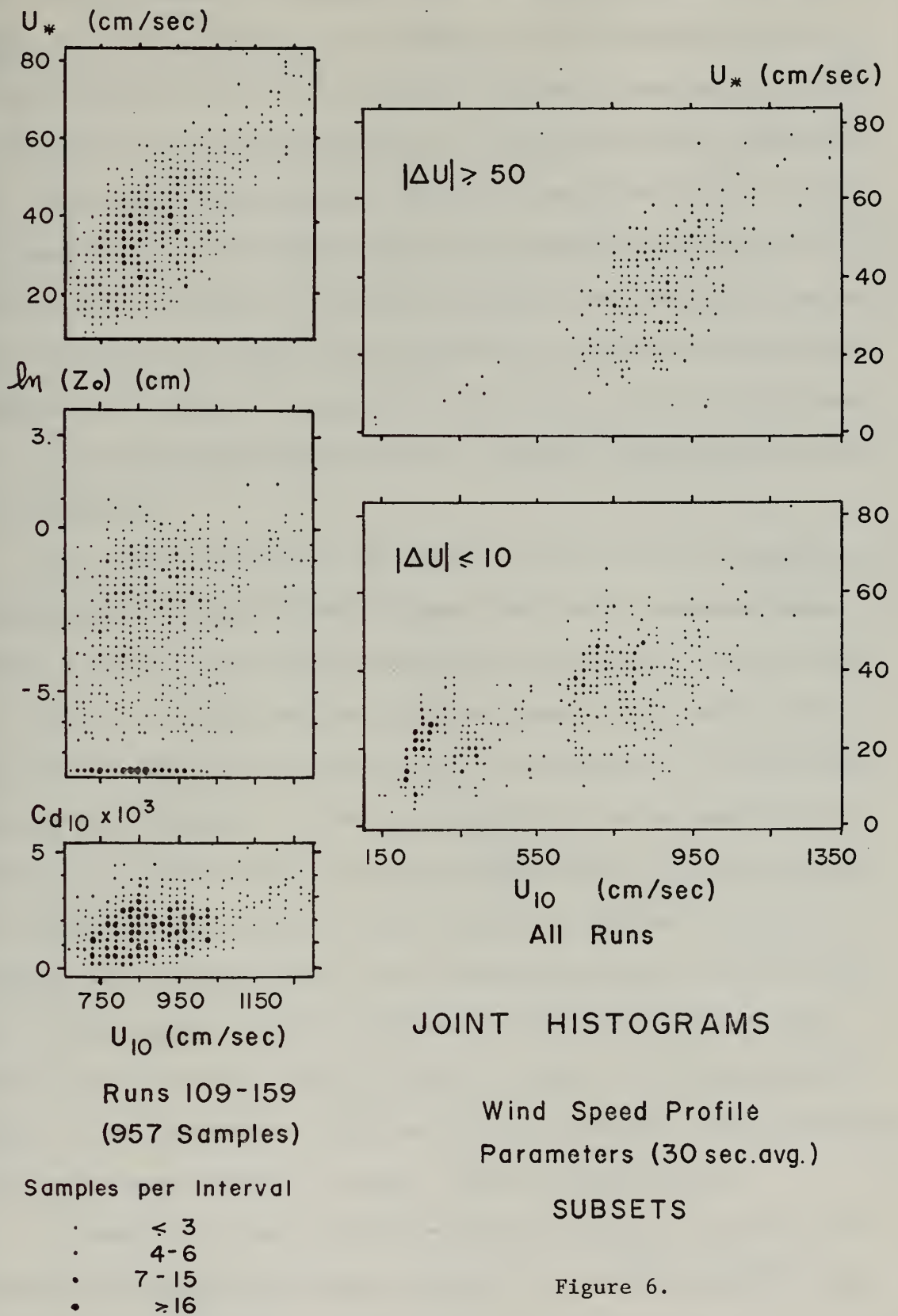
U* (cm/sec)
80
60
40
20
ln (Z0) (cm)
3.
0
-5.
Cd10 x10^3
5
0
750 950 1150
U10 (cm/sec)
Runs 109-159
(957 Samples)
Samples per Interval
· ≤ 3
· 4-6
• 7-15
• ≥16
U* (cm/sec)
|ΔU| ≥ 50
|ΔU| ≤ 10
80
60
40
20
0
150 550 950 1350
U10 (cm/sec)
All Runs
JOINT HISTOGRAMS
Wind Speed Profile
Parameters (30 sec.avg.)
SUBSETS

Figure 6.

field, occupy concentrated segments of the overall diagrams. Significantly, most of the anomalies are missing, and as previously noted Cd_{10} for these runs was 0.9×10^{-3} lower than the overall average; the value for these runs is in rough agreement with that found by most investigators. This set of runs apparently satisfies the criteria for a single or homogeneous wave generation regime (the bimodalities of the other relationships also disappear or decrease when these runs are plotted separately). The division by mean velocity derivative magnitude shows that the parameter relationships do vary with time history, and that (as in the cat's paw study) higher wind speeds are in general associated with stronger fluctuations.

Fig. 7 shows examples of the results of the JH of the parameters of the logarithmic underwater profile (runs 109 - 159). 30-second mean current speed (at 10m) was approximately 10 cm/sec, with a range of -3 to 27 cm/sec. The diagrams show quite consistent relationships among the profile values, with no indication of the anomalies or bimodalities found in the atmosphere. U_* values are negative, as the wind drift is strongest near the surface. Joint histograms between air and water profile parameters from this set of runs failed to show any overall statistical relationships; this is not surprising in view of the fact that most of the momentum from the wind goes directly into the wave field (Stewart, 1967; Dobson, 1971), so that the effect on the surface drift current is not immediate or else (see section B.2, Figs. 28 and 29) causes the short average profiles to become highly nonlogarithmic.

In summary, the mean velocity profiles in both air and water are predominantly logarithmic during conditions of neutral stability. Anomalies in the atmospheric profile parameters demonstrate the importance of

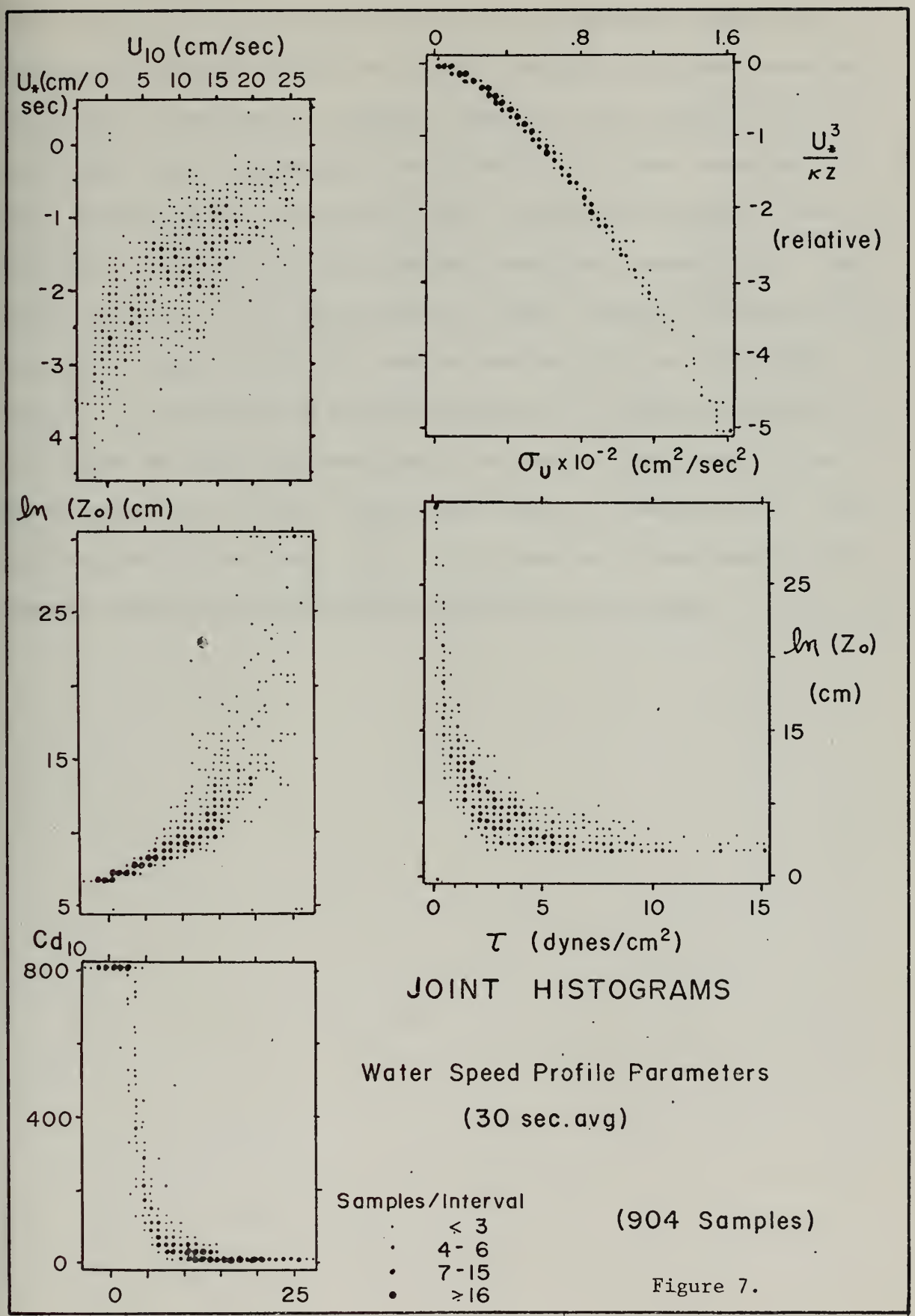
U_{10} (cm/sec)
U_*(cm/sec)
0 5 10 15 20 25
0
-1
-2
-3
4
0 .8 1.6
0
-1
-2
-3
-4
-5
$\frac{U_*^3}{\kappa z}$
(relative)
$\sigma_U \times 10^{-2}$ (cm^2/sec^2)
ln (Z_o) (cm)
25
15
5
25
ln (Z_o)
(cm)
15
0
0 5 10 15
τ (dynes/cm^2)
Cd_{10}
800
400
0
0 25
JOINT HISTOGRAMS
Water Speed Profile Parameters
(30 sec. avg)
Samples/Interval
· ≤ 3
· 4- 6
• 7-15
• ≥16
(904 Samples)

Figure 7.

time history and the existence of more than one wind-wave generation regime, with enhanced activity at certain critical wind speeds under as yet unknown circumstances. Anomalies stand out most strongly and the air boundary layer becomes much less logarithmic at short averaging times, indicating the importance of short, intermittent events in the development of unstable shear layers and associated instabilities. The profile can not be well represented by a single similarity parameter, and there is no simple relationship between wind velocity and the profile measures. Attempted use of such relationships for characterizing the wind regime and predicting wave growth can lead to significant errors. Consideration must be given to the time history of generation and to the importance of intermittency, i.e., to the enhanced air-sea coupling and momentum transfer at certain wind speeds or in short events.

B. Time History

The 51, 10 minute/hour runs (consecutive except for 1 hour gaps between runs 20 and 21 and 42 and 43) selected for detailed analysis were taken from 21 to 23 October, 1970. The wind direction had switched from N to S 30 hours prior to the first run, as a large high pressure system (> 1040mb at the center) passed the site moving NE. Winds increased and weather deteriorated throughout the three day period, then winds slacked and weather cleared on October 24. Analysis of current records and of the tide record at Wood's Hole, Massachusetts, showed that the surface drift continued NE, into Vineyard Sound, after the NE flood tide on the morning of October 21. The buoy thus faced into the wind and waves throughout this set of runs. This was confirmed by visual observation.

B.1. 5 and 10 Minute Averages

Figs. 8 and 9 depict the time changes of the 10 minute average horizontal wind speed at 10m (computed) and 2.4m (measured) and the wind extrema at 2.4m. The figures also show current speed at Z = -1.52m, and stress ($\tau = \rho U_*^2$) computed from air and water profiles. Short lines connect the averages of 2, 5 minute periods from each run and give an indication of the variability on shorter averaging times (the large offsets in Runs 111 and 142 are due to noise; those in 120 and 157 are real; 2.4m velocity extrema from runs 129-133 were unavailable).

There are strong periodicities in all of the variables. Mean wind shows an overall increase from 8-12m/sec; winds increased slowly through run 132, then increased rapidly to 10m/sec, stayed near that level for 10 hours, decreased and remained moderate for a similar period, and then again increased rapidly starting around run 152. Superimposed upon this long modulation is a shorter but strong periodicity of roughly 2-4 hours.

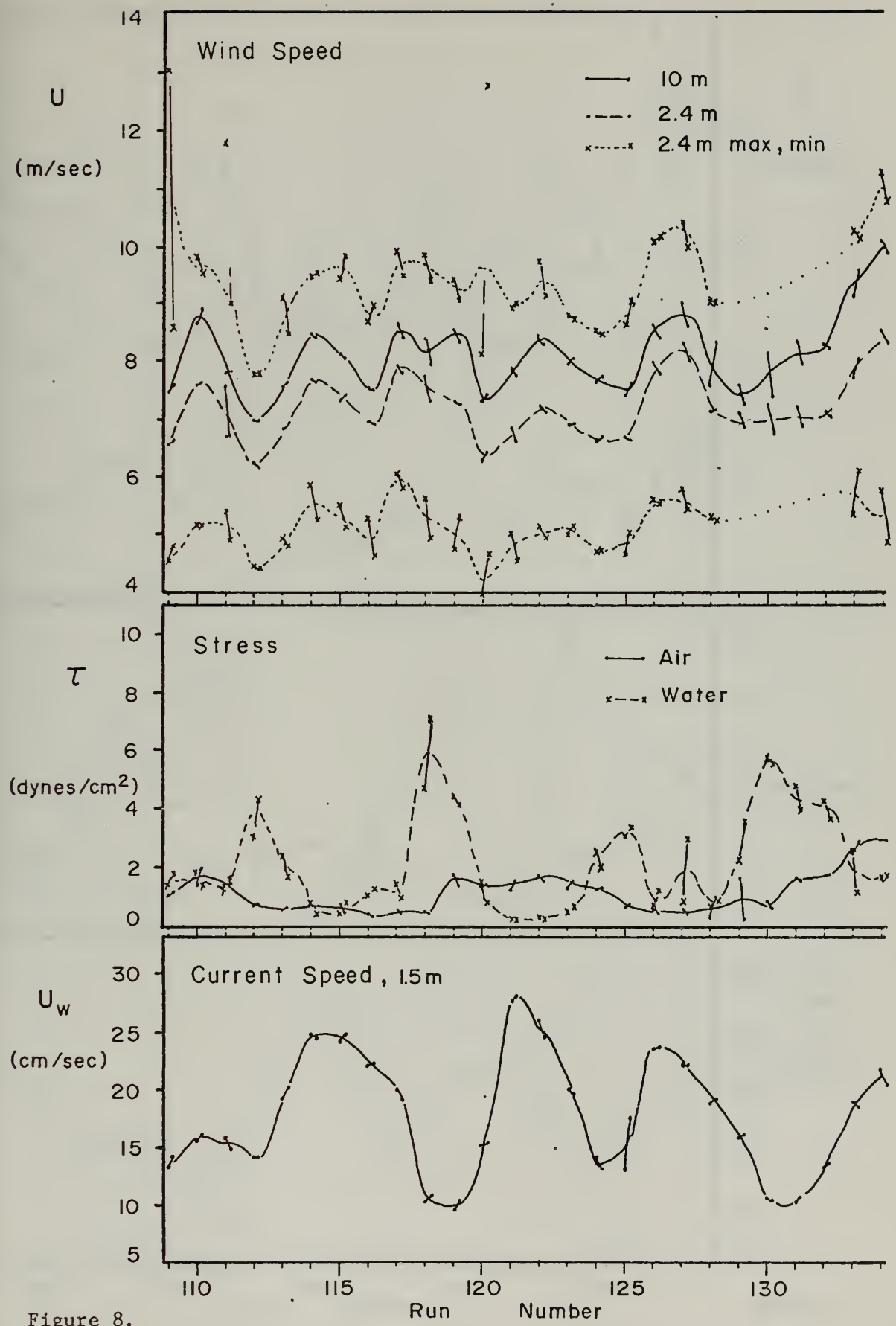
Wind Speed
10 m
2.4 m
2.4 m max, min
U
(m/sec)
14
12
10
8
6
4
Stress
Air
Water
τ
(dynes/cm²)
10
8
6
4
2
0
Current Speed, 1.5m
U_w
(cm/sec)
30
25
20
15
10
5
110
115
120
125
130
Run Number

Figure 8.

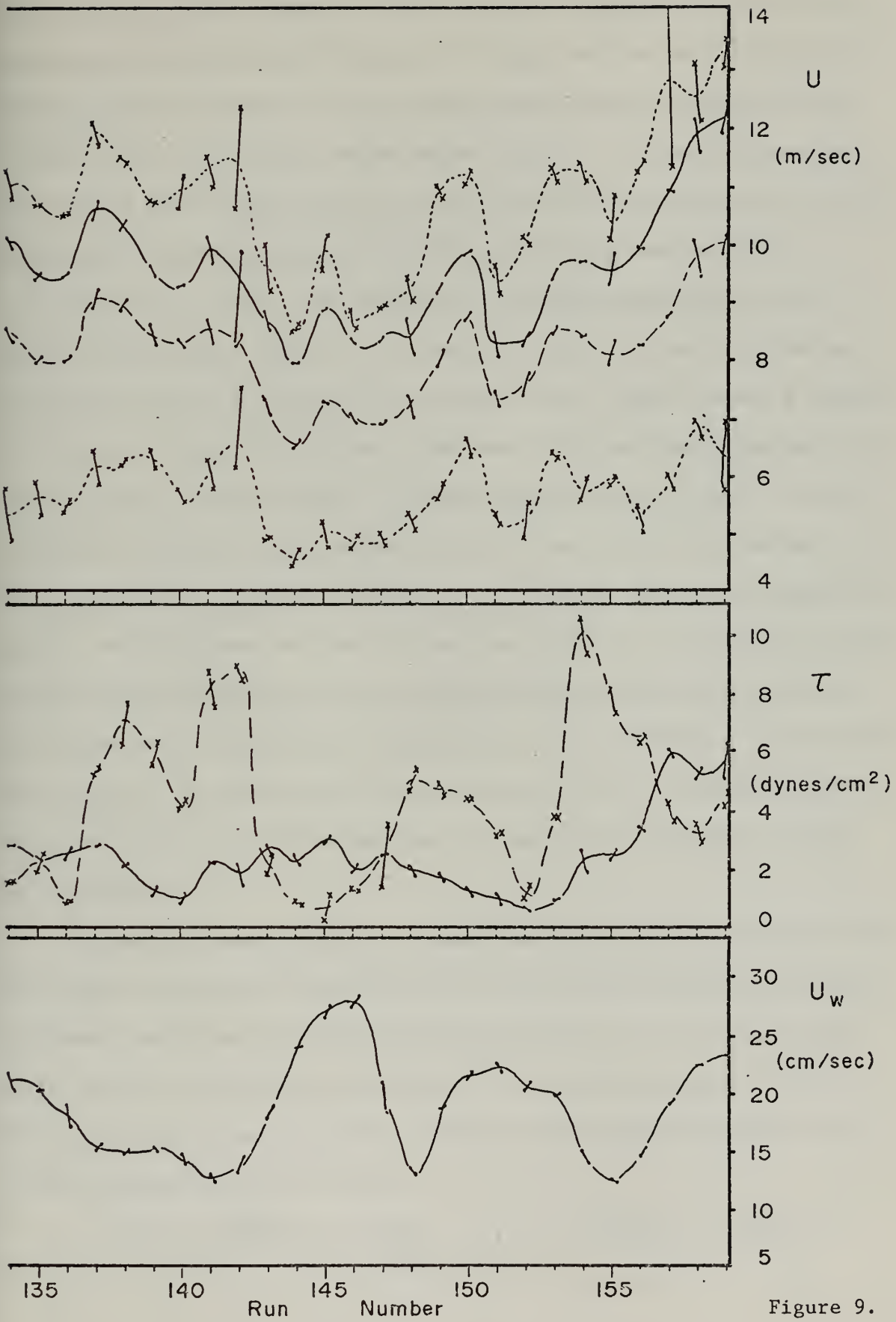
14
12
10
8
6
4
U
(m/sec)
10
8
6
4
2
0
τ
(dynes/cm²)
30
25
20
15
10
5
U_w
(cm/sec)
135
140
145
150
155
Run Number

Figure 9.

Velocity shear and extrema also show an overall increase with time, with superimposed shorter periodicities. The water current has a strong semi-diurnal tidal component with alternating times between maximum flood of 5 and 7 hours; the current maxima around run 139 is strongly suppressed. Some of the wind fluctuations occur with the tidal frequency and its 2nd harmonic; local wind maxima frequently occur during maximum flood.

The effect of the tidal modulation is vividly displayed in the water boundary layer profile as an excess during ebb, when the wind and tidal components are opposing and relative wind to water speeds a maximum. The short 2-4 hour fluctuations of the wave field are also apparent in the water stress. Air stress has a diurnal periodicity and a small 2-4 hour component as well as local maxima during the two major wind increases; it also temporarily increases in runs 141 - 146 when the winds decrease rapidly. Mean stresses are thus largest when there is a significant disturbance of the equilibrium balance between current, wind and wave fields. The stress values from air and water are in rough agreement. Differences may be partly accounted for by the momentum carried by propagating swell and wind waves, and by the momentum and equilibrium inbalances caused by the tides.

Mollo-Christensen (personal communication) has noted that except for the tidal variations, 10 minute mean air and water velocities are comparable when normalized by their dynamic viscosities, i.e., $\mu_a U_a \doteq \mu_w U_w$. This is shown in Fig. 10 (from Mollo-Christensen and Groscup [1971]). This relationship can be accounted for by assuming that the main shear is in the viscous sublayer, so that

$$\tau_{air} = \mu_a \left(\frac{\partial U_a}{\partial z} \right)_{z=0} \doteq \mu_a \frac{U_a}{\delta_a} \quad , \quad \tau_w = \mu_w \left(\frac{\partial U_w}{\partial z} \right)_{z=0} \doteq \mu_w \frac{U_w}{\delta_w} .$$

If $\delta_w \doteq \delta_a$, e.g., if the sublayer thickness in both media is controlled by the same elements (say the wavelets), then since the stresses are in rough balance the boundary layers are shear coupled and related by the ratio of their dynamic viscosities, $U_a = \frac{\mu_w}{\mu_a} U_w$. The long term average values thus again support the assumption that the major air sea coupling can be simply described, in spite of the known intermittent discontinuities. Fig. 10 also shows the weak relationship between the shorter

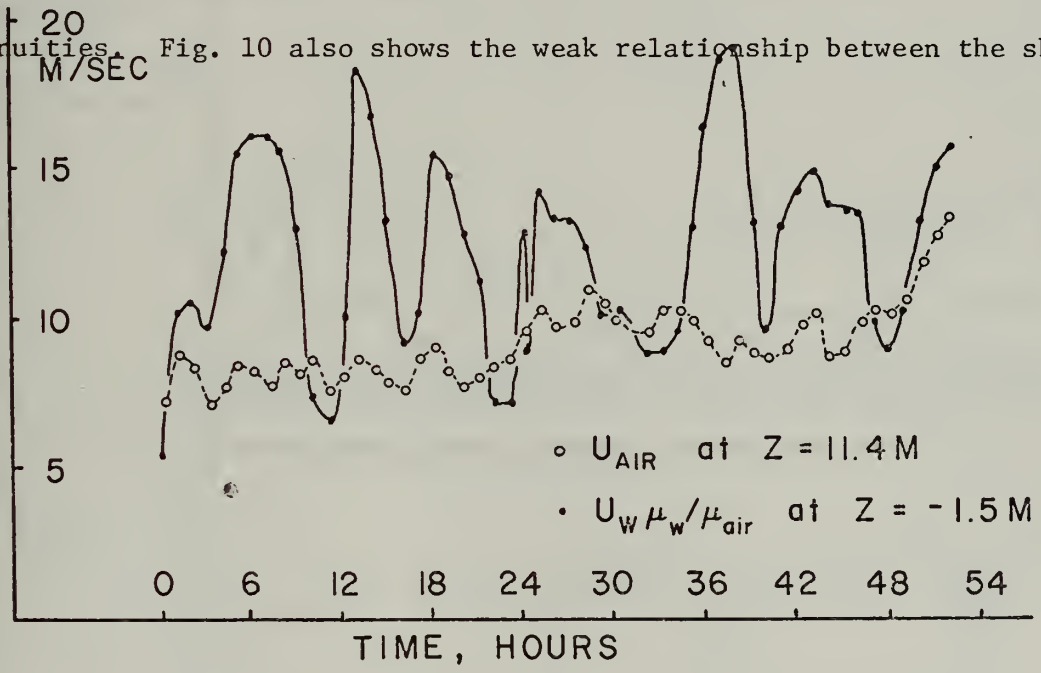

Figure 10

term variations of air and water stress.

Fig. 11, Fig. 12 and Fig. 13 show the variability with time of the wave field parameters. Fig. 14 shows the corresponding wave spectra, and Fig. 15 the development of selected frequency components (cross sections of Fig. 14). 80% and 90% confidence limits at $\Phi = 10^3$ are shown by ticks inside the Φ axis of Fig. 15. E is mean energy density, $E = \rho g \overline{\eta^2}$ and momentum density M = E/c (c = wave celerity) computed by spectral summation. C (Φ_{max}) and M (Φ_{max}) are respectively the celerity of the wave of maximum spectral density and the momentum computed by assuming that the energy density is concentrated at that one frequency. The

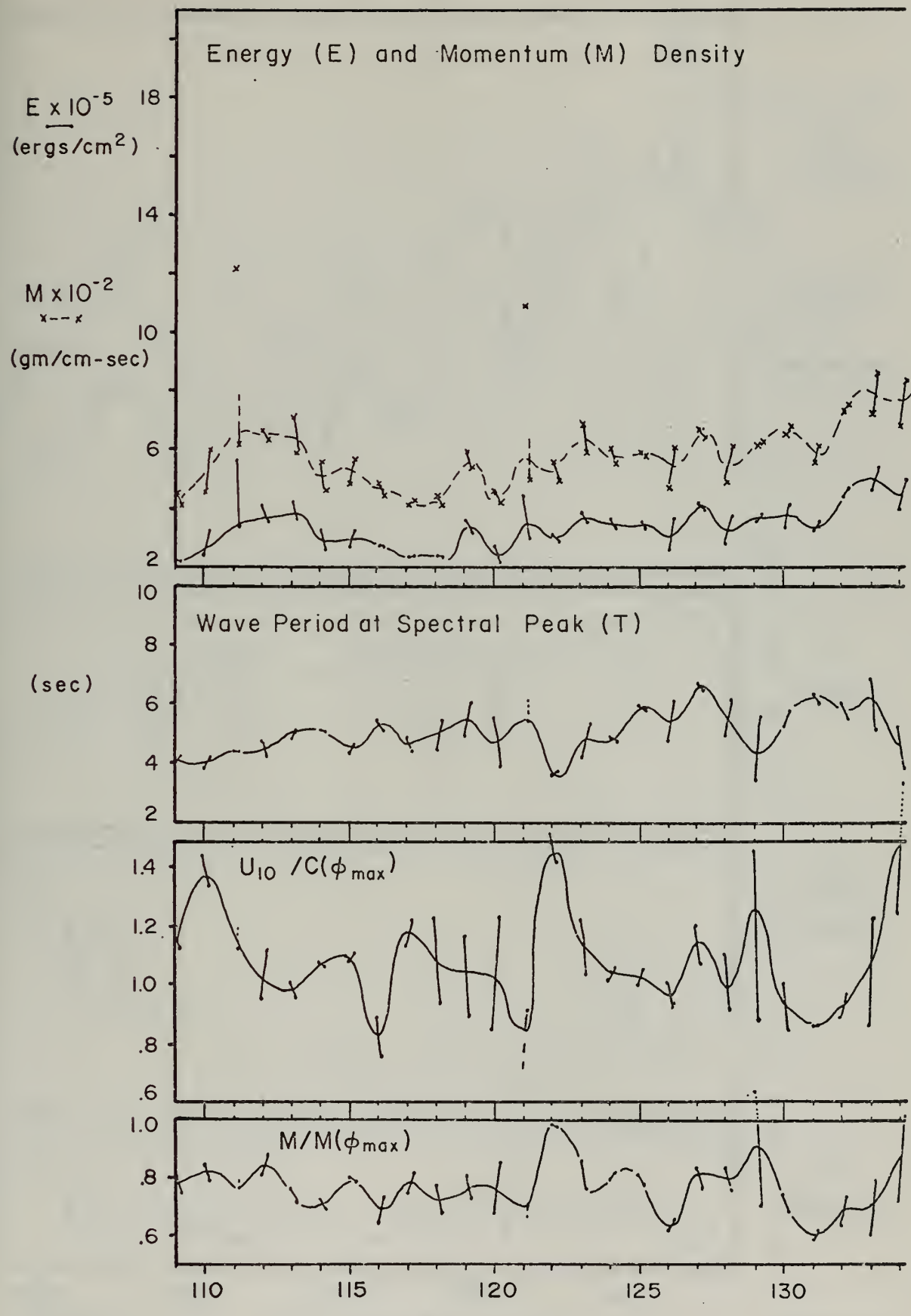
Energy (E) and Momentum (M) Density
E x 10^-5
(ergs/cm^2)
18
14
M x 10^-2
10
(gm/cm-sec)
6
2
10
8
Wave Period at Spectral Peak (T)
(sec)
6
4
2
1.4
U10 /C(φmax)
1.2
1.0
.8
.6
1.0
M/M(φmax)
.8
.6
110
115
120
125
130
Run Number

Figure 11.

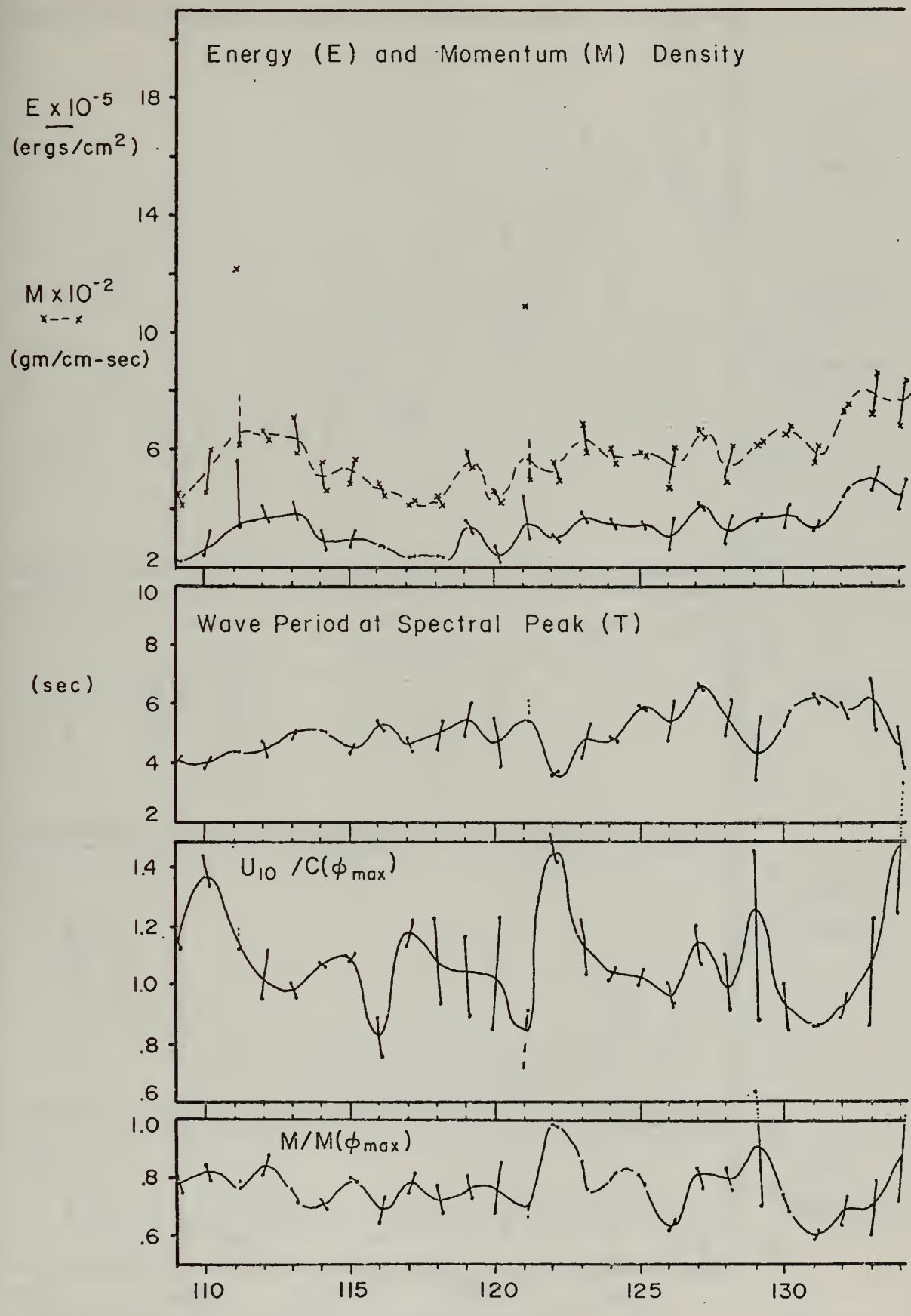
Energy (E) and Momentum (M) Density
E x 10^-5
(ergs/cm^2)
18
14
M x 10^-2
x--x
10
(gm/cm-sec)
6
2
10
8
Wave Period at Spectral Peak (T)
(sec)
6
4
2
1.4
U10 /C(φmax)
1.2
1.0
.8
.6
1.0
M/M(φmax)
.8
.6
110
115
120
125
130
Run Number

Figure 11.

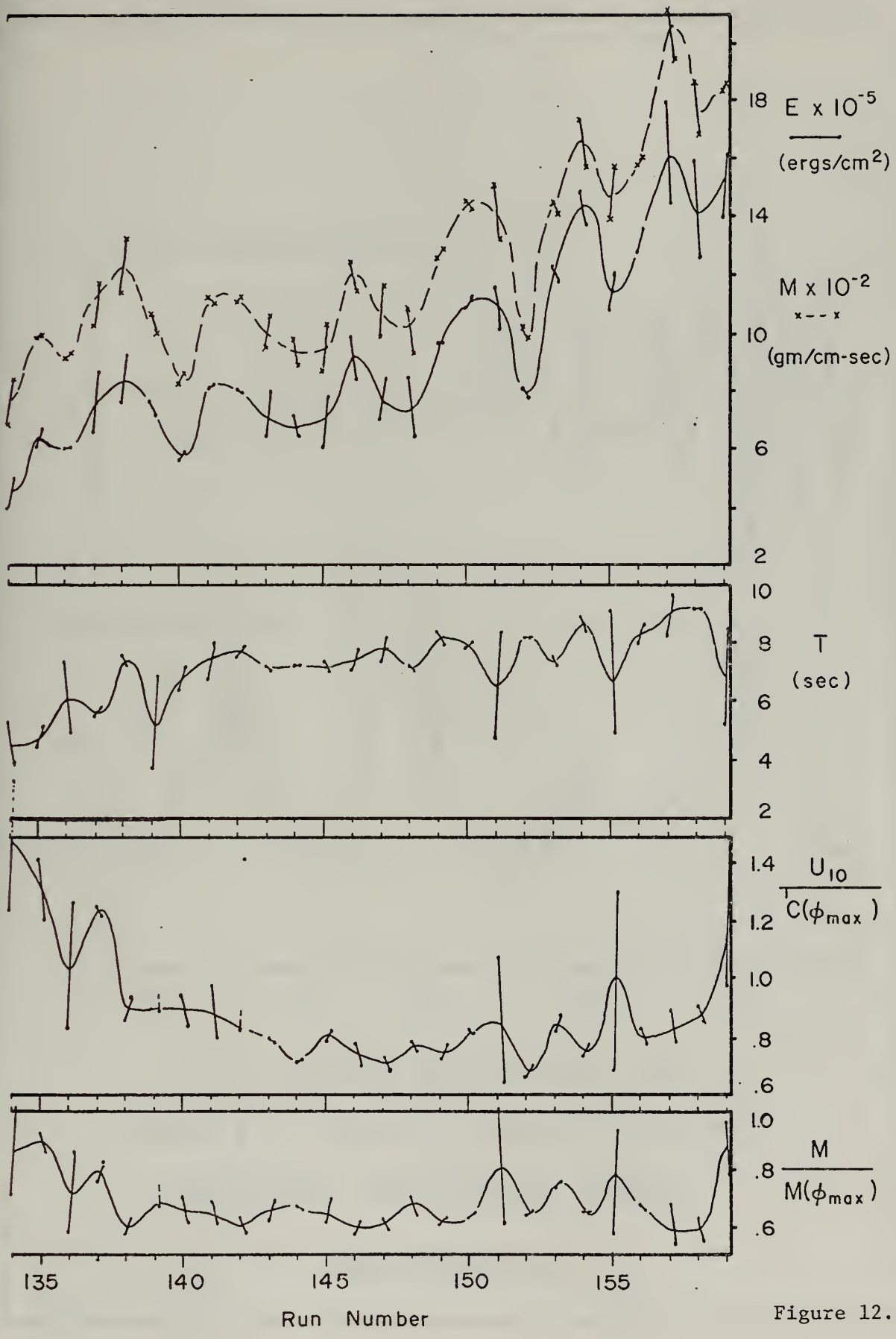
18
14
10
6
2
E x 10^-5
(ergs/cm^2)
M x 10^-2
(gm/cm-sec)
10
8
6
4
2
T
(sec)
1.4
1.2
1.0
.8
.6
U10 / C(φmax)
1.0
.8
.6
M / M(φmax)
135
140
145
150
155
Run Number

Figure 12.

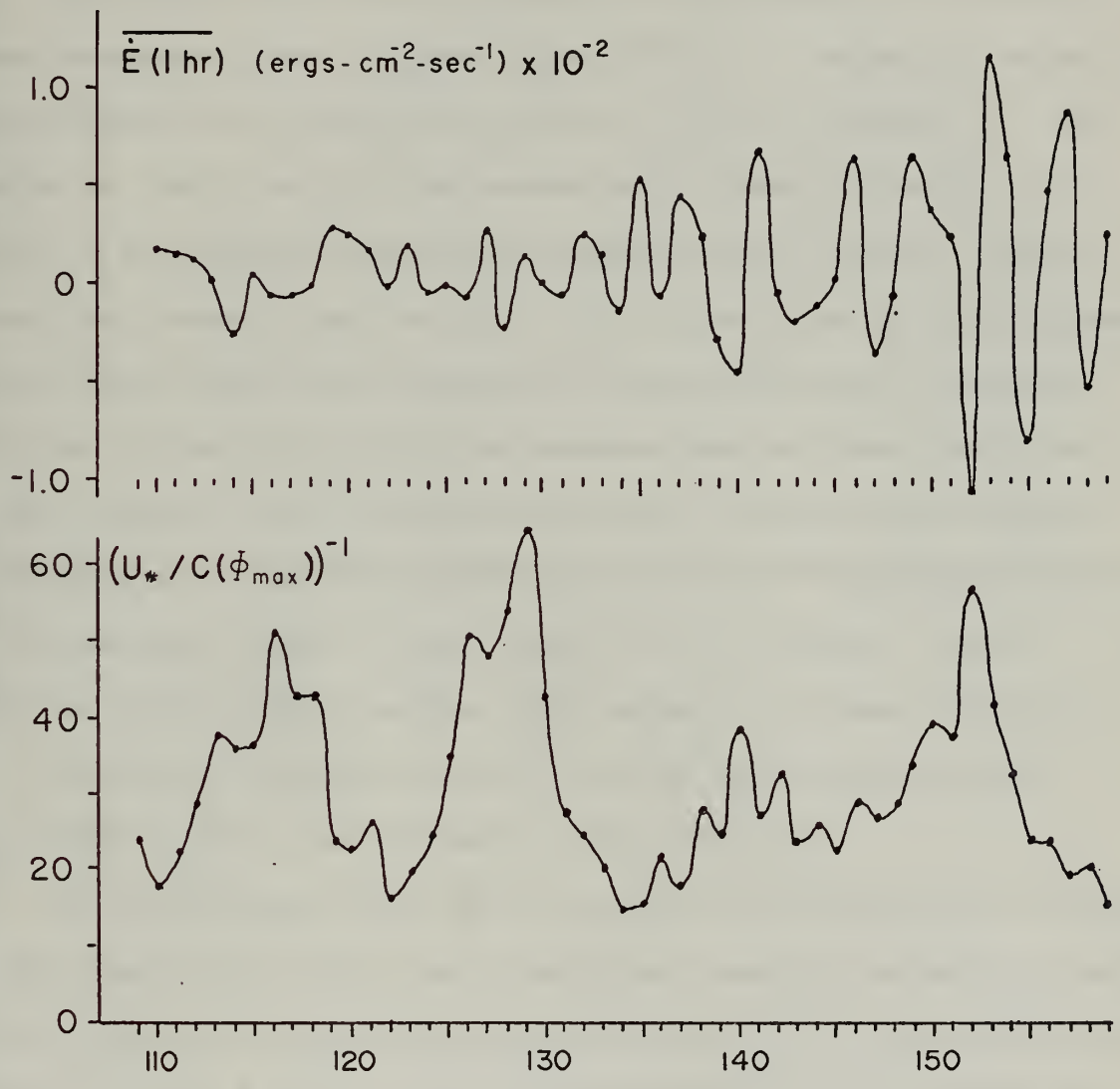

Energy Density Growth Rate, and

Celerity of wave of Spectral Maximum

Normalized with Friction Velocity

Runs 109 - 159

Figure 13.

information in these figures may be summarized as follows.

During the two-day period the mean energy density of the wave field increased by nearly an order of magnitude, from 2×10^5 to 17×10^5 ergs/cm^2. The period of the wave of maximum spectral density (T) shifted to lower frequencies, from 4 seconds at run 109 to > 8 seconds at the end. These changes can be clearly seen in Fig. 11, Fig. 12 and Fig. 14. The changes in T and E are slow and comparatively steady for the first 23 hours. E then increased rapidly in conjunction with the rapid wind increase that started around run 132. Fig. 14 shows that the spectral peak turned sharply toward lower frequencies during this velocity increase; after run 132 the separation of the spectrum into two peaks (swell and locally generated waves) becomes more distinct and the peaks continue to separate as the swell peak shifts to still lower frequencies. The equilibrium range above the local peaks has a very rough f^{-5} slope (Phillips [1958]) with occasional local maxima in the range of 0.5 to 1 hz. The distinct separation between local and swell peaks was wiped out during the rapid wind increase of runs 148 and 149.

All of the figures show that the growth of the wave field, in terms of both mean energy density and of individual spectral components, is not steady. There are large, significant variations of E, T, normalized parameters, and of $\overline{\Phi_{\eta\eta}}(f)$, the spectral density at selected frequencies (Fig. 15). $\dot{E}$ (1 Hour) (Fig. 13) becomes as large as $\pm$ .1% of the hourly average E during later runs. The hourly changes, both growth and decay, are largest when the wave field is most energetic and during major wind speed changes.

Fig. 15 demonstrates that even the higher frequency components (.6310 and .3550 hz), which are always above the spectral peak and in the 'equili-

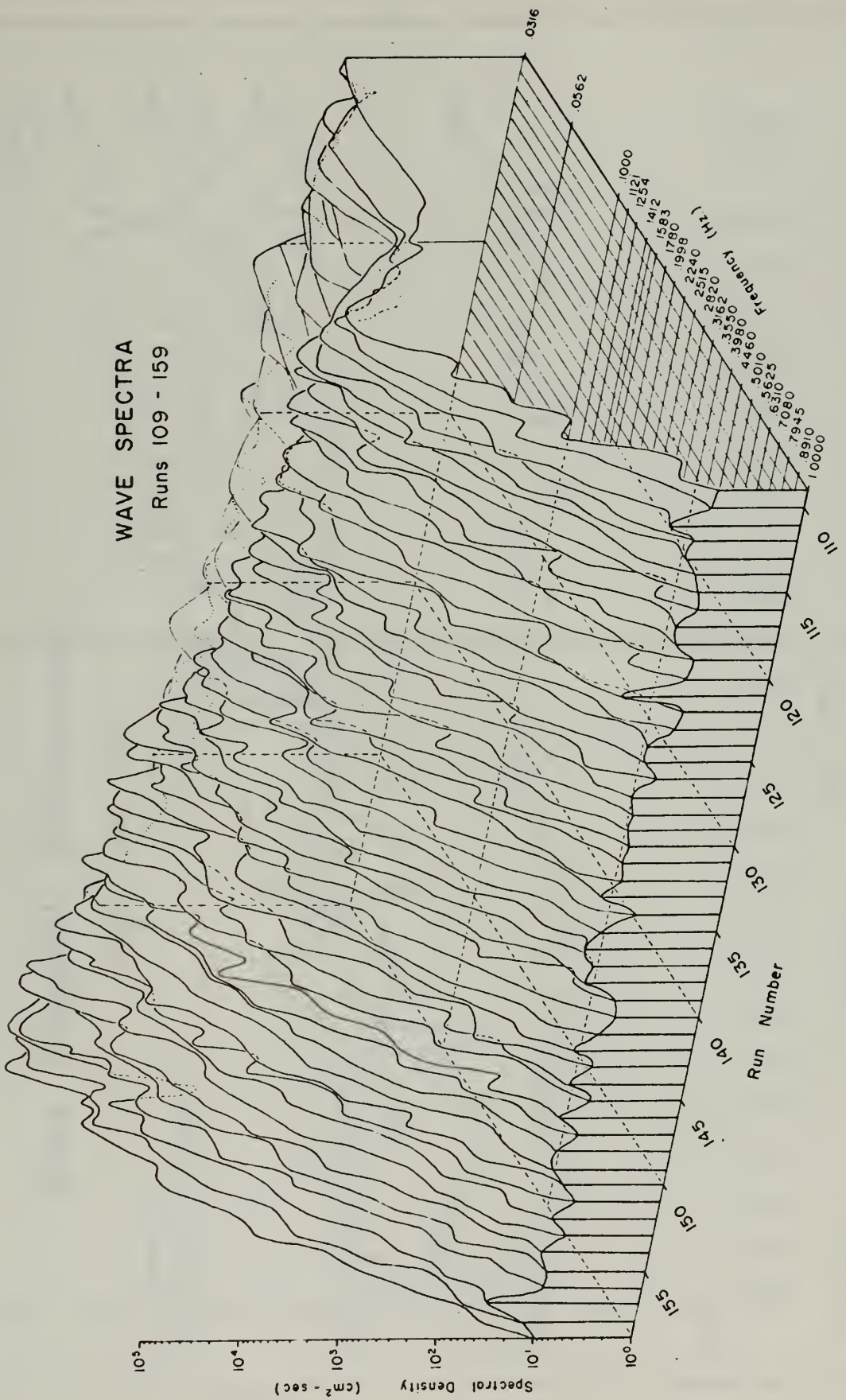
WAVE SPECTRA
Runs 109 - 159
Spectral Density (cm² - sec)
Frequency (Hz)
Run Number

Figure 14.

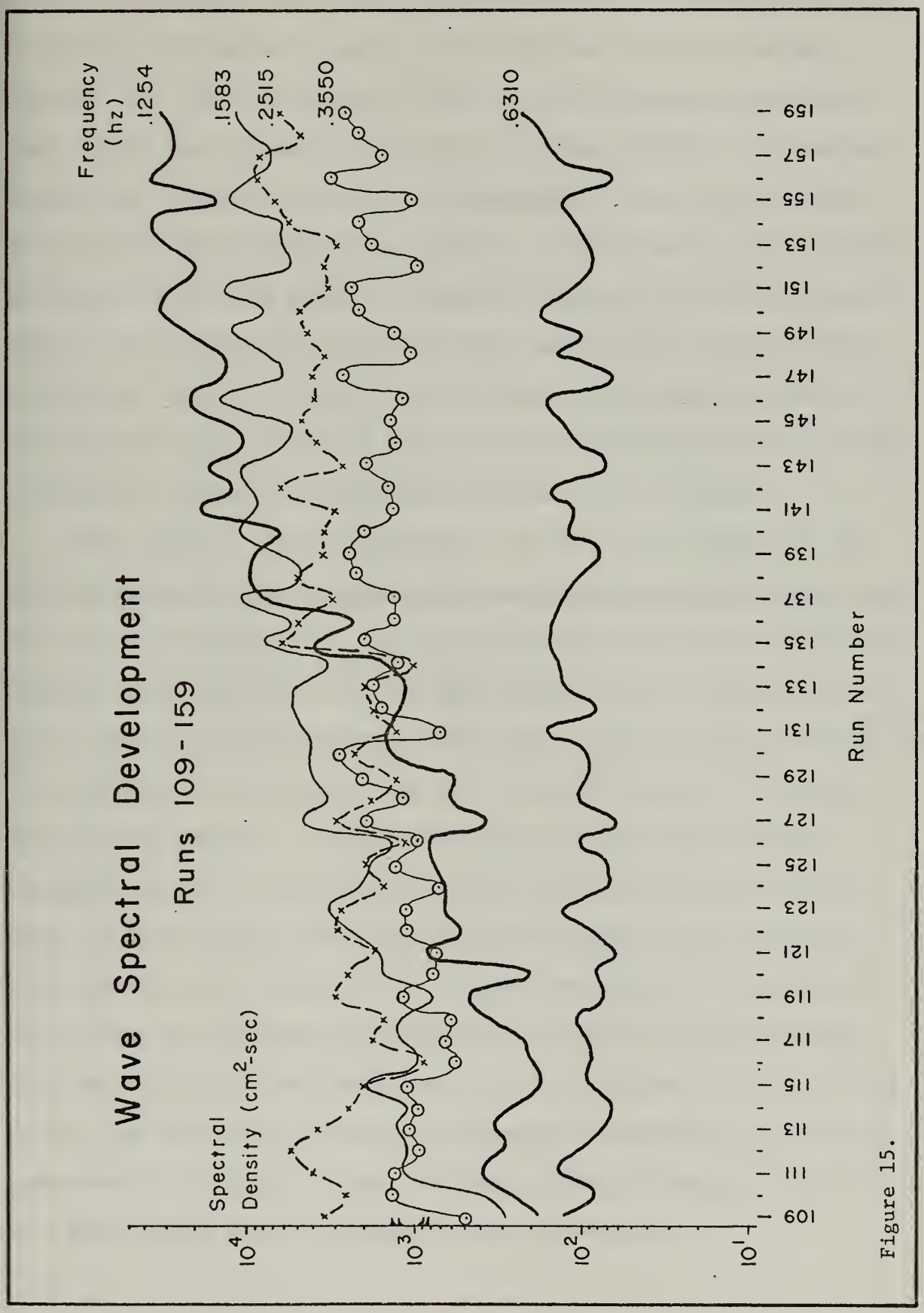
Wave Spectral Development
Runs 109-159
Frequency (hz)
.1254
.1583
.2515
.3550
.6310
Spectral Density (cm²-sec)
10⁴
10³
10²
10¹
109
111
113
115
117
119
121
123
125
127
129
131
133
135
137
139
141
143
145
147
149
151
153
155
157
159
Run Number

Figure 15.

brium' or saturation range, have significant (at the 90% confidence level) increases and decreases of energy content on these one hour averaging periods. The .2515 hz component, which was at the spectral peak at the start of the runs, appears to 'overshoot' in runs 110-112. Its spectral density then falls off to a lower, 'equilibrium' value during the slow growth period that extends through run 132. After that run, the 4 second waves again show major growth, 'overshoot' slightly at the same spectral density they had earlier reached, and then settle into a second, higher 'equilibrium' level. In runs 154 - 156 their energy content increases to still higher levels. The wave field can apparently support more than one overshoot and saturation range under different wind conditions.

The .1583 and .1254 hz components both grow until around run 139, when the higher of the two frequencies reaches a quasi-steady state level. The most rapid growth of the low frequency waves occurs in the rapid wind increase starting at run 132. The major wind decrease of runs 142 - 143 is not accompanied by significant decay; the $\Phi_\eta(f)$ decrease, and $\overline{\dot{E}(1 \text{ hour})}$ for this period, are no larger than those found in the minor fluctuations during growth periods. The fluctuations of the individual frequency components is not in phase; some portions of the spectrum grow, others decay, in what appears to be a random fashion except during the major wind increase at run 132, which is followed around run 135 by growth of all but the highest frequency components. The locally generated waves, .2515 and .3550 hz, show similar periodicities to those of the local wind field. The individual swell and high frequency components are essential- independent of these short term variations, while the total wave field - E, T and M - does show the effect of local generation.

A comparison of the plot of $U_{10}/C\ (\Phi_{max})$ with those of E and M shows that spectral development is most rapid when the wind is moving faster than the waves of the spectral peak. Some growth still occurs even when the waves move faster than the wind (where Miles theory is clearly inapplicable due to the absence of a 'critical layer'). The general range of $U_{10}/C\ (\Phi_{max})$ is quite low for the entire set of runs. These features indicate that swell was propagating into the area, but do not account for the lack of local decay of low frequency components between runs 137 and 158 when $U_{10}/C\ (\Phi_{max})$ was continuously less than 1. It may be hypothesized that energy was being transferred to the low frequency waves by nonlinear resonant interactions within the wave field, (e.g., Garrett [1970]) or that wind generation occurs at these frequencies during brief but intense periods when U was larger than C (Φ_{max}).

The plot of $C\ (\Phi_{max})/U_*$ shows a strong diurnal periodicity, and lags the similar variation in τ_{air} by roughly $\pi/2$. There is no apparent relationship between this parameter and $U_{10}/C\ (\Phi_{max})$, or between it and energy density growth rates.

The normalized wave momentum plot indicates that only 60-80% of the total wave momentum is carried by waves at the spectral peak; most of the remainder is carried by waves at higher frequencies (lower phase speeds). Fig. 16 shows the momentum spectrum (5 minute averages, 6 dof) from several runs (ordinates have been normalized to the spectral maximum). These plots show the overall increase in M and M_{max}, the shift of M_{max} to lower frequencies, the bi- and trimodality associated with the separation of swell and local wind wave peaks, and the occasional very strong concentration of momentum in a single swell frequency. The momentum spectra have roughly the same shape as the power spectra, but tend to emphasize the

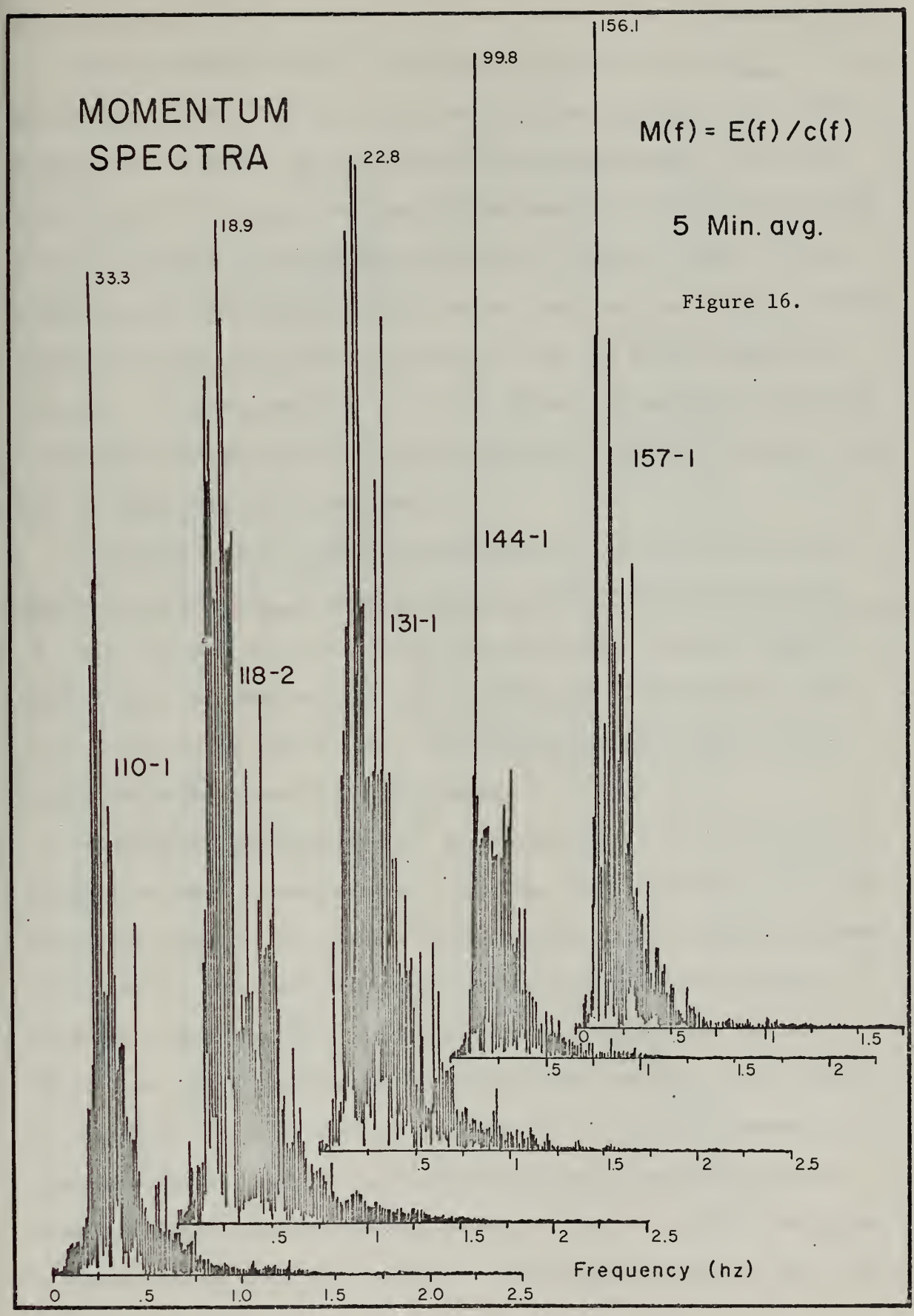
MOMENTUM
SPECTRA
M(f) = E(f) / c(f)
5 Min. avg.
156.1
99.8
22.8
18.9
33.3
157-1
144-1
131-1
118-2
110-1
0
.5
1.0
1.5
2.0
2.5
Frequency (hz)

Figure 16.

concentration of the wave momentum in one or more narrow frequency bands.

The 10% momentum levels -- the range of f for $M(f) \geq .1M_{max}$ -- were approximately .15 to .55 hz through run 131, and then decreased slowly to roughly .09 - .40 hz. Wave momentum was indistinguishable from noise level above 1.40 hz near the start of the runs, and this limit decreased, starting at run 132, to approximately 1.00 - 1.20 hz. Most of the momentum spectra had several discrete peaks, and there was usually a considerable difference in the minor features of the 2,5 minute segments in each run. Current spectra at -1.5m (not shown) had maxima at both swell and locally generated wave frequencies, and were generally coherent with both of these wave field components.

Coherence between horizontal wind speed at 2.4m and waves at the spectral peak ($\gamma_{u\eta}(f_{\Phi_{max}})$) measured on the 5 minute subintervals) was $\geq$ 0.65 for 50%, and $\geq$ 0.50 for 97% of the 102, 5 minute samples. Phase ($\Theta_{u\eta}$) at that peak was $\pm\pi$ for 82% of the coherent runs, and $> \pm$ 2 radians for all of them. As noted by Seesholtz (1968), wind speeds are maximum over the wave troughs.

Examples of $\gamma_{u\eta}$ and $\Theta_{u\eta}$ are displayed in Fig. 17. The shift of the peak to lower frequencies with time, and its bifurcation into local and swell segments, are clearly evident; there was a secondary maximum of $\gamma_{u\eta}$ at the local wave frequency (roughly .32 hz) for about 80% of the samples after run 131. In the majority of these cases (note run 137-2) there was a decrease in $\gamma_{u\eta}$ between the two peaks, with a shift in $\Theta_{u\eta}$ from π to $\pi/2$ and then back to π . Winds were generally incoherent with the waves ($\gamma_{u\eta}$ statistically indistinguishable from 0) above the local wave peak on this averaging time; one notable exception is segment 157-1; this run contained a very strong generation event and

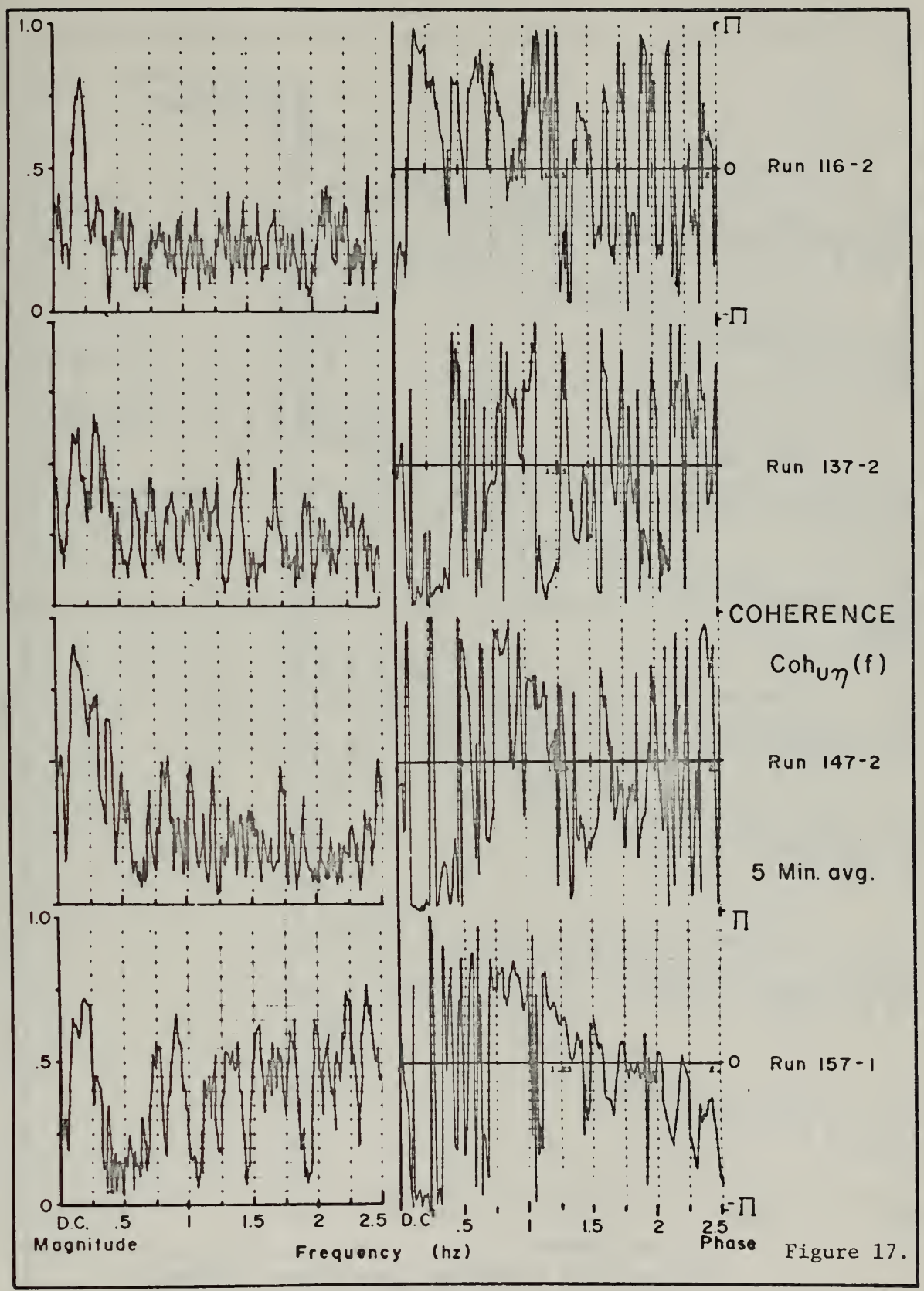
1.0
.5
0
Run 116-2
Run 137-2
COHERENCE
$Coh_{u\eta}(f)$
Run 147-2
5 Min. avg.
Run 157-1
D.C. .5 1 1.5 2 2.5
Magnitude
Frequency (hz)
Phase

Figure 17.

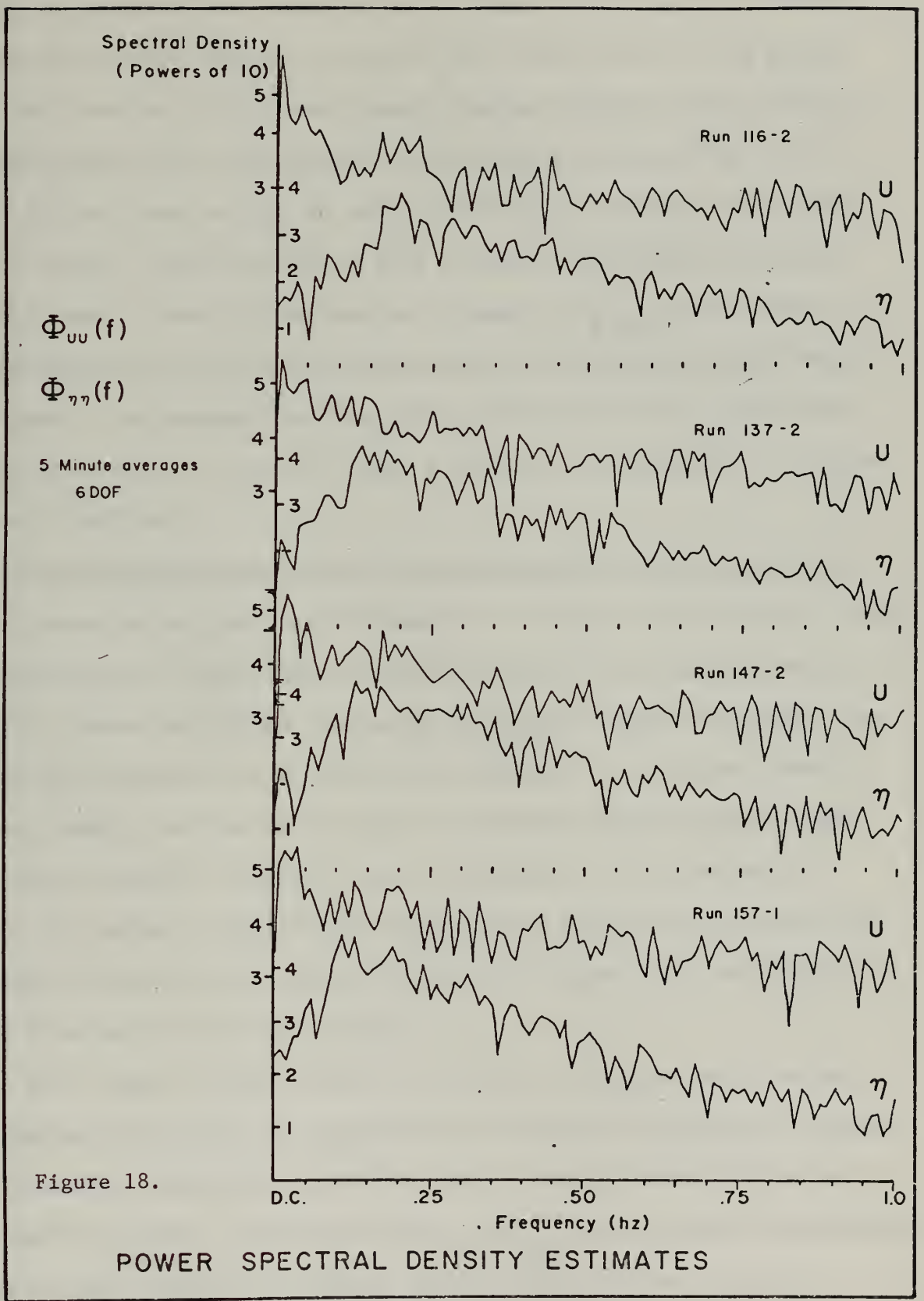
Spectral Density
(Powers of 10)
$\Phi_{uu}(f)$
$\Phi_{\eta\eta}(f)$
5 Minute averages
6 DOF
Run 116-2
Run 137-2
Run 147-2
Run 157-1
U
η
D.C.
.25
.50
.75
1.0
Frequency (hz)
POWER SPECTRAL DENSITY ESTIMATES

Figure 18.

is discussed in detail in section B.2. In roughly 30% of the runs, $\gamma_{u\eta}$ was fairly high at the D.C. level; in all of these cases, $\Theta_{u\eta} = 0$. With the exception of the occasional D.C. peak, $\gamma_{u\eta}$ was low for $f < f_{\Phi_{max}}$.

Wind spectra did not consistently display distinct peaks at the wave spectral maxima (Fig. 18, 80% and 90% confidence limits at $\Phi_{\eta\eta} = 10^4$ and $\Phi_{uu} = 10^5$ are shown on the Φ axis of run 142). They were fairly white (< 1 decade dropoff in the .2 to 2 hz band). Nevertheless there was nearly always a spectral increase at or around $f_{\Phi_{max}}$, and in cases of a double-peaked coherence the wind spectra showed a local minimum between the peaks. The examples show $\Phi_{\eta\eta}(f)$ and $\Phi_{uu}(f)$ for the same run segments as in Fig. 17 (they are rough, 6 dof, and the jaggedness is probably not significant).

From these facts and figures the following inferences may be drawn. Wave generation and spectral development is strongly non-stationary. There are significant, rapid changes in spectral growth and these changes are poorly represented by long term means; no single parameter or simple combination of parameters can describe the process. Air and water boundary layers (both velocities and stress) are viscously shear coupled. Modulations at the tidal frequency and its harmonics (or of the period ΔTide/ Δ t) appear in the wind and wave fields; changes in the tidal flow disrupt the equilibrium between wind and wave fields and cause modification of momentum advection patterns.

Even though the high frequency portions of the wave field are near saturation and account for insignificant portions of the spectral density and momentum, they show significant,rapid (hourly) variations and can account for spectral growth when the $U_{10}/C(\Phi_{max})$ relationship would normally predict major continuous damping. Measured growth rates (long term

averages) of these high frequency components are inherently incapable of displaying major changes, since on the mean these waves are near saturation, and also because the very high frequencies are continuously being generated by the larger waves (Longuet-Higgins,[1963];Crapper [1970]). The importance of these high frequency waves lies in their ability to couple the wind with larger waves and to assist the growth of low frequency instabilities by nonlinear coupling between scales. It will be shown in the next section that these components have extremely rapid growth rates in intermittent generation 'events', but again these important physical momentum transfer features are obscured by the averaging process.

The influence of waves on the turbulent atmospheric boundary layer is strong at both the swell and the locally generated spectral peaks. Furthermore, the 2-4 hour periodicity of wind and both the locally generated and overall wave fields are strongly related. Changes in measures of the wind and wave fields (e.g., $\overline{\dot{E}\ (1\ \text{hour})}$) are largest when the magnitude of the measures is largest, similar in nature to the pattern of higher frequency components during strong gusts that was noted in the cat's paw study.

The major conclusion from this section is that study of the time history of generation and spectral development is essential for an understanding of the physics involved. Wind, wave and current fields show evidence of strong interrelationships that are poorly represented by parameterization of the mean. The rapid variations in E, $\overline{\dot{E}\ (1\ \text{hour})}$, U_{10} and τ all indicate that generation is predominantly an intermittent process, characterized by rapid transfer of momentum and followed by weaker couplings and nonlinear interchange between spectral components.

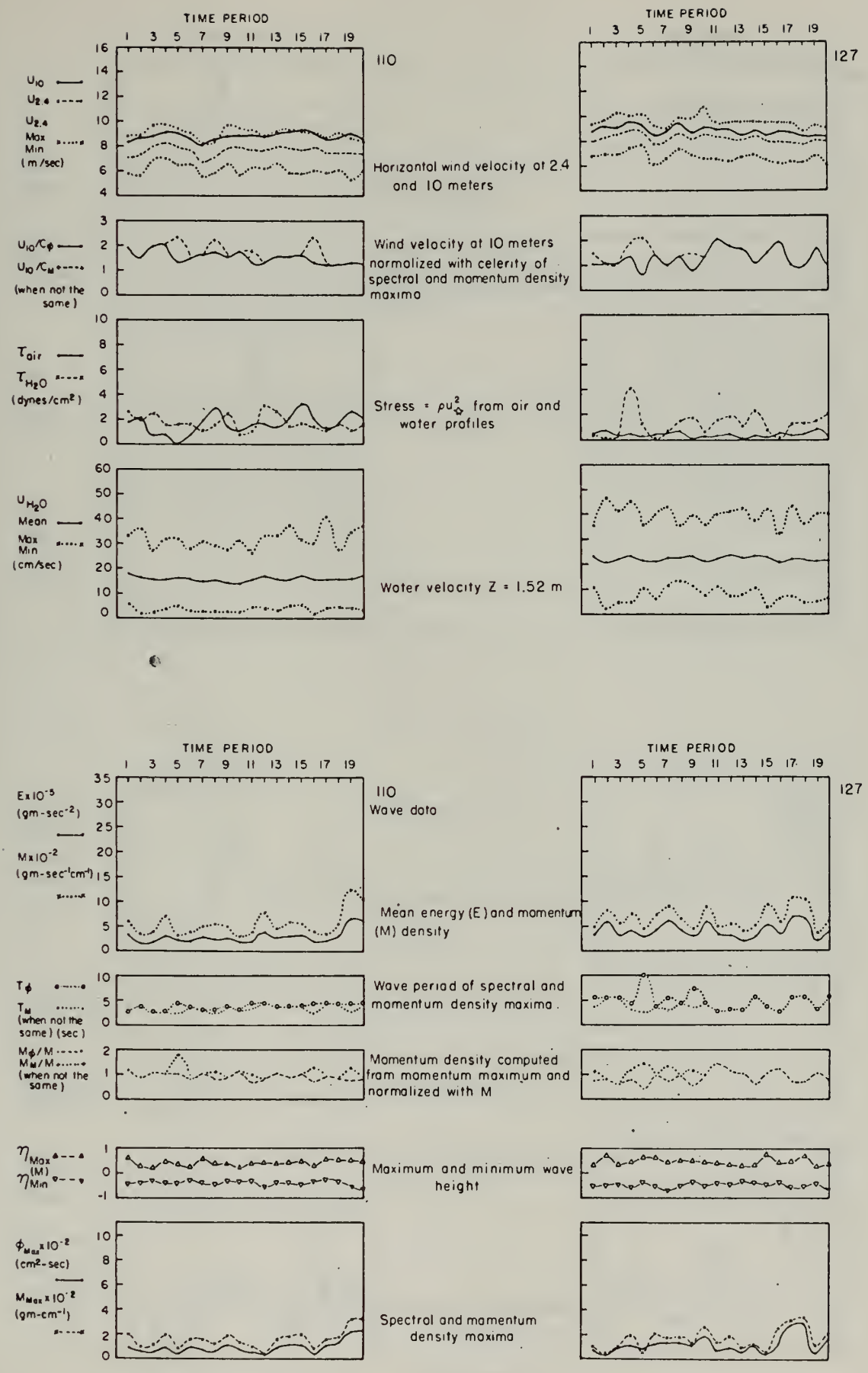
TIME PERIOD
1 3 5 7 9 11 13 15 17 19
110
127
U_{10}
$U_{2.4}$
$U_{2.4}$ Max Min (m/sec)
Horizontal wind velocity at 2.4 and 10 meters
U_{10}/C_ϕ
U_{10}/C_M (when not the same)
Wind velocity at 10 meters normalized with celerity of spectral and momentum density maxima
τ_{air}
τ_{H_2O} (dynes/cm²)
Stress = ρu_*^2 from air and water profiles
U_{H_2O} Mean Max Min (cm/sec)
Water velocity Z = 1.52 m
E x 10⁻⁵ (gm-sec⁻²)
M x 10⁻² (gm-sec⁻¹cm⁻¹)
110 Wave data
Mean energy (E) and momentum (M) density
T_ϕ
T_M (when not the same) (sec)
Wave period of spectral and momentum density maxima.
M_ϕ/M M_M/M (when not the same)
Momentum density computed from momentum maximum and normalized with M
η_{Max} (M) η_{Min}
Maximum and minimum wave height
ϕ_{Max} x 10⁻² (cm²-sec)
M_{Max} x 10⁻² (gm-cm⁻¹)
Spectral and momentum density maxima

Figure 19.

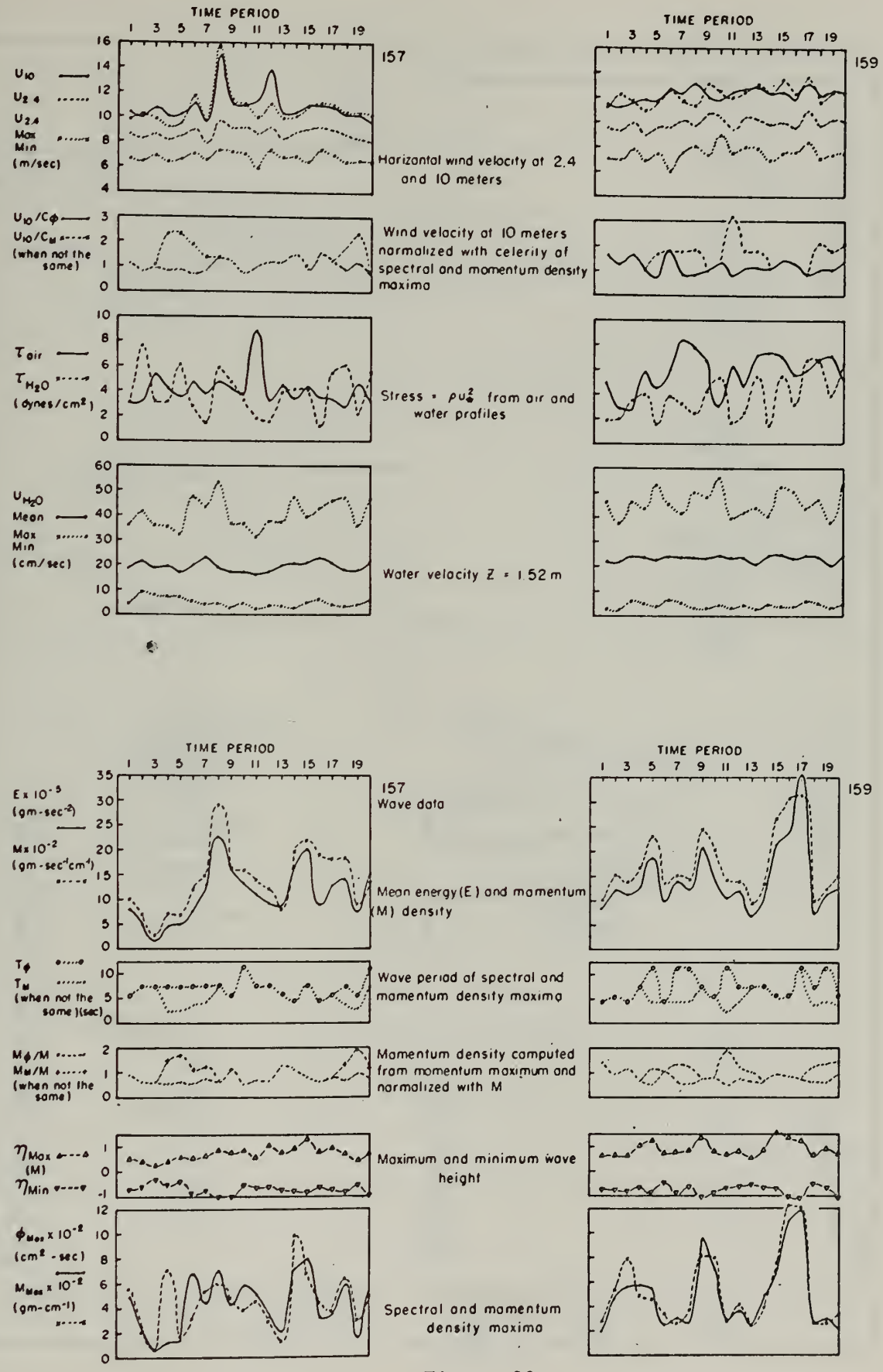
TIME PERIOD
1 3 5 7 9 11 13 15 17 19
157
159
U_{10}
$U_{2.4}$
$U_{2.4}$ Max Min
(m/sec)
Horizontal wind velocity at 2.4 and 10 meters
U_{10}/C_ϕ
U_{10}/C_M (when not the same)
Wind velocity at 10 meters normalized with celerity of spectral and momentum density maxima
τ_{air}
τ_{H_2O}
(dynes/cm²)
Stress = ρu_*^2 from air and water profiles
U_{H_2O} Mean
Max Min
(cm/sec)
Water velocity Z = 1.52 m
E x 10^{-5} (gm-sec^{-2})
M x 10^{-2} (gm-sec^{-1}cm^{-4})
157 Wave data
Mean energy (E) and momentum (M) density
T_ϕ
T_M
(when not the same) (sec)
Wave period of spectral and momentum density maxima
M_ϕ/M
M_M/M
(when not the same)
Momentum density computed from momentum maximum and normalized with M
η_{Max} (M)
η_{Min}
Maximum and minimum wave height
ϕ_{Max} x 10^{-2} (cm² - sec)
M_{Max} x 10^{-2} (gm-cm^{-1})
Spectral and momentum density maxima

Figure 20.

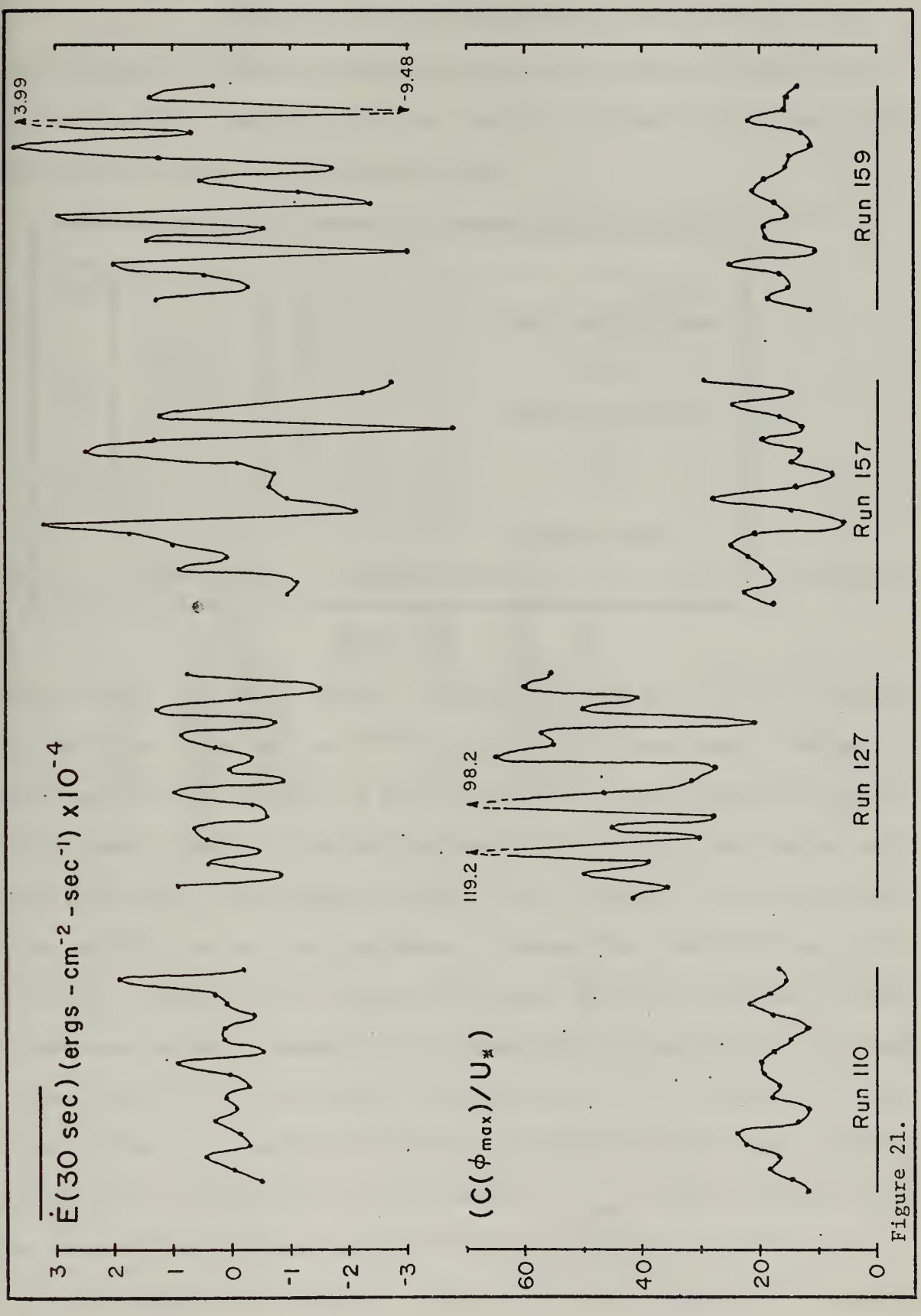
3
2
1
0
-1
-2
-3
$\dot{E}$(30 sec) (ergs - cm^{-2} - sec^{-1}) x 10^{-4}
3.99
-9.48
60
40
20
0
(C(ϕ_{max})/U$_*$)
119.2
98.2
Run 110
Run 127
Run 157
Run 159

Figure 21.

B.2. 30 Second Averages.

Several of the 10 minute runs were chosen for detailed analysis to help determine the nature and scales of intermittency and the resultant momentum transfer. Analysis and data display were similar to those used for the 10 minute runs.

Fig. 19 and Fig. 20 depict the changes with time of 30 second

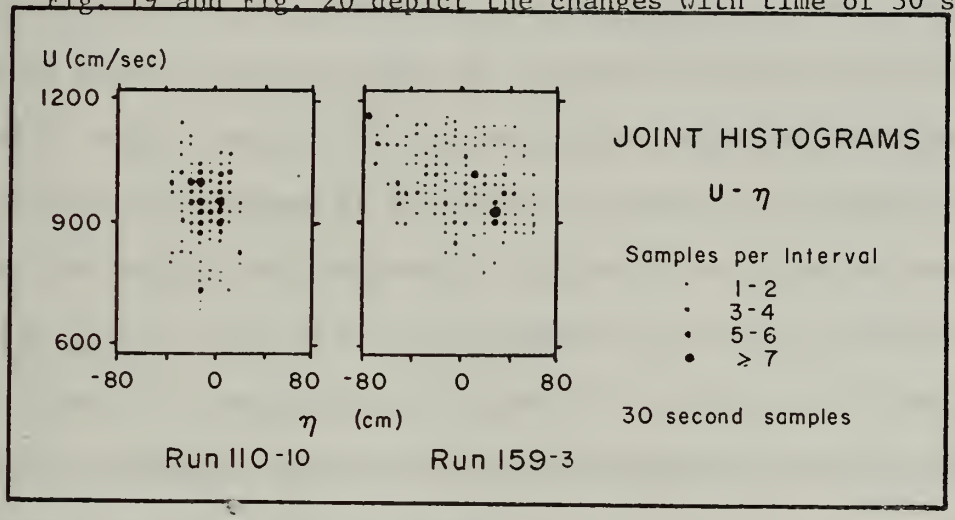

Figure 22

averages of variables in the air and water for runs 110, 127, 157 and 159. Fig. 21 shows $\overline{E}$ (30 sec) and C (Φ_{max})/U_* for the same runs. The major features of the 10 minute runs also stand out in these displays of short term change. There is a general increase in U, E, M, T, wave height and spectral density and momentum extrema. Stress computed from the air and water profiles are in rough agreement, although they show different periodicities. The short term changes are largest and most rapid when the magnitudes are largest; changes in U are paralleled by increases in E, though not as clearly as in the longer averages because of the influence of wave groups (these had a roughly 40 second periodicity for later runs, and also significantly affected the τ_w measurements). U_{max} is again normally over the troughs, but with much scatter; this is illustrated in Fig. 22, JH ($U_{2.4}$, η) from 2 short segments, and is more clearly shown in the coherence

diagrams (Figs. 29 and 30).

In these runs, the waves of the spectral peak carry roughly 80% of the total momentum density (again implying that a significant portion is carried by waves of higher frequency, or slower phase speed), while the waves of the momentum peak (when different from the spectral peak) over-account for the total momentum. $U_{10}/C(\Phi_{max})$ is in the range of 1 - 2, and is in fact largest during the earliest run, due to the absence of swell. This parameter shows no significant peaks at the points of wind and E maxima; this may be interpreted to mean that the wind is strongest over the largest wave components, indication of selective coupling. $C(\Phi_{max})/U_*$ shows no distinct relation to spectral growth or decay; E (30 sec) has comparable variations in runs 110 and 127, and the parameter is similar in magnitude in runs 110 and 159 when the energy growth patterns are radically different.

For these short averaging times E(30 sec) is 1% to 10% of the mean energy density for the corresponding 10 minute periods. The rapid changes in spectral shape and content are well shown in Fig. 23, from run 157. Cross-sections of this diagram are shown in Fig. 24 (n.b. 80% and 90% confidence limits at 10^3 on $\Phi_{\eta\eta}(f)$ axis). It is immediately apparent that the lower frequencies (referring here both to swell [.1254 hz] and to local wind generated waves [.2515 hz]) are relatively constant, with variations primarily attributable to propagating wave groups (this was checked by examination of analog strip chart displays of the filtered signals). The change in the high frequency components, however, is very dramatic, with 30-second variations of up to 2 orders of magnitude (3 orders of magnitude for the 4.46 hz waves, Fig. 23). The change of shape of the 'equilibrium range' in Fig. 23 also demonstrates this

variation; there is a repeated pattern of large excesses in specific high frequencies followed by a filling out of the spectrum. The subjective impression of high frequency excesses climbing the slope of the spectrum and transferring their energy to lower frequency components is hard to avoid. Fig. 24 also shows that the excesses do not always occur simultaneously in all frequency bands and that on the 30 second averaging period the high frequency growth does not always correspond to the presence of low frequency peaks. Further, intermittent high growth rate events are of short duration, typically lasting between 30 and 60 seconds; i.e., similar to the period of the major wave groups.

Changes in the wave field and the wind-wave relationships through an 'event' are illustrated for the burst of segment 8, run 157, in Figs. 25 and 26. Fig. 25 shows the coherence of U and η from before, during, and after the event (segments 6-10); Fig. 26 shows the momentum spectra from the same period. Before the event $\gamma_{u\eta}$ is high and $\theta_{u\eta} \doteq -\pi$ for the low frequency components; $\gamma_{u\eta}$ is insignificant for most higher frequencies. During the event $\gamma_{u\eta}$ increases dramatically in the 1.25-3.25 hz range. $\theta_{u\eta}$ shows a continuous 'slip' through this range; this is probably accounted for by the averaging time being much larger than the high frequency instabilities so that both generation and detritus is represented, and by the deceleration of the gust parcel during generation. Immediately after the event $\gamma_{u\eta}$ has decreased for frequencies > 1 hz; it is still lower in segment 10, except for the local peak at 1.25 hz where the waves lead the wind (an opposite phase relationship from that of segment 9). Before the event the wave momentum is strongly concentrated in the local waves (0.32 hz) and swell (0.15 hz). During the burst the high frequency components, out to over 3 hz, carry a much larger portion of the momentum than at any other

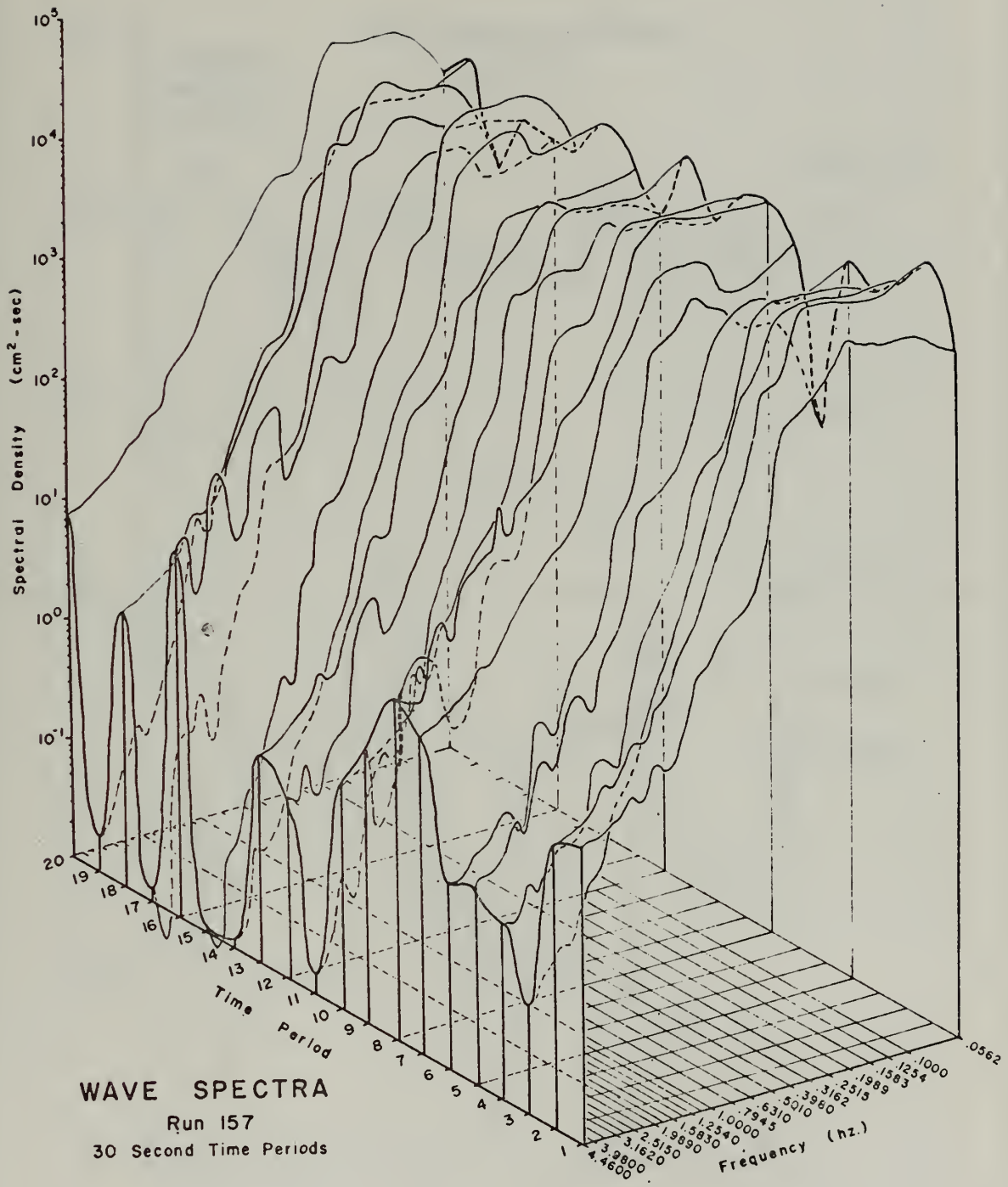
Spectral Density (cm²-sec)
10³
10⁴
10³
10²
10¹
10⁰
10⁻¹
20
19
18
17
16
15
14
13
12
11
10
9
8
7
6
5
4
3
2
1
Time Period
.0562
.1000
.1254
.1583
.1989
.2513
.3162
.3980
.5010
.6310
.7945
1.0000
1.2540
1.5830
1.9890
2.5150
3.1620
3.9800
4.4600
Frequency (hz.)
WAVE SPECTRA
Run 157
30 Second Time Periods

Figure 23.

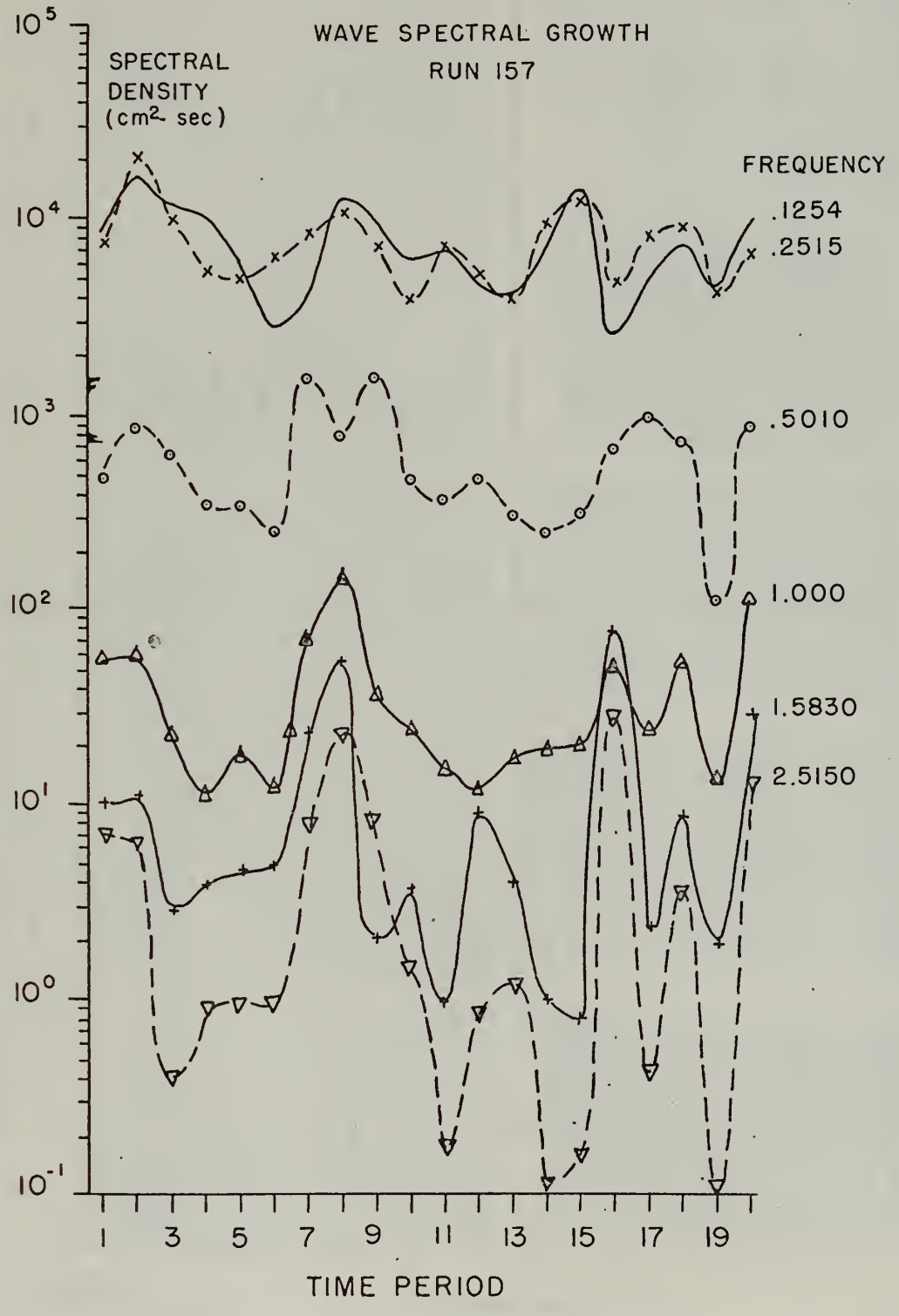
WAVE SPECTRAL GROWTH
RUN 157
SPECTRAL DENSITY (cm² sec)
FREQUENCY
.1254
.2515
.5010
1.000
1.5830
2.5150
10⁵
10⁴
10³
10²
10¹
10⁰
10⁻¹
1
3
5
7
9
11
13
15
17
19
TIME PERIOD

Figure 24.

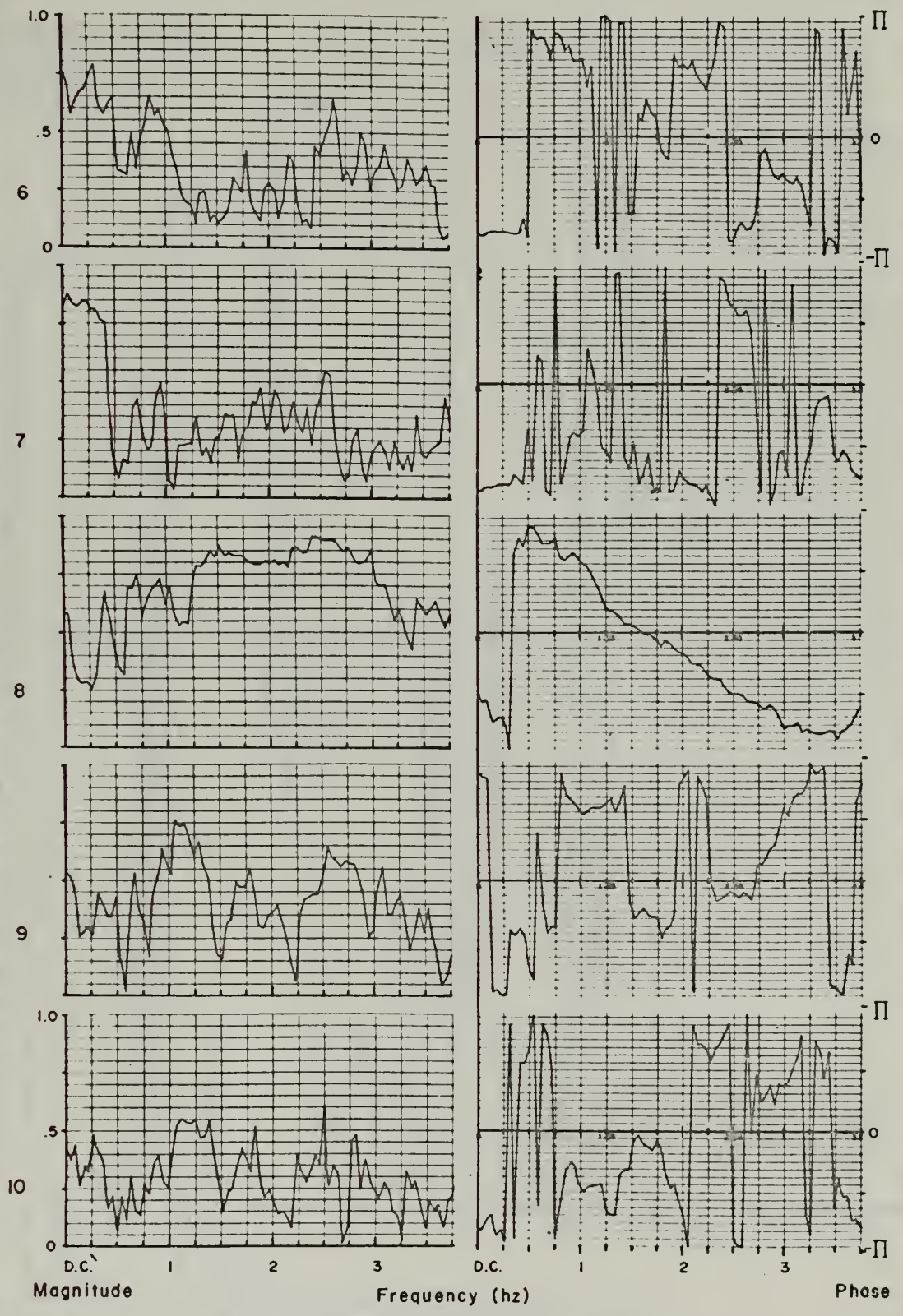

Coherence Between Wind Speed (U) and Wave Height (η)

Run 157 30 sec. avgs. Time Periods 6-10

Figure 25.

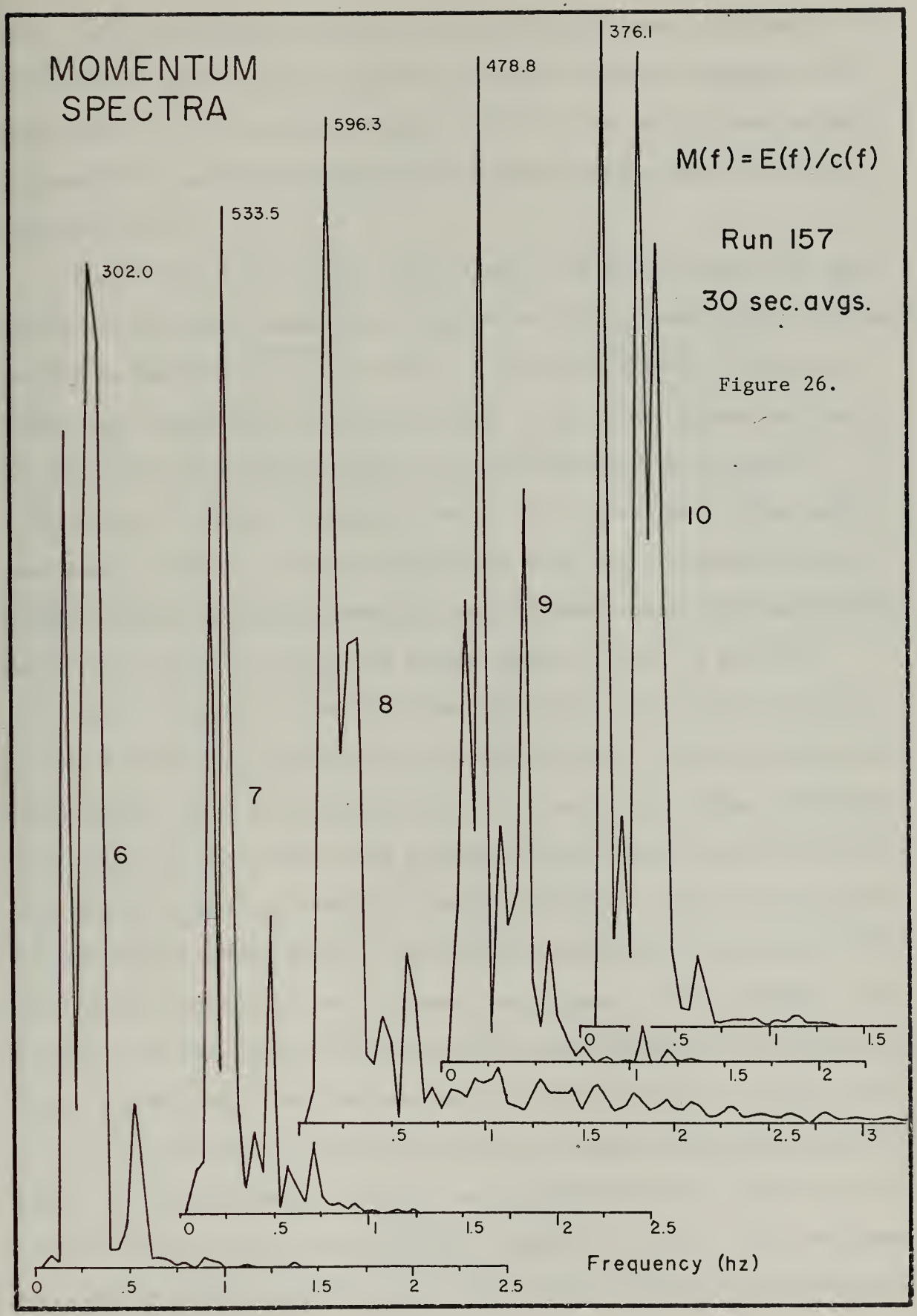
MOMENTUM
SPECTRA
M(f) = E(f)/c(f)
Run 157
30 sec. avgs.
302.0
533.5
596.3
478.8
376.1
6
7
8
9
10
0
.5
1
1.5
2
2.5
3
Frequency (hz)

Figure 26.

time. Immediately after the event the very high frequency components have disappeared, and the 0.45 hz component has been strongly augmented. This peak shifts to a still lower frequency (0.40 hz) in the following segment, and eventually nearly all the momentum is again concentrated in the local waves and swell.

Fig. 20 and Fig. 21 show that the event, on the 30 second averaging basis, was notable by anomalously high values of U_{10}, wind shear, wave height, current maximum, E, $\dot{E}$(30 sec), and M. T increased slightly during the event, and significantly 60 seconds later. τ_{air} is not excessively large, but the profile for segment 8 had a low correlation with the model (ρ = 0.91) so that the computed value of τ is unrealistic. The large departure of profiles from the logarithmic mean, and the development of unstable shear layers, are characteristic of such intermittent events (as noted in the cat's paw study and further shown in Figs. 28 and 29).

Fig. 27 depicts the detailed (analog strip chart output) structure of such a burst type generation event from run 116. Isotachs (from profile measurements), wind velocity fluctuations at two heights (high pass filtered at 0.05 hz), wave height, and a measure of the energy content in low and high frequency bands of wind and waves are depicted. Scales are relative. The major burst occurs after a rapid wind increase and is associated with the coupled occurance of low frequency wave groups in air and water. The generation of atmospheric turbulence (very high frequency wind fluctuations) occurs predominantly over the wave peaks in air and water, and these peaks occur simultaneously. Both low frequency and high frequency wind and wave energy are maximum during the burst, and some intermittent activity continues after the major gust had passed. The low frequency wave components are slightly damped after the gust leading edge, when the burst is strong-

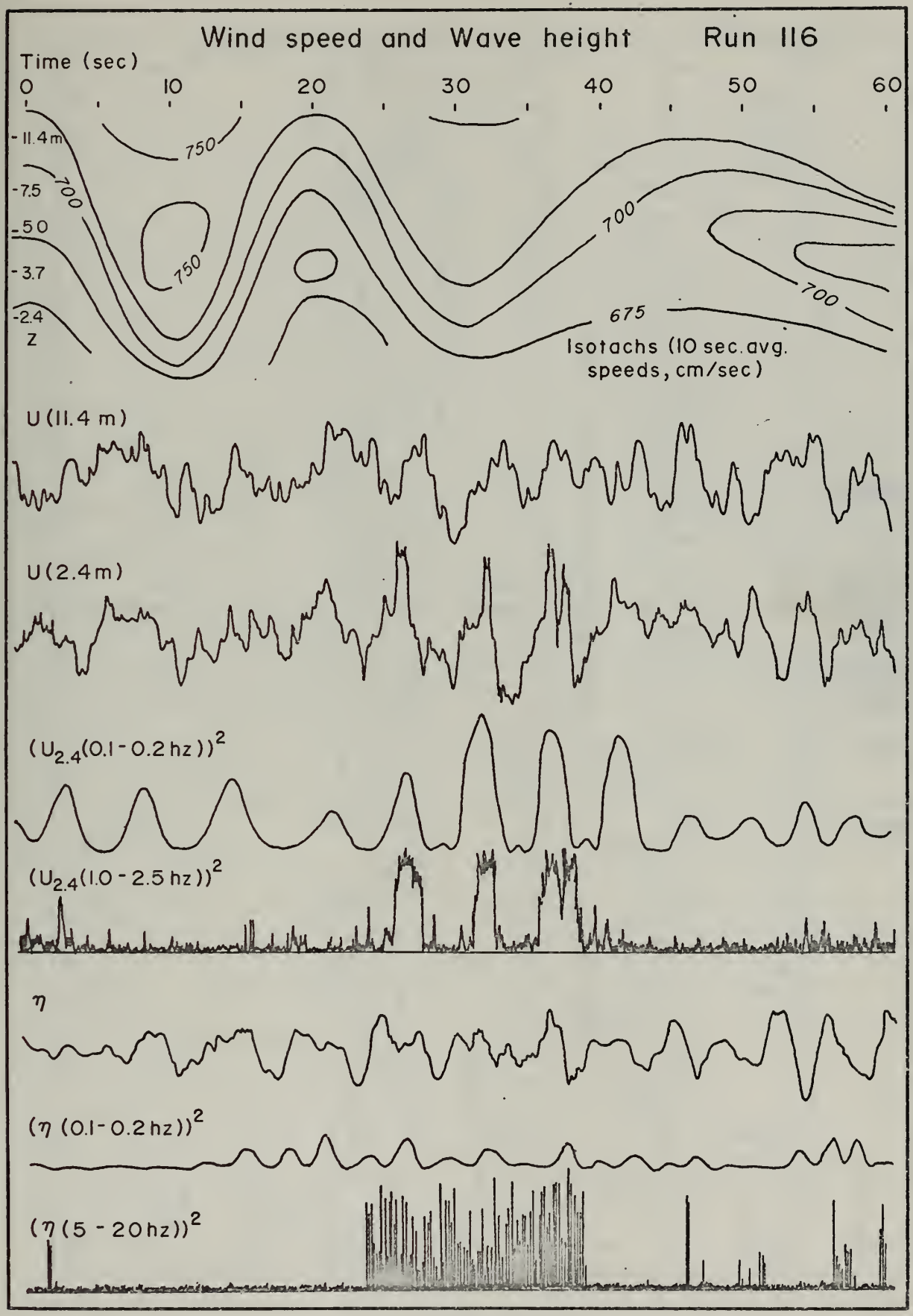
Wind speed and Wave height Run 116
Time (sec)
0
10
20
30
40
50
60
-11.4m
-7.5
-5.0
-3.7
-2.4
Z
750
700
750
700
700
675
Isotachs (10 sec. avg. speeds, cm/sec)
U(11.4 m)
U(2.4m)
$(U_{2.4}(0.1-0.2\,hz))^2$
$(U_{2.4}(1.0-2.5\,hz))^2$
η
$(\eta\,(0.1-0.2\,hz))^2$
$(\eta\,(5-20\,hz))^2$

Figure 27.

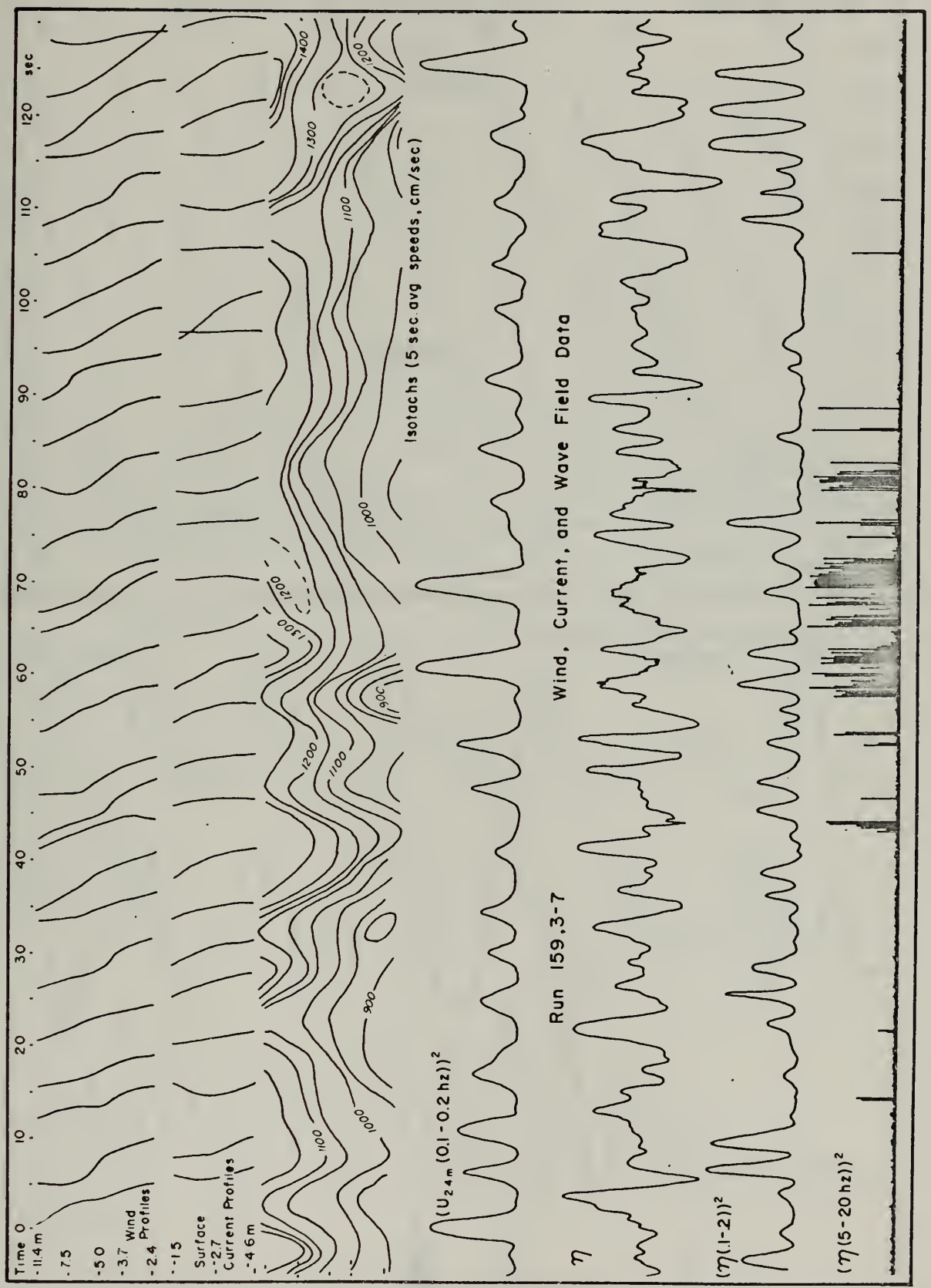
Time 0
-11.4 m
-7.5
-5.0
-3.7 Wind Profiles
-2.4
-1.5
Surface
-2.7
Current Profiles
-4.6 m
10
20
30
40
50
60
70
80
90
100
110
120
sec
900
1000
1100
1200
1300
1400
Isotachs (5 sec. avg speeds, cm/sec)
$(U_{24m}\ (0.1-0.2\ hz))^2$
Run 159.3-7
Wind, Current, and Wave Field Data
η
$(\eta(.1-2))^2$
$(\eta(5-20\ hz))^2$

Figure 28.

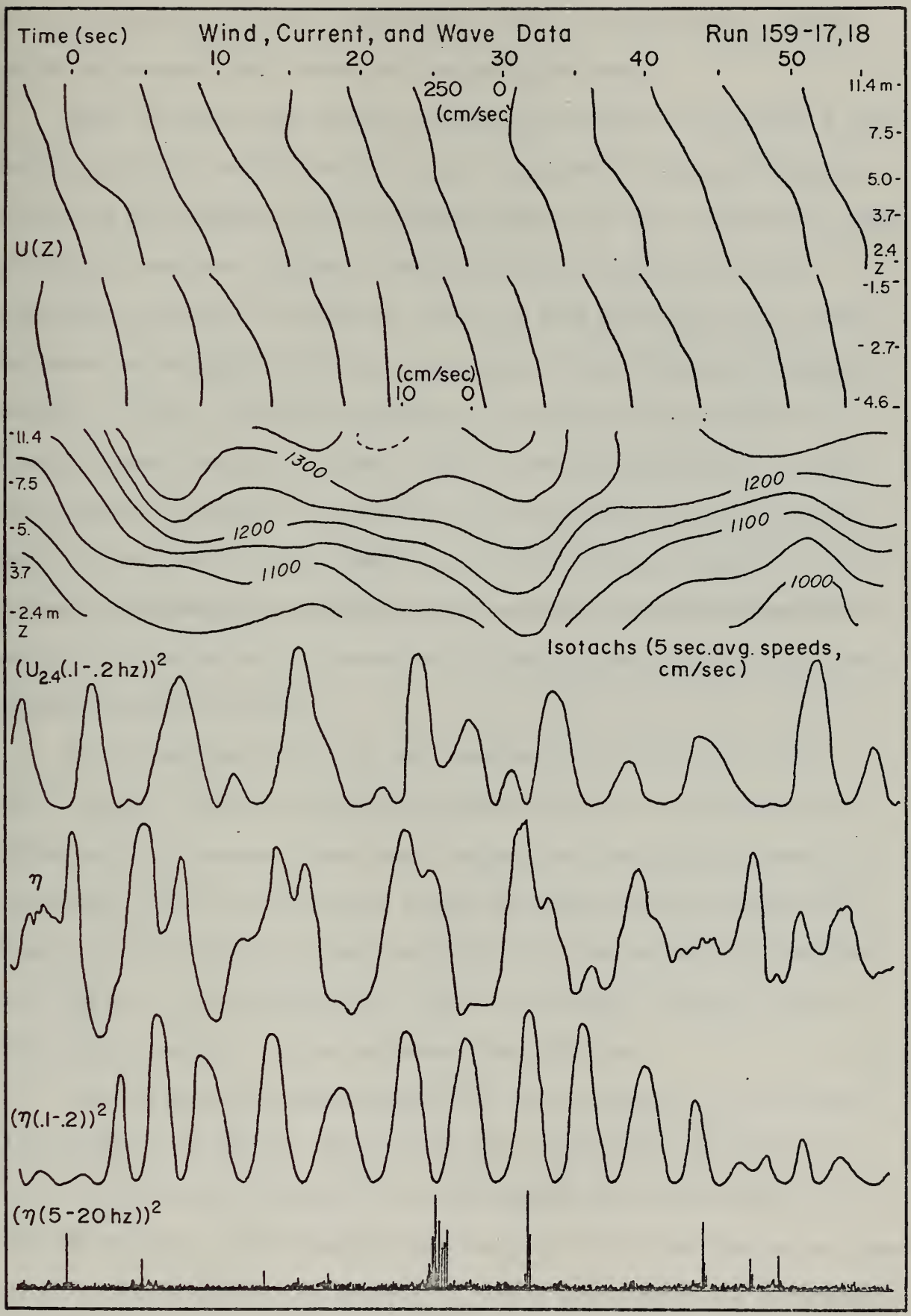
Time (sec)
Wind, Current, and Wave Data
Run 159-17,18
0
10
20
30
40
50
250 0
(cm/sec)
11.4 m
7.5
5.0
3.7
2.4
Z
1.5
2.7
4.6
U(Z)
(cm/sec)
10 0
11.4
7.5
5.
3.7
2.4 m
Z
1300
1200
1100
1000
Isotachs (5 sec. avg. speeds, cm/sec)
$(U_{2.4}(.1-.2\,hz))^2$
η
$(\eta(.1-.2))^2$
$(\eta(5-20\,hz))^2$

Figure 29.

est. This figure clearly demonstrates a very strong coupling between media and between widely separated frequency components.

Figs. 28 and 29 are similar diagrams from the first and third E peaks (see Fig. 20) of run 159 (the η scale is comparable in Figs. 27 and 29; all others are relative). These figures again show that intermittent, high growth rate wave and turbulence generation occurs during the coupled occurrance of large, low frequency groups in wind and surface wave fields. The event is preceeded by profile distortions, a wind decrease then rapid increase. In Fig. 28 the low frequency components are again seen to be slightly damped during the intense high frequency instabilities. Large, low frequency components of the wind and wave fields that occur independently do not lead to this intense coupling and momentum transfer to high frequency components; it is the strong nonlinear coupling between the media which results in the generation of high frequency instabilities and enhanced coupling of scales.

The strong shear layers in the atmospheric profiles are of very short duration. They are almost invariable associated with large wave groups and high frequency wave energy spikes, and then quickly revert to logarithmic form as the mean wind energy is drained and the atmospheric dynamics recover from the local instabilities. The current profiles show the effects of the momentum of the large wave groups; they have little direct relationship to the instantaneous wind profiles.

The coherence and phase diagrams for the last event of run 159 are shown in Figs. 30 and 31. Most of the large energy peak for this time period was due to the presence of an exceedingly large wave group, and the high frequency generation was less intense than in the similar set from run 157. Nevertheless, the sequence of events associated with the instabil-

Coherence Between Wind Speed (U) and Wave Height (η)

Figure 30. Run 159 30 sec. avgs. Time Periods 16-20

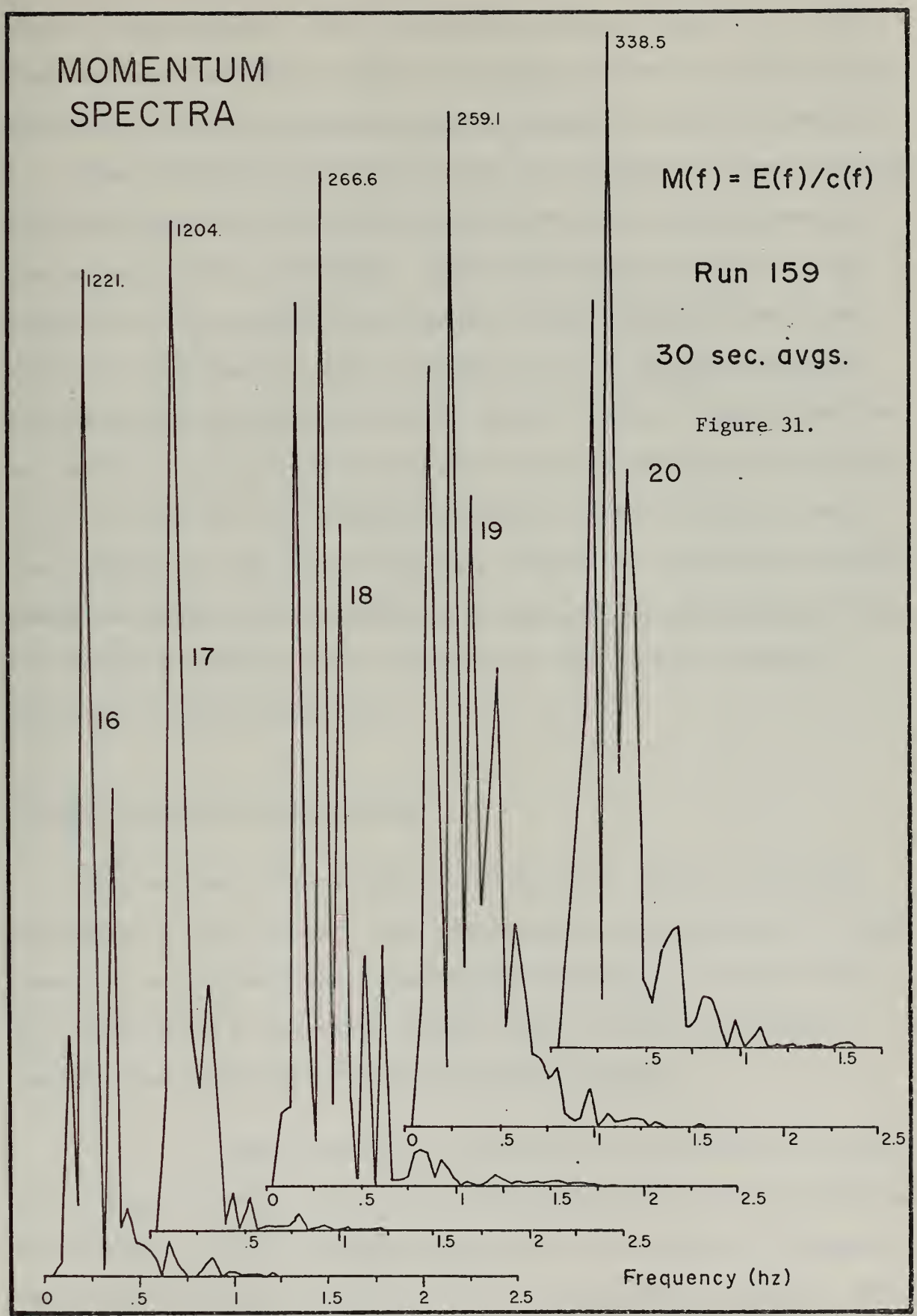
MOMENTUM
SPECTRA
M(f) = E(f)/c(f)
Run 159
30 sec. avgs.
1221.
1204.
266.6
259.1
338.5
16
17
18
19
20
0
.5
1
1.5
2
2.5
Frequency (hz)

Figure 31.

ity are again apparent. There is the same pattern of high $\gamma_{u\eta}$ at low frequencies and momentum carried in long waves, followed by enhanced high frequency coupling and temporary momentum excesses in higher frequencies.

These figures have demonstrated the short duration, strong coupling, rapid growth rate, highly nonlinear and intermittent nature of wave generation and spectral development. Even the 30 second averages blur the intensity of the coupling by overlapping between generation events and detritus or propagation. The microstructure is of critical importance, both because the majority of momentum transfer occurs at high frequencies and because the high frequency instabilities and waves serve as catalysts in the coupling and low frequency interactions between scales and media. Long sequences of measurements and long averages can predict the background conditions under which generation occurs, and can show the effects of very low frequency coupling, but are incapable of depicting the essential physics of wind-wave generation.

Summary of Results and Conclusions

The cat's paw study showed the importance of 'bursts' in initial generation of high frequency waves and turbulence and indicated the significance of intermittency and strong nonlinear coupling. The data from this study, where a much larger dynamic range of scales is involved, support those conclusions and the following statements.

1. Wave generation is intermittent and involves strong nonlinear coupling among a wide range of frequency components in the wind and wave fields. The high frequency instabilities are critical to the momentum transfer process, and much of the air to sea momentum flux goes directly

into high frequency waves. The important scales are those of the major waves and wave groups, and those of the high frequency wavelets coupled to them. These facts are substantiated by the large and rapid fluctuations in E, M, and $\dot{E}$ for both 1 hour and 30 second averaging periods (Figs. 11-13, 19, 20, and 23), by the simultaneous occurrance of large magnitude, coherent fluctuations of wave height, velocity, and energy content in widely separated frequency bands in air and water (Figs. 25, 27-30), and by the resultant excesses in spectral density and momentum in high frequency waves (Figs. 23, 24, 26, 31).

2. The high frequency wavelets act as drag elements to couple the mean wind to the major wave field; they also aid the growth of lower frequency instabilities by nonlinear stress-strain coupling. This was demonstrated in the cat's paw data, and is shown herein by the variations in coherence patterns between wind and waves (Figs. 25, 30) and the coupled occurrance of bursts in widely separated frequency bands (Figs. 27-29). The results of Wu, who makes a similar contention, are not supported by the short term profile averages, primarily because of the complicated dynamics of air sea interaction.

3. The wave field is modulated by surface currents; this perturbation in turn causes an imbalance in the equilibrium between wind and wave fields. The wind and surface current fields are viscously shear coupled and their profiles yield comparable mean stress values (Figs. 8-10).

4. There appear to be a variety of wave generation regimes. These regimes can be only poorly represented by mean parameters or by simple fits to the mean profile conditions. The different regimes are

characterized by bimodal distributions of profile parameters (Figs. 2-5) that are not present when a 'homogeneous' set of runs is considered separately (Fig. 6). Profile parameters for a non-homogeneous set of runs have larger variances and a much more complicated pattern of values than do those of a homogeneous set, and there are no simple formulas which can adequately describe the relationships between them.

5. Study of time history is important for an understanding of spectral development. The time history is poorly represented by mean parameters or long averages. The approach of the profile to a logarithmic form with increasing averaging time obscures the importance of the instabilities associated with short, intermittent perturbations and development of shear layers (Figs. 28, 29). The long average spectra (Figs. 14-16) can depict the general growth of the wave field but fail to reveal the significant flux to high frequencies during intermittent generation (Figs. 23, 24). The rough quantitative agreement between stresses and viscously normalized velocities in air and water boundary layers is strongly modulated by tidal forces.

6. Boundary layer profiles in air and water are essentially logarithmic for averaging times $\geq$ 30 seconds and for neutral stability. The profile parameters U_* and z_o can not be expressed in terms of a single parameter. The criterion $\rho \geq 0.94$ for a fit of measured values to the model is satisfactory (Fig. 4). There do exist anomalous or 'critical' wind speeds, in the sense that around these speeds the variability in profile structure is increased and the resulting profile parameters have anomalous means, variances, and amplitude distributions (Figs. 3-5). The mechanics responsible for these anomalies have not yet been demonstrated.

7. The growth of the major portion of the spectrum is hypothesized to be due both to the wind-wave coupling enhanced by the high frequency wavelets and to nonlinear transfer of energy within the wave field. The shift from high to low frequency content is best illustrated by the momentum spectral changes in Figs. 26 and 31. Spectral growth can occur even at $U/C(\Phi_{max}) < 1$ (Figs. 11, 12) and this fact is unexplained by either propagation or by available theories.

8. Both the overshoot phenomenon and the equilibrium range are meaningful only in terms of long averages. The wave field can support a range of equilibrium levels under different wind conditions (Fig 15, particularly the .2515 hz component), and the wave field is never in a steady saturation state (Figs. 15, 23, 24).

On the basis of these results it is concluded that a large portion of wave generation occurs intermittently and is due to strong coupling between a large range of scales of motion and between wind and waves. Local instabilities and direct nonlinear interactions between waves and turbulence are crucial factors in generation, and most of the momentum flux from these 'bursts' goes directly into high frequency waves.

IV. CONCLUSIONS AND RECOMMENDATIONS

The questions posed in the introduction may be answered as follows:

1. The important time scales in the transfer of momentum from wind to waves are those of and within the intermittent turbulent bursts. These in turn are determined by nonlinear coupling to the period of the major waves (localized instabilities or subbursts) and the wave groups (the gusts or bursts themselves). The transfer is rapid, produces high growth rates of high frequency waves, and quickly drains the available energy from the mean wind field. Nonlinear interactions, and transfer of energy within the wave field by breaking and dissipation, operate on similar time scales. Transfer is effectively completed within two or three periods of the waves or wave groups. The time scale of equilibrium imbalance and restoration between the mean wind, wave, and current fields is on the order of 2 to 4 hours.

2. The fluctuations involved in wind wave generation are intermittent and strongly nonlinearly coupled, involving interactions between a wide range of scales. The short instability fluctuations, and the resultant energy density growth rates of high frequency waves, are roughly three orders of magnitude larger than those observed on the mean. The generation of waves and the generation of turbulence are inseparable.

3. There are several types of coupling between media. These include the strong interactions during instability fluctuations; the form drag of the wavelets on the mean wind flow and the resultant coupling between low frequency, large amplitude wave groups; the interaction of wave induced Reynolds stresses at swell and locally generated wave fre-

quencies with turbulent Reynolds stresses; an undetermined anomalous interplay between wind and waves at discrete critical wind speeds; and viscous shear coupling between mean wind and surface drift. Many of these interactions appear to depend strongly on the presence and position of high frequency fluctuations (the microscales).

Coupling between scales involves both the weakly nonlinear resonant wave interactions, and the strongly nonlinear stress-strain relationships involved in the interactions between Reynolds stress and shear. These latter operate both within and between media. High frequency instabilities aid the growth of lower frequencies; fluctuation magnitudes are largest when the range of scales involved in the fluxes are largest.

4. Generation 'events' may be distinguished by the short time average approach to, and deviations from, lognormal distribution of velocity fluctuations; by strong coherence between high frequency waves and turbulent Reynolds stress or horizontal velocity; by temporary excesses of energy and momentum in high frequency (> 1 hz) surface waves; and by the enhancement in magnitude and frequency of stress and buoyancy fluctuations caused by the strong nonlinear couplings. These features can not as yet be parameterized in terms of the mean or of profile parameters, but can be used for conditional sampling in a real time data collection/analysis system. The criterion $\tau \geq 100$ dynes/cm^2, when smoothed over a time period ≤ 0.5 seconds, is a good first approximation for a switch to determine the presence of a burst within a cat's paw.

5. There are no easily measurable similarity parameters which can describe the dynamics of air-sea coupling. The apparent effect of fluctuations depends strongly on the averaging scale over which they

are evaluated, i.e., the effect is different for different physical scales. There are more than one distinct regimes of generation and there are large anomalies in the relationships between wind field parameters. There is a gross, qualitative similarity in the appearance of weak and strong fluctuations, and of large bursts and subbursts, but the intense nonlinear interactions and resulting enhancement of the magnitude of fluctuations and fluxes preclude any strict similarity representation of the physics of momentum transfer.

The mechanics of the development of a wind-wave field can be heuristically described in terms of these features:

Initial generation is caused by the forcing of random turbulent pressure fluctuations (the Phillips resonance mechanism); the critical time scales involved in this coupling are those of the waves generated. In the presence of a strong thermal stratification the generation of waves is delayed until the boundary layer is destabilized. The work done on the waves creates reaction stresses in the air which generate small scale turbulence. The small scale fluctuations do work on the larger scale shear in air and water, which aids the development of larger scale instabilities and stronger fluctuations. The energy from the mean flow is rapidly depleted through transfer to the water surface and dissipation to heat. The subbursts occur predominantly within larger scale anomalies or gusts that are initially triggered by atmospheric dynamics.

After an isolated gust has passed, buoyancy forces rapidly reestablish boundary layer stability. The packet of free surface waves generated by the gust and bursts appears as roughness elements to the wind. In the presence of increasing wind or recurrent gusts the disruption of flow caused by the

roughness elements acts to enhance the probability of occurrance of instabilities over the packet. The scales of interaction between media have increased to include not only the bursts and subbursts but also the group or patch of roughness elements and the major waves within it. In successive interactions the scales are similarly increased and the energy in the initial waves and groups which enhanced the coupling is augmented. The scales are yet further enlarged by nonlinear resonant wave interactions within and among the wave groups. The very high frequency wavelets, which received much of the momentum during the localized high frequency instabilities, either break or otherwise transfer their energy to other components, or are 'organized' by the convergences and divergences of orbital velocity in the underlying longer waves. The concentration of high frequency components on the crests and leading faces localizes the drag elements in a favorable position, since stresses exerted upon them are in the same direction as the orbital velocity and celerity of the longer waves. Under the influence of the drag elements the mean wind decelerates over the crests, accelerates over the troughs.

As the lower frequency waves increase in size their effect on the atmospheric boundary layer increases. Fluctuations in the wind field become coherent with these components, and wave induced or reaction Reynolds stresses develop which both enhance the pressure feedback from the mean flow to themselves (Miles's mechanism) and interact with atmospheric shear and turbulence. The surface waves are generated and propagate in groups, and enhanced perturbations of the boundary layer on the scale of the groups causes similar forcing and feedback on that scale.

The selectively increased forcing of the wind field by the longer waves and wave groups, and by the roughness elements associated with

the major crests, increases the probability that shear layer instabilities will be triggered over them. The gusts are thus selectively coupled to these areas. During these instabilities, as in a cat's paw over a calm surface, the majority of momentum transfer occurs during the high frequency bursts and subbursts, and the momentum flux goes directly into the high frequency wave components. Energy growth rates are locally three orders of magnitude larger than the mean, and the available atmospheric energy is rapidly depleted. The high frequency waves again break or otherwise transfer their energy to the longer waves and swell. The process occurs intermittently and can cause spectral growth even when the largest waves are moving faster than the mean wind.

The generation and spectral development process is self-enhancing and involves strong coupling between scales of motion in both wind and wave fields. During periods of relatively steady winds a quasi-equilibrium balance is maintained, but this is easily broken by changes in surface current or by wind velocity shifts. A large portion of the momentum flux to the surface occurs during the intermittent, large magnitude, strongly coupled bursts; and most of this flux goes directly into high frequency waves. The microscales play a dominant role both by being the active recipients in the momentum transfer and by assisting the growth of lower frequency components by stress-strain coupling, by acting as roughness or drag elements, and by weakly resonant interactions.

Many questions concerning the physics of wind-wave generation remain unanswered. This study has demonstrated the importance of intermittency, strong nonlinear coupling, and microscales in momentum transfer, but has given no indication of the percent of the total transfer attributable to these features. Further, the effects but not the physics of

energy transfer within the wave field have been described.

Meaningful future experimentation must provide a better description of the horizontal and vertical structure of Reynolds stress in air and water; quantitative measurement of wave growth during intermittent generation and its relation to the development of the wave field; a statistical description of the structure and spacing of intermittencies and their relationship to waves and wave groups; simultaneous measurements of high and low frequency wave energy and their spatial and time relationships; a detailed examination of the air-sea coupling at the anomalous critical wind speeds; and controlled determination of the effects of high frequency degrading slicks.

Open ocean measurements of velocity and turbulence in the troughs of major waves are still unavailable; the role of breaking and the effect of the resulting vertical vortices on spectral transfer is poorly understood; and the effects of wind-surface current coupling and the underwater boundary layer on wave generation have still been inadequately described. Future studies must consider the importance of time history and intermittency during generation, and most progress will be made through detailed, near naviface measurements.

APPENDIX I. INSTRUMENTS AND CALIBRATION

A. Sites and Platforms.

Buoy Experiment. Instruments were mounted on the M.I.T. Air-Sea Interaction Buoy (Mollo-Christensen and Dorman,(1971)). The site was at the southwestern end of Vineyard Sound (41^{o} 20' 40" N, 70^{o} 55' 45" W). The buoy is shown in Fig. AI.1. The site is 8.9 km south of Cuttyhunk Harbour, 7.8 km west of Gay Head Light, Martha's Vineyard, and approximately 50 km ENE of Block Island. The bottom in the vicinity is very fine sand and mud, depth 31.1 m at MLLW, and mean tidal range less than 1 m. The bottom is nearly flat to the south and southwest, and shoals slowly to the north and northeast.

The experiment was conducted from July to November, 1970. Winds in the area are dominated by a land-sea breeze regime during the summer, and are predominantly southwesterly in the fall. Tidal currents are primarily semidiurnal with a clockwise ellipse. They are strongly affected by the winds. Recorded current maxima were around 1.5 m/sec with a typical slack duration of 20 minutes and nearly equal duration of flood (NE) and ebb (SW).

A shore support and data collection facility was housed in the Coast Guard Station (deactivated) on Cuttyhunk. The facility had line-of-sight communication with, and visual observation of the buoy. Ship support was provided by the R/V R. R. Shrock (M.I.T.'s oceanographic research vessel) and by project owned and local smallcraft. The Shrock was equipped with an electronic bathythermograph used to monitor thermal structure during experiments. A small weather station was maintained on Cuttyhunk.

The buoy was slack moored (scope of 2) and consequently faced into the

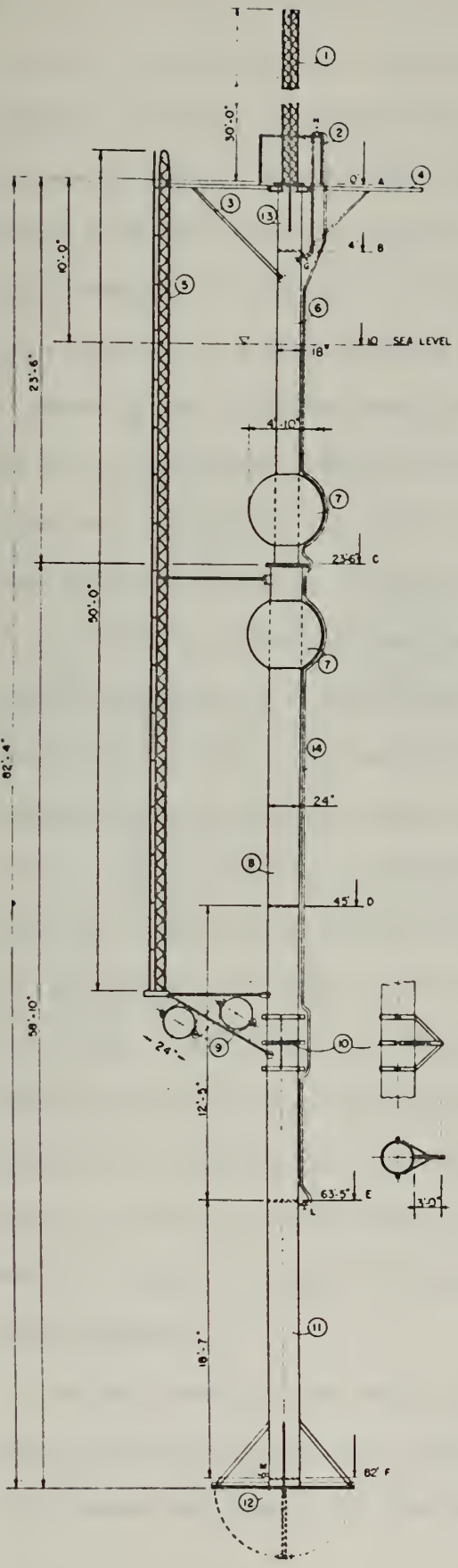

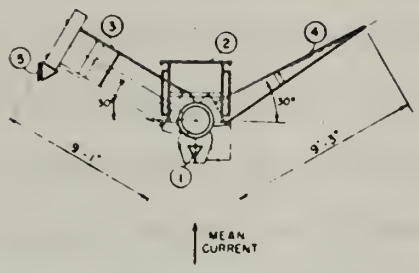

1. 10m. Meteoralogical Tower
2. Personnel Platform
3. Tower Support
4. Wave gauge & Boom Support
5. 2-track Underwater Tower
6. Compressed Air Compartment
7. Buoyancy Spheres
8. Floodable Ballast / Buoyoncy Tube
9. Balancing Spheres
10. Mooring Bridle
11. Same as 8.
12. Damping Plate
13. Electronics Compartment
14. Air Hose

M.I.T. AIR-SEA INTERACTION BUOY

Figure AI.1.

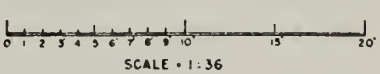

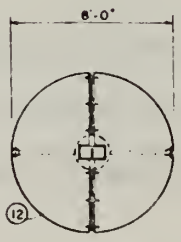

tide (one notable exception being runs 109-159 when continuous high wind reversed the surface flow and kept the buoy pointing southwest). Torque balance to counter the drag of the underwater instrument tower was accomplished by angular preadjustment of the mooring bridle. The bridle was placed near the center of lateral resistance so the buoy and attached instruments had $< 1^{o}$ mean tilt during all current conditions.

The buoy and its small motions had little effect on the data. This may be shown by the following considerations. Static stability was high due to the 4.27 m metacentric height and small surface peretrating cross-section. A vertical load of 100 lbs, 10' from the centerline at platform height, caused only 0.23^{o} tilt. The large virtual mass and damper plate resulted in a critically damped natural heave period of 21.3 seconds, with an amplitude response for 6 second waves of A == (Buoy Amplitude)/(Sea Surface Amplitude) = 0.074. Yaw was determined by field experience to be of significance only during the hour or so at and around slack. Fluctuating tilt was measured with a pendulum pot and showed a maximum response at around 10 seconds with maximum tilts of 1.5^{o}. Instruments were positioned 30^{o} forward of the normal to the mean current to minimize interference calculated on the basis of potential flow. Crude estimates on this basis indicated that velocity distortion ($\Delta U/U$) was 0.028 for the minimeters, 0.009 for the anemometers. The estimates are of course worst near the navi-face, in regions of high shear. Wave gauges were placed on both outriggers and their outputs compared to eliminate buoy interference during adverse wave directions.

The buoy was equipped with a thermoelectric generator to allow unattended operation for up to 2 weeks under mean condition run schedules (12 minutes eash hour), or four hours of continuous operation with over-

CATAMARAN and
COUPLING ARRANGEMENT

Figure AI.2.

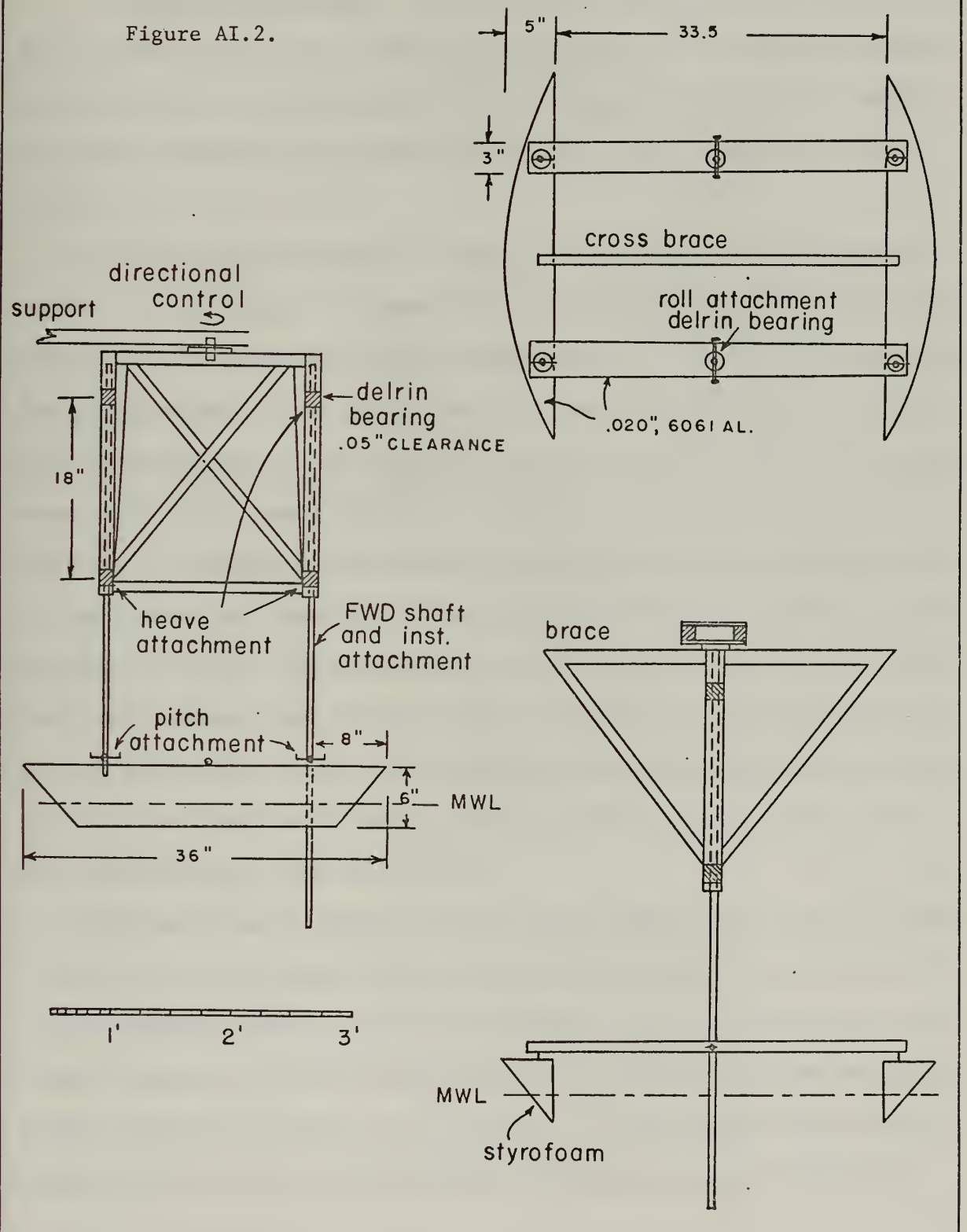

night recharge. Primary power source was a set of eight, 12 volt 120 amp-hour nicad batteries. The buoy has been in use for two years and has operated successfully in winds over 20 m/sec.

Catamaran Experiment. This experiment was conducted in March, 1971, from the dock of the M.I.T. Yacht Club boathouse. Bulk atmospheric conditions were generally stable (see Table 1, Section II). Data were useful only when winds were in the southern quadrants, such that the fetch was over 300 m.

A diagram of the catamaran is shown in Fig. AI.2. It was designed to support up to 1.5 kg of instrumentation in a nearly constant position relative to the instantaneous surface components of $f < 1.2$ hz. Heave decoupling and minimization of mean instrumental tilt were accomplished by the use of two vertical supports, each sliding through two delrin bearings which were separated by 0.8 m and affixed to a carefully leveled support structure. Pitch and roll bearings were located respectively at the attachment point of the fore and aft crossbars to the pontoons, and at the vertical support-crossbar attachment. This arrangement gave the catamaran a 60 cm vertical range and allowed pitch and roll angles of up to 20° with less than 1.5° tilt of the sensors. Construction materials were polystyrene foam and .020", 6061 aluminum sheeting and tubing. Total weight was 3.2 kg, draft 5 cm, and design natural frequency 1.5 hz.

Instruments were attached to the forward support tube from 15 cm below to 30 cm above the surface. They were positioned within 5 cm of the bow line to minimize flow obstruction. Additional sensors were mounted on the support structure. Cables were floated aft of the cat to lessen weight and permit directional control for a full 360°. Accelerometry tests were conducted with full instrumental complement during most runs. They showed

that the cat closely followed waves of $f < 1.3$ hz, and had negligible response to those over 1.85 hz. Waves excited by catamaran motion caused extraneous spectral peaks at 50 and 70 hz but had little effect on frequencies of interest.

B. Instruments. Most of the instruments were designed and constructed at M.I.T. and have seen several years of use and development. In addition to precision and accuracy, a major design criterion has been systematization of the entire array of transducers to insure that data formats will be compatible and easy to process. Hardware and electronics will be described in Project reports now in preparation, and also have been discussed at length in other reports from the Project (Seesholtz (1968); Ruggles (1969) Von Zweck (1969)). The essential characteristics and calibration results are as follows.

Velocity Sensors. Profile velocities were measured with a set of 5 matched cup anemometers in the air and 3 ducted propeller 'minimeters' in the water. Both instrument types use chopper wheels to interrupt a light beam that is sensed by photoresistors. Static and dynamic anemometer calibrations were conducted in the M.I.T. low turbulence wind tunnel. The results indicated that the instruments had a distance constant of 101 cm and a static linear calibration of $U(cm/sec)=2.325x(pulses/min) + 62$ in the speed range 0.8 to 30 m/sec. A repeat calibration at the end of the summer showed deviations from initial values to be less than 2%. Directional tests showed that the units had little sensitivity to vertical components. The anemometers are dynamically nonlinear (Wyngaard, et al (1971)) due to a faster response to wind increases than to decreases. Overestimates in gusty winds were roughly 6%. Minimeters were calibrated in a tow tank at Woods Hole Oceanographic Institution, at speeds of 8 to 105 cm/sec. The static

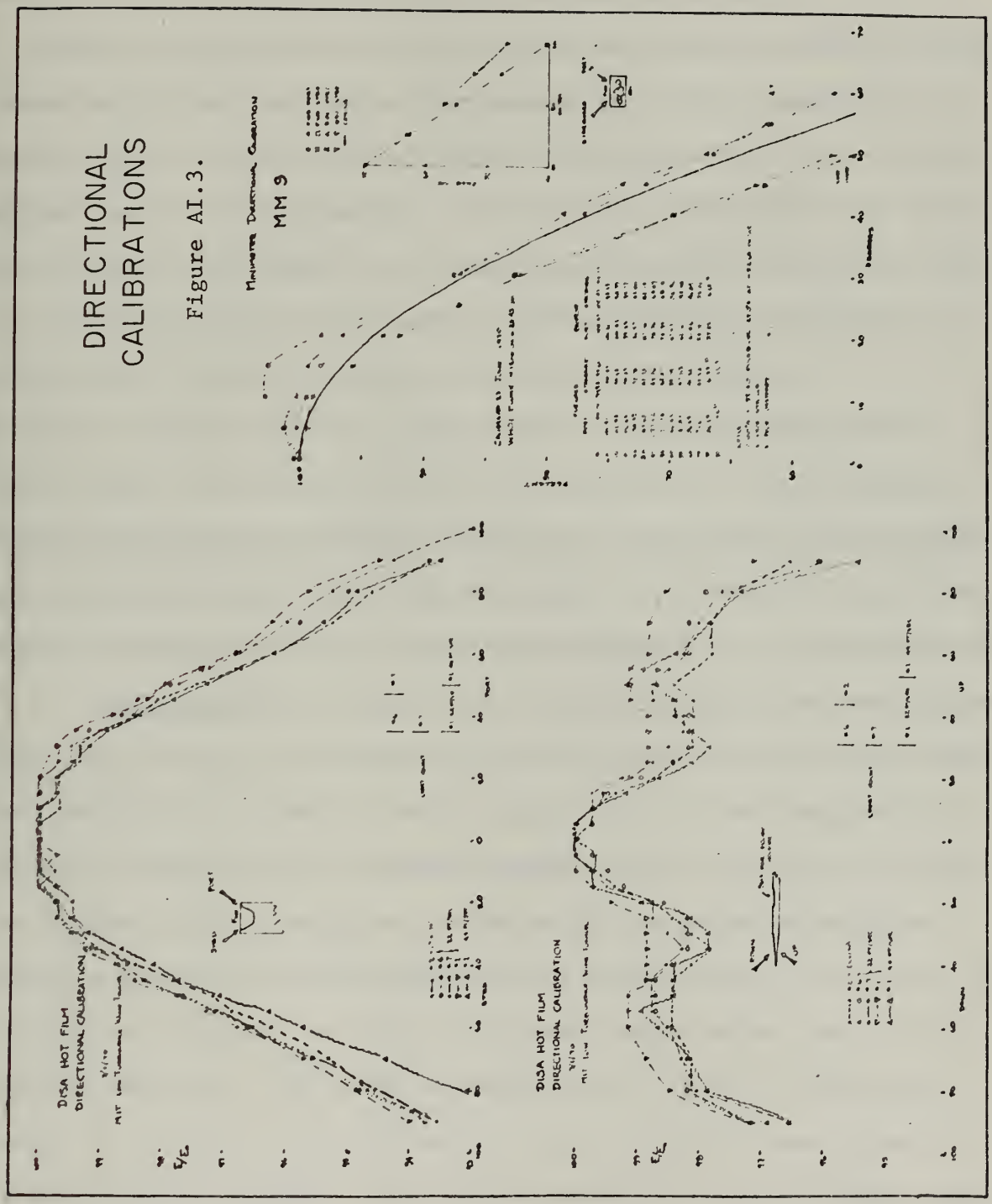
DIRECTIONAL
CALIBRATIONS
MM 9
DISA HOT FILM
DIRECTIONAL CALIBRATION
DISA HOT FILM
DIRECTIONAL CALIBRATION

Figure AI.3.

response was linear, U(cm/sec) = 0.9111x(pulses/sec) + 2.5. Distance constant was 8 cm. Directional response (Fig. AI.3) was best fit by a $\cos\Theta + K \sin\Theta$ curve with K differing between instruments.

Velocity measurements from the catamaran were made with DISA type 55A81 industrially coated hot film probes operated as constant temperature anemometers with overheat ratios of 1.55/1 in air and 1.08/1 in water. Static calibrations were simultaneously conducted with all 5 probes in the M.I.T. low turbulence wind tunnel. The response was expressed in terms of a best fit (in the least mean squares sense) quartic polynomial. Directional response (Fig. AI.3) was similarly fit by the linear relation $U(cm/sec) = Q(1.0 - 0.0021(\Theta - 25))$, where Q = actual velocity and Θ = attack angle, in the range $25^\circ < \Theta \leq 80^\circ$ (correlation = 0.92). Dynamic response (Rasmussen and Bellhouse (1968)) was satisfactory for the frequencies encountered during cat's paws and in fact compensated for the slight velocity overestimate at high attack angles inherent in the directional fit.

Wave Sensors. Wave gauges were capacitance type; they were designed and built at M.I.T. and have provided satisfactory results in the field and laboratory for 4 years, at wave heights up to 5 m and frequencies up to 100 hz. The output is a variable frequency that is created by beating the frequency from an oscillator controlled by the sensor capacitance against a standard. The wave gauges used on the buoy had a 4.6 m long, .95 cm diameter stainless steel wire core steering cable sensor, and a 30.1 hz standard oscillator. Full range bandwidth was 400 hz with resultant response of 3.2 hz/cm. The capillary wave gauge for the catamaran had a 15 cm long, 0.076 cm diameter teflon coated sensor and a 200 hz standard oscillator. Full range variation was 1.4 to 2.2 khz, or amplitude response of 3.88 hz/mm. Sensors were frequently cleansed with alcohol to reduce film effects.

Temperature Sensors. Two types of thermistors, both with 15 kΩ resistance at 25°C were used to permit interchangability in the bridge circuit and provide roughly equal time constants in air and water. Water temperature was measured with matched Fenwall K496 oceanographic isocurve submini thermistors. Each unit had two, 0.076 cm diameter bead-in-glass tips. Air to still water time constant was 70 ms. The Fenwalls were epoxy mounted in 1.3 cm diameter stainless steel tubing fitted with retractable, ventilated shields. The shields were kept forward during the mean condition runs (removed during catamaran runs), and decreased the time constant in moving water to approximately.2 seconds. Air thermistors on the catamaran were VECO model 42A70, .0508 cm diameter bead-in-glass probes mounted in .63 cm diameter tapered wooden dowling. Their air to still water time constant was 35 ms. Using the result of Aagaard (1964) for similar units, amplitude response at nyquist frequency (125 hz) for the VECOs was 0.44.

The differential bridge circuit was designed at M.I.T. It was used in the absolute mode with a 6° - 26° C window for mean condition runs; accuracy and precision with both thermistor types was ± 0.1°C. Measurements from the catamaran used the relative mode (thermistors balanced against precision resistors selected on the basis of mean temperature) with a 5°C window, and had a precision of ± 0.02°C. A bomb calorimeter was employed as field and calibration temperature standard.

Additional instruments included a pendulum pot for measurement of buoy tilt, a tri-axial strain gauge accelerometer for measurement of catamaran motion, and an electronic bathythermograph connected to an x-y plotter on the Shrock.

C. Mounting.

Buoy. Cup anemometers were attached to aluminum channel which in

turn was bolted to the meteorological tower. Cups were slightly more than 1 m from the tower. Heights (for runs 67 - 159) were 2.4, 3.7, 5.0, 7.5, and 11.4 m. Minimeters were attached to carts which ran on one set of tracks on the underwater tower. They could be depth-positioned by hand from the buoy outrigger. Sensors were over 50 cm from the tower which in turn was 2.5 m from the main spar. Mean depths (runs 109 - 159) were -1.52, -2.74, and -4.7 m. Thermistors were mounted on the arms of the minimeters and anemometers. The primary wave gauge was located directly above the minimeters; the secondary was on the opposing outrigger. Hot film and thermistor electronics were housed in a wooden box located between the braces of the tower support, and the main electronics package was in a compartment in the main spar, directly under the personnel platform.

Catamaran. The accelerometer and wave gauge electronics were set in the forward cross-brace. Orthogonal hot films and thermistors were attached to the forward vertical support with delrin mounts. The wave gauge sensor was stretched between two delrin braces on the forward support. Cross-stream separation between the wave gauge and hot film tips was 0.95 cm; between the wave gauge (air) or hot films (water) and thermistors 1.3 cm (see Table 1, Section II). Downstream sepatation was < 1 mm. Orthogonal positioning of hot films was insured by pre-fixed mounting and was checked by measurements on projected photographs. Separation between hot film tips was 3 mm.

APPENDIX II. DATA COLLECTION AND ANALYSIS

Both hard- and software packages will be described in detail in forthcoming reports of the M.I.T. Buoy Project. This section will describe the functional nature of the system and outline the major subroutines and alogrithms used in the analysis. The major components of the system are depicted in Figs. AII.1 and AII.2.

A. Collection and Format.

Buoy System. Information from the transducers passes through conditioning amplifiers designed to produce 0 - 5 volts variable D.C. output. This output drives voltage controlled oscillators set on standard IRIG channels 3 - 15 and 17. The channels were matched against anticipated data bandwidth to insure at least a 5:1 bandwidth ratio. Accelerometer pulses (and minimeter pulses during some runs) were sampled at 100 hz and combined on a single IRIG channel. A standard 25 khz signal was also transmitted and later used for synchronization and pulse separation during breakout. Signals from up to 22 separate transducers could be accomodated simultaneously. Signals from all IRIG channels were mixed and then used to frequency modulate the transmission signal (243.8 mhz). The major components of the buoy data handling package were modified from an Atlas Missle Telemetry System (USAF excess equipment).

Data received at the base station on Cuttyhunk was recorded in analog, direct mode on a single channel of $\frac{1}{4}$" magnetic tape on a Hewlett Packard Model 3960B (HP3960B) 4 track recorder. A second channel was reserved for voice narration, weather log, and time signal. Both sides of 2400' tapes were used for mean condition runs; one tape held four, 12 minute hourly runs.

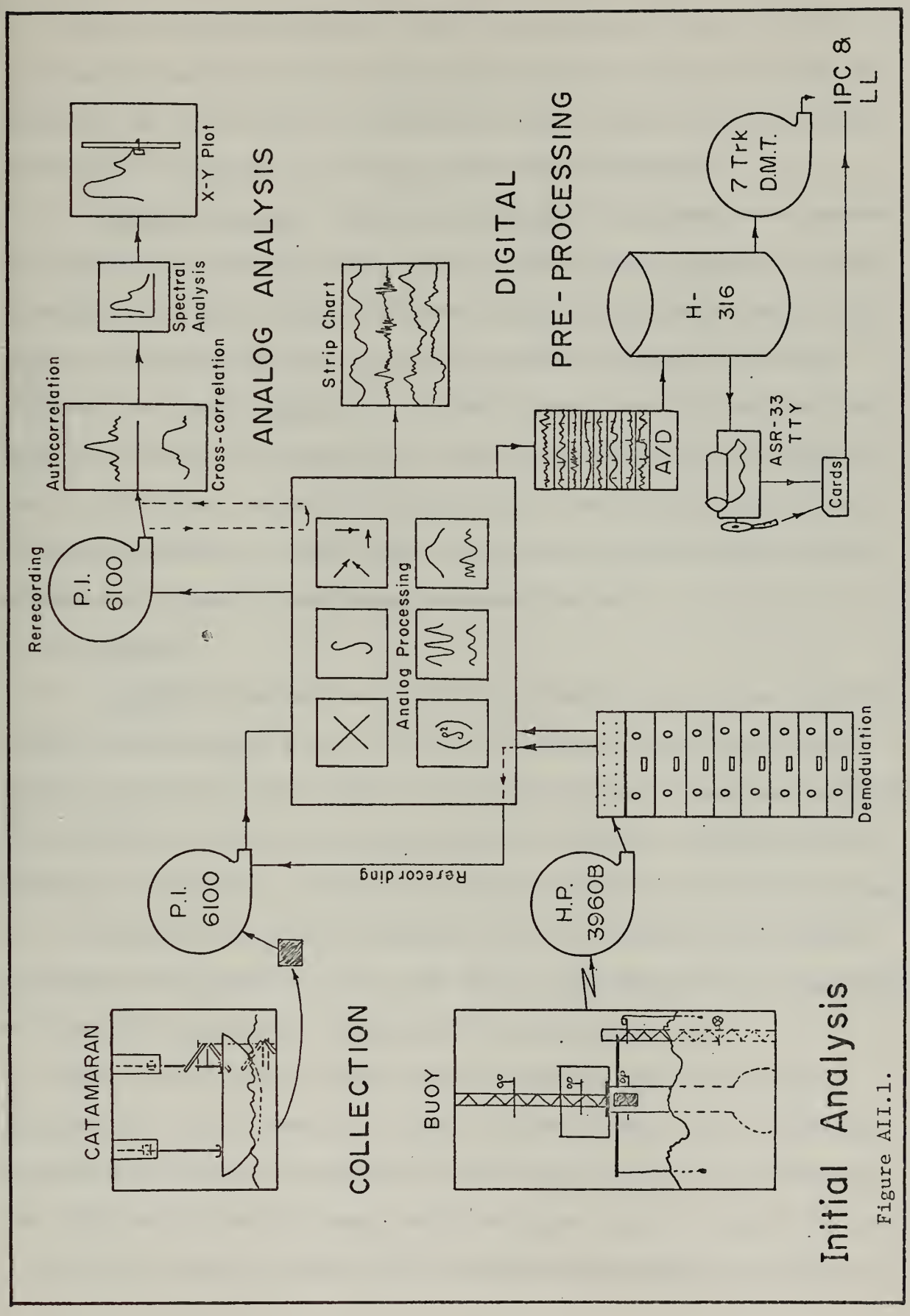
Initial Analysis
COLLECTION
CATAMARAN
BUOY
P.I. 6100
H.P. 3960B
Rerecording
Demodulation
Analog Processing
Rerecording
P.I. 6100
Autocorrelation
Cross-correlation
Spectral Analysis
X-Y Plot
ANALOG ANALYSIS
Strip Chart
DIGITAL
PRE-PROCESSING
A/D
H-316
7 Trk D.M.T.
ASR-33 TTY
Cards
IPC & LL

Figure AII.1.

The only analysis attempted at the site was demodulation and monitoring of selected channels to insure signal quality and continuity. The buoy was turned on and off remotely by a modified Heathkit radio control set which activated a microswitch in the buoy electronics compartment.

Catamaran System. Signals from catamaran transducers were recorded on a Princeton Instruments Model 6100 (PI6100) 8 track recorder. Hot film, thermistor, and accelerometer data were passed through conditioning amplifiers to optimize voltage bias and gain, and then recorded in FM mode. Capillary wave gauge signals, in frequency format, were recorded in direct mode. One channel was reserved for voice narration; this was subsequently used to help select segments for digitization. The incoming data was continuously monitored to insure signal quality and continuity. 2400' tapes allowed over 2 hours of continuous recording per run.

B. Analysis.

General. A combination of digital and analog analysis was employed. Analog processing with strip chart and x-y recorder display was used for initial evaluation. Energy content in selected frequency bands was estimated by filtering and squaring the signals prior to plotting. Analog spectral analysis of potentially interesting events was performed with the assistance of a PI correlator and Fourier analyzer and the x-y plotter. The initial processing familiarized the user with the data and permitted early estimates of fluctuation magnitude for later use in digital processing.

Three digital computers were used for secondary and final analysis. Digitization, preprocessing, and simple analyses such as pulse counts and calibration checks were performed on the Project's Honeywell H-316 computer. This unit has an 8 k memory and is equipped with a 16 channel Raytheon 'miniverter' analog to digital (a/d) converter Model MADC 12A. The miniver-

ter outputs 12 bit a/d words for a full range of ± 10 volts; least bit precision is 5 mv. Programming was in Honeywell's DAP-16 Assembler level language. Output from the Honeywell was in two forms: the digitized data in bit-string, a/d word format on 7 track magnetic tape, and pulse count and calibration information on either the ASR-33 teletypewriter or paper tape. The latter information was transferred to punched cards.

A PDP-7 computer (at Linclon Laboratory) equipped with miltiple tape drives and cathode ray tube (CRT) display was used to examine in detail the tapes produced by the H-316. The bit-string data was first converted to geophysically meaningful units; statistics were calculated; values from orthogonally mounted hot films were converted to U and W; and the resulting information was then rerecorded in a format standard to the facility. The resultant data were displayed on the CRT, limited filtering and spectral analysis performed, and hard copy graphical output obtained for further study. Programming was done in Fortran IV by Mr. B. Laird.

Final analysis was done on the IBM 360 at the M.I.T. Information Processing Facility (IPC). Programs were written in PL/1 to reduce I/O problems, and extensive use was made of a Stromberg-Carlson 4020 (SC-4020) plotter for display of time series, probability distributions, and spectra.

The data handling system is capable of statistical, time history, and frequency domain analysis of up to 16 channels of input data simultaneously. Analog preprocessing capabilities include rerecording at a choice of speeds and formats, filtering, integration, squaring, orthogonal decomposition, amplification, and pulse separation, as well as totally analog computation and display of time history, correlations, and auto-and cross-spectra. The H-316 allows digitization at up to 250 hz.

Buoy Data. The mixed signals from the HP3960B were separated in a

set of 8 demodulators (from the Atlas Missle System). Sampled anemometer signals were separated using ring counters and the 25 khz clock signal for timing. Sections of the data were filtered, squared, amplified and displayed on a 4-track Sanborn recorder to provide an initial overview. Two separate digitizing passes were then made. The first yielded velocity profile information from a pulse counting program on the H-316. Twenty, 30 secon d counts from 10 minutes of each mean condition run were made, transferred to punched cards, and run through a two part program on the IBM 360. The first digital program computed profile parameters on the basis of the logarithmic profile model. The second program used punched card output from the first to compute single and joint histograms and statistical information, displayed on SC-4020 plots. Velocity values from selected runs (with averaging times as short as 5 seconds) were hand plotted in profile, isotach, and vertical shear format for comparison with the strip chart analog data.

In the second digitizing pass, the runs selected for time history analysis were rerecorded on the PI6100 in demodulated form. The data was filtered to avoid aliasing (velocity values at 2.5 hz and wave height at 5 hz using matched Rockwell Model 1010F operational filters), amplified to the full range of the miniverter, and digitized at 10 hz. Calibration during this preprocessing was maintained by passing sinusoidal and D.C. signals through the entire system. The calibration data were displayed on the ASR-33 and transferred to cards for use in the main analysis. Additional calibration checks during digital processing were made by comparison of pulse count and digitized velocity values. The time signal initially recorded on the voice channel of the HP3960B was used to synchronize the two passes. Final analysis used the software package described below.

Catamaran Data. All of the cat's paw data was pre-viewed using

analog techniques. Selected portions were then digitized at 250 hz; the data had been low-pass filtered at 100 hz using the internal PI6100 filters. The voice narration was used to aid in distinguishing the presence of gusts until their imprint on the analog signals became readily recognizable. Nine tapes containing some 2.5×10^7 data points from each of 8 channels were obtained. These tapes contain information from over 75 well identified cat's paws as well as a large amount of background data. The tapes were examined on the L.L. PDP-7 and segments selected for final analysis.

IBM 360 Software. The analysis package was designed to permit rapid, standardized analysis of time series information sampled at equal intervals. Flexibility and user control were major design criteria. The package can handle up to 16 channels of information simultaneously, and allows for the inclusion of two additional channels of computed values such as Reynolds stress and buoyancy fluctuations. In addition, the initial information can be replaced during analysis by other computed values. The package may be of use to other investigators, and is consequently briefly described herein.

Program flow is diagrammed in Fig. AII.2. It is highly modular and designed to handle a wide variety of time series information, with a minimal number of routines specifically restricted to air-sea interaction studies. Flexibility is maintained by user option control from punched card parameters. There is provision for a user supplied routine (OTHER) which can be reached from both time and frequency domains. Time domain analysis is performed first; in the frequency domain segment the original data (stored in a three-dimensional matrix) is replaced by its fourier transform coefficients. The major features and alogrithms are as follows; details will be given in a forthcoming Project report.

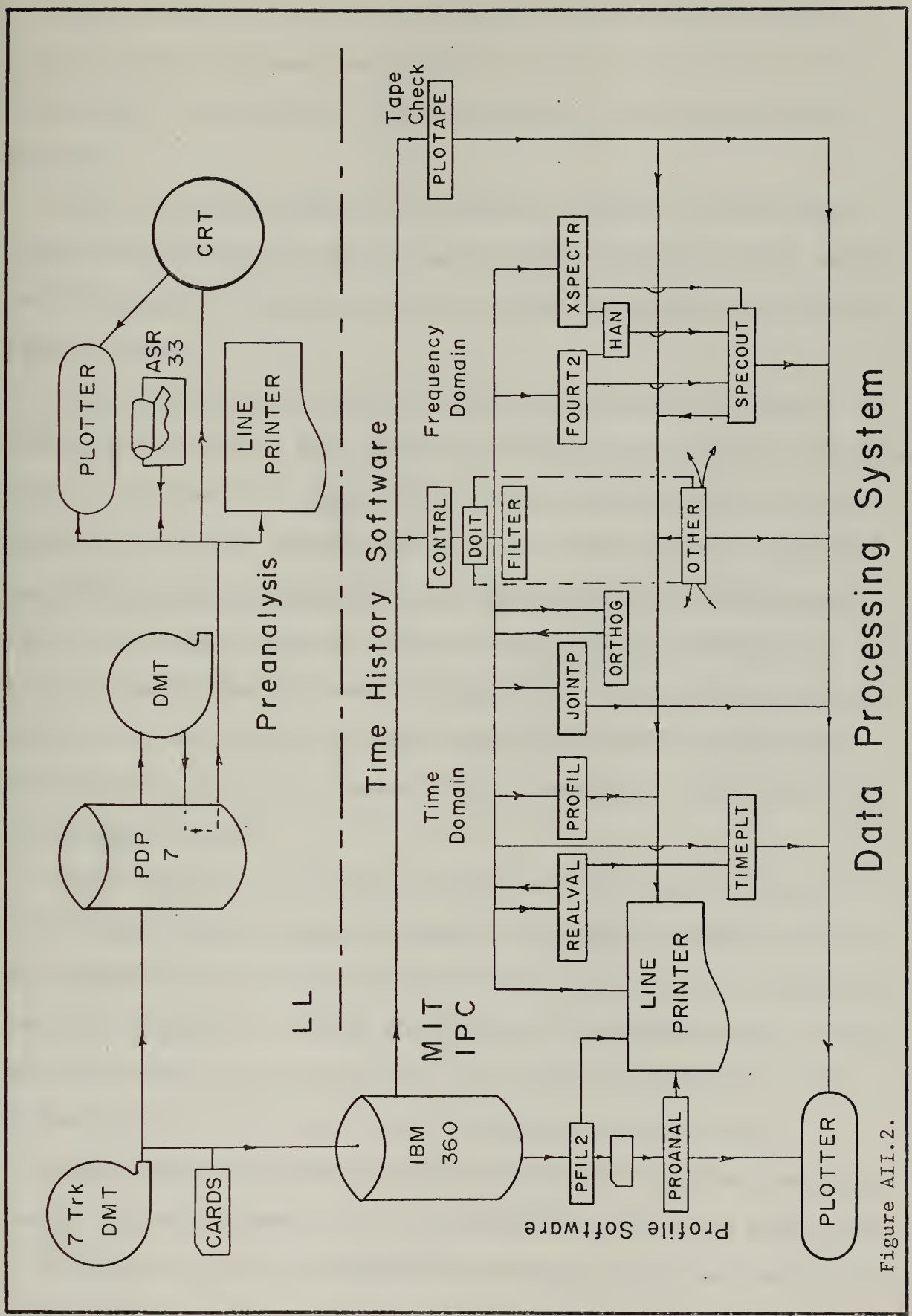
Data Processing System
Time History Software
LL
Preanalysis
MIT
IPC
Time
Domain
Frequency
Domain
Tape
Check
7 Trk
DMT
CARDS
IBM
360
PDP
7
DMT
PLOTTER
ASR
33
CRT
LINE
PRINTER
PFIL2
PROANAL
Profile Software
REALVAL
PROFIL
JOINTP
ORTHOG
CONTRL
DOIT
FILTER
OTHER
FOURT2
HAN
XSPECTR
SPECOUT
TIMEPLT
PLOTAPE
LINE
PRINTER
PLOTTER

Figure AII.2.

CONTRL handles tape positioning, dimensions the major data matrix, selects plot/no plot mode, and inputs data from the tape. This is the only routine that is specifically linked to the H-316 7 track magnetic tape format.

DOIT is called by CONTRL upon completion of input. This subroutine does little computing, but determines which other routines will be called and the sequence of their use. It does contain the hanning and stress formation routines.

REALVAL performs, with operator option, the following functions: conversion of a/d words into voltage; conversion from voltage to real values with up to a quartic fit (required for linearization of the hot films); determination of trend, extrema, and the 1st 4 central moments; computation and plotting of a histogram with user-supplied number of intervals and limits set either to computed extrema or user-supplied; adjustment of values to a calibration standard (used for comparison of pulse count and digital velocities) and/or removal of mean (supplied or computed) and/or trend. Mean and trend may also be removed in DOIT immediately prior to the frequency domain segment.

FILTER operates by fast fourier transforming the data, modifying or deleting the selected frequency components, and then retransforming. The user supplies the modification factors so that effectively any desired window may be employed. A standard cosine taper of adjustable length is included. This routine can be called from up to 3 different locations in DOIT so that the data may be used in both filtered and unfiltered form.

ORTHOG computes horizontal (U) and vertical (W) velocities from orthogonally mounted instruments. The decomposition is done in two steps; first an estimate of U and W is obtained from the known directional response and

velocity readings of the two instruments, and then an alignment correction is made to compensate for mean tilt or oscillatory fluctuations of the probe holder. The background and details of this procedure were discussed at length by Ruggles (1969). There is a choice of either a $\cos\Theta + K \sin\Theta$ or a linear directional fit to the data. The alignment correction assumes that $\overline{W} = 0$ over a number of data points selected by the user, and that the instruments are truly orthogonally mounted. A known mean horizontal velocity, if available, can be used for additional correction. The choice of the averaging interval for $\overline{W} = 0$ is critical, and is made by a consideration of the dynamics of the system and by post-facto examination of plots of the data to insure continuity of values at interval end points. For the catamaran data, 60 points were used for air hot films, 250 for water hot films.

PROFIL computes parameters of the assumed logarithmic profile model; effectively, it compares $U(z)$ to $(U_*/k) \ln(z/z_o)$ by a best fit in the least mean squares sense, taking the instrument heights as known (In previous work from this project, e.g. Ruggles (1969), velocity values were taken as known, z as the variable. In the initial stages of this analysis both methods were used, and for profiles showing correlations with the model better than 0.94 the resulting differences in U_* and z_o were always less than 5%.). If Reynolds stress values are available, the production term of the horizontal component of turbulent kinetic energy equation ($-\overline{u'w'}\ d\overline{U}/dz$) can be calculated. The separate program to handle the pulse count data uses similar alogrithms.

JOINTP computes and plots joint histograms, and also provides one-way histograms and means-on-interval of the input variables.

TIMEPLT plots variables against time, with user controlled or computed scaling and number of strips per SC-4020 frame. It can be accessed both

before and after filtering. This subroutine also plots histograms.

FOURT2 is a USASI Basic Fortran version of the Cooley-Tukey fast fourier transform, written by N. Brenner. It can handle real or complex data in multidimensional, arbitrarily sized arrays. End values are dropped and tapered in DOIT to provide a window prior to transforming; in this analysis approximately 10% of the data was so treated to limit Gibbs effect. The returned coefficients are normalized and hanned in DOIT, then a density factor is applied to result in the power spectral density estimate. The hanned estimate has a χ^2 distribution with 6 dof; restriction of averaging to 3 values was necessary in the catamaran study to preserve detailed resolution in view of the high sampling rate and relatively few points available for analysis (core and averaging limitations).

XSPECTR utilizes the normalized fourier transform coefficients to determine cross-spectral densities (Co and Quad spectra). These are then used to compute coherence magnitude (γ) and phase (θ). The averaging interval used to compute coherence is selectable by the user; in this study 9 points were used for samples under 500 points, 15 for the 5-minute mean condition run segments, and 25 for the 10-second catamaran time periods. The results were then hanned for the longer samples.

SPECOUT prints and plots spectral data. Autospectra were plotted on a log(magnitude) linear (frequency) grid (log-log is also available). Magnitude scaling is based on spectral extrema (up to 10 decades can be accomodated), but the user controls the frequency range. Coherence and phase were plotted from the cross-spectral analyses; the user again controls the frequency range and number of plots.

OTHER is the user supplied routine. It can be accessed from two locations in the time domain and at the end of the frequency domain computations

in DOIT. Two major versions were used in this study, one each for the buoy and catamaran experiments. The buoy version computed mean energy density, both directly from wave height data and by spectral accumulation, and wave momentum at individual frequency components and by considering the energy to be concentrated in waves at the frequency of energy and momentum spectral maxima. The catamaran version had four segments; one computed buoyancy fluctuations and determined joint histograms between buoyancy and other variables; a second formed the natural logarithm of squared and normalized velocity derivatives for the lognormality study; a third created the switch function that was used to evaluate intermittency; and the fourth contained a band pass filter for rapid examination of filtered signals.

Computational Methods. Let x_i, $i = 1, 2, \ldots N$ represent the sampled data values where $N\Delta t = T$ is the total sample length and $1/\Delta t = \Delta f$ the sampling frequency. Then for any a/d word y_i, voltage $v_i = -10.0 + y_i \times 204.8$ from the known characteristics of the miniverter, and $x_i = \sum_{j=0}^{4} A_j v_i^j$ in geophysical units where the A_j's are the conversion values from calibration. Then

$$\text{mean} = \overline{x_i} \equiv \overline{x} = \frac{1}{N} \sum_{i=1}^{N} x_i \qquad \text{and}$$

$$j^{th}\ \text{moment} = \frac{1}{N} \sum_{i=1}^{N} (x_i - \overline{x})^j \qquad \text{so that}$$

$$\text{variance} = \overline{x_i^2} - \overline{x}^2 \equiv \sigma_x^2 ,$$

$$\text{skewness} = \overline{x_i^3} - 3\overline{x_i^2}\,\overline{x} + 2\overline{x}^3 \equiv S_x , \qquad \text{and}$$

$$\text{kurtosis} = \overline{x_i^4} - 4\overline{x_i^3}\,\overline{x} + 6\overline{x_i^2}\,\overline{x}^2 - 3\overline{x}^4 \equiv K_x .$$

Trend (T) is found from a best fit in the least mean squares sense to the data. Define $x_T = Ti + \beta$, and minimize

$\delta^2 \equiv (x_i - x_T)^2 = (x_i - Ti - \beta)^2$, where both x_i and i are considered to be random variates. Then the expectation of δ^2 is

$$E(\delta^2) = E\left[(x_i - \bar{x}) - T(i - \bar{i}) - (\beta - \bar{x} + T\bar{i})\right]^2$$

$$= \sigma_x^2 + T^2\sigma_i^2 + (\beta - \bar{x} + T\bar{i})^2 - 2T\sigma_{xi}^2$$

where σ_{xi}^2 is the covariance of x_i and i. The positive definite part must = 0 for minimum δ^2, thus $\beta = \bar{x} - T\bar{i}$.

With the correlation coefficient $\rho \equiv \dfrac{\sigma_{xi}^2}{(\sigma_x^2\sigma_i^2)^{1/2}}$,

adding and subtracting $\rho\sigma_x^2$, $E(\delta^2) = (T\sigma_i - \rho\sigma_x)^2 + (1-\rho^2)\sigma_x^2$

so that for minimum δ^2, $T = \rho\dfrac{\sigma_x}{\sigma_i} = \dfrac{\sigma_{xi}^2}{\sigma_i^2}$ and $E(\delta^2) = (1-\rho^2)\sigma_x^2$.

Thus, $$T = \frac{\frac{1}{N}\sum_{i=1}^{N} i x_i - \bar{i}\,\bar{x}}{\frac{1}{N}\sum_{i=1}^{N} i^2 - \bar{i}^2} \quad ;$$

but $\bar{i} = \dfrac{N+1}{2}$, $\sum_{i=1}^{N} i^2 = \dfrac{N(N+1)(N+2)}{6}$,

so that $$T = \frac{12\sum_{i=1}^{N} i x_i - 6N(N+1)\bar{x}}{N(N^2-1)} \quad ,$$

and if the mean and trend are removed,

$$\delta_i = x_i - \left(\bar{x} + T\left(\frac{-(N+1)}{2} + i\right)\right)$$

For the calculation of profile parameters, the assumed model is

$$U(z) = \frac{U_*}{\kappa}\ln\left(\frac{z}{z_o}\right)$$

where U_* is friction velocity, κ is Von Karman's constant (= 0.40) and z_o is roughness length. Using the least squares method developed above, substituting U_i for x_i, $S \equiv U_*/\kappa$ for T , $\ln(z)$ for i and $(-U_*/\kappa)\ln(z_o)$ for β ,

$$\rho = \frac{\sigma_{U\cdot\ln(z)}^2}{\sigma_U\,\sigma_{\ln(z)}} \quad , \quad S = \frac{\sigma_{U\cdot\ln(z)}^2}{\sigma_{\ln(z)}^2} \quad ,$$

$$U_* = \kappa S \quad , \quad \ln(z_o) = \overline{\ln(z)} - \frac{\bar{U}}{S} \quad .$$

Further, stress $\tau = DU_*^2$ where D= density of the medium,

$$U(10M) \equiv U_{10} = \frac{U_*}{K}\left(3 \times 2.302585 - \ln(z_0)\right)$$

for velocity in cm/sec and heights in cm, and drag coefficient

$$C_{d_{10}} = \left(U_*/U_{10}\right)^2$$

Figure AII.3 shows the assumed mounting and notation for orthogonal decomposition. Assuming that the hot films have a linear directional response in some appropriate range of ϕ, let the velocity recorded be V_i, so that

$$V_i = Q_i\left(1 - P(\phi - \psi)\right)$$

where Q_i is the actual velocity and P and ψ are determined from calibrations. For the DISA hot films, $\psi = 25^\circ$, P = .0021 and the relationship holds ($\rho = 0.92$) in the attack angle range $25^\circ \leq \phi \leq 80^\circ$.

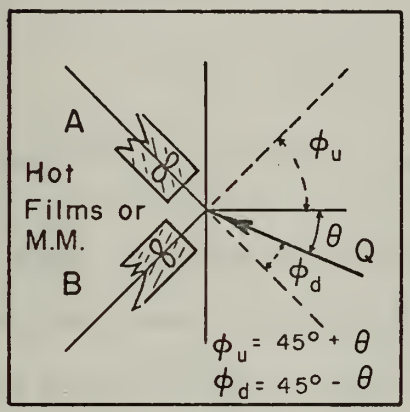

Figure AII.3

But $\phi_u = 45^\circ + \theta$ and $\phi_d = 45^\circ - \theta$ so that

$$V_{A_i} = Q_i\left(1 - P(20 - \theta_i)\right), \quad V_{B_i} = \left(1 - P(20 + \theta_i)\right),$$

$$Q_i = \frac{V_{A_i} + V_{B_i}}{2(1 - 20P)}, \quad \theta_i = \frac{(1-20P)\left(1 - \frac{V_{B_i}}{V_{A_i}}\right)}{P\left(1 + V_{B_i}/V_{A_i}\right)}.$$

Then horizontal (U) and vertical (W) velocity estimates are obtained from

$$W_i = Q_i \sin\theta_i, \quad U_i = Q_i \cos\theta_i.$$

For minimeters, the directional response is best given by

$$V_i = Q_i\left(\cos\phi_i + P\sin\phi_i\right)$$

in the range $0^\circ < \phi \leq 80^\circ$, with the value of P varying between instruments. Substituting for ϕ in terms of θ and then in terms of W and U,

$$U_i = \frac{\sqrt{2}}{2}\left(\frac{V_{A_i} + V_{B_i}}{1 + P}\right), \quad W_i = \frac{\sqrt{2}}{2}\left(\frac{V_{A_i} - V_{B_i}}{1 - P}\right).$$

To correct for tilt, assume W_i and U_i found as above are actually at an angle α_i to the correct axis. Then essentially, letting $\mathcal{U}$ and $\mathcal{W}$ represent the corrected values,

$$\mathcal{W}_i = W_i \cos\alpha_i - U_i \sin\alpha_i \quad , \quad \mathcal{U}_i = W_i \sin\alpha_i + U_i \cos\alpha_i \ .$$

Require $\overline{\mathcal{W}} = 0$; then if a known $\overline{U}$ is available, the correction to lowest order is found from

$$\sin\alpha_i \doteq \frac{\langle W \rangle}{\overline{U}} \quad , \quad \cos\alpha_i \doteq \frac{\langle U \rangle}{\overline{U}}$$

while if $\overline{U}$ is not known, $\tan\alpha_i \doteq \frac{\langle W \rangle}{\langle U \rangle}$ is used. The averaging times are selected by the user to minimize mean or fluctuating tilt. Total rms error in computed Reynolds stress using this lowest order technique can be as large as 20%. For very small values of ϕ, say $\phi < 10^\circ$, the linear hot film directional response fit overestimates V_i by roughly 1.5%. Assuming 10% rms turbulence levels for normal atmospheric conditions, the probable rms deviation of ϕ around 45° is roughly 10°; thus this type of fit overestimates only extremely high turbulence values. This is somewhat compensated for by the frequency response of the units, but still tends to emphasize anomalously high stress values which is useful for detection.

In spectral computations, FOURT2 returns the real and imaginary coefficients of the discretized fourier transform,

$$F(k\Delta f) = \sum_{j=-N/2}^{N/2} x(j\Delta t)\, e^{2\pi i j k \Delta t \Delta f} \ .$$

Where $t = j\Delta t$ and $s = k\Delta f$, $F(s) = \alpha(s) + i\,\beta(s)$ is returned. The coefficients are normalized by the number of data points, e.g. $a(s) = 2\alpha(s)/N$, and the power or variance spectral estimate is formed:

$$\Phi_{xx}(s) = |F(s)|^2 = a(s)^2 + b(s)^2 \ .$$

Hanning is applied:

$$\Phi_{xx}(s) = \frac{1}{4}\Phi_{xx}(s-1) + \frac{1}{2}\Phi_{xx}(s) + \frac{1}{4}\Phi_{xx}(s+1)$$

and the power spectral density estimate is formed by multiplying by the density factor, $D = N\Delta t = T$

i.e., $\Phi_{xx}(s) = \Phi_{xx}(s) \cdot D$ or $\Phi_{xx}(s) = (\alpha(s)^2 + \beta(s)^2)/f_n$

where f_n is the Nyquist or folding frequency = $1/2\Delta t$.

Computation of the cross-spectrum (following Wunsch,(1970)) is based on the hypothesis that the variables are related by the convolution relationship, $x_i = \sum_{k=-\infty}^{\infty} \xi_k y_{i-k}$

for all realizations of x and y, taking x and y as random variates so that ξ is a known transient. Then

$$F_x(s) = \Xi_\xi(s)\, G_y(s)$$

where Ξ and G are the fourier transforms of ξ and y. Then

$$\Xi_\xi(s) = \frac{F_x(s)}{G_y(s)} = \frac{|F_x(s)|}{|G_y(s)|}\frac{e^{i\mu(s)}}{e^{i\nu(s)}} \equiv |\gamma(s)|e^{i\theta(s)}.$$

For the hypothesized convolution relationship to have meaning, $\theta(s)$ must be a smoothly varying function of s, and coherence is a measure of this smoothness, i.e.,

$$Coh(s) = \lim_{M\to\infty} \sum_{m=-M/2}^{M/2} e^{i\theta(s+m)}$$

For peaked spectra this is best computed in a form which includes a weigting by the power at the various frequencies, i.e.,

$$e^{i\theta(s)} = e^{i(\mu(s)-\nu(s))} = \frac{F_x(s)\, G_y^*(s)}{|F_x(s)|\,|G_y(s)|}$$

where * denotes the complex conjugate. But

$F_x(s)\,G_y^*(s) \equiv Co_{xy}(s) + i\,Quad_{xy}(s)$, and $|F_x(s)||G_y(s)| = \left(\Phi_{xx}(s)\,\Phi_{yy}(s)\right)^{1/2}$

Coherence magnitude is thus defined as

$$\gamma_{xy}(s) = \frac{\left\langle \left(Co_{xy}(s)^2 + Quad_{xy}(s)^2\right)^{1/2} \right\rangle}{\left\langle \left(\Phi_{xx}(s)\;\Phi_{yy}(s)\right)^{1/2} \right\rangle} .$$

Using R and I to denote real and imaginary parts of the fourier transform, the alogrithm is

$$\gamma_{xy}(s) = \frac{\frac{1}{M}\sum_{m=-M/2}^{M/2}\left[\left(F_R(s+m)\,G_R(s+m)\right)^2 + \left(F_I(s+m)G_R(s+m) - F_R(s+m)G_I(s+m)\right)^2\right]^{1/2}}{\frac{1}{M}\sum_{m=-M/2}^{M/2}\left[\left(F_R(s+m)^2 + F_I(s+m)^2\right)^{1/2}\left(G_R(s+m)^2 + G_I(s+m)^2\right)^{1/2}\right]}$$

Similarly, phase

$$\Theta_{xy}(s) = \frac{1}{M}\sum_{m=-M/2}^{M/2} TAN^{-1}\left(\frac{Quad_{xy}(s)}{Co_{xy}(s)}\right)$$

M is chosen by the user and end values are assumed symmetrical for the averaging. The alogrithm is designed so that positive $\Theta_{xy}(s)$ means y leads x.

Mean wave energy density is computed from the relationship

$$E = \rho g \overline{\eta^2}$$

where η is wave height, ρ density, and g gravity. But $\overline{\eta^2} = \varphi_{\eta\eta}(0)$ where φ is the autocorrelation function (not computed); in turn,

$$\varphi_{\eta\eta}(0) = \int_{-\infty}^{\infty} \eta^2(t)\,dt = \int_{-\infty}^{\infty} |F_\eta(s)|^2\,ds = \int_{-\infty}^{\infty} \bar{\Phi}_{\eta\eta}(s)\,ds \doteq \sum_{-N}^{N} \bar{\Phi}_{\eta\eta}(s)\,\Delta s$$

Both direct and spectral summation techniques were used. The results were always within 1.5% of each other for spectra with 6 dof or more. Departures of 20% with mean departure roughly 5% occured with 2 dof (raw or unhanned short spectral estimates).

Momentum was computed from the relationship

$$M(s) = E(s)/c(s)$$

where c is linear wave celerity,

$$c^2(s) = \frac{g}{k} \operatorname{Tanh}(kh) = \frac{g^2}{4\pi^2 s^2} \operatorname{Tanh} \frac{4\pi^2 s^2 h}{g}$$

k = wave number and h = 31 m. Thus,

$$M(s) = \rho g \Phi_{\eta\eta}(s)/c(s)$$

Mean momentum density was computed both by summation over the spectral components and by assumption that E was primarily attributable to the wave of maximum variance or momentum, i.e.,

$$M = \frac{E}{c(s(\Phi_{max}))} = \frac{E}{c(s(M_{max}))}$$

Bibliography

Aagaard, E. E., 1964, Dynamic Characteristics of Sensors for Marine Temperature Measurements, Marine Technology Symposium Rpt., 117-125.

Amos, D. E., and L. H. Koopmans, 1963, Tables of the Distribution of the Coefficient of Coherence for Stationary Bivariate Gaussian Processes, Scandia Corp. Monograph, SCR-483.

Barger, W. R., W. D. Garrett, E. L. Mollo-Christensen, and K. W. Ruggles, 1970, Effects of an Artificial Sea Slick upon the Atmosphere and the Ocean, J. Appl. Met., 9, 3.

Barnett, T. P., and J. C. Wilkerson, 1967, On the Generation of Ocean Wind Waves Inferred from Airborne Radar Measurements of Fetch Limited Spectra, J. Marine Res., 25, 3.

Businger, J. A., J. C. Wyngaard, Y. Izumi, and E. F. Bradley, 1970, Flux-Profile Relationships in the Atmospheric Surface Layer, J. Atmos. Sci., 28.

Chambers, A. J., P. A. Mangarella, R. L. Street, and E. Y. Hsu, 1970, An Experimental Investigation of Transfer of Momentum at an Air-Water Interface, Dept. Civil Eng., Stanford, T.R. 133.

Chen, W. Y., 1971, Lognormality of Small Scale Structure of Turbulence, to be published.

Cox, C. S., 1958, Measurements of Slopes of High-Frequency Waves, J. Marine Res., 16, 3.

Cramér, H., 1955, The Elements of Probability Theory and Some of Its Applications, John Wiley and Sons, New York.

Crapper, G. D., 1970, Nonlinear Capillary Waves Generated by Steep Gravity Waves, J. Fluid Mech., 40, 1.

Davidson, K. L., 1970, An Investigation of the Influence of Water Waves on the Adjacent Airflow, Dept. Met. and Ocean., Univ. Michigan, ORA Project 08849.

Davis, R. E., 1970, On the Turbulent Flow Over a Wavy Boundary, J. Fluid Mech., 42, 4.

Dobson, F. W., 1969, Observations of Normal Pressure on Wind Generated Waves, I.O.U.B.C. Ref. No. T.56.

Dobson, F. W., 1971, Measurements of Atmospheric Pressure on Wind-Generated Sea Waves, J. Fluid Mech., 48, 1.

Elliott, J. A., 1970, Microscale Pressure Fluctuations Measured Within the Lower Atmospheric Boundary Layer, I.O.U.B.C. Ref. No. T.65.

Frenkiel, F. N., and P. S. Klebanoff, 1971, Statistical Properties of Velocity Derivatives in a Turbulent Field, J. Fluid Mech., 48, 1.

Garrett, J., 1970, Field Observations of Frequency Domain Statistics and Nonlinear Effects in Wind-Generated Ocean Waves, I.O.U.B.C. Ref. No., T.60.

Greenspan, H. P., and D. J. Benney, 1963, On Shear-Layer Instability, Breakdown, and Transition, J. Fluid Mech., 15, 1.

Groscup, W. D., 1971, Observations of the Mean Wind Profile over the Open Ocean, M.S. Thesis, Dept. Met., M.I.T.

Gupta, A. K., M. T. Landahl, and E. L. Mollo-Christensen, 1968, Experimental and Theoretical Investigation of the Stability of Air Flow Over a Water Surface, J. Fluid Mech., 33, 4.

Gurvich, A. S., and A. M. Yaglom, 1967, Breakdown of Eddies and Probability Distributions for Small-Scale Turbulence, Phys. Fluids Suppl., 10.

Hasselmann, K., 1967, Non-Linear Interactions Treated by the Methods of Theoretical Physics (With Application to the Generation of Waves by Wind), Proc. Roy. Soc. A, 299.

Hasselmann, K., 1971, On the Mass and Momentum Transfer Between Short Gravity Waves and Larger Scale Motions, to be published.

Haugen, D. A., J. C. Kaimal, and E. F. Bradley, 1971, An Experimental Study of Reynolds Stress and Heat Flux in the Atmospheric Surface Layer, Quart. J. Roy. Met. Soc., 97.

Hicks, B. B., and A. J. Dyer, 1970, Measurements of Eddy Fluxes Over The Sea from an Offshore Oil Rig, Quart J. Roy. Met. Soc., 96.

Jeffreys, H., 1925, On the Formation of Water Waves by Wind, Proc. Roy. Soc. A, 107.

Jeffreys, H., 1926, On the Formation of Water Waves by Wind, Proc. Roy. Soc. A, 110.

Kendall, J. M., 1970, The Turbulent Boundary Layer Over a Wall with Progressive Surface Waves, J. Fluid Mech., 41, 2.

Kinsman, B., 1965, Wind Waves, P-entice Hall Inc., Englewood Cliffs, New Jersey.

Klebanoff, P. S., K. D. Tidstrom, and L. M. Sargent, 1962, The Three-Dimensional Nature of Boundary Layer Instability, J. Fluid Mech., 12.

Kline, S. T., W. C. Reynolds, F. C. Schraub, and P. W. Runstadler, 1967, The Structure of Turbulent Boundary Layers, J. Fluid Mech., 30,4.

Kolmogorov, A. N., 1962, A Refinement of Previous Hypotheses Concerning the Local Structure of Turbulence in a Viscous Incompressible Fluid at High Reynolds Number, J. Fluid Mech., 13.

Landau, L. D., 1959, Fluid Mechanics, Addison-Wesley, London.

Longuet-Higgins, M. S., 1963, The Generation of Capillary Waves by Steep Gravity Waves, J. Fluid Mech., 16.

Longuet-Higgins, M. S., 1969a, On the Action of a Variable Stress at the Surface of Water Waves, Phys. Fluids, 12, 4.

Longuet-Higgins, M. S., 1969b, A Non-Linear Mechanism for the Generation of Sea Waves, Proc. Roy. Soc. A, 311.

Longuet-Higgins, M. S., and R. W. Stewart, 1960, Changes in the Form of Short Gravity Waves on Long Waves and Tidal Currents, J. Fluid Mech., 8.

Longuet-Higgins, M. S., and R. W. Stewart, 1961, The Changes in Amplitude of Short Gravity Waves on Steady Non-Uniform Currents, J. Fluid Mech., 10.

Lumley, J. L., and H. A. Panofsky, 1964, The Structure of Atmospheric Turbulence, Interscience Publishers, New York.

Mangarella, P. A., A. J. Chambers, R. L. Street, and E. Y. Hsu, 1970, Energy and Mass Transport Through an Air-Water Interface, Dept. Civil Eng., Stanford, T.R. 134.

McBean, G. A., 1970, The Turbulent Transfer Mechanisms in the Atmospheric Layer, I.O.U.B.C. Ref. T.66.

McGoldrick, L. F., 1965, Resonant Interactions Among Capillary-Gravity Waves, J. Fluid Mech., 21, 2.

McGoldrick, L. F., 1970, An Experiment on Second-Order Capillary Gravity Resonant Wave Interactions, J. Fluid Mech., 40, 2.

Miles, J. W., 1957, On the Generation of Surface Waves by Shear Flows, J. Fluid Mech., 3.

Mitsuyasu, H., 1969, On the Growth of the Spectrum of Wind Generated Waves (II), Rsch. Inst. Appl. Mech., Kyushu Univ., Fukuoka, Japan, XVII, No. 59.

Mollo-Christensen, E. L., 1970, Observations and Speculations on Mechanics of Wave Generation by Wind, Dept. Meteor., M.I.T., Rpt. 70-2.

Mollo-Christensen, E. L., 1971, Physics of Turbulent Flow, A.I.A.A. Jour., 9,7.

Mollo-Christensen, E. L., and C. E. Dorman, 1971, A Buoy System for Air-Sea Interaction Studies, Dept. Meteor., M.I.T., Rpt. 71-4.

Mollo-Christensen, E. L., and W. D. Groscup, 1971, Observations of the Boundary Layer Near the Sea Surface, Proc. Xth Symposium on Advanced Methods and Problems in Fluid Dynamics, Rynia, Poland.

Munk, W., 1955, High Frequency Spectrum of Ocean Waves, J. Marine Res., 14, 4.

Obukhov, A. M., 1962, Some Specific Features of Atmospheric Turbulence, J. Fluid Mech., 13.

Phillips, O. M., 1957, On the Generation of Waves by Turbulent Wind, J. Fluid Mech., 2.

Phillips, O. M., 1958, The Equilibrium Range in the Spectrum of Wind-Generated Waves, J. Fluid Mech., 4.

Phillips, O. M., 1966, The Dynamics of the Upper Ocean, University Press, Cambridge.

Ramzy, J. R., and E. T. Young, 1968, Investigation of Temperature Fluctuations Near the Air-Sea Interface, M.S. Thesis, Naval Postgraduate School, Monterey, California.

Rao, K. N., and M. A. B. Narayanan, 1971, The 'Bursting' Phenomenon in a Turbulent Boundary Layer, J. Fluid Mech., 48, 2.

Rasmussen, C. G., and B. F. Bellhouse, 1968, Low Frequency Characteristics of Hot-Film Anemometers, DISA Info. Bull. No. 6, DISA S&B, Midland Park, New Jersey.

Ruggles, K. W., 1969, Observations of the Wind Field in the First Ten Meters of the Atmosphere above the Ocean, Dept. Meteor., M.I.T., Rpt. 69-1.

Ruggles, K. W., 1970, The Vertical Mean Wind Profile Over the Ocean for Light to Moderate Winds, J. Appl. Met., 9, 3.

Sadeh, W. Z., J. E. Cermak, and T. Kawatani, 1971, Flow Over High Roughness Elements, Boundary Layer Met., 1.

Saeger, J. C., and W. C. Reynolds, 1971, Perturbation Pressures over Travelling Sinusoidal Waves with Fully Developed Shear Flow, Dept. Mech. Eng., Stanford, T.R. FM-9.

Schule, J. J., L. S. Simpson, and P. DeLeonibus, 1971, A Study of Fetch-Limited Wave Spectra with Airborne Laser, J. Geo. Res., 76, 18.

Seesholtz, J. R., 1968, A Field Investigation of Airflow Immediately Above Ocean Surface Waves, Ph.D. Thesis, Dept. Meteor., M.I.T.

Shemdin, O. H., and R. J. Lai, 1970, Laboratory Investigation of Wave-Induced Motion Above Air-Sea Interface, Dept. Coastal and Ocean. Eng., Univ. Florida, T.R. 6.

Shonting, D. H., 1967, Measurements of Particle Motions in Ocean Waves, J. Marine Res., 25, 2.

Shonting, D. H., 1968, Autospectra of Observed Particle Motions in Wind Waves, J. Marine Res., 26, 1.

Simmons, W. F., 1969, A Variational Method for Weak Resonant Wave Interactions, Proc. Roy. Soc. A, 309.

Snyder, P. L., and C. S. Cox, 1966, A Field Study of the Wind Generation of Ocean Waves, J. Marine Res., 24, 2.

Steiner, A., 1971, On the Reverse Transition of a Turbulent Flow Under the Action of Buoyancy Forces, J. Fluid Mech., 47, 3.

Stewart, R. H., 1970, Laboratory Studies of the Velocity Field Over Deep-Water Waves, J. Fluid Mech., 42, 4.

Stewart, R. W., 1961, The Wave Drag of Wind Over Water, J. Fluid Mech., 10.

Stewart, R. W., 1967, Mechanics of the Air-Sea Interface, Phys. Fluids Suppl., 10

Stewart, R. W., and M. J. Manton, 1971, Generation of Waves by Advected Pressure Fluctuations, Geo. Fluid Dyn., 2, 3.

Stewart, R. W., and H. L. Grant, 1962, Determination of the Rate of Dissipation of Turbulent Energy Near the Sea Surface in the Presence of Waves, J. Geo. Res., 67.

Sutherland, A. J., 1968, Growth of Spectral Components in a Wind-Generated Wave Train, J. Fluid Mech., 33,3.

Van Dorn, W., 1953, Wind Stress on an Artificial Pond, J. Marine Res., 12.

Von Zweck, O. H., 1969, Observations of Propagation Characteristics of a Wind Driven Sea, Dept. Meteor., M.I.T., Rpt. 69-4.

Wilton, J. R., 1915, On Ripples, Phil. Mag., 29, 6.

Wu, J., 1969a, A Criterion for Determining Air-Flow Separation from Wind Waves, Tellus, 21, 5.

Wu, J., 1969b, Wind Stress and Surface Roughness, J. Geo. Res., 74, 2.

Wu, J., 1970, Wind-Wave Interactions, Phys. Fluids, 13, 8.

Wunsch, C. I., 1970, Lecture Notes on Oceanographic Time Series, M.I.T.

Wyngaard, J. C., J. T. Bauman, and R. A. Lynch, 1971, Cup Anemometer Dynamics, Sympos. on Flow, Pittsburg, Pennsylvania, Paper 2-17-195.

Yefimov, V. V., and G. N. Khristoforov, 1969, Some Features of the Velocity Field in the Layer of Wind-Driven Swell, Izvestia, Atmos. and Oceanic Phys., 5, 10.

ACKNOWLEDGEMENTS

The author wishes to express his deepest appreciation to his advisor, Prof. E. L. Mollo-Christensen, whose ideas and experience formed the backbone of this study and whose guidance and support were indispensible to its conclusion.

The experiments were made possible by the efforts of Mr. K. Morey who designed most of the sensors and the analog analysis system and by the seaworthy advice and friendship of Mr. Dan Clark whose firm constructed and set the main buoy. The assistance of Mr. J. Peers in equipment design and maintenance and in data collection was deeply appreciated. The seamanship of Capt. L. Letourneau of the Shrock, and of Mr. D. Jenkins and Mr. A. Wilder of Cuttyhunk who filled in in time of need, made the buoy operation successful and safe. Mr. E. Bean and Mr. J. Mazarini constructed and helped design the catamaran and most of the hardware.

Thanks are also due to Cdr. W. Groscup, USN, Mr. J. D'Albora, and Mr. T. Burch who as fellow students assisted in the buoy experiment; to Mr. R. Gaston who designed the cat support structure and assisted in the experiment; to Mr. R. Paquette who helped with equipment and rigging; to Mrs. J. Bow and Mrs. L. Mandl of the M.I.T. IPC who helped eliminate system bugs; to Mr. S. Ricci who assisted with the graphics; and to Miss. S. Berson and Miss. K. Higgins who typed the manuscript.

The author also wishes to express his gratitude to Capt. P. Bucklew, USN (Ret.) who had the foresight to long ago acknowledge the need for oceanographic research in the Naval Special Warfare program and whose conviction made the author's academic pursuits possible.

BIOGRAPHICAL NOTE

The author was born on 27 August, 1940, in Cambridge, Massachusetts. He graduated from high school in Bedford, Massachusetts in 1958 and then attended Dartmouth College under a NROTC scholarship. At Dartmouth he was awarded a Senior Fellowship in Geography; he received his B.A. in 1962. He then served in the U.S. Navy on board a frigate and with Naval Special Warfare units prior to attending the Naval Postgraduate School. He received his M.S. in Oceanography in 1968; his thesis, under Prof. W. Thompson, was a sediment budget for southern Monterey Bay. He next received orders to duty under instruction at M.I.T., and upon completion of the Ph.D. in Oceanography in October 1971, was assigned to the Naval Inshore Warfare Command, Pacific. He is a Lieutenant Commander in the U. S. Navy.